POLITECNICO
MILANO 1863

DOCTORAL PROGRAM IN ARCHITECTURE, BUILT ENVIRONMENT AND CONSTRUCTION ENGINEERING
(31st cycle)

Seismic analysis of Underground works and practice: The case of MetroLima

Supervisors:

prof. eng. Alberto Franchi
prof. eng. Pietro Crespi
eng. Giammichele Melis

PhD Candidate:

eng. Marco Zucca

Tutor:

prof. eng. Carmelo Gentile

ABSTRACT

The evaluation of the seismic behavior of underground structures represents one of the most actual seismic geotechnical and structural engineering research topics.
In the last decades, different types of simplified and numerical approaches have been developed for the correct analysis of the seismic vulnerability of these important infrastructures and a series of laboratory tests for the seismic behavior characterization of the soils (e.g. resonant column test, etc.) and of the coupled soil-structure system (e.g. centrifuge test, etc.) have been conducted, especially after the recent strong earthquakes where the underground structures have been subjected to significant damages. In the same way, in the last few years, the Technical Codes are beginning to pay attention to the seismic design of these structures.
Despite the significant development of knowledge, described above, still remain open several uncertainties of the correct reproduction of the underground structures behavior under seismic load.
The goal of this research project is to further improve the knowledge of the underground structures behavior under seismic load, with the application of different simplified approaches, numerical models and laboratory tests, taking as case study the new Lima Metro line 2.

In the first chapter, a short description of the underground structures behavior under seismic action is presented. Particular attention is devoted to the description of the underground structure seismic response during the most important recent earthquake events.
Following the introduction, the second chapter reports a detailed description of the actual techniques for the evaluation of the seismic response of the underground structures, taking into special consideration the evolution of the numerical approaches of the coupled soil-structure interaction system and the definition of the non-linear behavior of the soil.
In the third chapter, the attention is focused on the comparison between numerical methods and simplified approaches through the execution of sensitivity analysis considering the variation of the soil mechanical properties (in particular of the shear modulus) remaining within the category type B according to the limit, in terms of shear waves velocity, defined by Eurocode 8. The results, obtained by the application of the different type of approaches, are discussed from a critical point of view.
The fourth chapter reports a detailed description of the case study: the project of the new Lima Metro line 2. Otherwise the structural characteristics of the metro stations, particular attention is devoted to the hydrogeological, geological and geotechnical characterization of the project area. A series of laboratory and in situ tests have been carried out in order to obtain the mechanical properties of the soils. In particular, the attention is focused on the Mercado Santa Anita metro station that is the first metro station built. For the evaluation of the seismic behavior of this station simplified decoupled approaches and numerical analysis are performed.
In the fifth chapter, the final considerations of the results obtained by the execution of the different types of analysis are discussed, also considering as observed by the case study described in the fourth chapter.

KEYWORDS: underground structures, soil-structure interaction, finite element analysis, finite difference analysis, earthquake, seismic vulnerability

Summary

1. INTRODUCTION

1.1. Seismic behavior of underground structures: overview and some open issues

Underground structures can be grouped into two broad categories: large multi-story structures (e.g. metro stations, parking, etc.) and long underground structures (e.g. tunnels). From the construction method point of view, underground structures con be classified as follow (Bickel, 1996): bored or mined tunnels, cut and cover tunnels and immersed tube tunnels (Figure 1).

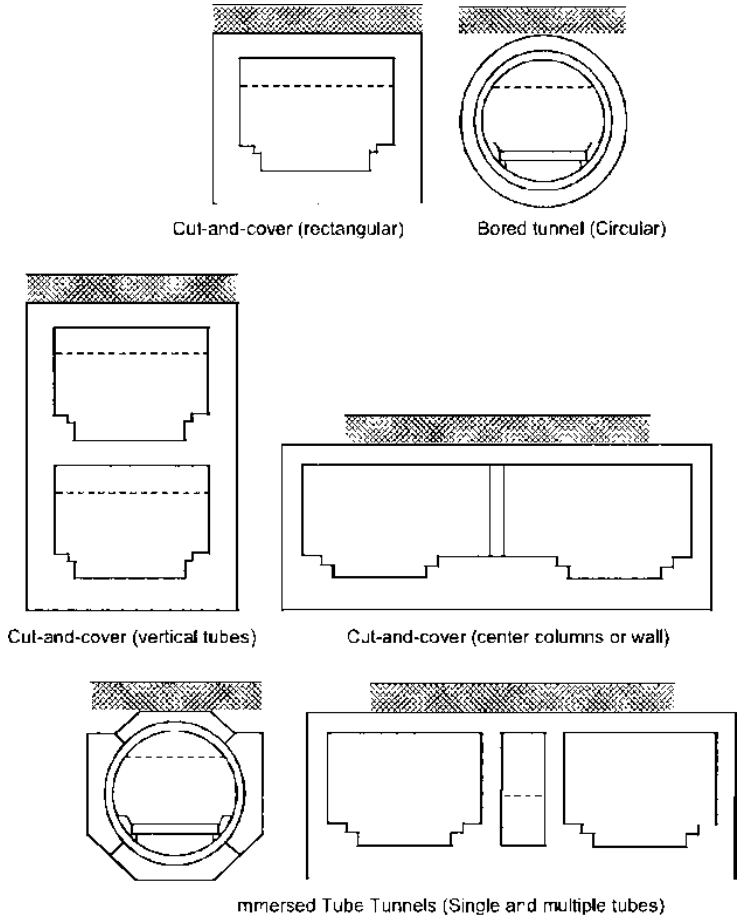

Figure 1: Cross sections of tunnels (Power et al., 1998)

Unlike surface constructions, underground structures were considered, for a long period, practically invulnerable to earthquakes. This consideration about underground structures safety, however, has been changed after some of them suffered serious damages caused by recent earthquakes, including the 1995 Kobe (Japan), the 1999 Chi-Chi (Taiwan) and the 1999 Kocaeli (Turkey) earthquakes (Hashash et al., 2001), when their seismic design was not adequate. For this reason, an efficient and more accurate seismic design is of great importance, especially in areas characterized by a high level of seismic intensity.
Despite the differences in terms of construction method and structural characteristics of the various underground structures typologies, described above, the seismic response of these structures is, generally, dominated by similar parameters.

The correct seismic design requires a very good knowledge of the behavior of this type of structures under seismic loads but the different seismic response of these structures related to surface constructions and the complex soil-structure interaction phenomena contribute to create uncertainty on the evaluation of their seismic behavior.
During last decades, this knowledge shortfall, that is also reflected on the technical code regulations and guidelines, motivated a relevant number of research project, aiming to study the response of embedded structures under ground shaking or earthquake induced ground failures.
The underground structures seismic behavior during recent earthquakes has been studied by several researchers (Dowding & Roze, 1978, Owen & Scholl, 1981, Yoshikawa & Fukuchi, 1984, Sharma & Judd, 1991, Power et al., 1998, Kawashima, 2000, Wang, 2001, 2009, Hashash et al., 2001, Kontoe et al., 2008) and although they have shown a better behavior then the surface structures, different cases of extensive damage have been reported in the literature. One of the most important example is the collapse of the Daikai metro station during Kobe earthquake (Japan, 1995) where the collapse of the station was due to the central columns failure, designed in order to resist only vertical loads (Figure 2) (Iida et al., 1996, Kawashima, 2000, Hashash et al., 2001).

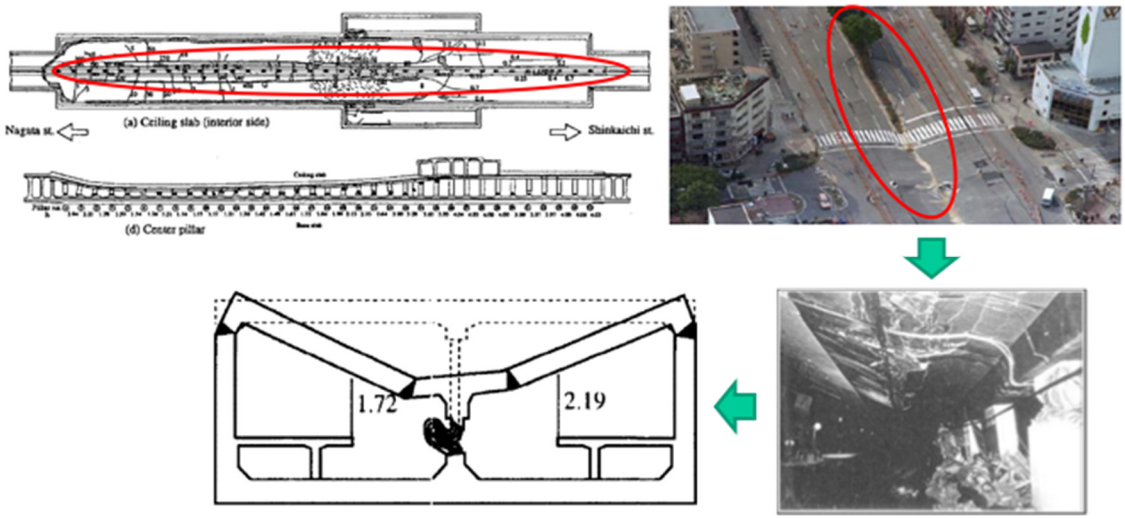

Figure 2: Damage to the Daikai Station (Kobe, 1995)

Past experiences have shown that shallow underground structures realized in soft soil are more vulnerable than the deep underground structures realized in rock and that the seismic vulnerability increase for the structures realized by cut and cover method but some of them designed with proper seismic design considerations showed a good behavior even during strong earthquakes (Gazetas et al., 2005).
Damaging effects of earthquakes on underground structures can be classified into two main groups: damages caused by vibratory motion (shaking) of the ground and damages due to ground failures (Pavlovic, 2004). In the first case, as a result of seismic waves propagation, generated by an earthquake, the ground will undergo vibrations, which is manifested as ground shaking (Kramer, 1996). Consequently, underground structures will suffer more or less deformations simultaneously with the ground deformations. The response of the structure is dominated by the kinematic action due to the shaking of the surrounding soil, while the inertial loads stemming from the oscillation of the structure itself are of secondary importance (Wang, 1993). The soil-structure relative stiffness and the mechanical properties of the interfaces represent the two most important parameters.

The second case include broad spectrum of different failure modes such as: faulting and tectonic uplift, liquefaction and subsidence, and various types of slope instabilities.

1.2. Effects of earthquakes on underground structures

Earthquake effects on underground structures, as mentioned in the previous paragraph 1.1, can be grouped in two categories: ground shaking and ground failure. Another important parameter is the depth of the structure which governs the type and intensity of loads.

1.2.1. Ground shaking

The major contribution to deformations and stresses in underground structures has shaking effects of seismic waves. As a result of these movements, two primary types of deformation are imposed on the underground structure: axial and curvature deformations in the longitudinal direction, and transverse deformations (ovaling for circular and racking for rectangular structures) in the direction perpendicular to the structure axis. Axial and curvature deformations (Figure 3) in a tunnel lining may occur when direction of propagation of seismic waves is parallel or under some angle of incidence to the tunnel axis. Usually, the axial strains are small enough that they can be easily accommodated by standard lining and will not impair structural behavior, especially if there is slippage between the lining and ground that typically reduces the strains. Whereas the axial deformation is induced by longitudinal (P) waves, the curvature is the consequence of the shear (S) waves. Due to curvature regions of compression and tension will alternate along the tunnel. In tunnels with flexible lining, surrounding ground will be in tension in the top and compression in the bottom. However, if the lining is stiff it will resist ground deformation and will be under compression in the top and tension in the bottom.
The ovaling (circular structures) or racking (rectangular structures) deformations (Figure 4) (Owen & Scholl, 1981, Wang, 1993) may be the consequence of any type of seismic waves advancing in a direction approximately at right angles to the structure axis. Usually, the main criterion for lining design is the deformational effect of shear waves that propagate in vertical direction. If the wavelength is short comparing to the tunnel diameter deformation will be asymmetric, resulting in an uneven distortion of the tunnel lining. However, if the wavelength is relatively long, as it is the common case, the problem can be treated as pseudo-static, so the deformation will be approximately symmetrical but still elliptical due to the difference in field stress magnitudes in the direction of wave propagation and normal to that direction. Racking is the seismic effect on rectangular tunnels, which is usual in cut-and-cover construction (at shallow depth). Such structures are subjected to lateral movement, as a consequence of shear deformations of the ground, and accordingly to shear and normal forces all around the structure.

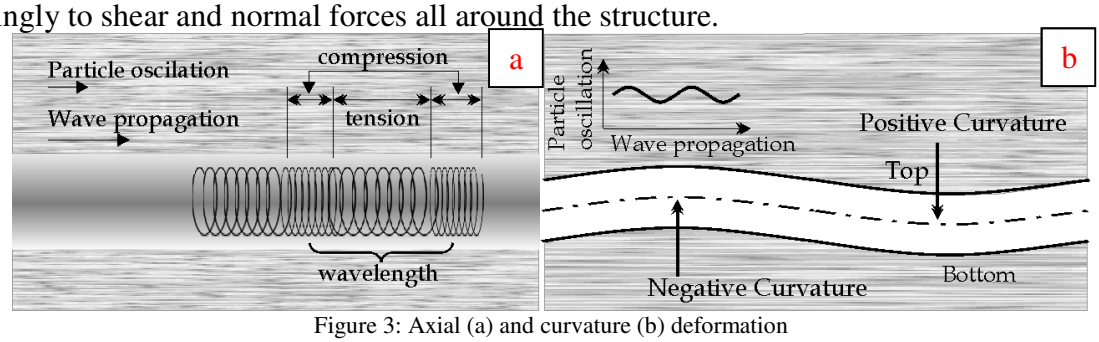

Figure 3: Axial (a) and curvature (b) deformation

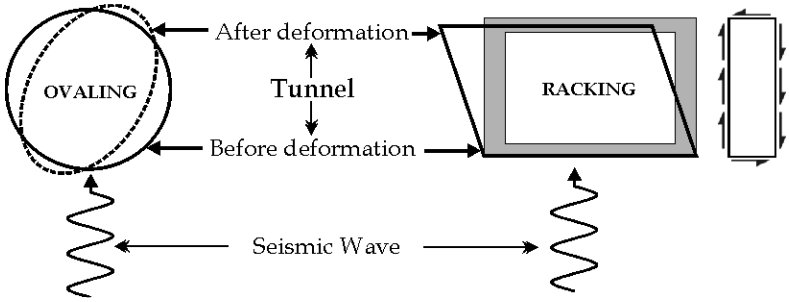

Figure 4: Ovaling and racking deformations

1.2.2. Ground failure

Ground failure as a result of seismic shaking includes liquefaction, slope instability, and fault displacement. This type of failure is prevalent at portals and in shallow structures.
Liquefaction is a term associated with a host of different, but related phenomena. It is used to describe the phenomena associated with increase pore water pressure and reduction in effective stresses in satured cohesionless soils. The rise in pore pressure can result in generation of sand boils, loss of shear strength, lateral spreading and slope failure. Underground structures located below the groundwater table in liquefiable deposits can experience increased lateral pressure, a loss of lateral passive resistance, flotation or sinking in the liquefied soil, lateral displacement if the ground experiences lateral spreading, and permanent settlement and compression and tension failure after the dissipation of pore pressure in consolidation of the soil.

1.3. Seismic design approach of underground structures

Underground structures are confined by the surrounding ground and cannot move separately, in fact, during an earthquake, they are affected by deformations of surrounding ground and by inertial forces acting on the structures.
The proper seismic design should reduce the hazards and risks providing structures capable to resist the loads or displacements generated by earthquakes. The principal goal is to protect the human lives in the case of earthquake and then to minimize economic losses. The design specifications should describe ways for balancing structural strength with the intensity of earthquakes likely to affect the structure.
It is common in engineering practice to evaluate the static and the seismic response separately but the final design involves both static and dynamic loads.
In Hashash et al. (2001), the principal steps for the analysis and the underground structures seismic design are described. In particular, four major steps are highlighted:

- seismic hazard assessment and selection of the design earthquake;
- evaluation of transient ground response and induced phenomena;
- evaluation of the seismic behavior of the structure;
- synthesis of seismic and static loads.

In order to define the seismicity of the area where the structure is located, it is possible to carry out a site-specific hazard analysis (Kramer, 1996). The seismic design approach is generally

characterized by two different type of earthquake events: the maximum design earthquake (MDE) and the operating design earthquake (ODE), typically defined as:

- MDE: is the earthquake event that has a return period of several thousand years. It has a small probability of exceedance, approximately 5 % or less, during the 100 year facility life. It is aimed at public life safety.
- ODE: is the event for which recurrence interval is several hundred years; the probability of exceedance of this event is approximately 40 % during the facility life. It is aimed to guarantee full functioning of the structures. The response of underground structures should therefore remain within elastic range.

Defined the outcrop motion, the characteristics of the ground motion at the depth of the structure may be obtained by different soil response analysis methods. Usually, a deconvolution method is used in order to obtain the seismic ground motion at the bedrock level, followed by one-dimensional (1D) site response analysis for upward propagating SH and SV waves in case of simple soil stratification while for complex geometries, instead, it is necessary to apply two-dimensional (2D) or three-dimensional (3D) numerical methods. The seismic ground motion is usually evaluated considering free-field conditions, without accounting the presence of the structure.Another aspect of the design procedure is the evaluation of the structure behavior under the expected ground shaking and earthquake induced deformations. It is possible to evaluate separately the transversal and the longitudinal contribution and, once the internal forces have been obtained, combine them later (ISO, 2005, FHWA, 2009). Several methods are available in literature for the seismic analysis and design in both directions. The internal actions, obtained by the seismic analysis, are combined with the results obtained by the static analysis to proceed at the final design of the underground structure. During last years, the numerical methods, for the study of the soil-structure coupled system, have had a strong development. For the evaluation of the seismic behavior of the underground structures, different types of numerical approaches are now used. Depending on the complexity of the problem, it is possible to use 2D or 3D numerical models (Soccodato & Tropeano, 2015). Usually, the seismic analysis is preceded by a construction stage analysis, that accounting all the main phases involved in the construction of the structure to reproduce the correct static initial condition (Zucca et al., 2017). The seismic analysis is generally conducted through the non-linear time history analysis or the 2D linear equivalent analysis, depending on the intensity of the seismic action (Lanzo & Silvestri, 1999). In Figure 5 is shown a simple flow chart which describes the fundamental steps of a correct seismic design approach of underground constructions.

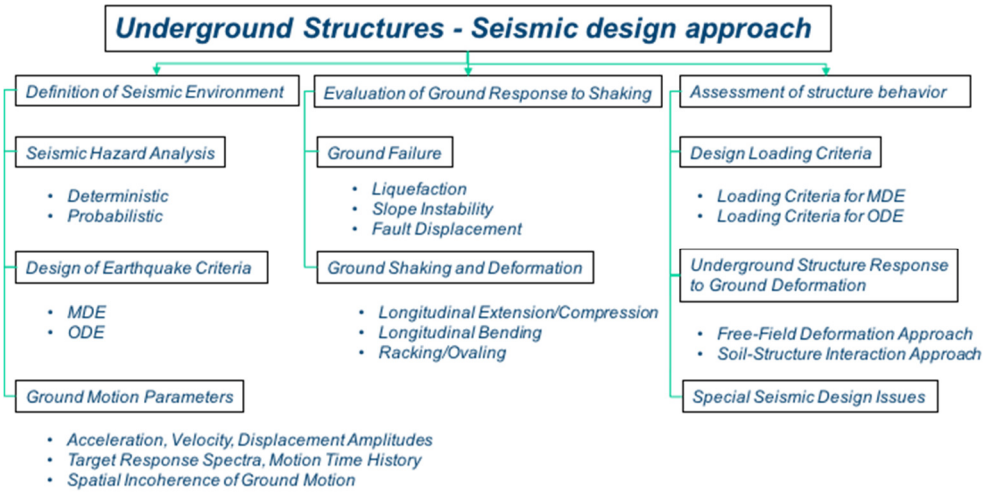

Figure 5: Seismic design approach of underground structures

2. SEISMIC DESIGN METHODS

2.1. Design methods for ground shaking

Different types of approaches are available in literature for the evaluation of the seismic behavior of tunnels, metro stations and other types of underground structures (St. John & Zahrah, 1987, Wang, 1993, Penzien, 2000). Depending on how the seismic action is considered, it is possible to classified the methods in three main groups (Pitilakis & Tsinidis, 2014): the force-based methods, the displacement-based methods and the numerical methods (finite element method, finite difference method, etc.), already mentioned in the previous paragraph 1.2. The methods included in the first two groups can be further classified in: methods that take into account the soil-structure interaction effects and methods that neglect these effects.

2.1.1. Transversal seismic analysis

In Table 1, a list of the principal methods used for the evaluation of the transversal response of the underground structures during a seismic event is shown.

Table 1: Methods for the transversal analysis of underground structures under seismic action

Force-based methods	R-F method (Wang, 1993, Penzien, 2000)
	Simplified equivalent static analysis method (JRA, 1992, Kawashima, 2006, ISO, 2005)
Displacement-based methods	Simplified analytical solutions (Hoeg, 1968, Wang, 1993, Penzien, 2000, Penzien & Wu, 1998, Bobet, 2003, Park et al., 2009, Bobet, 2010)
	Simplified equivalent static analysis method (JRA, 1992, Kawashima, 2006, ISO, 2005)
Numerical methods	Detailed equivalent static analysis method (ISO, 2005, FHWA, 2009)
	Full dynamic time history analysis (Lanzo & Silvestri, 1999, ISO, 2005, FHWA, 2009, Soccodato & Tropeano, 2015)

The R-F method, proposed by Wang (1993) for the transversal seismic analysis of underground structures characterized by a rectangular shape, is based on a simple static frame analysis where the structural distortion (racking effect) Δ_{str} is applied as an equivalent static load or pressure imposed on the structure (Figure 6). The distortion is evaluated by the free-field ground racking distortion (without accounting the presence of the structure) Δ_{ff}, corrected through the racking ratio, $R = \Delta_{str}/\Delta_{ff}$, to take into account the soil-structure interaction effects. This parameter is related to the flexibility ratio F which describes the soil-structure relative flexibility and is computed as follows:

$$F = \frac{G_s \cdot W}{S \cdot H}$$

where:

- G_s = soil shear modulus;
- W = width of the structure;
- H = height of the structure;

- S = required force to cause a unit racking deflection of the structure.

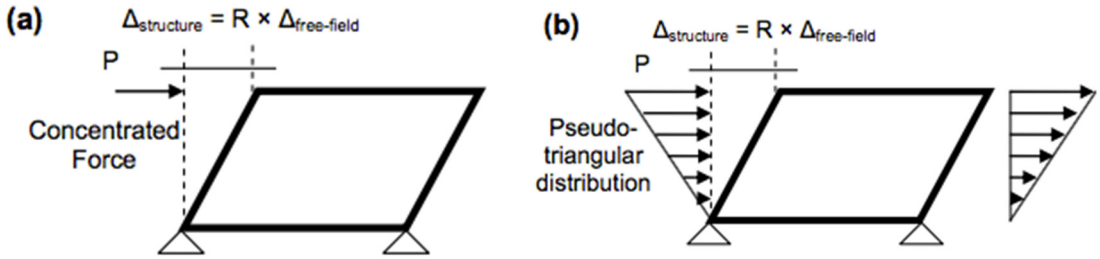

Figure 6: Simplified frame analysis model: (a) concentrated force and (b) pseudo-triangular distribution (modified after Wang, 1993)

Several analytical and empirical R-F relations are present in literature (Penzien, 2000, Huo et al., 2006, Anderson et al., 2008). The methodology is based on the hypothesis of pure shearing deformation of the structure.
In the simplified equivalent static analysis method, the structure is represented through beam elements while the presence of the surrounding soil is simulated by appropriate springs (Figure 7).

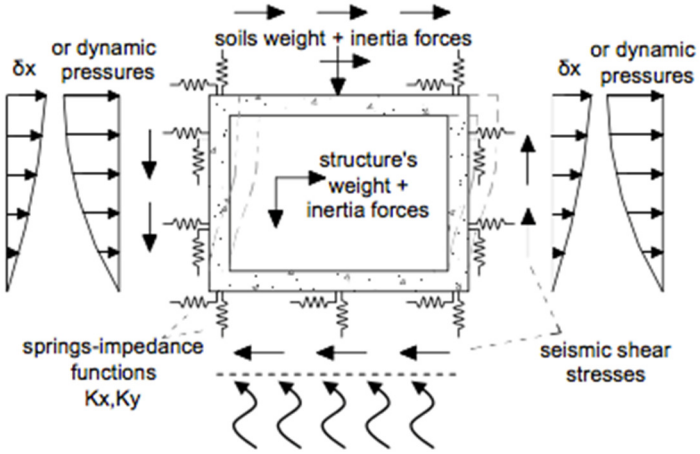

Figure 7: Simplified equivalent static method for the evaluation of the transversal seismic response of the underground structures

In the simplest cases, the soil-structure interaction effects are not considered and the analysis is carry out omitting the presence of the springs. The seismic action is introduced statically in terms of equivalent static inertial loads (due to the structure and the overburden soil masses), shear stresses along the structure perimeter or seismic earth pressure imposed on the underground structure retaining walls (usually applied at semi-embedded retaining walls, Okabe, 1926, Mononobe & Matsuo, 1929, Seed & Whitman, 1970). Alternatively, it is possible to apply the seismic ground deformation at the perimeter of the underground structure.
This method is very simple but presents several critical issues, in particular related to the seismic earth pressure magnitude and distribution which is not well known in the case of fully-embedded structures, in fact the evaluation done according to the regulations referring to semi-embedded structures can lead to erroneous results due to overestimation or underestimation of the seismic action to be applied. In the same way, the evaluation of the seismic shear stresses acting on the perimeter of the structure is still an open issue. Furthermore, the determination of the correct values

of the springs stiffness, that will simulate the presence of the surrounding soil, is a very complicate problem; in fact, in literature it is possible to find only few and poorly validated methods.
It is possible to identify different analytical solutions for the evaluation of the deformations and internal forces of the underground structures under seismic action. In particular, in literature it is possible to find different closed formulas for tunnels characterized by a circular shape (Heog, 1968, Wang, 1993, Penzien & Wu, 1998, Penzien, 2000, Bobet, 2003, Park et al., 2009, Bobet, 2010). In this approach, in the simplest cases the soil-structure interaction effects are ignored, as in the formulation proposed in Wang (1993) for the evaluation of the diametric deflection of the circular tunnels. The most used solution is that proposed by Penzien (2000) which is defined for full-slip or no-slip interface conditions to accounting the soil-structure interaction effects. The latter are expressed by the following ratios:

$$F = \frac{E_S \cdot (1 - \nu_l^2) \cdot R^3}{6 \cdot E_l \cdot I_l \cdot (1 + \nu_S)}$$

$$C = \frac{E_S \cdot (1 - \nu_l^2) \cdot R}{E_l \cdot t \cdot (1 + \nu_S) \cdot (1 - 2\nu_S)}$$

where:

- F = flexibility ratio;
- C = compressibility ratio;
- E_S = Young modulus of the soil;
- ν_S = Poisson ratio of the soil;
- E_l = Young modulus of the lining;
- ν_l = Poisson ratio of the lining;
- I_l = moment of inertia of the lining (per unit width);
- R = tunnel radius;
- t = lining thickness.

In Bobet (2003) a series of closed form solutions for the evaluation of the internal forces acting on the tunnels lining characterized by circular section, under static and dynamic loads, investigating the effects of pore water pressures, are presented.
Park et al. (2009) proposed different closed form solutions for the computation of the lining internal forces that account for potential slippage along soil-structure interface.
Excluded the solutions proposed in Bobet (2003), the formulations mentioned above consider the vertical propagation of the shear waves. This hypothesis is valid for free-field conditions and for the cases where the underground structure is deeply embedded in a homogeneous soil because in this cases the seismic energy is transferred almost totally by the shear waves. On the contrary, Kouretzis et al. (2014) showed the close form solutions to obtain the maximum internal forces acting on tunnel linings subjected to P waves.
Detailed equivalent static analysis method is based on the implementation of a 2D numerical model considering both structure and soil to take into account the soil-structure interaction effects (Figure 8). The seismic action, in pseudo-static condition, is defined as equivalent inertial load related to the effective or maximum ground free-field acceleration profile. It is possible to apply the equivalent seismic load also as a ground deformation pattern at the grid boundaries of the numerical model,

corresponding to the free-field ground response (Hashash et al., 2010). This method is valid in case of low and medium seismicity when large deformations of the soil are not expected.

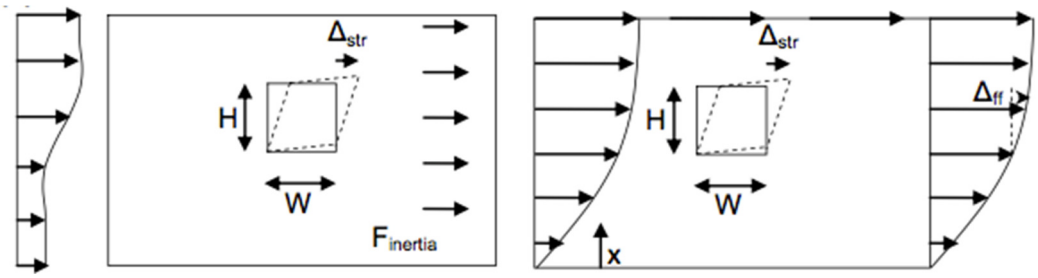

Figure 8: Detailed equivalent static analysis: (1) distributed inertial load, (2) ground distortion at the boundary

The dynamic time history analysis, where the numerical model is implemented considering both structure and soil, is the most significant and accurate method for the evaluation of the seismic behavior of the underground structures (Lanzo & Silvestri, 1999, ISO 2005, FHWA, 2009, Soccodato & Tropeano, 2015). In this case, the analysis is carry out imposing the seismic motion at the model base, usually at the bedrock level. The method can efficiently describe the kinematic and inertial aspects of the soil-structure interaction, while it can adequately simulate complex geometries, the heterogeneities of the soils and the interaction with other existing surface or underground structures. Thanks to the implementation of appropriate constitutive models, it is possible to simulate the non-linear behavior of the soil (and of the structure) and the interfaces.

2.1.2. Longitudinal seismic analysis

In Table 2, a list of the principal methods used for the evaluation of the longitudinal response of the underground structures during a seismic event is shown.

Table 2: Methods for the longitudinal analysis of underground structures under seismic action

Displacement-based methods	Simplified analytical solutions (Newmark, 1968, Kuesel, 1969, St. John & Zahrah, 1987, Power et. al, 1998, JRA, 1992)
	Mass-spring model method (Kiyomiya, 1995)
	Simplified equivalent static analysis (ISO, 2005)
	Simplified dynamic analysis (ISO, 2005)
Numerical methods	3D Full dynamic time history analysis (ISO, 2005)

The displacement-based methods schematise the problem through the use of a beam on springs and dashpots to simulate the soil-structure system and the seismic action is simulated by the ground deformation induced by the waves passage.
St. John & Zahrah (1987), based on Newmark (1968) work related to the pipelines, proposed a different types of analytical relations to evaluate the strains induced on an underground structure under seismic action. These relations are based on the theory of waves propagation in an elastic, homogeneous and isotropic soil. Moreover, in St. John & Zahrah (1987) are presented analytical

solutions for the evaluation of the seismic lining forces of an underground structure subjected to a sinusoidal horizontal shear wave with an angle of incidence θ (Figure 9).

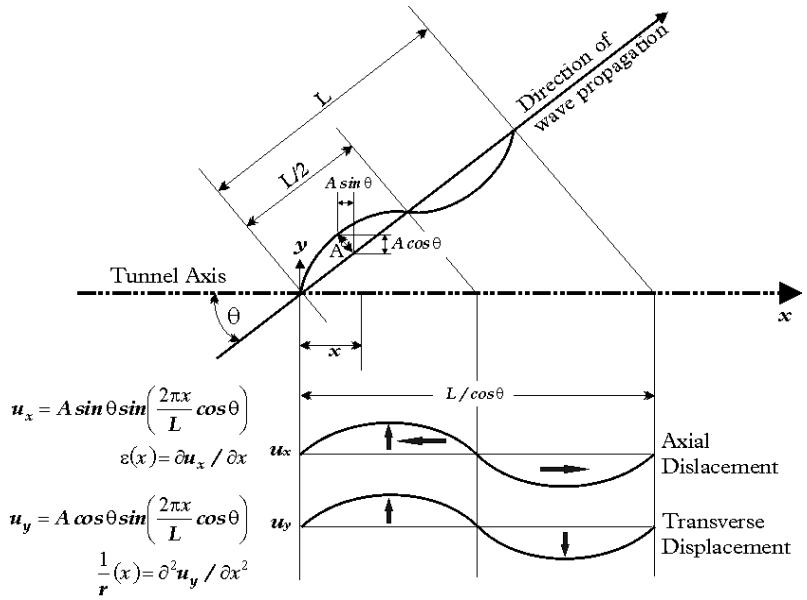

Figure 9: Seismic lining displacements of a lining subjected to a sinusoidal horizontal shear wave with an angle of incidence θ

These formulations have been developed not considering and considering the soil-structure interaction effects. In the latter case, the analytical solutions were derived by the implementation of elastic beam on elastic foundation, without accounting the inertial interaction effects. A similar procedure has been proposed by JRA (1992) for the evaluation of the seismic behavior of common utility tunnels (Kawashima, 2006).

Another displacement-based method is the mass-spring model method proposed by Kiyomiya (1995). In this procedure, the soil is modelled like a series of equivalent mass-spring-dashpot system, which are connected to each other with proper springs and dashpots. The ground displacement is obtain using the general dynamic equilibrium system equation. Once obtained, the ground displacement is applied at the tunnel line which is represented by a beam supported by springs.

The simplified equivalent static analysis method uses the concept of a beam on an elastic foundation in order to represent the soil-structure system (ISO, 2005). The seismic action is applied on the springs as equivalent static ground deformations (Figure 10).

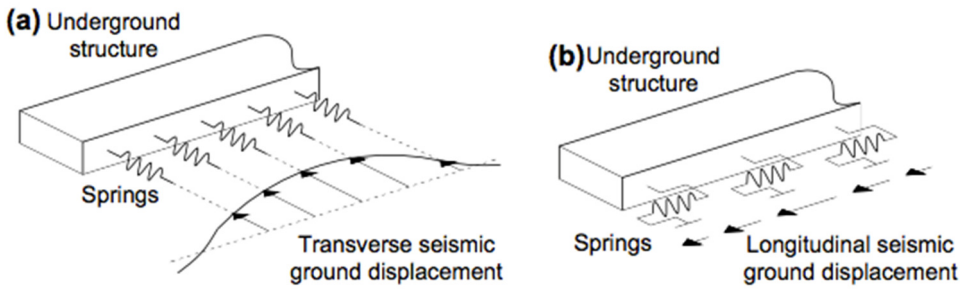

Figure 10: Simplified equivalent static analysis method

One of the most important parameters which conditions this method is the relative distance of the springs that is function of the predominant wave length and consequently of the frequency range of interest.
In the simplified dynamic analysis, the seismic action is represented by a series of displacement time histories that account for the spatial variation of the seismic ground motion.
The methods described above are based on the Winkler type model. The most critical aspect of these methods is, in fact, the evaluation of the soil impedance functions (springs and dashpots). As for the transversal direction, no plausible and well validated solutions are presented in literature for the longitudinal analysis of underground structures but only general formulations are found related to the theory of the elastic impedance functions for surface foundations, piles, etc. (Vrettos, 2005, Gazetas et al., 1991a, 1991b, Gerolymos & Gazetas, 2006).
The full dynamic time history analysis, usually, is carried out through the implementation of a 3D numerical model (finite element method, finite difference method, boundary element method, etc.) considering both structure and soil. With this approach, is possible to take into account the non-linear behavior of the soil (using appropriate constitutive laws) and the behavior of the soil-structure interfaces. The seismic action, generally, is represented through accelerograms applied at the base of the model. The main shortcoming of the full dynamic time history analysis is the high computational cost.

2.1.3. Methods overviews

The complexity of the soil-structure interaction phenomena led to the development of different types of simplified approaches and numerical methods in order to evaluate the correct response of the underground structures (tunnels, metro stations, etc.) under seismic actions. Despite this development, various uncertainties remain open, in particular, due to the aspects related to the response mechanisms of the underground structures under seismic actions. In Pitilakis & Tsinidis (2016) a series of aspects to be improve are highlighted for the different types of analysis described above. In particular, for the transversal seismic analysis, it is necessary to improve: the efficiency and the accuracy of conventional pseudo-static analysis methods and of analytical closed form solutions, the accuracy of the evaluation of the magnitude and distribution of the dynamic earth pressure along the perimeter of the underground structures characterized by a rectangular shape, the evaluation of the effects related to the yielding of the surrounding soil on the seismic response of underground structures, the evaluation of the complex deformation of the rectangular underground structures subjected to ground shaking and the accuracy of the evaluation of the impedance factors.
For the longitudinal seismic analysis, instead, is necessary to clarify the following aspects: the evaluation of the incoherent ground motion along the longitudinal axis of a tunnel and its effect on the seismic response, the seismic design of the joints, the accuracy of the evaluation of the impedance factors and the seismic design of the connections between various types of embedded structures.

2.2. Design methods for ground failure

As mentioned in the previous paragraph 1.2.2, the ground failure includes liquefaction, slope instability and fault movements.

2.2.1. Liquefaction

The liquefaction can generate significant longitudinal and transversal deformations on the underground structures, due to the lateral spreading and settlements of the liquefiable grounds. This type of deformation can be considered as a quasi-static deformation acting on the underground structure. Moreover, the liquefaction may lead to the occurrence of uplift phenomena. In order to reduce the liquefaction phenomena, different types of mitigation measures can be taken, as an example the soil improvement, the increase of the dead load of the underground structure and drainage or soil replacement (Power et al., 1998).

2.2.2. Slope instability and fault movements

Related to the slope instabilities, special mitigation measures in order to stabilize the ground are described in literature. Instead, in reference to fault movements, one of the most critical aspect is the accurate identification of the fault zone and the relative thrust angle because in different cases, the exact position and the angle of the fault trace are unknown. Also in this case, a detailed numerical approach represents the most appropriate method to evaluate this type of phenomenon (Anastasopoulos et al, 2007, Vazouras, 2010, 2012). It is possible to evaluate the fault displacement also using empirical relationship which correlate the displacement with the earthquake magnitude and the fault type (Wells & Coppersmith, 1994) and once obtained, apply this statically (as an imposed dislocation) at the base of the numerical model. Power et. al. (1998) suggest that the design approach is closely related to the magnitude of the expected fault displacement and the width of zone over which this displacement is distributed.

3. EVALUATION OF THE SESISMIC BEHAVIOR OF UNDERGORUND STRUCTURES

3.1. Performace-Based Design approach

The Performance-Based Earthquake Engineering (PBEE) approach has been developed in order to define a more rational and convincing design criteria compared to classical methods. The fundamental concept of the PBEE procedures is the prediction of the behavior of the system during and at the end of the seismic action. The parameters that characterized the performance of the system can be evaluated in different ways.
The methodology developed by the Pacific Earthquake Engineering Research Center (PEER) is based, in theory, on the evaluation of the performance level of a generic engineering system under seismic action, through the hazard curve definition of the decisional variables. In other words, the final goal is to assign an annual likelihood of exceedance value or a return period to the "limt state" which characterized the system intended as indicators of the "loss" in terms of human lives, functionality or cost of repairs.

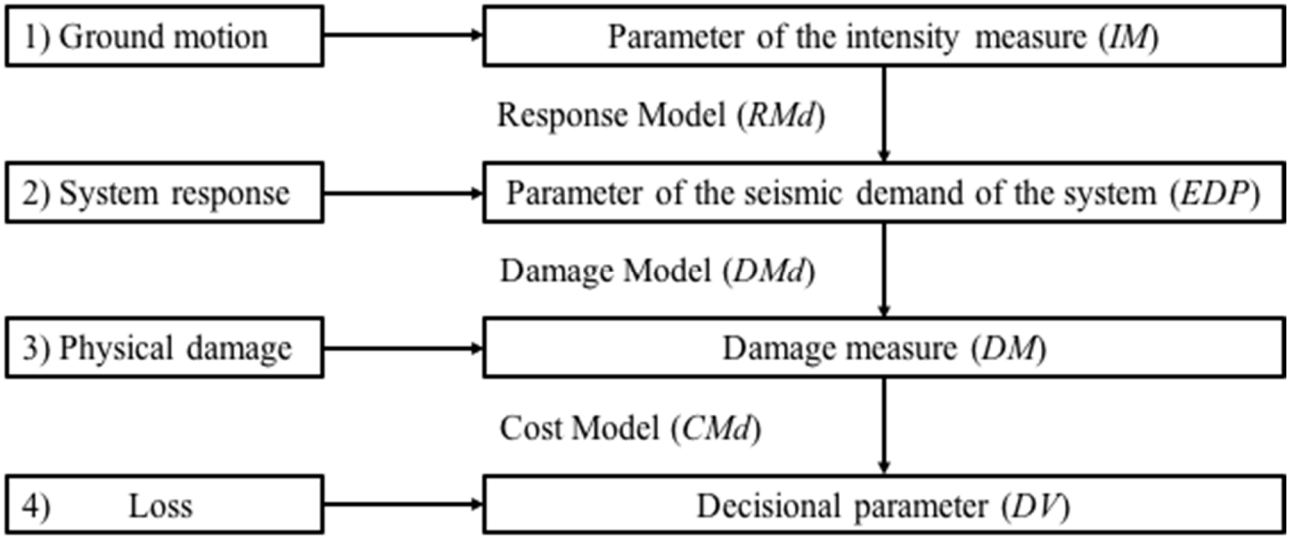

Figure 11: Logical scheme of the procedure for the evaluation of dynamic system losses

As shown in the Figure 11, an earthquake generates a ground motion (1) which induces the dynamic response of the system or of the analysed structure (2). This response involves the occurrence of a physical damage (3) and, consequently, the achievement of a determined "limit state". It is possible to associate one or more parameters to each of the phases highlighted in Figure 11, indicated below according to the PEER terminology:

1) *IM (Intensity Measure)*, namely one or more seismic motion parameters (e.g. a_g, T_m, $D_{5\text{-}95}$) or integral parameters (e.g. I_a, *SI*) that characterized the design earthquake;
2) *EDP (Engineering Demand Paramter)*, namely one or more system response parameters due to the seismic action (e.g. displacements);
3) *DM (Damage Measure)* which describes the measure of the physical damage of the system or of the single subsystems associated with the system response;
4) *DV (Decision Variable)* losses associated with the damage level expressed, usually, as design decisional variables.

The choice of parameters, that characterized all the phases involved in the procedure, must be carried out in such a way as to be directly realated to the parameters of the next phase. The parameters must be established according to two properties. In fact, stated A the set of the generic phase representative paramiters and B the set of the representative parameters considered for the next phase, are defined:

- *efficient*, the set of parameters A that induce a limited uncertainty on the estimation of the parameters B;
- *sufficient*, the set of parameters A that induce an uncertainty on the estimation of the parameters B which can not be improved with the introduction of additional parameters in A.

These properties are defined in detail in (Shome et al., 1998, Baker & Cornell, 2005, Vamvatsikos & Cornell, 2005, Thotong & Luco, 2007, Luco & Cornell, 2007).
To mantain the accuracy ot the system response prediction, the parameters of the seismic motion (IM) must be chosen in such a way as to be efficient and sufficient in the prevision of the EDP parameters. Moreover, it is necessary that the parameters of the motion are predictable or that can be estimate by appropriate relations (attenuation laws) according to the parameters and the distance of the source and characterized by a term with sufficiently low approximation identified by the value of the standard deviation of the regression, σ_{IM}.
The response parameters EDP, analogously at the IM parameters, must be closely related to physical damage. Generally, the main measure considered in the geotechnical systems response was based on criteria that took into account forces or stresses due to the seismic action, through the definition of the safety factors obtained from the ration between the capacity and the demand of the system, namely between the resistant force (or the shear strength) and the acting force (or the tangential stress induced by the seismic action). During the last years, thanks to the development of the numerical methods, the measure based on the deformations, which has proved to be more representative of the geotechnical system damage level, are used.
As for the two different variables types described above for the previuos phases, the variables that characterize the physical damage (DM) must be possibly sufficient and efficient predictors of losses namely the decision variables (DV). However, it is not always possible to define these variables in quantitative terms: in these cases an ordered qualitative variable is used (e.g. a discrete damage scale).
The variables representing the “losses” incurred on the system, indicated as decision variables (DV) in the PEER guidelines, may take different forms: loss of human life, repair cost or loss of functionality. The safety of human life is the fundamental aim of the seismic enginnering that is universally accepted as minimum design goal. The repair cost, instead, represents the decision variable which guarantees the design performance of the system: the repair cost should be maintened within acceptable limits on the basis of the structure classification.
The reliability of the previosion variables EDP, DM and DVis related to the accuracy of the models which link each other the variables:

- *response model* (*RMd*) that allows to evaluate the system behavior under seismic design action ($IM \Rightarrow EDP$);
- *damage model* (*DMd*) that is usuful in order to link the system response at the seismic action with the damage occured ($EDP \Rightarrow DM$);
- *cost model* (*CMd*) that defines the “losses” of the system related to the occured damage level ($DM \Rightarrow DV$).

The variables and the models are subjcted to uncertainties, therefore the hazard curve, $\lambda(DV)$, associate with the limit states *DV*, can be expressed in vectorial terms as:

$$\lambda(\boldsymbol{DV}) = \iiint G\left(\boldsymbol{DV}|\boldsymbol{DM}|dG(\boldsymbol{DM}|\boldsymbol{EDP})\right| \times \left|dG(\boldsymbol{EDP}|\boldsymbol{IM})\right||d\lambda(\boldsymbol{IM})|$$

where $G(a \mid b)$ denotes a complementary cumulative distribution function (CCDF) for a conditioned upon b (the absolute value of the derivative of which is the probability density function for a continuous random variable) and the bolt type denote vector quantities. From left to right, the three CCDFs result from loss, damage and response models; the final term ($d\lambda(\boldsymbol{IM})$) is obtained from the seismic hazard curve. The framing equation implictly assumes that the quantities used to describe ***IM***, ***EDP*** and ***DM*** are sufficient predictors of ***EDP***, ***DM*** and ***DV*** respectively.
The triple integral can be solved directly only for an idealized set of conditions, so it is solved numerically for most practical problems. When all variables are continuous, the numerical integration can be accomplished, assuming scalar paramters for simplicity, as:

$$\lambda_{DV}(dv) = \sum_{k=1}^{N_{DM}} P[DV > dv|DM = dm_k] \cdot \Delta\lambda_{DM}(dm_k)$$

$$\lambda_{DM}(dm) = \sum_{j=1}^{N_{EDP}} P\left[DM > dm_k|EDP = edp_j\right] \cdot \Delta\lambda_{EDP}\left(edp_j\right)$$

$$\lambda_{EDP}(edp) = \sum_{i=1}^{N_{IM}} P\left[EDP > edp_j\middle|IM = im_i\right] \cdot \Delta\lambda_{IM}(im_i)$$

where N_{DM}, N_{EDP} and N_{IM} are the number of increments of the random variables DM, EDP and IM respectively and $\lambda_{IM}(im)$, $\lambda_{DV}(dv)$, $\lambda_{DM}(dm)$ and $\lambda_{EDP}(edp)$ the hazard curves related to the realization of the corresponding random variables *im*, *dv* and *edp*.
The use of these relations implies that all the parameters are defined as continuous random variables. This condition, generally, shall be checked for the motion paramteres obtained by the model (e.g. forces, displacements, deformations, etc.). The use of damage parameters (DM) defined as continuous variables, in many cases, in addition to not be possible may be impractical. The damage can be discretized into a finite number of levels, N_{DM}, defined in qualitative terms (e.g. in five levels as reported in Table 3) and, consequently, also the limit state (DV) are to define as discrete terms.

Table 3: Damage state matrix for definition of *DM/EDP* relationship

Damage State (DM)	**Description**	**EDP interval**				
		***edp*$_1$**	***edp*$_2$**	***edp*$_3$**	***edp*$_4$**	***edp*$_5$**
dm_1	Negligible	X_{11}	X_{12}	X_{13}	X_{14}	X_{15}
dm_2	Slight	X_{21}	X_{22}	X_{23}	X_{24}	X_{25}
dm_3	Moderate	X_{31}	X_{32}	X_{33}	X_{34}	X_{35}
dm_4	Severe	X_{41}	X_{42}	X_{43}	X_{44}	X_{45}
dm_5	Catastrophic	X_{51}	X_{52}	X_{53}	X_{54}	X_{55}

In this approach, the damage levels are related to the EDP parameter, discretized into an integer number of EDP intervals, through the damage state matrix, *X*, where the X_{ij} element represents the conditional probability which the system suffers a *k* damage level for EDP belonging to the *j*-th range:

$$X_{ij} = P\left[DM = dm_k | EDP = edp_j\right]$$

In the previous Table 3 a generic damage state matrix which is characterized by five damage level (from "Negligible" to "Catastrophic") and five ranges of the EDP parameter defined by threshold values (e.g. EDP = 0 for the lower limit value of the "Negligible" damage level and EDP = ∞ for the upper limit value for "Catastrophic" level) is reported.
Each EDP range may lead the system, or part of it, within one of the defined damage states and this likelihood is defined by a probability value. The condition for the damage matrix definition is that the sum of the values of each column is equal to 1:

$$\sum_{k=1}^{N_{DM}} X_{jk} = 1 \qquad for\ j = 1, 2, \dots N_{EDP}$$

The total probability theorem can then be used to compute the probability of being in a given damage state using the conditional distribution of DM | EDP and the distribution of EDP ranges as:

$$P[DM = dm_k] = \sum_{j=1}^{N_{EDP}} P\left[DM = dm_k | EDP = edp_j\right] \cdot P\left[EDP = edp_j\right] = \sum_{j=1}^{N_{EDP}} X_{jk} \cdot P\left[EDP = edp_j\right]$$

The DV variable can be defined as discrete terms. Generally, it is desirable to define the decison variable as ratio between the repair cost and the total cost of the structure to be able to quantify the losses and, consequently, to define the limit states. Analogously, also for the DM variable, it is possibile to define the limit states matrix (Table 4), *Y*, where each element is obtained as:

$$Y_{kl} = P[DV = dv_l | DM = dm_k]$$

Table 4: Limit states matrix

Limit State	**Damage state**				
DV	dm_1	dm_2	dm_3	dm_4	dm_5
dv_1	Y_{11}	Y_{12}	Y_{13}	Y_{14}	Y_{15}
dv_2	Y_{21}	Y_{22}	Y_{23}	Y_{24}	Y_{25}
dv_3	Y_{31}	Y_{32}	Y_{33}	Y_{34}	Y_{35}
dv_4	Y_{41}	Y_{42}	Y_{43}	Y_{44}	Y_{45}
dv_5	Y_{51}	Y_{52}	Y_{53}	Y_{54}	Y_{55}

Similarly, to the damage parameter, the total probability associated with a generic limit state is obtained as:

$$P[DV = dv_l] = \sum_{k=1}^{N_{DM}} P[DV = dv_l | DM = dm_k] \cdot P[DM = dm_k] = \sum_{k=1}^{N_{DM}} Y_{kl} \cdot P[DM = dm_k]$$

In the previous equation by replacing the probability value $P[DM = dm_k]$ by the value obtained by the damage state matrix, is derived the following relation:

$$P[DV = dv_l] = \sum_{k=1}^{N_{DM}} \sum_{j=1}^{N_{EDP}} X_{jk} Y_{kl} \cdot P\left[EDP = edp_j\right]$$

used to obtain the exceedance probability which defines the hazard curve $\lambda_{DV}(dv)$:

$$P[DV > dv_l] = \sum_{l=l+1}^{N_{DV}} \sum_{K=1}^{N_{DM}} \sum_{j=1}^{N_{EDP}} X_{jk} Y_{kl} \cdot P\left[EDP = edp_j\right]$$

The loss model described by the matrix *Y* is, in fact, the most complex step of the methodology. The generic concept of loss, difined by the PEER, includes uncertainties on the quantification and homogeneization of the DV parameter, in particular in the definition of the loss of the intangible assets such human lives and cultural heritage. Considering the losses only in economic terms, does not simplify the problem but add factors of uncertainty related to the prediction of the total costs, for example materials, repair times, etc.

3.2. Sensitivity analysis

As mentioned in the previous paragraph 1.3, the behavior of the underground structures under seismic action is strictly related to the response of the surrounding soil to a given seismic input, in particular for the occurrence of the possible resonance effects if the fundamental frequencies of the soil profile are near to the frequencies of the seismic input chacartecized by the maximum energy content (Soccodato & Tropeano, 2015).
Different types of approach were developed for the evaluation of the seismic behavior of the underground structures that consider (coupled approach) or not (decoupled approach) the soil-structure interaction effects. This fact can lead to obtaining different values of internal actions on the structural elements.
In this work, the attention is focused on the shallow underground structures embedded in type B soils, according to Eurocode 8 classification (Table 5).
To evaluate the correct seismic behavior, a sensitivity analysis, based on the performance-based design approach described in the previous paragraph 3.1 (Figure 12), was conducted considering the variation of shear modulus (related to the shear waves velocity) of the homogeneous soil which the structure is embedded (Figure 13). The model used is composed by the presence of 31.57 m of soil profile overlying 51.30 m of sandstone and the bedrock (Figure 14).

Four different soil profile have been chosen characterized, respectively, by a shear waves velocity equal to 360 m/s, 450 m/s, 600 m/s and 750 m/s. Table 6 lists the main mechanical properties of the soil profiles considered in this analysis.

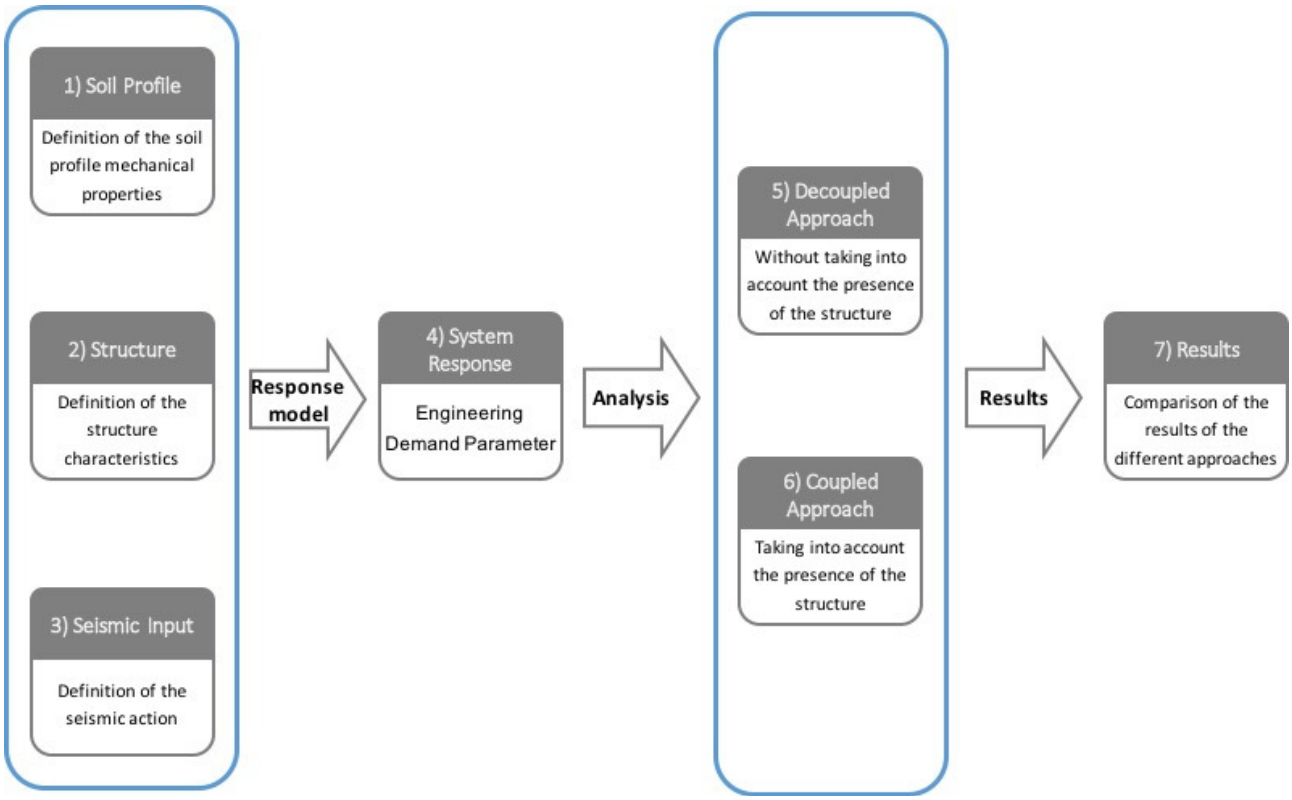

Figure 12: Perfomance-based deisgn approach

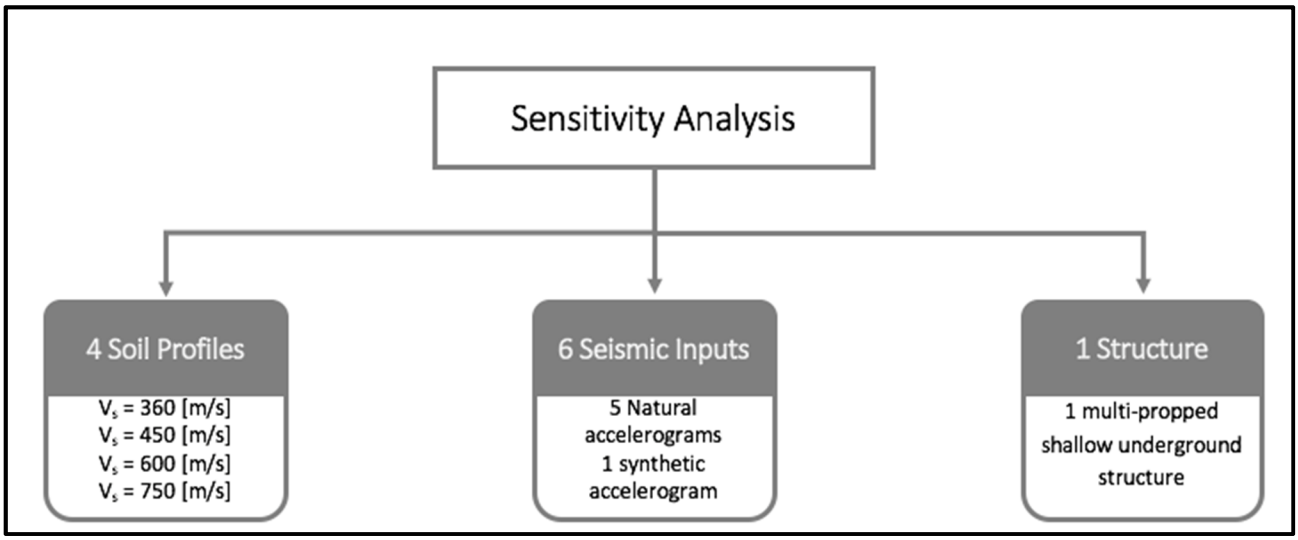

Figure 13: Sensitivity analysis

Table 5: Ground types according to Eurocode 8 (paragraph 3.1.2, Table 3.1)

Ground type description	$V_{S,30}$	N_{SPT}	C_U
A: Rock or other rock-like geological formation, including at most 5 m of weaker material at the surface.	>800		
B: Deposits of very dense sand, gravel, or very stiff clay, at least several tens of meters in thickness, characterized by a gradual increase of mechanical properties with depth.	360-800	>50	>250
C: Deep deposits of dense or medium dense sand, gravel or stiff clay with thickness from several tens to many hundreds meters.	180-360	15-50	70-250
D: Deposits of loose-to-medium cohesionless soil (with or without some soft cohesive layers), or of predominantly soft-to-firm cohesive soil.	<180	<15	<70
E: A soil profile consisting of a surface alluvium layer with V_s values type C or D and thickness varying between about 5 m and 20 m, underlain by stiffer material with V_S > 800 m/s.			
S_1: Deposits consisting, or containing a layer at least 10 m thick, of soft clays/silts with a high plasticity index (PI > 40) and high water content.	<100		10-20
S_2: Deposits of liquefiable soils, of sensitive clays, or any other soil profile not included in types A - E or S_1.			

Table 6: Mechanical properties of the different soil profiles (Poisson ratio (ν) is equal to 0.3 for all profiles)

Profile n°	Unit weight (γ) [kN/m^3]	Cohesion (c') [kPa]	Friction angle (φ') [°]	Shear wave velocity (V_S) [m/s]
1	21	40	39	360
2	21	40	39	450
3	21	40	39	600
4	21	40	39	750

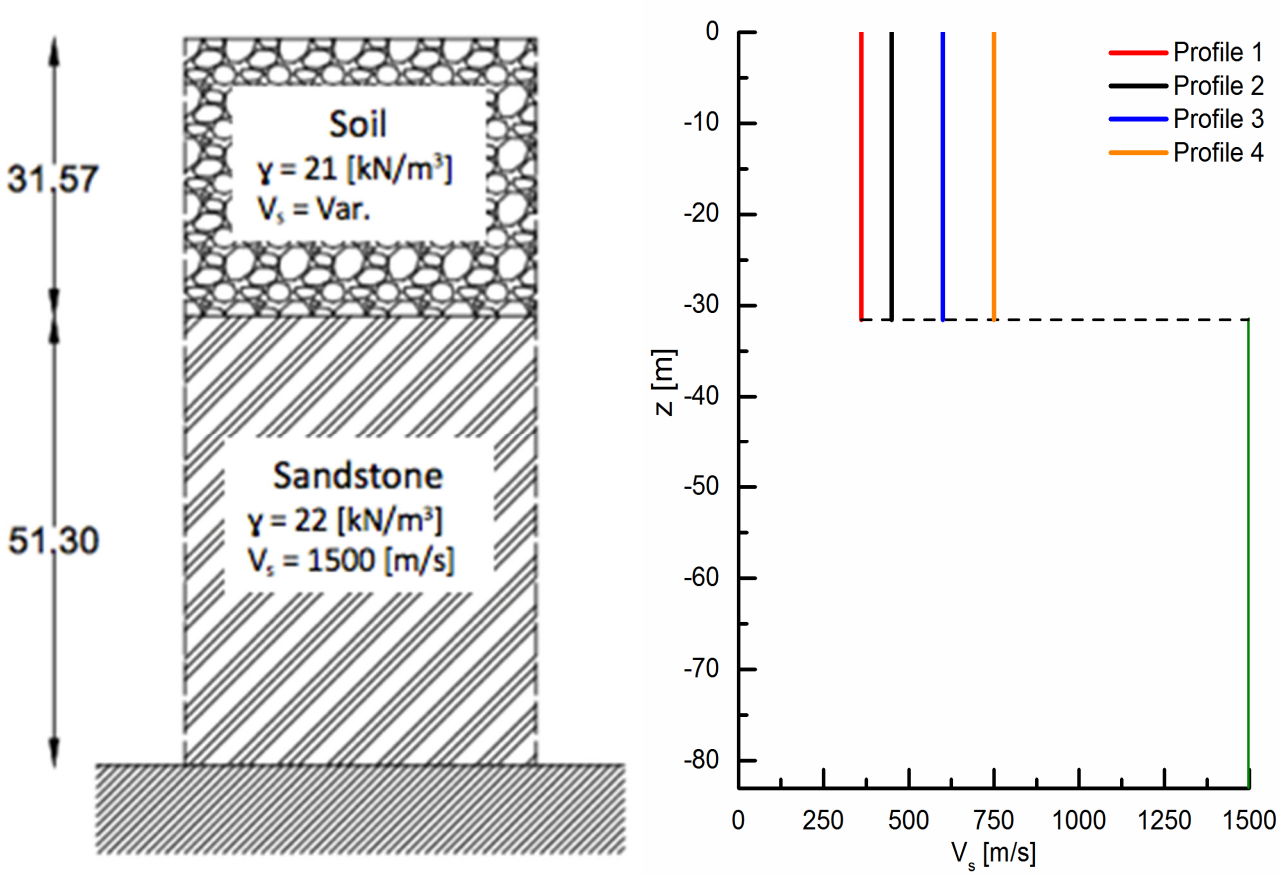

Figure 14: Model and relative shear wave velocity profile

The structure considered in this analysis, in terms of shape, dimensions and material mechanical properties, is the Mercado Santa Anita metro station (Figure 15), which will be described in detail in the following Chapter 4, characterized by a rectangular plan (132.16 × 29.00 m).

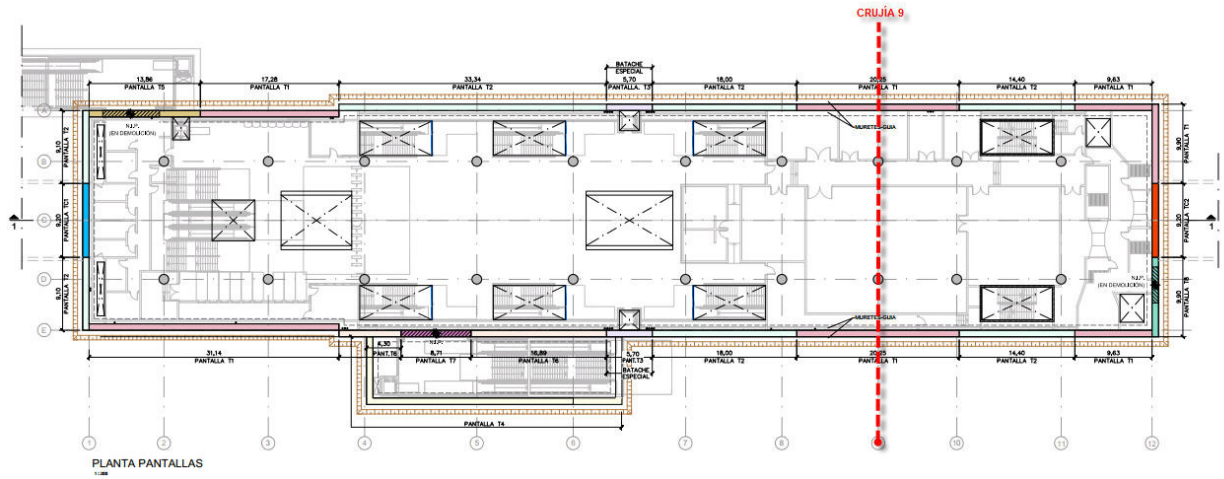

Figure 15: Metro station plan

The principal structural elements that characterized the metro station are the concrete retaining walls, 1 m thick, and a series of concrete circular columns, 1.2 m diameter, positioned in a regular grid 14.70 × 12.00 m. The foundation of the columns consists of circular concrete piles, 1.8 m diameter and 9 m deep. The materials mechanical properties of these elements are listed in Table 7. In Figure 16 the representative section of the metro station, indicated with the red dashed line in the previous Figure 15, is reported.

Table 7: Materials mechanical properties of the structural elements

Structural Elements	**Concrete** (f_{ck}) [MPa]	**Steel** (f_{yk}) [MPa]
Columns	40	420
Piles	40	420
Retaining Walls	30	420
Slabs	40	420
	30	420

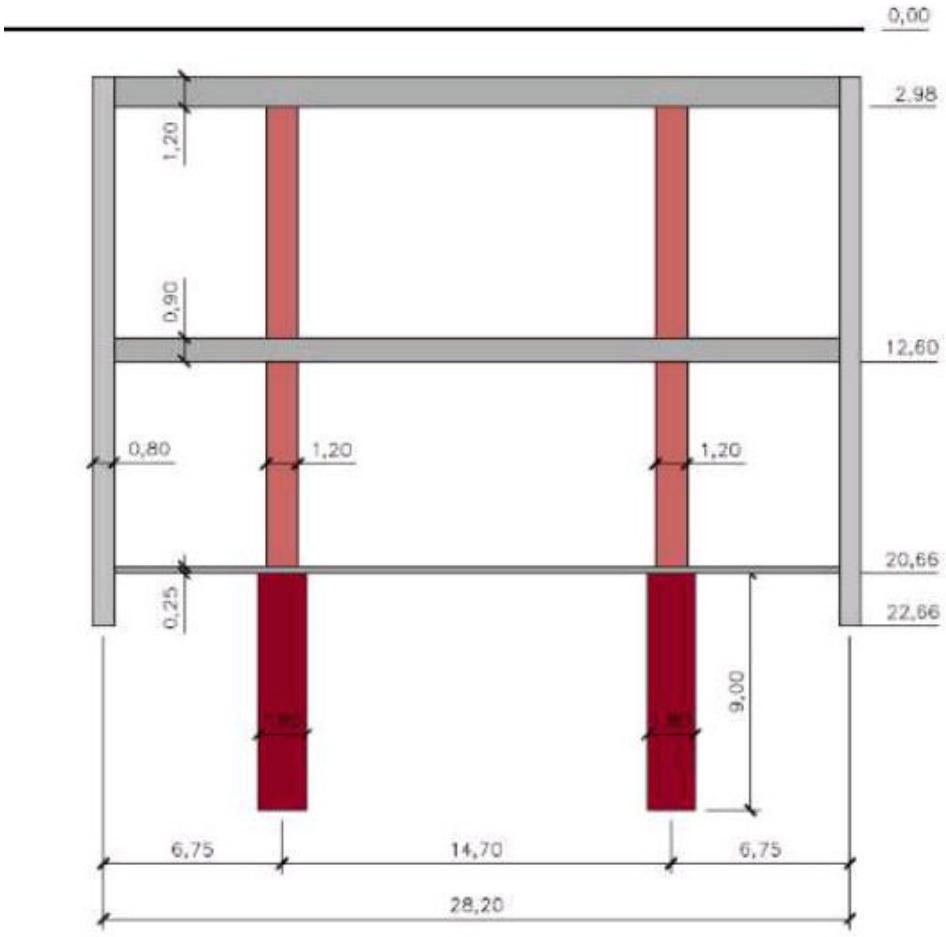

Figure 16: Representative section of the metro station (dimensions in meters)

For the seismic analysis, five acceleration times histories recorded during different European seismic events (Greece, Amatrice, L'Aquila, Friuli and Montenegro), included within the European Strong-Motion Database and one accelerogram analytically rebuilt for the design of metro-Lima (Lima) according to the local seismic hazard described in the paragraph 4.3, have been used. The principal characteristics of the seismic inputs (PGA= peak ground acceleration, PGV = peak ground velocity, PGD = peak ground displacement) are listed in Table 8. The Arias Intensity is an integral parameter of severity of ground motion. Considering the function of motion intensity:

$$I(t) = \frac{\pi}{2g}\int_0^t a^2(\tau)\, d\tau$$

where $a(t)$ is the acceleration at time t, the Arias Intensity is the maximum value of this function i.e. it is the value $I(t_d)$, where t_d represents the accelerogram total duration. Dimensionally, the Arias Intensity, is a velocity.
The Housner intensity is defined as follows:

$$SI(\xi) = \int_{0.1}^{2.5} PSV(T,\xi)dT$$

where PSV is the pseudo-velocity response spectrum, T and ξ are the structural natural period and damping, respectively. This parameter of seismic motion deverity is related to the potential damage expected from the considered earthquake, since the majority of structures have a fundamental period of vibration in the range between 0.1 and 2.5 s.

Table 8: Characteristics of the seismic inputs

Event	**Event id**	**Station**	**Year**	**PGA**	**PGV**	**PGD**	**Magnitude (M_w)**	**Arias Intensity**	**Housner Intensity**
[-]	[-]	[-]	[-]	[g]	[cm/s]	[cm]	[-]	[cm/s]	[cm]
Greece	GR-1995-0047	AIGA	1995	0.52	51.3	8.3	6.5	117.1	118.1
Amatrice	EMSC-20161030_0000029	AMT	2016	0.53	37.9	7.5	6.5	156.4	90.7
L'Aquila	IT-2009-0009	AQG	2009	0.49	35.8	6.0	6.1	132.4	115.2
Friuli	IT-1976-0030	FRC	1976	0.35	23.7	5.3	6	84.5	74.1
Montenegro	ME-1979-0003	PETO	1979	0.45	38.5	6.9	6.9	455.7	148.9
Lima	synthetic	-	2017	0.50	125.5	449.0	8.1	1492.0	

The natural accelerograms have been chosen in such a way as to be have a Magnitude between 6 and 7 and the peak ground acceleration value between 0.4 g and 0.6 g but characterized by different integral parameters values to have the maximum variability of the ground motion characteristcs. The Friuli IT-1976-0030 seismic event turns out to be affected by local site effects but, exactly for this reason was chosen to evaluate the behavior of the structure also under particular conditions.

The seismic signals have been applied both unscaled and scaled through the PGA value about 0.13 and 0.22 g. The scaled accelerograms have been used only for the evaluation of the response system.
The inputs are shown in Figures 17, 18, 19, 20, 21 and 22.

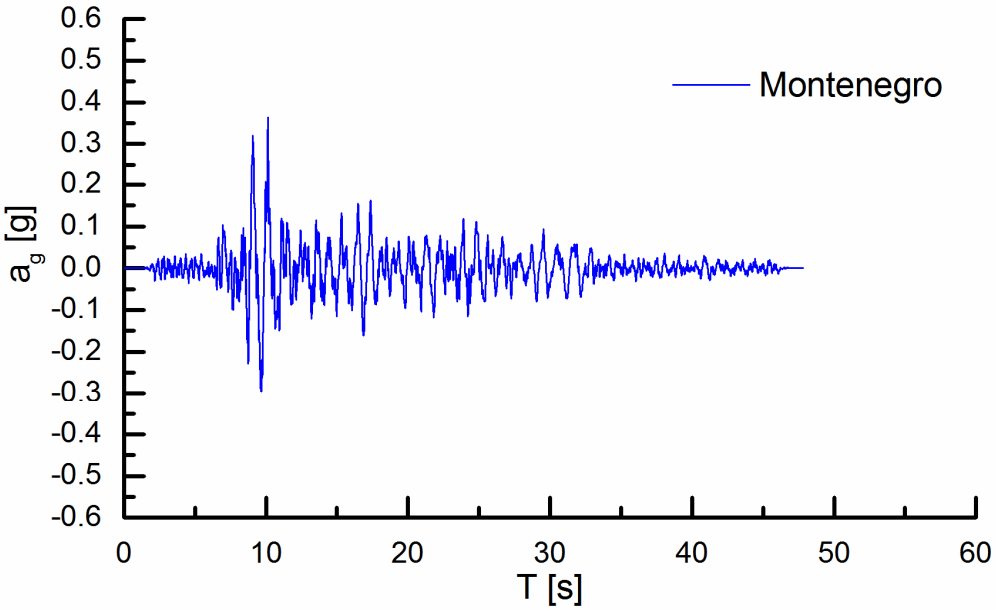

Figure 17: Montenegro ME-1979-0003 seismic event

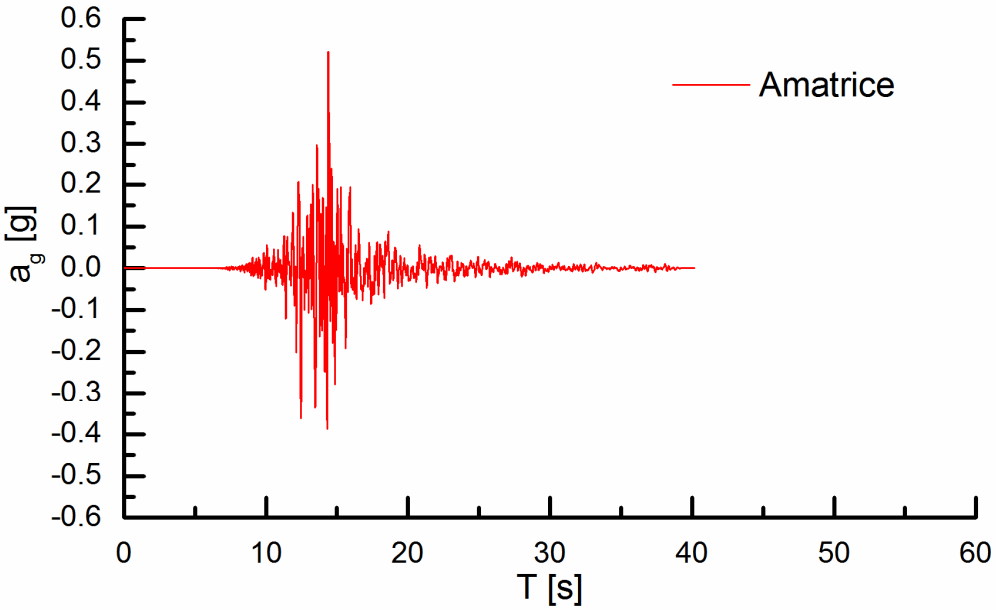

Figure 18: Amatrice EMSC-20161030_0000029 seismic event

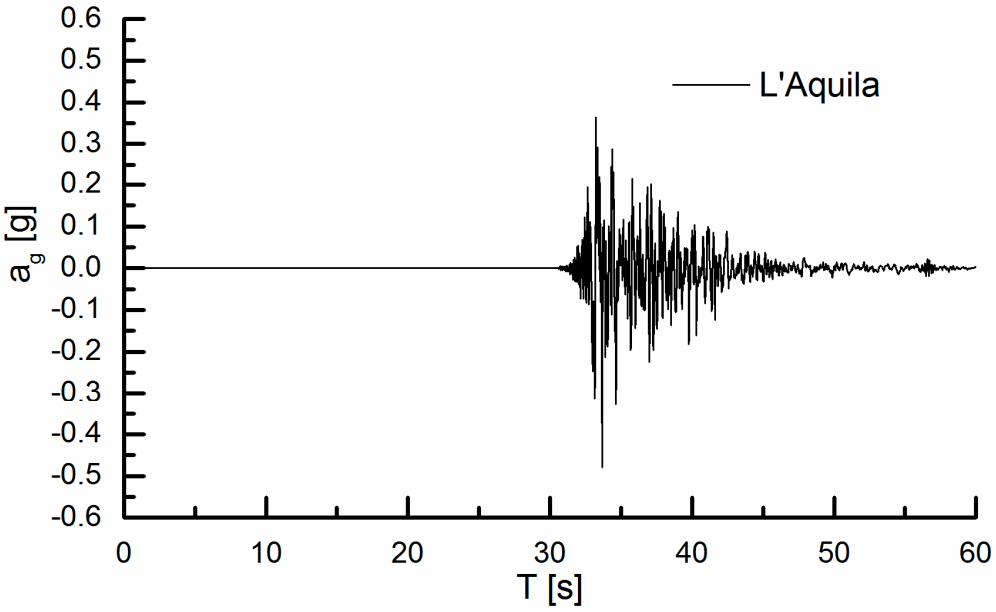

Figure 19: L'Aquila IT-2009-0009 seismic event

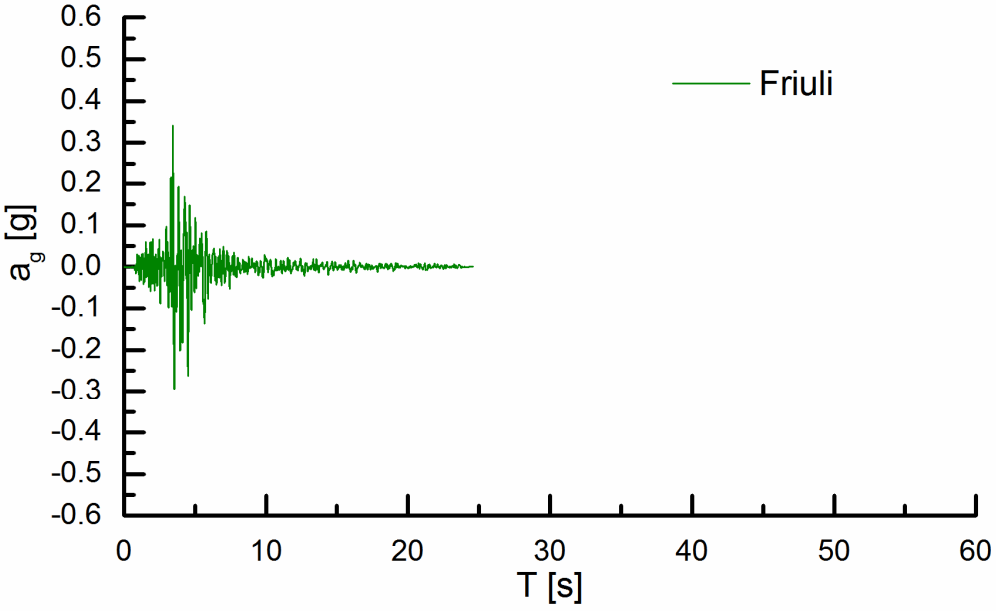

Figure 20: Friuli IT-1976-0030 seismic event

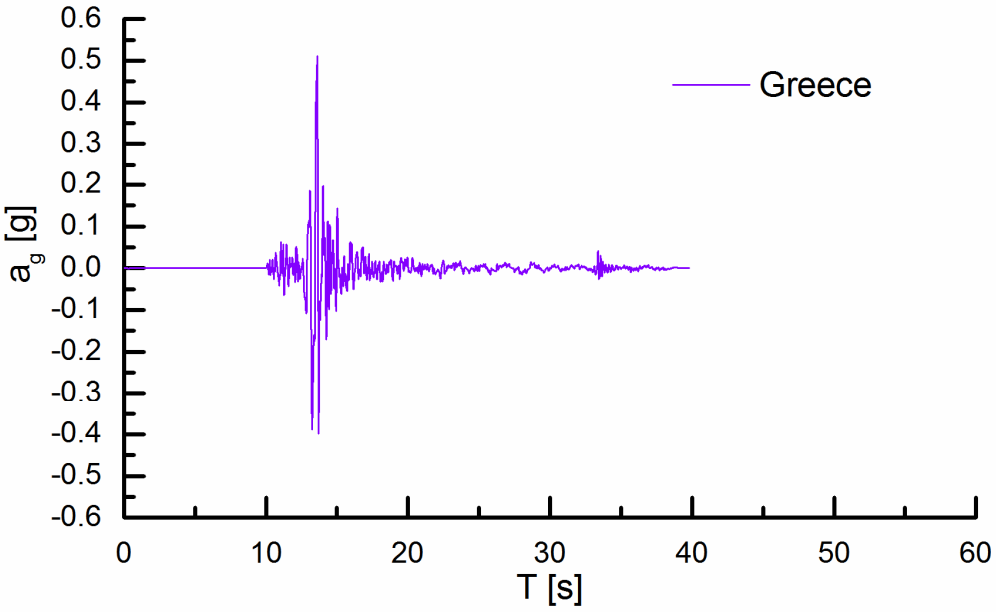

Figure 21: Greece GR-1995-0047 seismic event

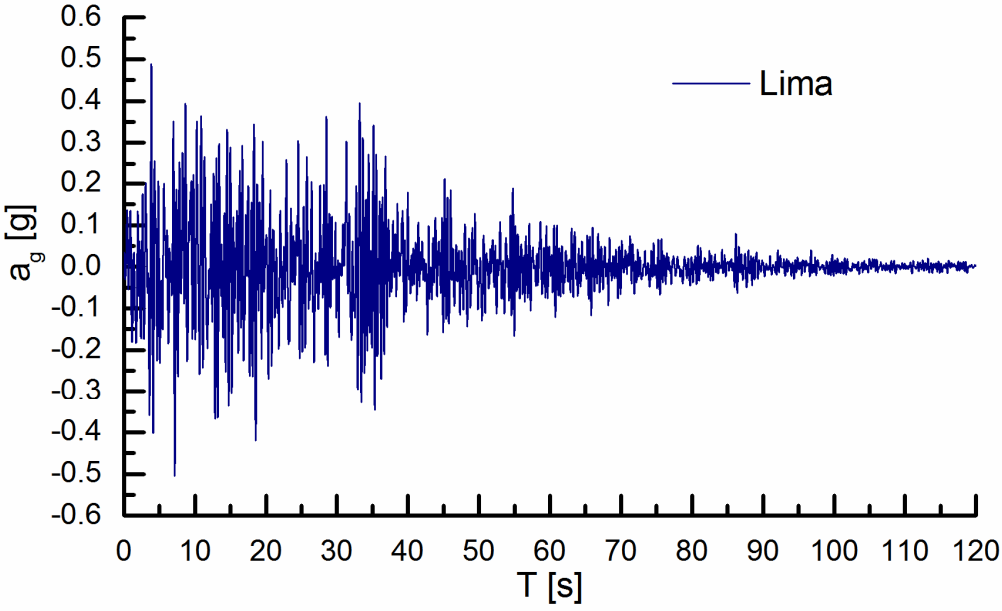

Figure 22: Lima seismic event

In Figures 23, 24, 25, 26, 27 and 28 the related response spectra with the first three fundamental periods and the seismic signals in frequency domain (Fourier transform) with the first three fundamental frequencies of the four different soil profiles, described in the previous Table 6, are

reported. The fundamental periods (and, consequently, the fundamental frequencies), listed in the next Table 9, are evaluated according to Maugeri et al. (1988).
This relation between the frequency content of the seismic signals and the soil profiles fundamental frequencies is useful in such a way as to understand the occurrence of possible resonance effects.

Table 9: Soil profiles fundamental periods

Profile	T_1 [s]	T_2 [s]	T_3 [s]
V_S = 360 [m/s]	0.490	0.162	0.097
V_S = 450 [m/s]	0.420	0.140	0.084
V_S = 600 [m/s]	0.350	0.117	0.07
V_S = 750 [m/s]	0.310	0.103	0.062

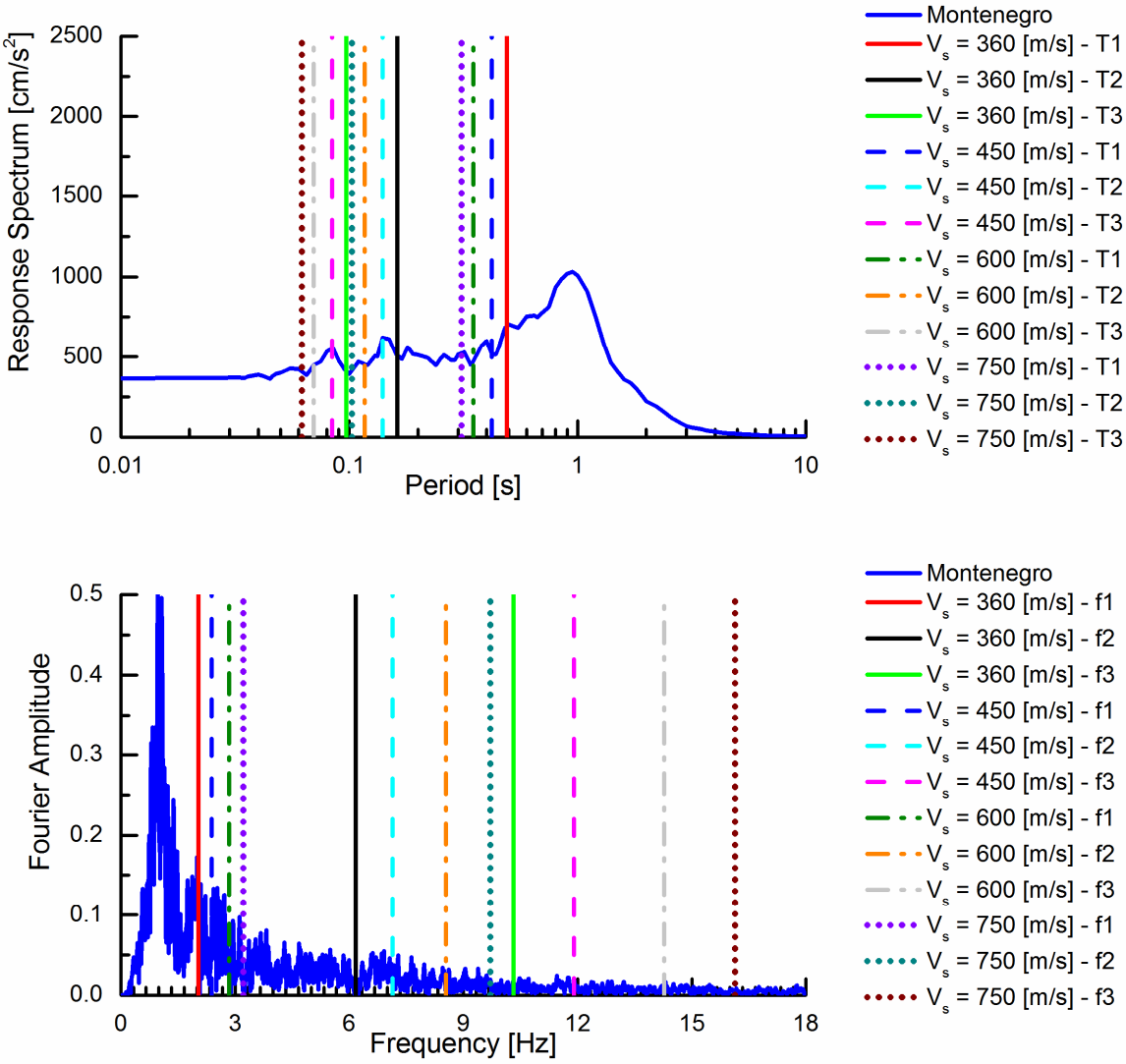

Figure 23: Montenegro ME-1979-0003 response spectrum and seismic signal in frequency domain

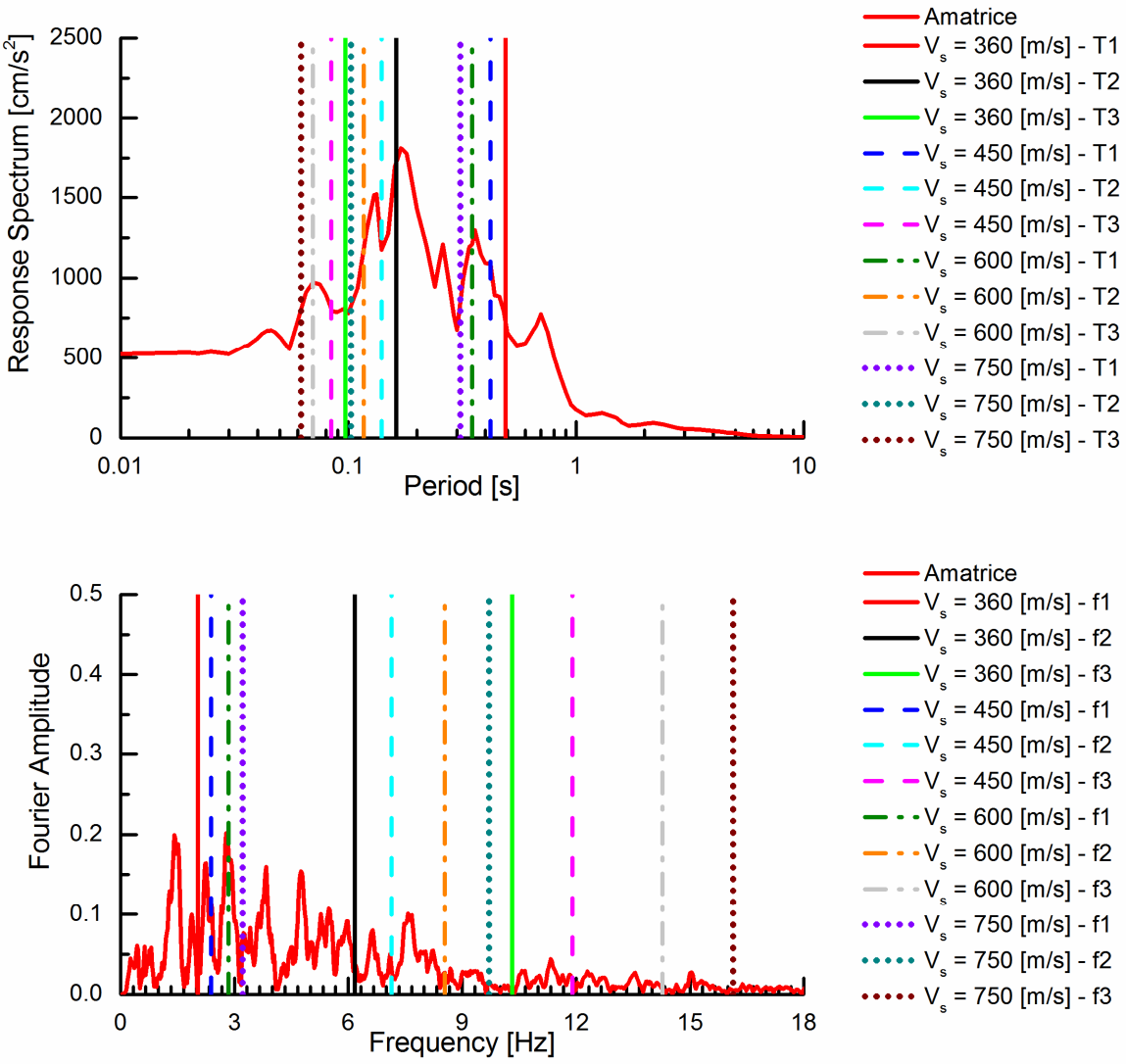

Figure 24: Amatrice EMSC-20161030_0000029 response spectrum and seismic signal in frequency domain

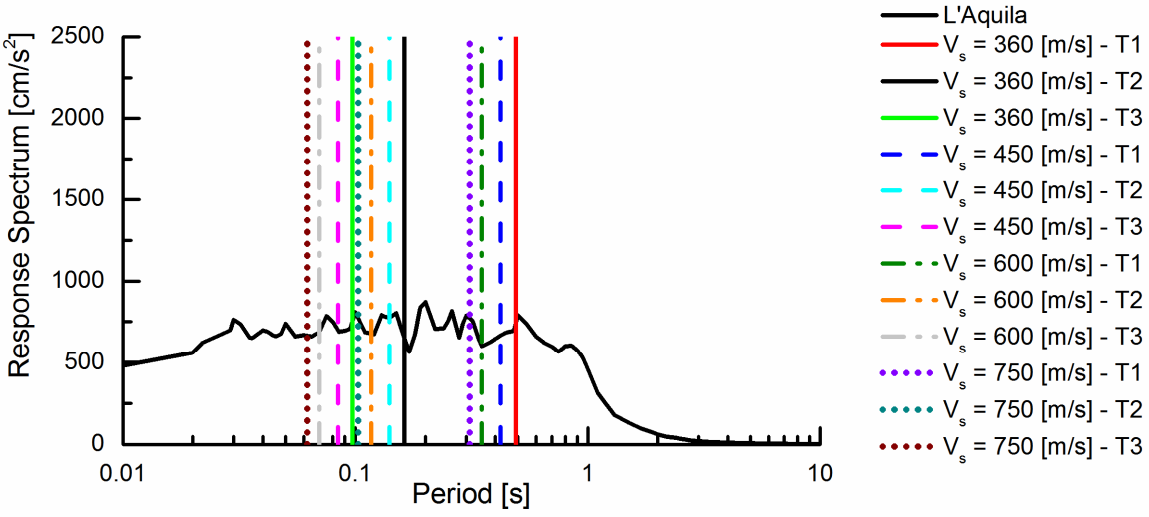

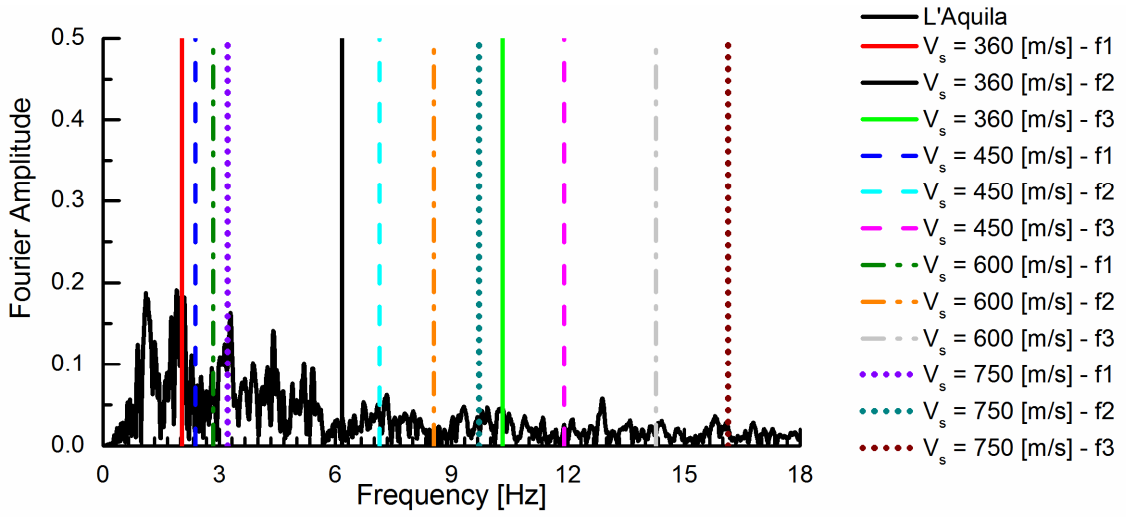

Figure 25: L'Aquila IT-2009-0009 response spectrum and seismic signal in frequency domain

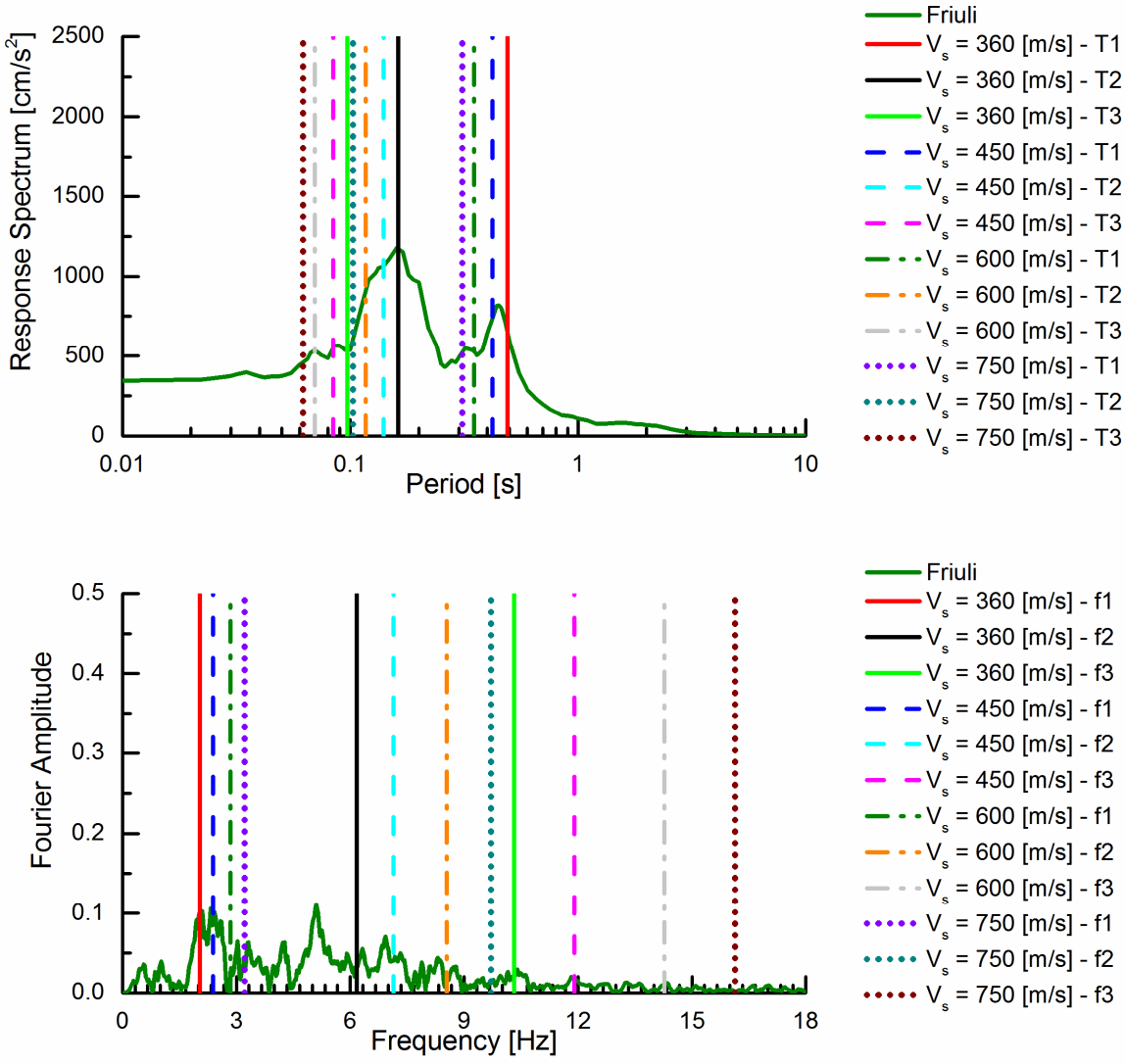

Figure 26: Friuli IT-1976-0030 response spectrum and seismic signal in frequency domai

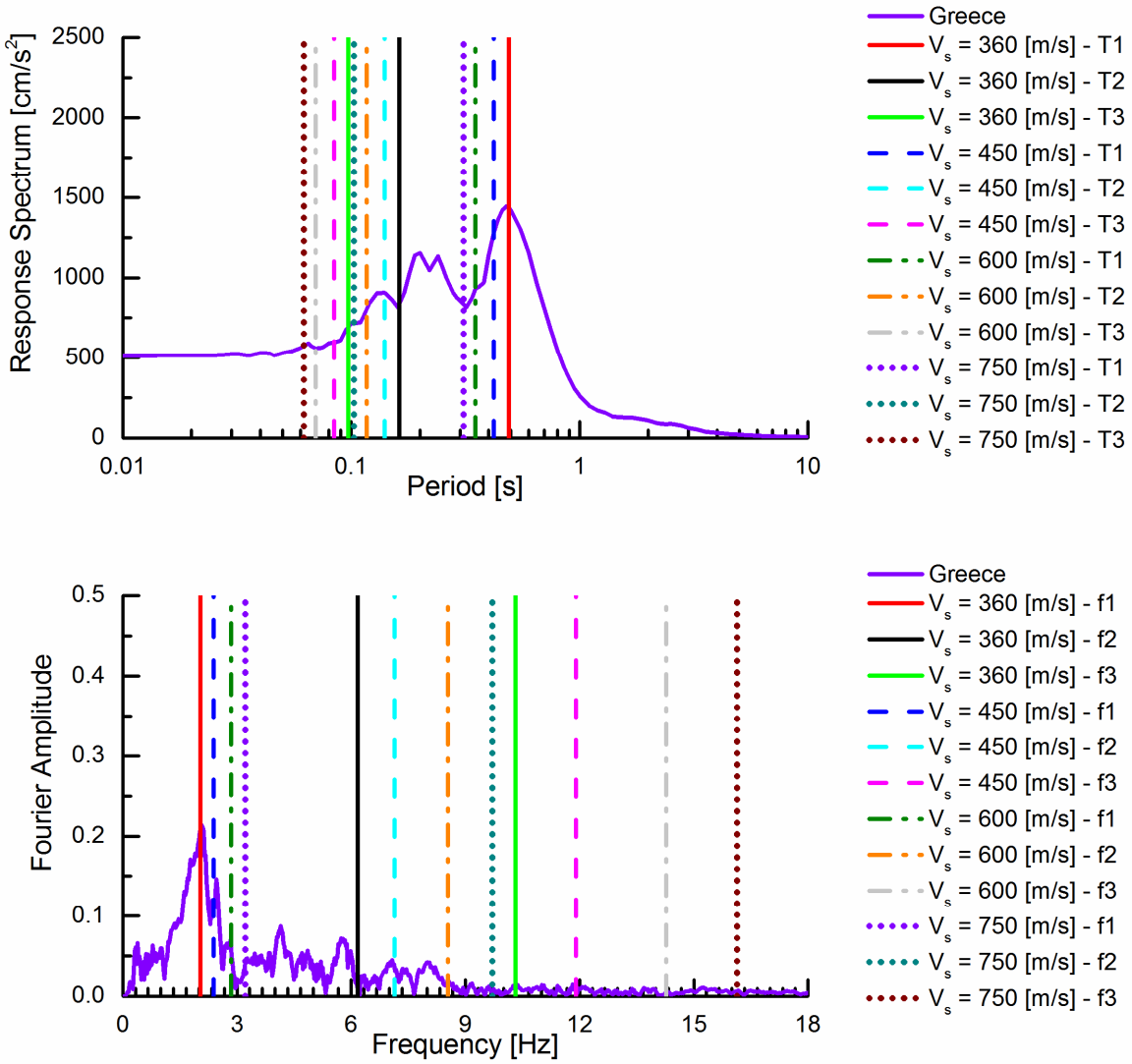

Figure 27: Greece GR-1995-0047 response spectrum and seismic signal in frequency domain

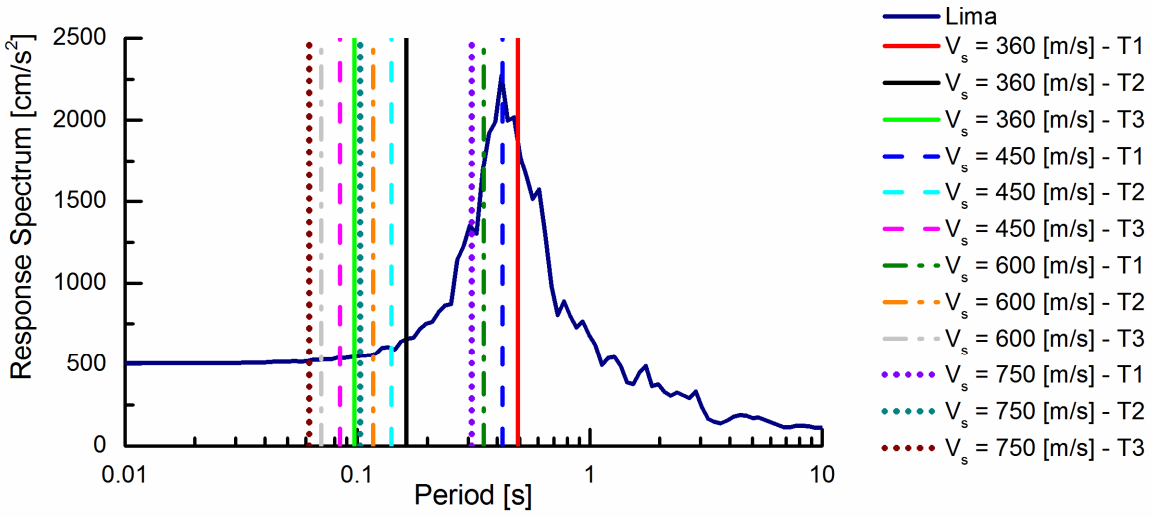

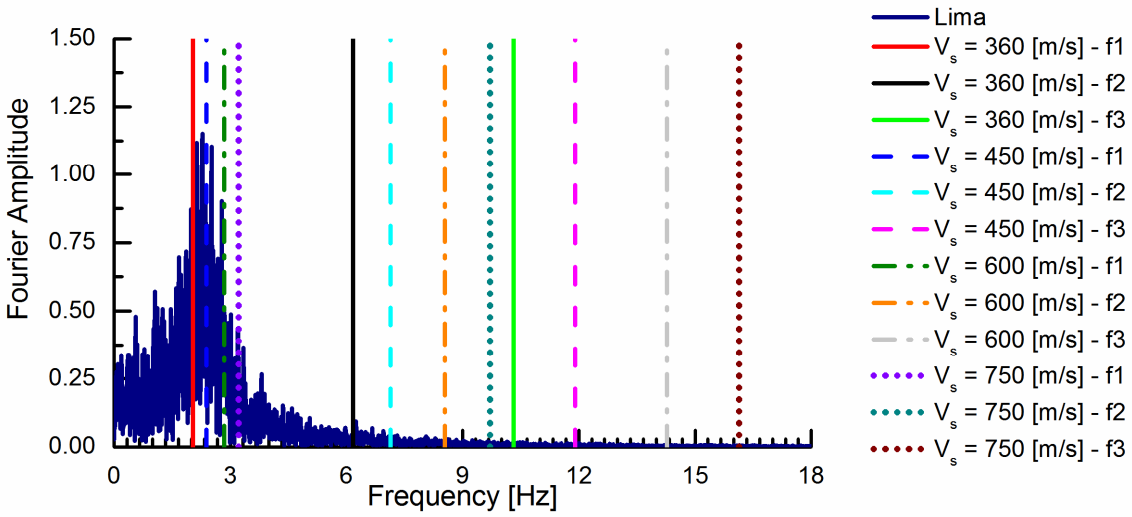

Figure 28: Lima response spectrum and seismic signal in frequency domain

As shown in the previous Figures is possible to notice that Greece and Lima seismic inputs have the maximum energy content near to the first fundamental period of the soil profiles, in particular for Greece seismic input (Figure 27) in correspondence to the first fundamental period of the soil profile characterized by $V_S = 360$ m/s while for the Lima seismic input in correspondence to the first fundamental period of the soil profile that has $V_S = 450$ m/s (Figure 28).
For Amatrice and Friuli seismic inputs (Figures 24 and 26) the maximum peak of the response spectrum is in correspondence to the second fundamental period of the soil profile characterized by $V_S = 360$ m/s.
For the Montenegro seismic input (Figure 23) the peak of the response spectrum is at greater periods than 0.49 s which represents the first period of the less stiff soil profile (Table 9).
Similar considerations may be made by analyzing the seismic signals in frequency domain where, see previous Figures, that the peaks of the Fourier transform of the different seismic inputs are localized near the frequencies range that include the first fundamental frequency of the four soil profiles. Only for the Montenegro seismic input, all the main picks are found at lower frequencies compared to the first fundamental frequency that characterized the different soil profiles.
In the Figure 29 the functions of the Arias Intensity of the different seismic inputs are reported.

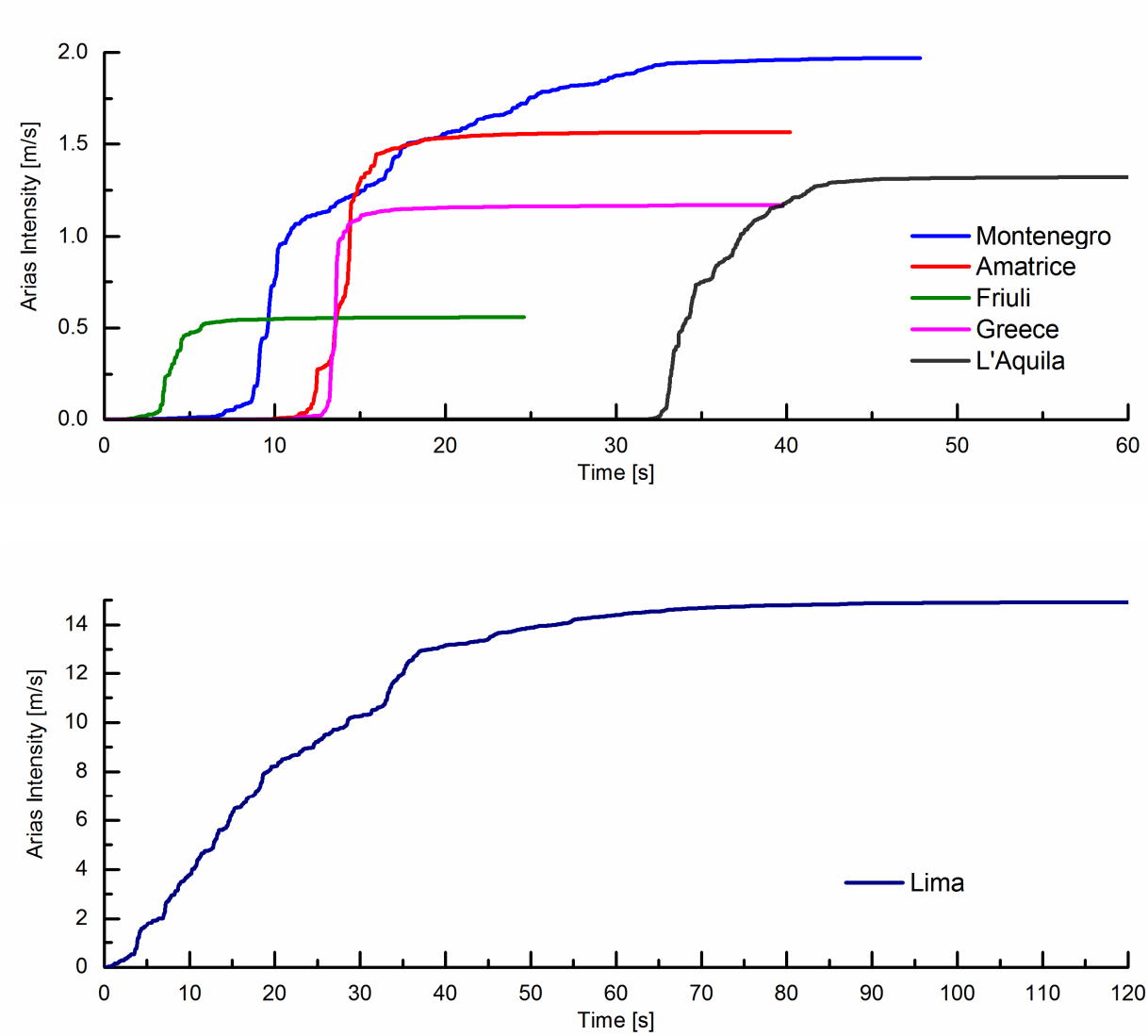

Figure 29: Arias Intensity of the seismic inputs

3.3. Numerical modelling

The dynamic analyses were carried out, under plane strain conditions, through the finite difference code FLAC (Itasca, 2007). The numerical model and the relative computation grid are show in the next Figure 30.
An elastic perfectly plastic model with Mohr Coulomb strength rule for the soil, characterized by the mechanical properties listed in Table 6, was adopted while for the sandstone a simple elastic constitutive law was chosen. The shear stiffness at small strain, G_0, is calculated as a function of the shear waves velocity value (V_S):

$$G_0 = \rho \cdot V_s^2$$

The maximum size of the computation mesh elements has been fixed to allow the correct propagation of harmonics with a 18 Hz, which is the maximum frequency of the seismic inputs used

in this work, according to Kuhlemeyer & Lysmer (1973). The formulation to optimize the size of the mesh is given in Pagliaroli et al. (2007).
To minimize reflection effects on vertical lateral boundaries of the grid, free field boundary conditions available in FLAC 7.0 library have been used. The soil hysteretic behavior was modeled using the shear modulus decay curves given by Seed & Idriss (1991) and Stokoe et al. (2013) (Figure 31). For the hysteretic damping, the code FLAC uses the weel-know generalized Masing rules. Furtermore, the contact between soil and walls was modeled by using elastic-perfectly plastic interface elements, with a friction angle equal to 20°.

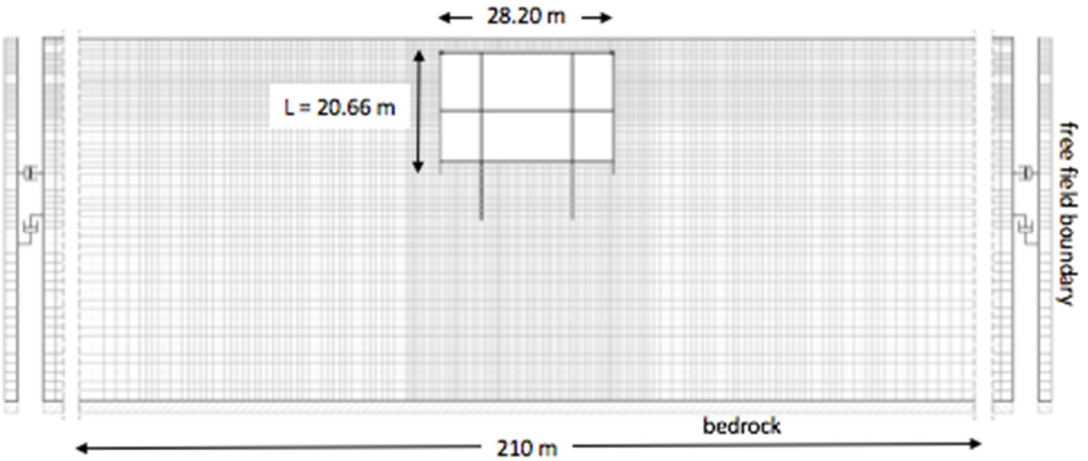

Figure 30: Model geometry and mesh for 2D analysis

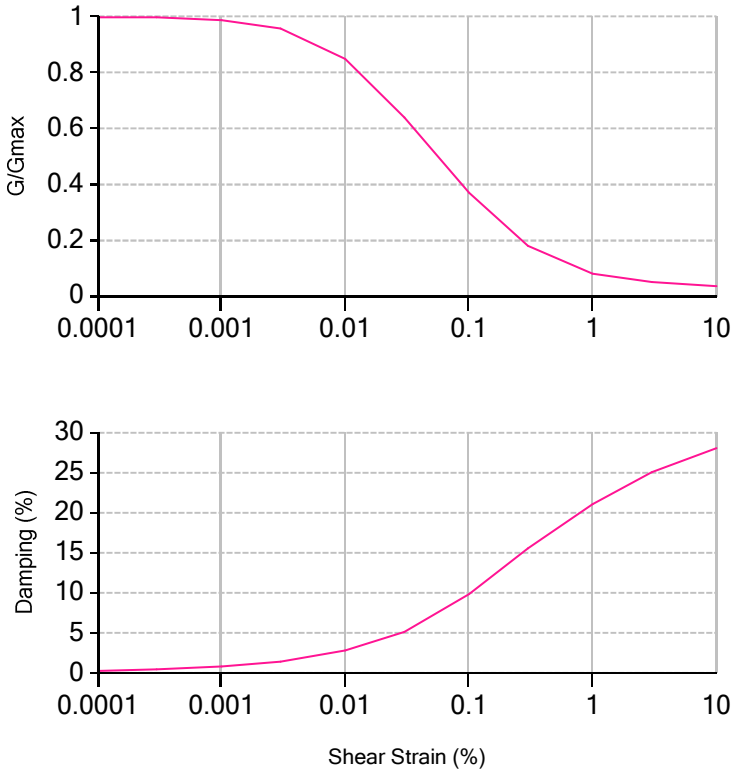

Figure 31: Seed & Idriss, 1991 Upper Bound G-γ and D-γ decay curves

3.4. Seismic system response

The response of ground motion obtained from the sensitivity analysis appears significantly influenzed by different overlapping effects:

1. different stiffness of the soil profiles, due to the different values of shear wave velocity (V_S);
2. non-linear behavior of the soil;
3. geometry of the system (2D effects);
4. soil-structure interaction effects.

The comparison between the parameters of the seismic inputs and those obtained at ground level enables an evaluation of the magnitude of the seismic action in relation to the first two effects mentioned above.
The results of the *free field* analysis (i.e. in 1D condition for the scheme considered in this study), in terms of acceleration ratio (ratio of maximum acceleration at ground level, $PGA_{S\text{-}1D}$ and maximum acceleration of the seismic input, PGA), are showed for each soil profiles in the Figures 32, 33, 34 and 35.
The soil response, at the different seismic inputs, is related to the system vibration modes excited by the signal. In fact, the seismic response of the soil column is meaningfully influenced by the soil motion and straining, in particular for the markedly non-linear behavior of the soil.
As mentioned before, Amatrice, Friuli and Greece seismic inputs show resonance effects with the first vibration mode of the different soil profiles, leading to an increase of the shear strain in the deeper soil layers and, consequently, additional damping according to the strongly non-linear behavior of the soil (Kramer, 1996, Lanzo & Silvestri, 1999, Soccodato & Tropeano, 2015).
Same consideration can be done for the Lima synthetic accelerogram that presents the major peaks all at frequencies below 3 Hz. Montenegro and L'Aquila seismic inputs are, also, characterized by peaks near the first vibration mode bandwidths.
For these reasons, the *free field* analysis shows larger amplification of the peak acceleration. Only for the unscaled accelerograms, the *free field* analysis shows a deamplification of the peak acceleration due to characteristics of the inputs which amplify the dissipation effects due to the non-linear behavior of the soil. This consideration is corroborated by the response spectra of the unscaled inputs obtained, always, in *free field* condition and shows in Figures 36, 37, 38, 39, 40 and 41 where it is possible to notice the deamplification of the PGA and the shift of some picks corresponding to determinate frequencies.
The effects 3 and 4 are evaluated considering the ratio between the maximum acceleration at the 2D model surface, $PGA_{S\text{-}2D}$, and the peak acceleration at the surface obtained in *free field* condition, $PGA_{S\text{-}1D}$. The results are summarized in the Figures 42, 43, 44, 45, 46 and 47.
The geometry of the system and the presence of the structure generate an amplification of the seismic motion behind the walls and at the center of the excavation for the focusing phenomena of the waves and seismic motion attenuation in front of the retaining walls due to the diffraction phenomena of the waves. Only for the Lima seismc input is possibile to see a seismic motion attenuation in the center of the excavation but a greater amplification of the seismic action behind the walls compared to the other seismic inputs. This is due to the system damping of some frequencies that characterized the seismic input.
The presence of the structure, furthermore, due to the its high stiffness, produces additional reflections for the soil-structure interaction effects. The interaction of reflected and incident wave fields modifies the shaking amplitude that depends on the phase shift of the two signals. The geometrical amplification and the phase shift are closely related to the frequency content of the

signal that changes due to the non-linear behavior of the soil (Kuhlemeyer & Lysmer, 1973, Kramer, 1996, Soccodato & Tropeano, 2015).

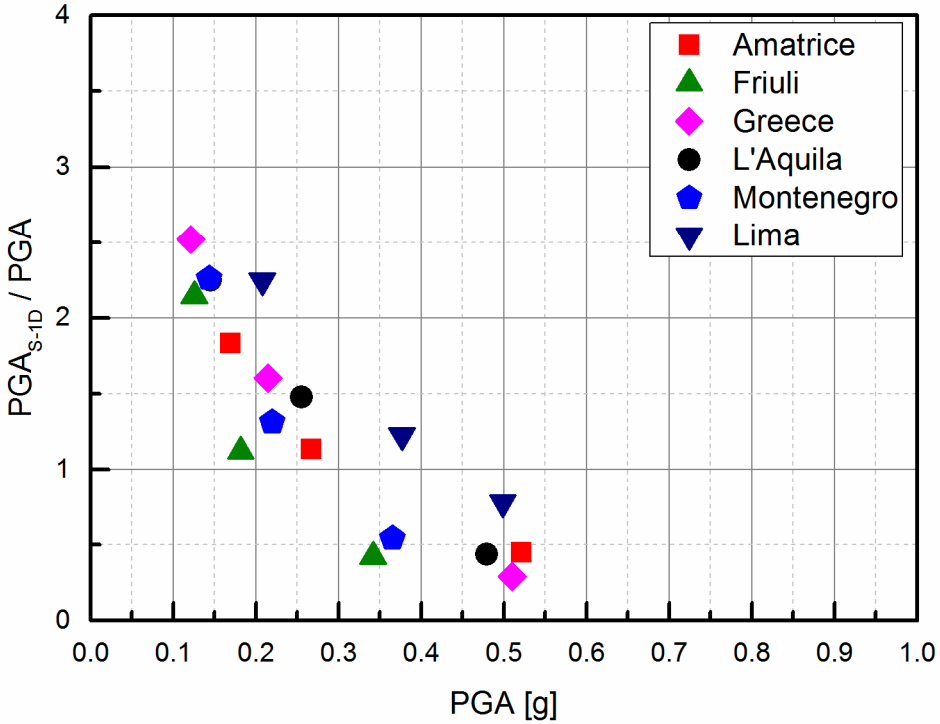

Figure 32: 1D response factor, in terms of acceleration ratio, for the soil profile characterized by *Vs* = 360 m/s

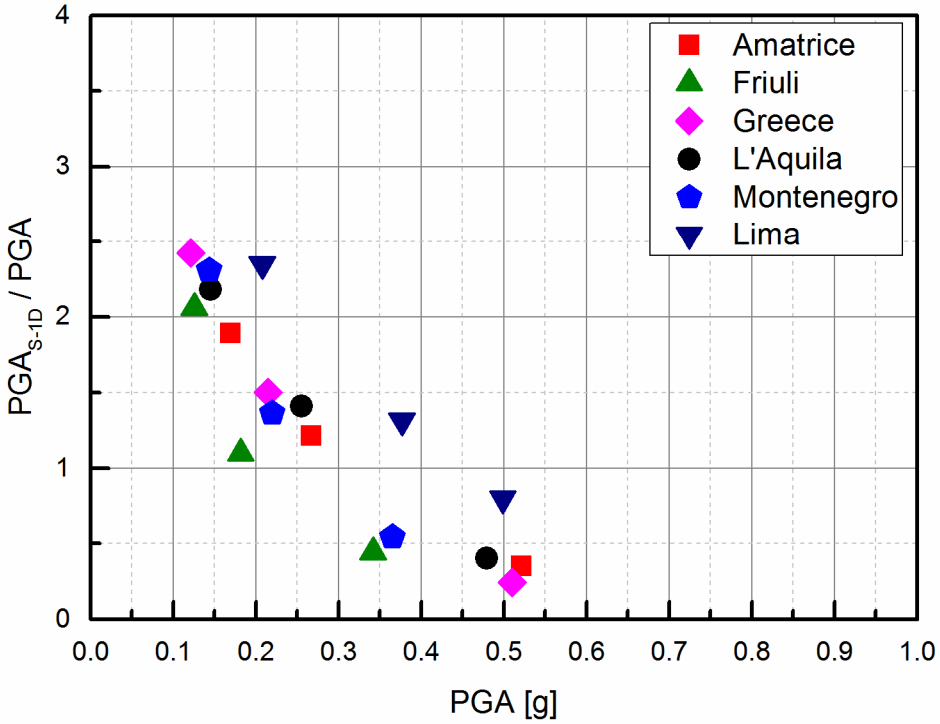

Figure 33: 1D response factor, in terms of acceleration ratio, for the soil profile characterized by *Vs* = 450 m/s

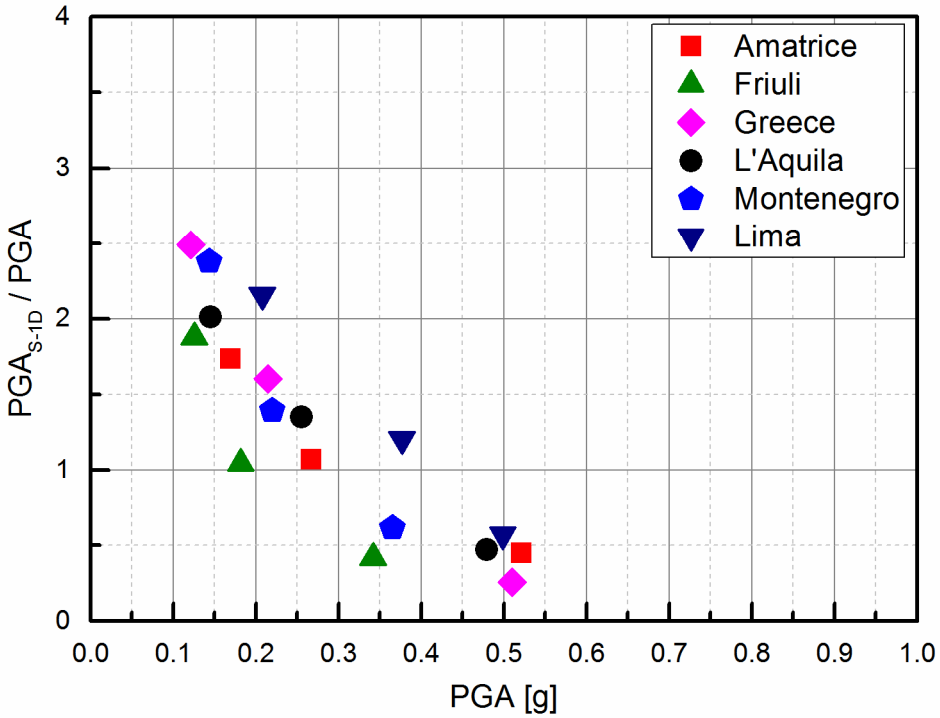

Figure 34: 1D response factor, in terms of acceleration ratio, for the soil profile characterized by *Vs* = 600 m/s

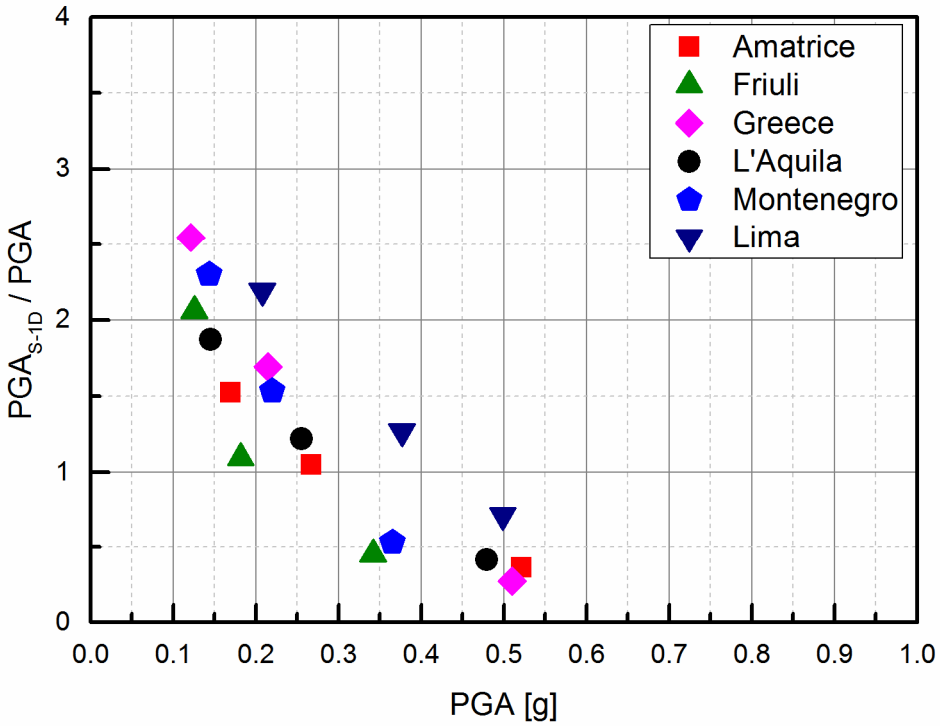

Figure 35: 1D response factor, in terms of acceleration ratio, for the soil profile characterized by *Vs* = 750 m/s

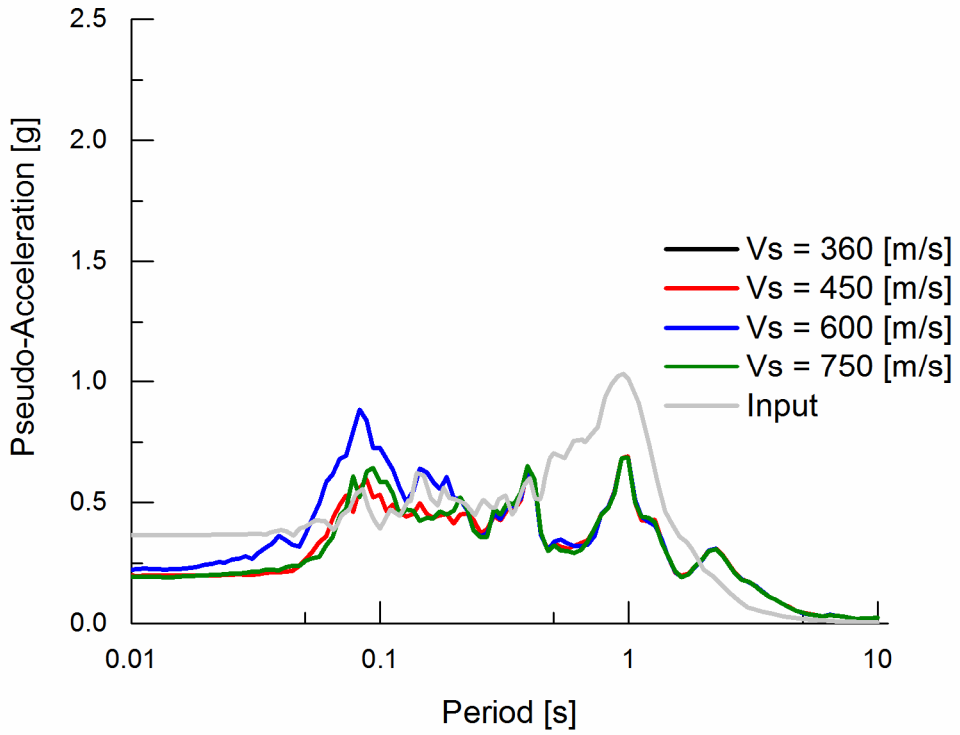

Figure 36: Response Spectra of Monetenegro seismic input evaluated at ground level in *free field* condition

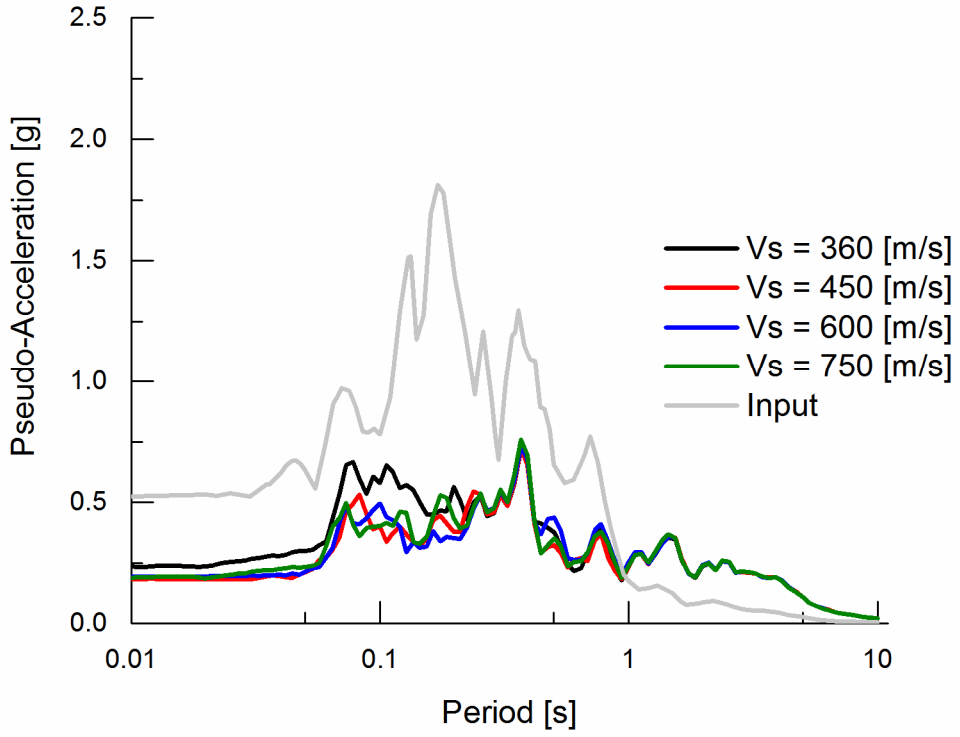

Figure 37: Response Spectra of Amatrice seismic input evaluated at ground level in *free field* condition

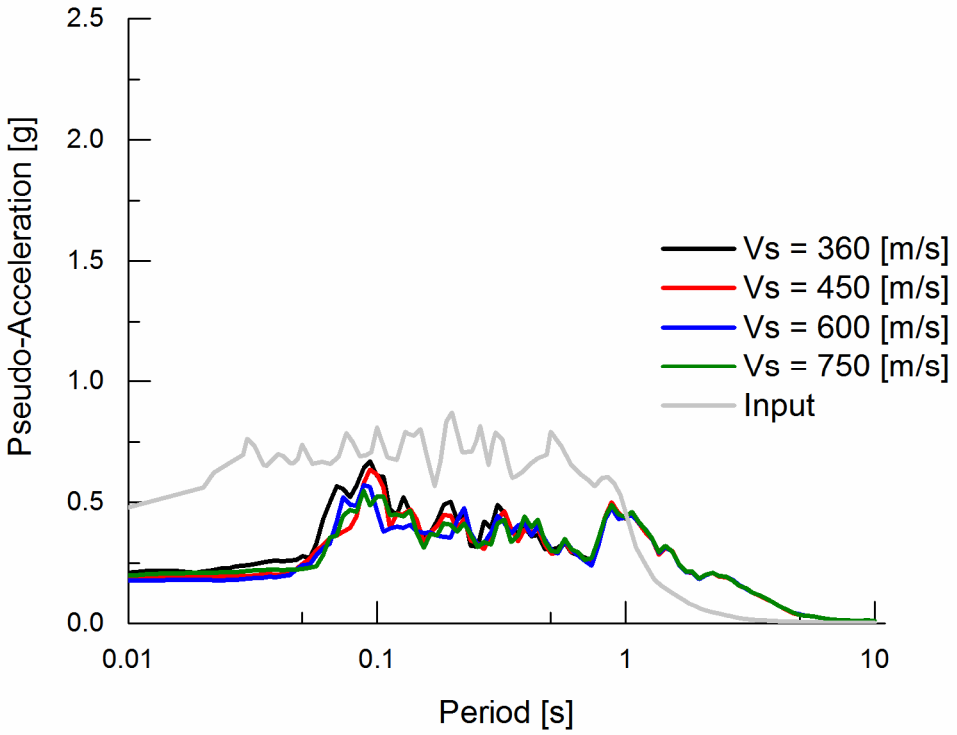

Figure 38: Response Spectra of L'Aquila seismic input evaluated at ground level in *free field* condition

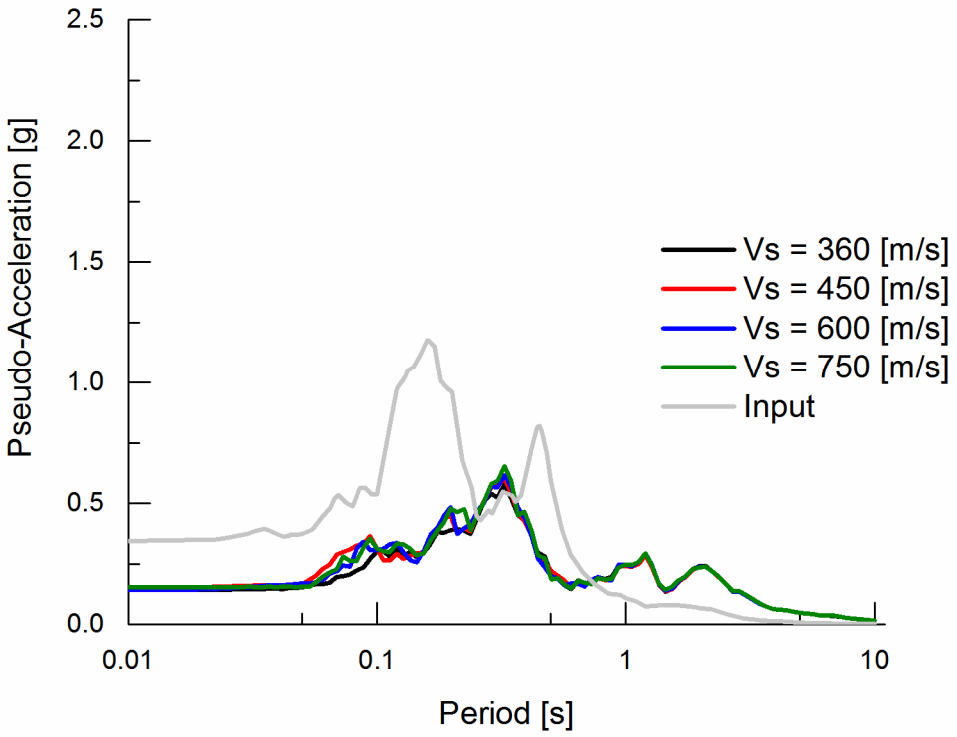

Figure 39: Response Spectra of Friuli seismic input evaluated at ground level in *free field* condition

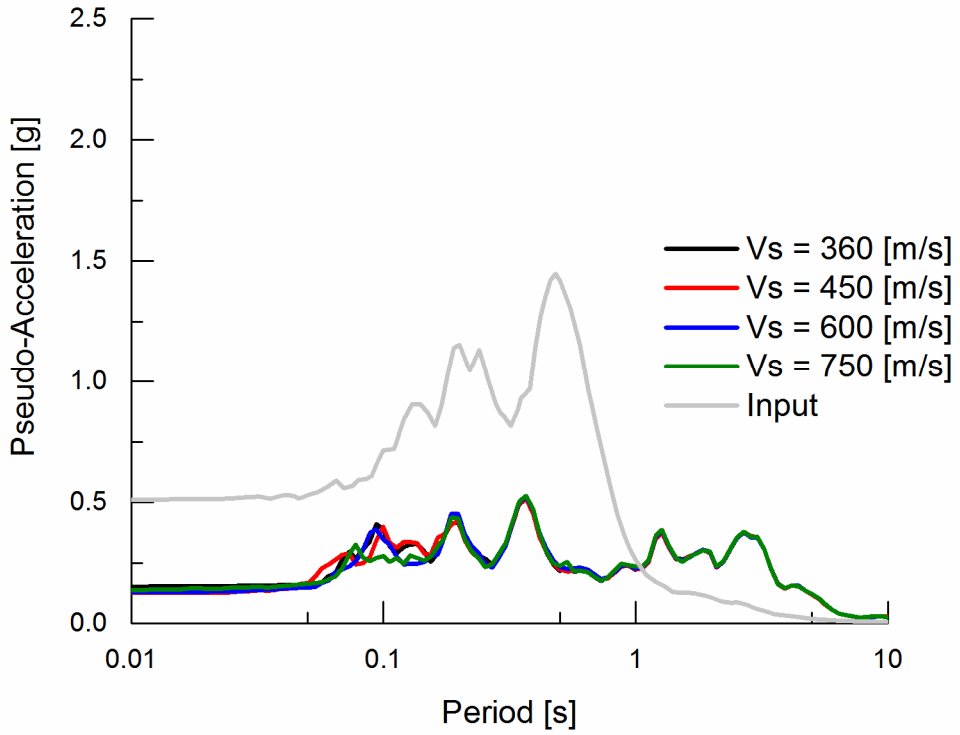

Figure 40: Response Spectra of Greece seismic input evaluated at ground level in *free field* condition

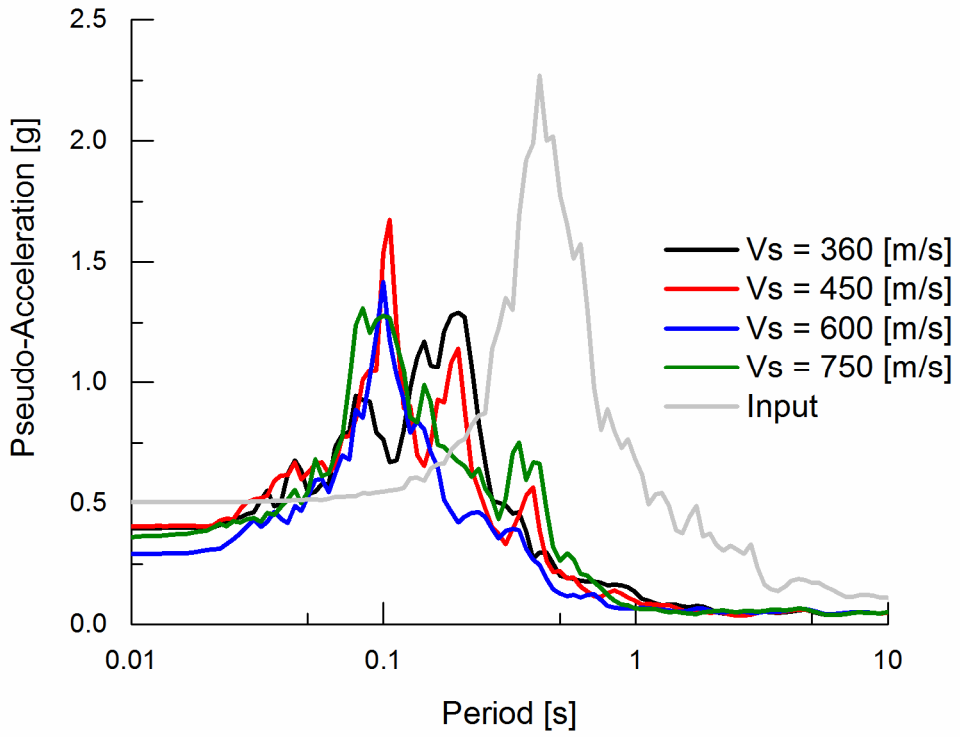

Figure 41: Response Spectra of Lima seismic input evaluated at ground level in *free field* condition

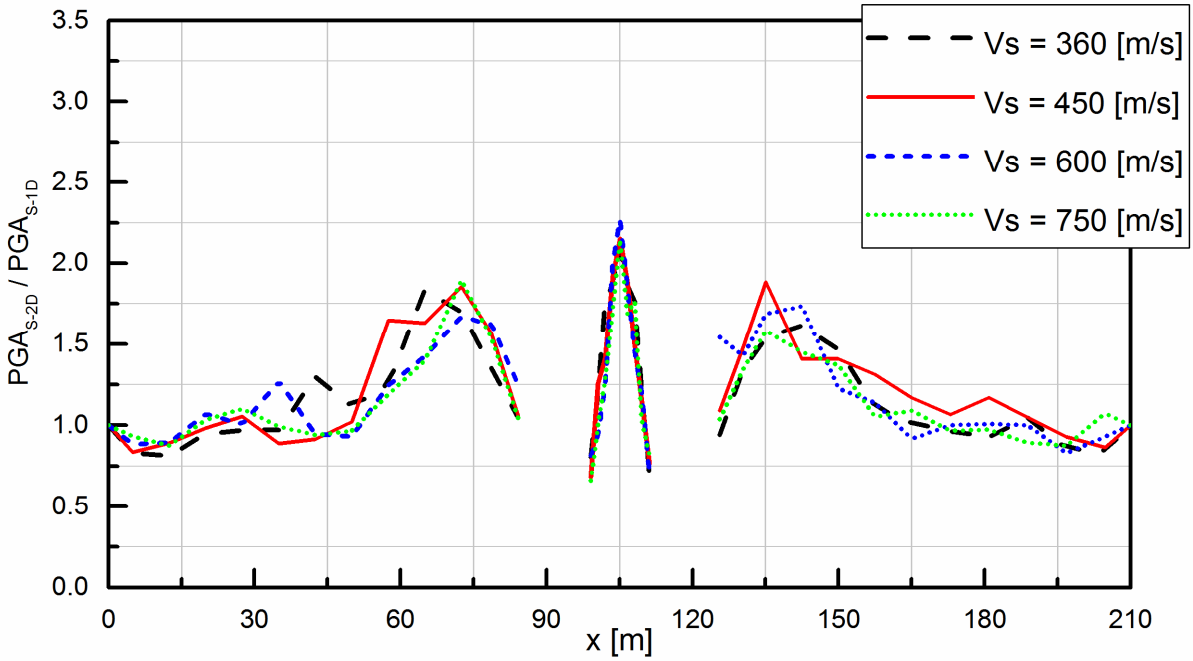

Figure 42: 2D surface response factor for Montenegro seismic input

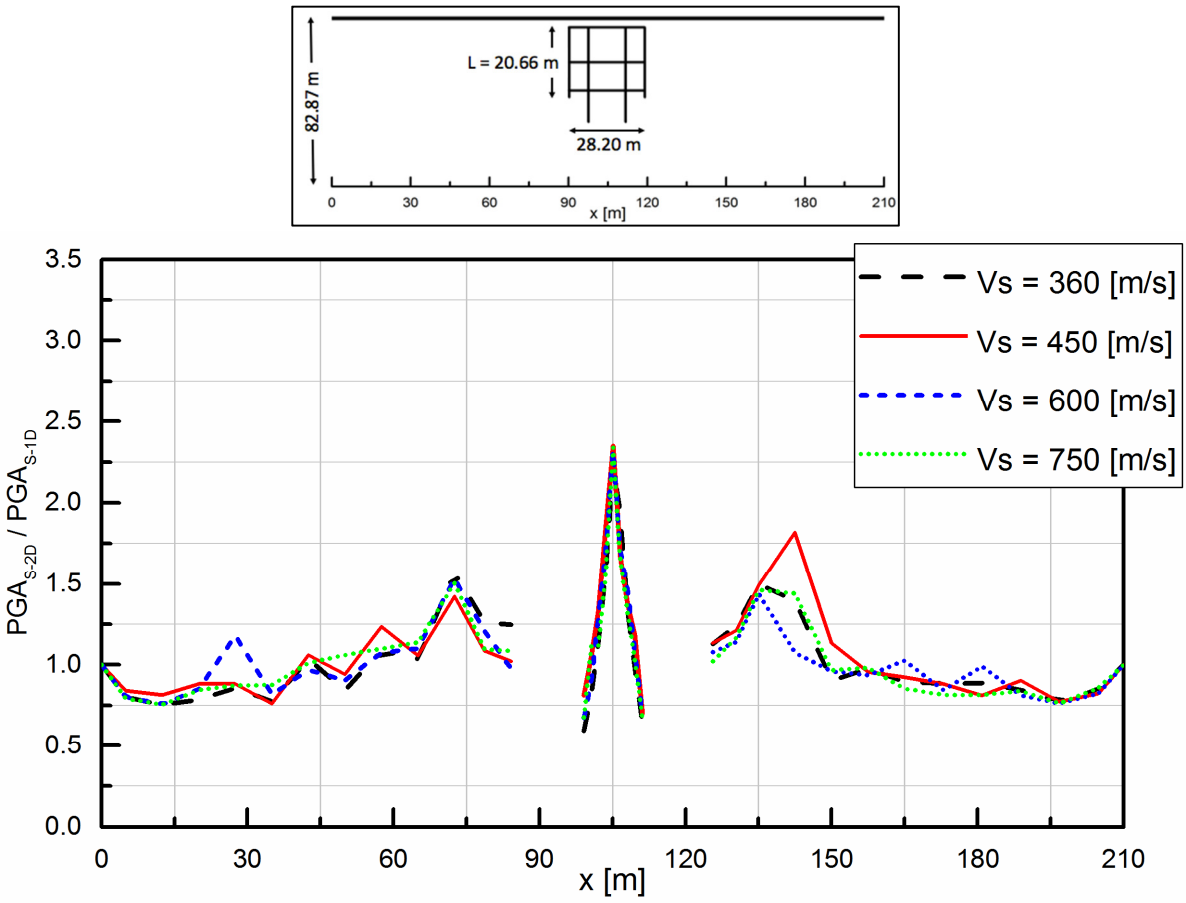

Figure 43: 2D surface response factor for Amatrice seismic input

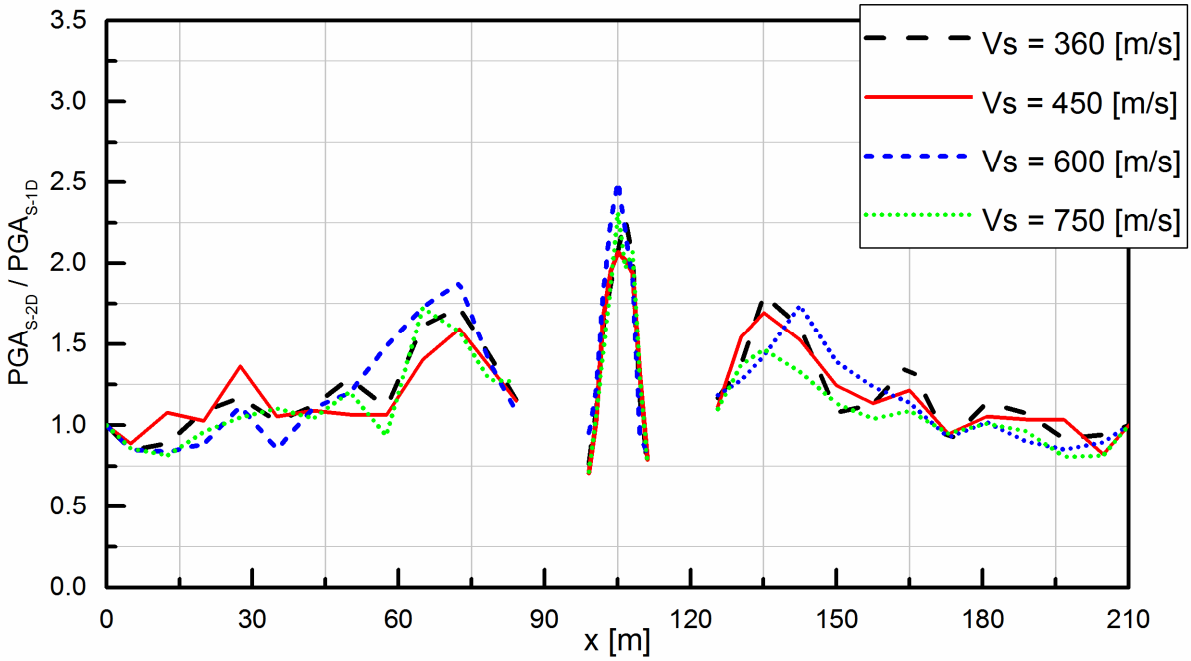

Figure 44: 2D surface response factor for L'Aquila seismic input

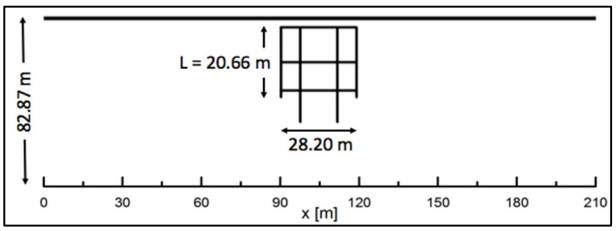

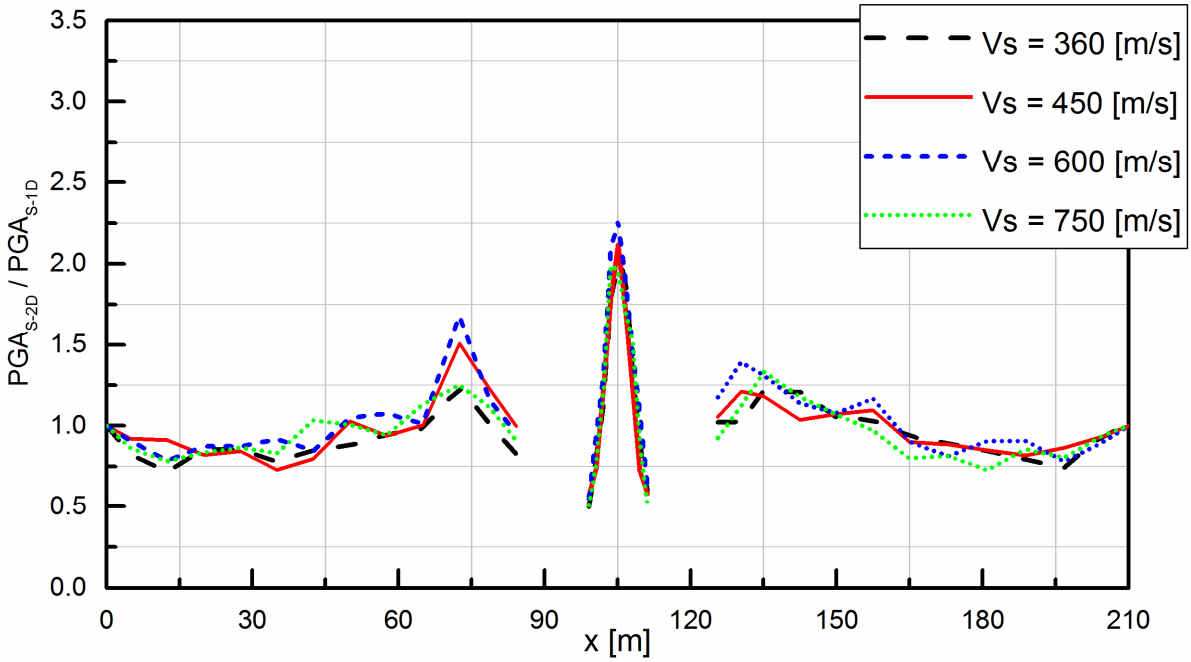

Figure 45: 2D surface response factor for Friuli seismic input

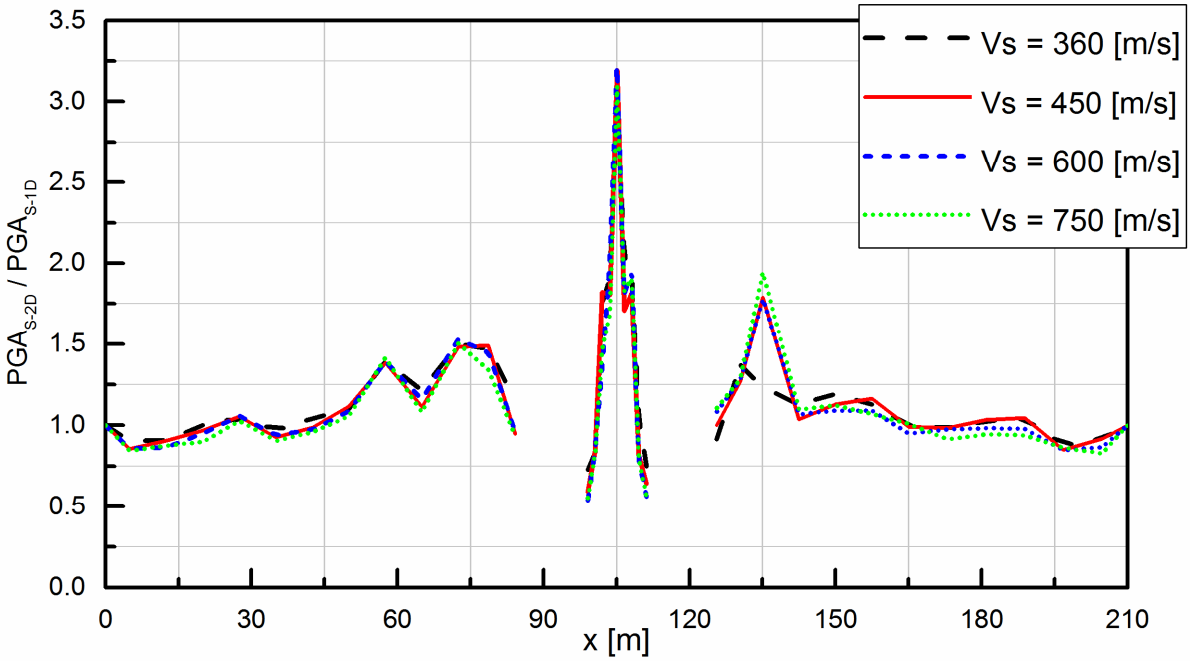

Figure 46: 2D surface response factor for Greece seismic input

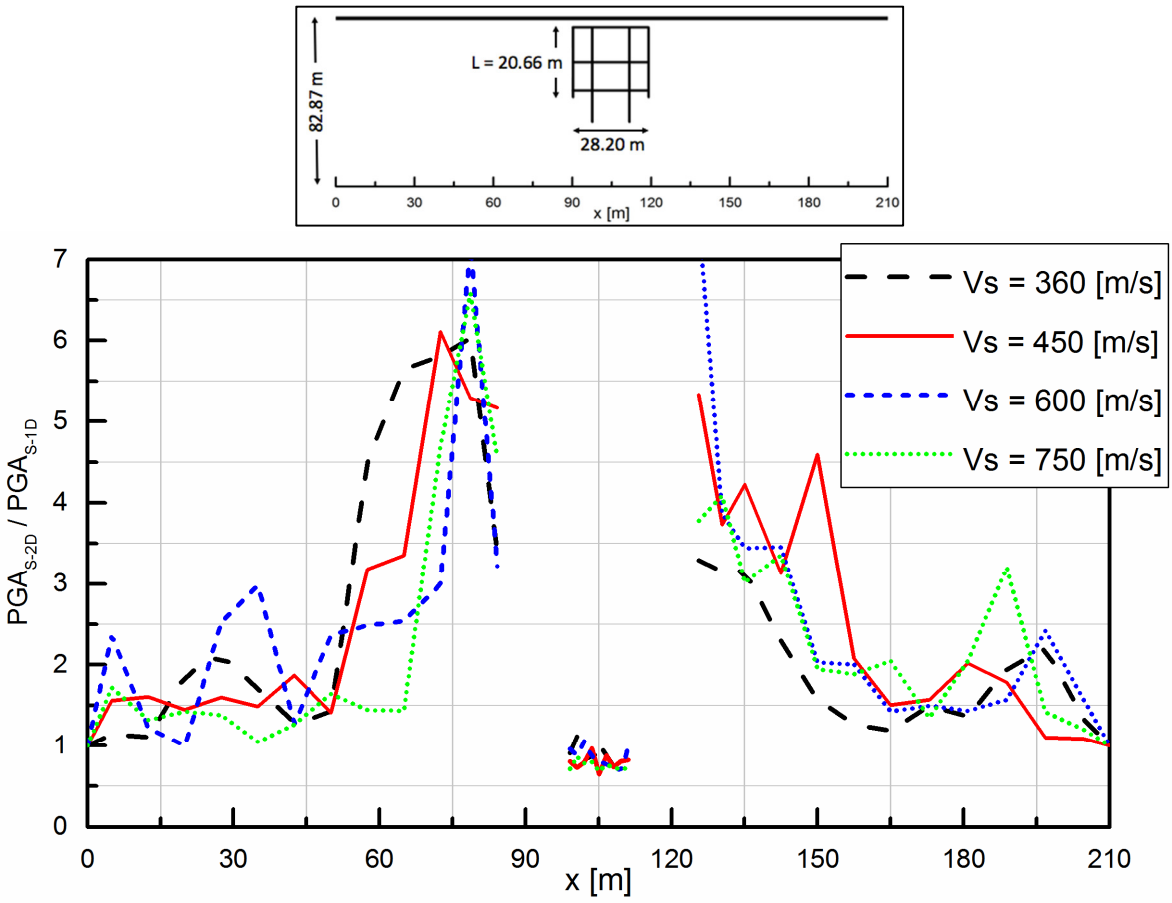

Figure 47: 2D surface response factor for Lima seismic input

3.5. Decupled Approach

The decoupled approach, considered in this study, consists in the evaluation of the ground deformation without taking into consideration the presence of the structure (i.e. in free field condition) and in the application of such deformations (valued at the depth of the structure) to the structure, according to the scheme reported in Figure 48.

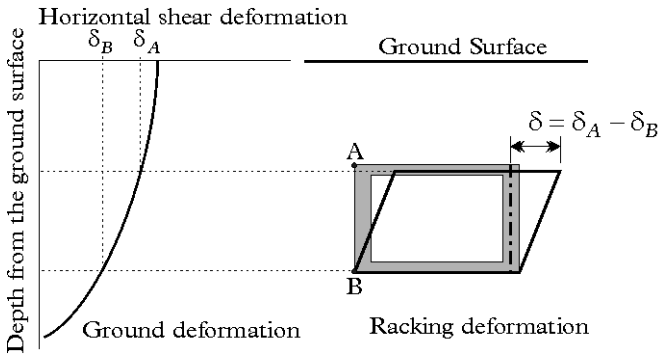

Figure 48: Decoupled approach procedure

To simulate numerically the seismic response of the soil profiles and, consequently, obtain the displacements at the roof and the base of the structure, two different types of approach have been used. In the first, the soil profiles, described in the previous Table 6, have been implemented in DEEPSOIL (Hashash et al., 2016) and an equivalent linear analysis has been performed.
The theory of the approximation of the non-linear behavior of the soil in dynamic condition by equivalent linear approach was proposed first by Schnabel et al. (1972), Idriss and Sun (1992) and Kramer (1996). The equivalent linear approach uses relationships that consider the variation of soil shear modulus, G, and the variation of the hysteretic damping ratio, D (or ξ), with shear strain, γ. These relationships are referred to as the already mentioned G-γ and D-γ decay curves (Figure 31). One of the first code that implemented this procedure was SHAKE (Schnabel et al., 1972) which computes the response in a horizontally layered soil profile under transient and vertical travelling shear waves. The procedure is based on the wave propagation solutions of Kanai (1995), Roesset and Whitman (1969) and Tsai and Housner (1970). This code based on the multiple reflection theory and the non-linear behavior of the soil profile is considered by the equivalent linear approach. The fundamental hypotheses are the following:

- the layers of the soil profile are horizontal and infinitely extended (1D conditions);
- the soil layers are completely defined by the shear modulus and damping as a function of strain, the thickness and the unit weight;
- the non-linear cyclic behavior is described by the Voigt constitutive model and implemented with the equivalent linear method;
- the incident earthquake motions are spatially-uniform, horizontally-polarized shear waves and propagate vertically.

Another code that implemented the equivalent linear method is EERA (Equivalent linear Earthquake Response Analysis) that uses the same algorithm of SHAKE. Consider uniform soil layers lying on an elastic layer of rock that extends to infinite depth (Figure 49), the EERA approach is described in the following steps.

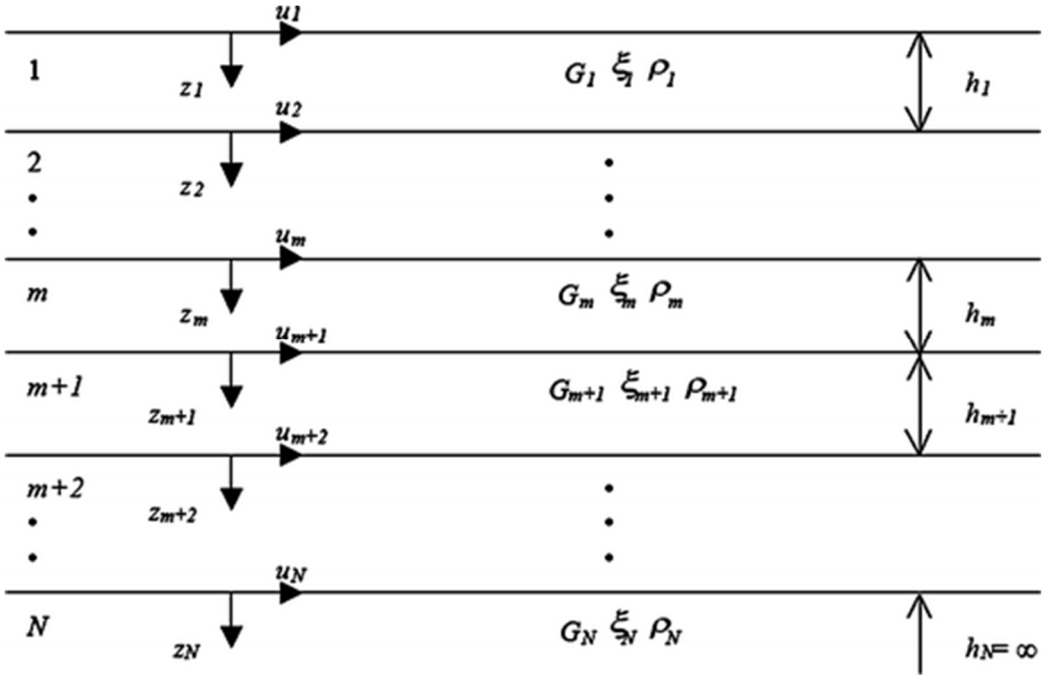

Figure 49: 1D layered soil deposit schematization (EERA, 1998)

The solution of 1D equation of motion, in the case of harmonic waves, for vertically propagating shear waves gives the displacements and, consequently, the related stresses by the following relations:

$$u(z,t) = Ee^{i(\omega t + K^* z)} + Fe^{i(\omega t - K^* z)}$$

$$\tau(z,t) = G^* \frac{\partial u}{\partial z} = (G + i\omega\eta)\frac{\partial u}{\partial z} = G(1 + 2i\xi)\frac{\partial u}{\partial z}$$

where ω is the circular frequency of the harmonic wave and K^* the complex wave number defined as:

$$K^* = \frac{\omega}{V_S^*}$$

where V_S^* represents the complex shear waves velocity obtained as:

$$V_S^* = \sqrt{\frac{G^*}{\rho}} = \sqrt{\frac{G(1 + i2\xi)}{\rho}} \approx \sqrt{\frac{G}{\rho}}(1 + i\xi) = V_S(1 + i\xi)$$

Compatibility of dispacements at the interface between two layers indicated, generally, as m and m+1 and continuity of shear stresses imply that:

$$E_{m+1} = \frac{1}{2}E_m(1 + \alpha_m^*)e^{iK_m^* h_m} + \frac{1}{2}F_m(1 - \alpha_m^*)e^{-iK_m^* h_m}$$

$$F_{m+1} = \frac{1}{2}E_m(1 - \alpha_m^*)e^{iK_m^* h_m} + \frac{1}{2}F_m(1 + \alpha_m^*)e^{-iK_m^* h_m}$$

with α_m^* which represents the complex impedence ratio at the interface between layers *m* and *m*+1 and defined as:

$$\alpha_m^* = \frac{K_m^* G_m^*}{K_{m+1}^* G_{m+1}^*} = \frac{\rho_m (V_s^*)_m}{\rho_{m+1} (V_s^*)_{m+1}}$$

Consequently, the thansfer function (A_{mn}) relating the displacements evaluated at the top of layers *m* and *n* are obtained by Hosseini et al. (2010):

$$A_{mn}(\omega) = \frac{u_m}{u_n} = \frac{\dot{u}_m}{\dot{u}_n} = \frac{\ddot{u}_m}{\ddot{u}_n} = \frac{E_m + F_m}{E_n + F_n}$$

The theory of the equivalent linear method consists of modifying the model proposed by Kelvin-Voigt accounting the non-linear behavior of the soil. The model is defined by the following equation (Figure 50):

$$\tau = G\gamma + \eta \frac{\partial y}{\partial t}$$

where *G* is the shear modulus and η the viscosity.

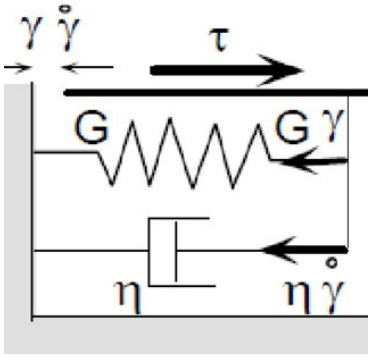

Figure 50: Stress-strain modeling scheme for the equivalent linear model (after Bardet & Lin, 2000)

The hysteretic τ- γsoil behavior during cyclic loading is approximated as shown in Figure 51.

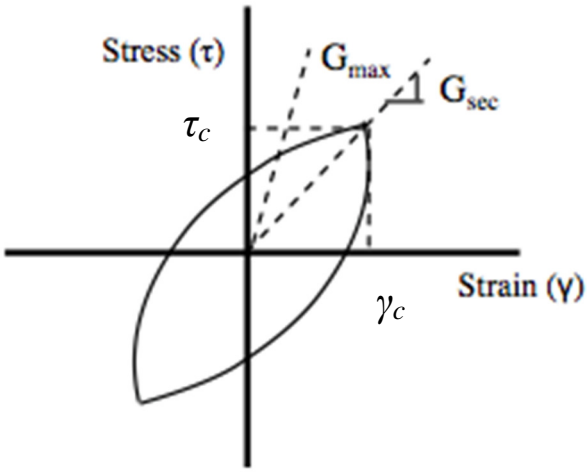

Figure 51: Equivalent linear model: the hysteresis stress-strain curve (after Kramer, 1996)

The equivalent linear shear modulus, G_s, is taken as the secant shear modulus, G_{sec}, that is function of the shear strain amplitude. The secant shear modulus at the ends of symmetric strain-controlled cycles is equal to:

$$G_{sec} = \frac{\tau_c}{\gamma_c}$$

where τ_c is the shear stress and γ_c the strain amplitude at the cycle inversion point. The equivalent linear damping ratio, ξ, is defined as the dampio ratio which generates the same energy loss in a single cycle as the hysteresis stress-strain loop of the irreversible soil behavior. Consequently, the critical damping ratio, ξ_c, is obtained considering the terms W_D e W_S:

$$\xi_c = \frac{W_D}{4\pi W_S} = \frac{1}{2\pi}\frac{A_{loop}}{G_{sec}\,\gamma_c^2}$$

where W_D and W_S are the energy dissipated during a complete loading cycle and the maximum strain energy stored in the system, respectively.
In the equivalent linear method, as mentioned before, the shear modulus and the damping ratio are taken as function of shear strain amplitude by iterations so which they become consistent with the level of the strain induced in each layer. The equivalent linear analysis effective shear strain is obtained by the following relation:

$$\gamma_{eff} = R_y \gamma_{max}$$

where γ_{max} represents the maximum shear strain level in the layer and R_y is a strain reduction factor defined as follows:

$$R_y = \frac{M-1}{10}$$

with *M* magnitude of earthquake. The equivalent linear approach uses linear properties for each element that remain constant during the history of the seismic action and are evaluated from the mean level of the dynamic motion.
The equivalent linear analysis implemented in DEEPSOIL follows the same theory described above. The discretization of 1D equivalent linear models, represented the different soil profiles, is listed in Table 10.

Table 10: Soil profiles discretization

Layer	Thickness	Unit Weight	Shear Velocity
[n°]	[m]	[kN/m^3]	[m/s]
1	1	21	Var.
2	1	21	Var.
3	0.6	21	Var.
4	0.6	21	Var.
5	1	21	Var.
6	1	21	Var.
7	1	21	Var.
8	1	21	Var.
9	1	21	Var.
10	1	21	Var.
11	1	21	Var.
12	1	21	Var.
13	0.81	21	Var.
14	0.45	21	Var.
15	0.45	21	Var.
16	1	21	Var.
17	1	21	Var.
18	1	21	Var.
19	1	21	Var.
20	1	21	Var.
21	1	21	Var.
22	1	21	Var.
23	1	21	Var.
24	1.06	21	Var.
25	1	21	Var.
26	1	21	Var.
27	1	21	Var.
28	1	21	Var.
29	1	21	Var.
30	1	21	Var.
31	1	21	Var.
32	1	21	Var.
33	1	21	Var.
34	0.6	21	Var.
35	51.30	22	1500

As well as 2D analyses, for the 1D equivalent linear analysis the degradation of the soil shear modulus is modelled with the Seed & Idriss (1991) decay curves (Figure 31).
Figures from 52 to 76 shown the results, in terms of displacement, for the four profiles subjected to the seismic inputs described above (the solid line indicates the displacements profile starting from the depth of the base of the structure).

The displacements obtained by the equivalent linear analysis shows a trend resulting from the first vibration mode shape of the soil column. These results are in according to the considerations expressed in the previous paragraph 3.4, i.e. the seismic signals mainly excite the first fundamental frequency of the soil profiles. Moreover, it is possible to notice that the displacement, evaluated at the ground level, decreases, significantly, when the stiffness of the soil column increases, in fact the maximum displacement, equal to 12 cm, is obtained for the soil profile characterized by V_S = 360 m/s under Lima seismic signal while for the soil profile characterized by V_S = 750 m/s, always under Lima seismic input, the same displacement is about 7 cm.
The minimum displacements are obtained for the Friuli seismic input which it is the signal characterized by the lowest PGA and Arias Intensity values.

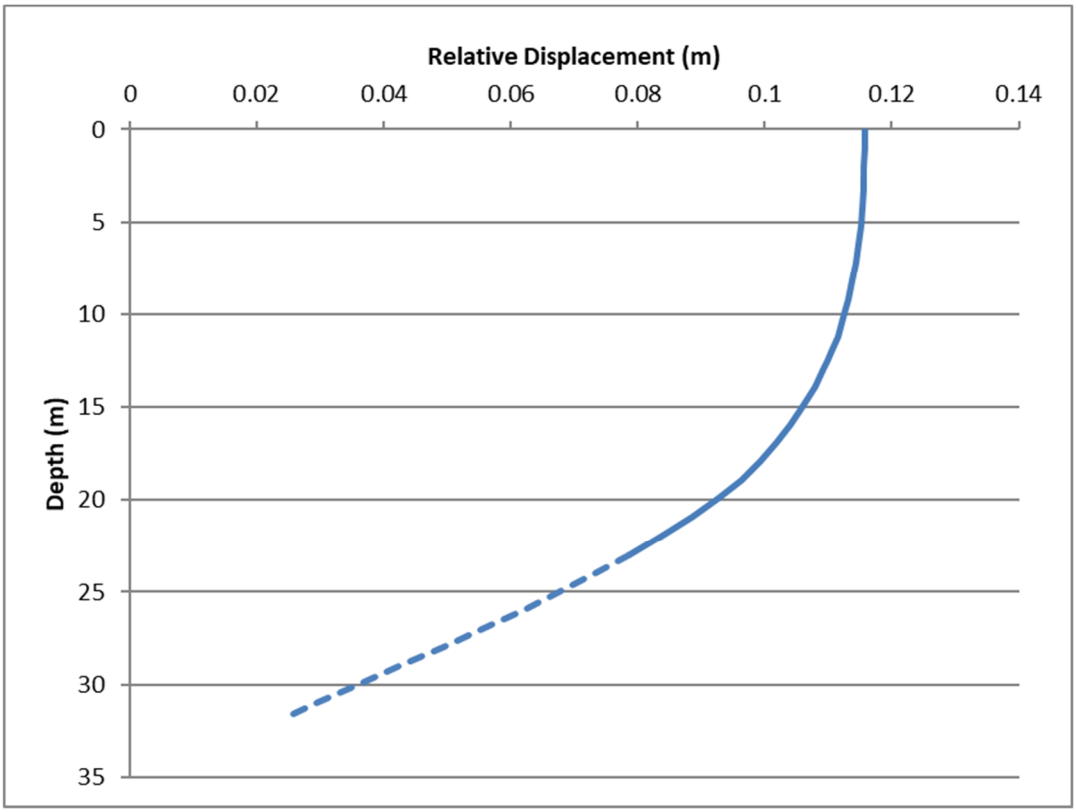

Figure 52: Trend of the displacements of the profile characterized by *Vs* = 360 m/s subjected to the Montenegro seismic input

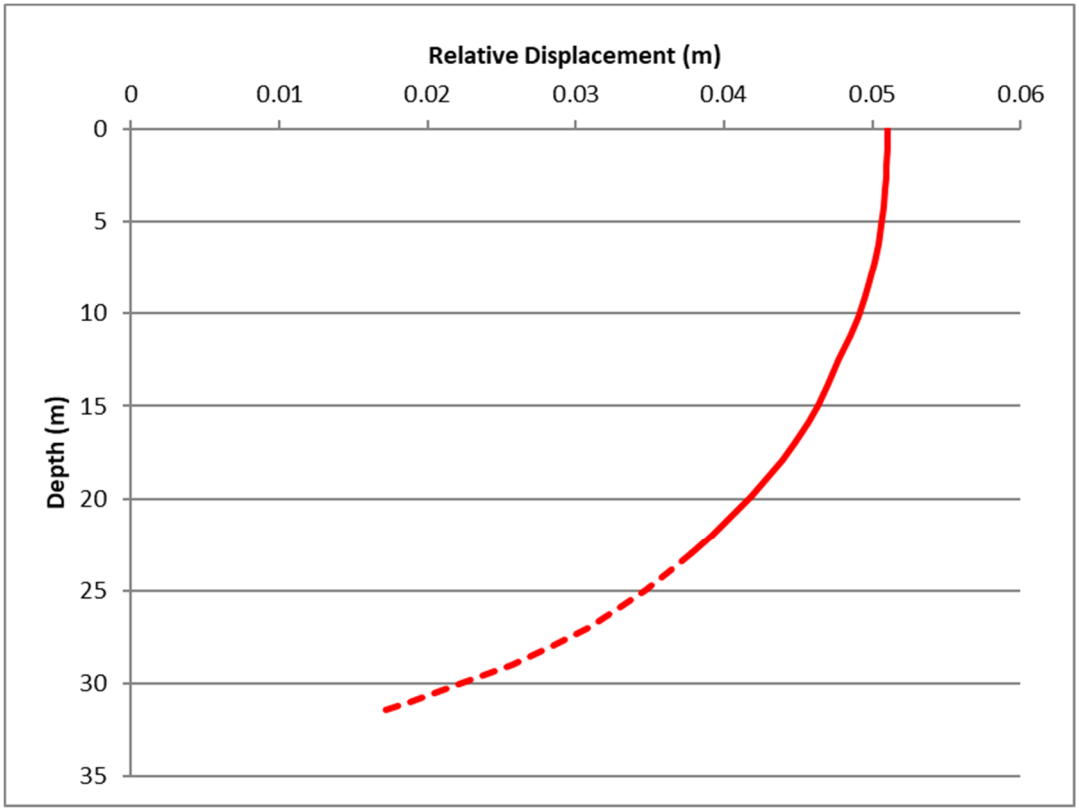

Figure 53: Trend of the displacements of the profile characterized by *Vs* = 360 m/s subjected to the Amatrice seismic input

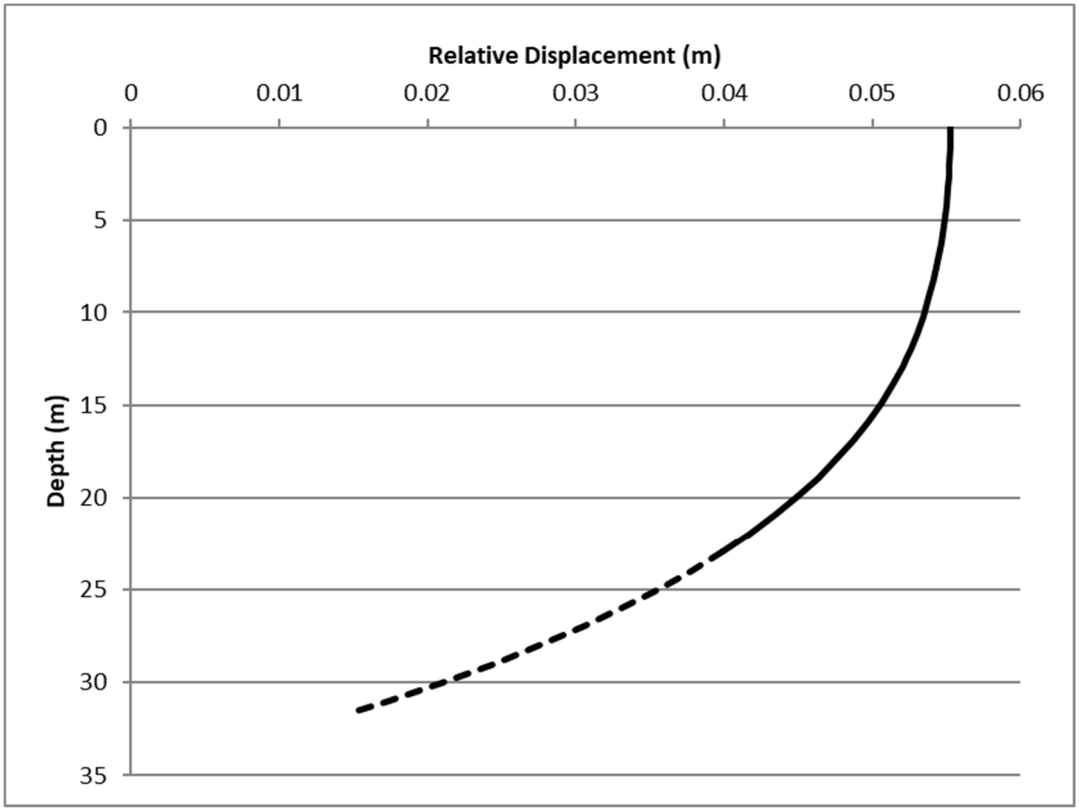

Figure 54: Trend of the displacements of the profile characterized by *Vs* = 360 m/s subjected to the L'Aquila seismic input

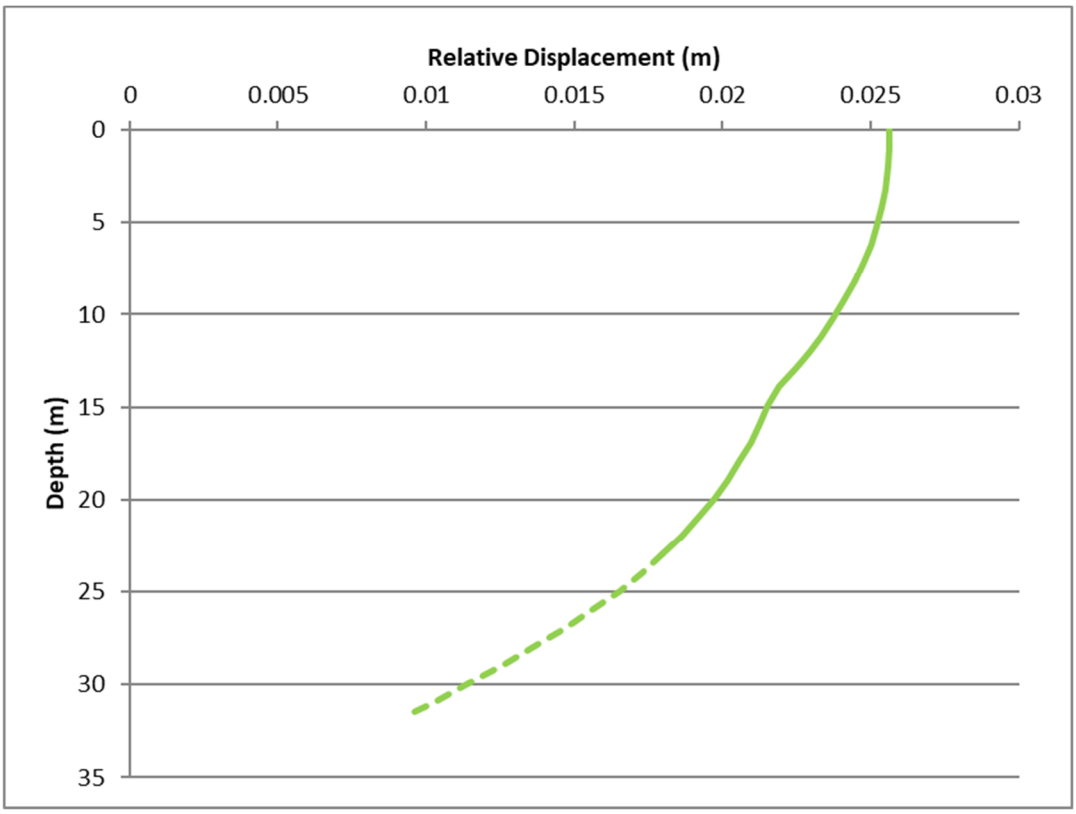

Figure 55: Trend of the displacements of the profile characterized by *Vs* = 360 m/s subjected to the Friuli seismic input

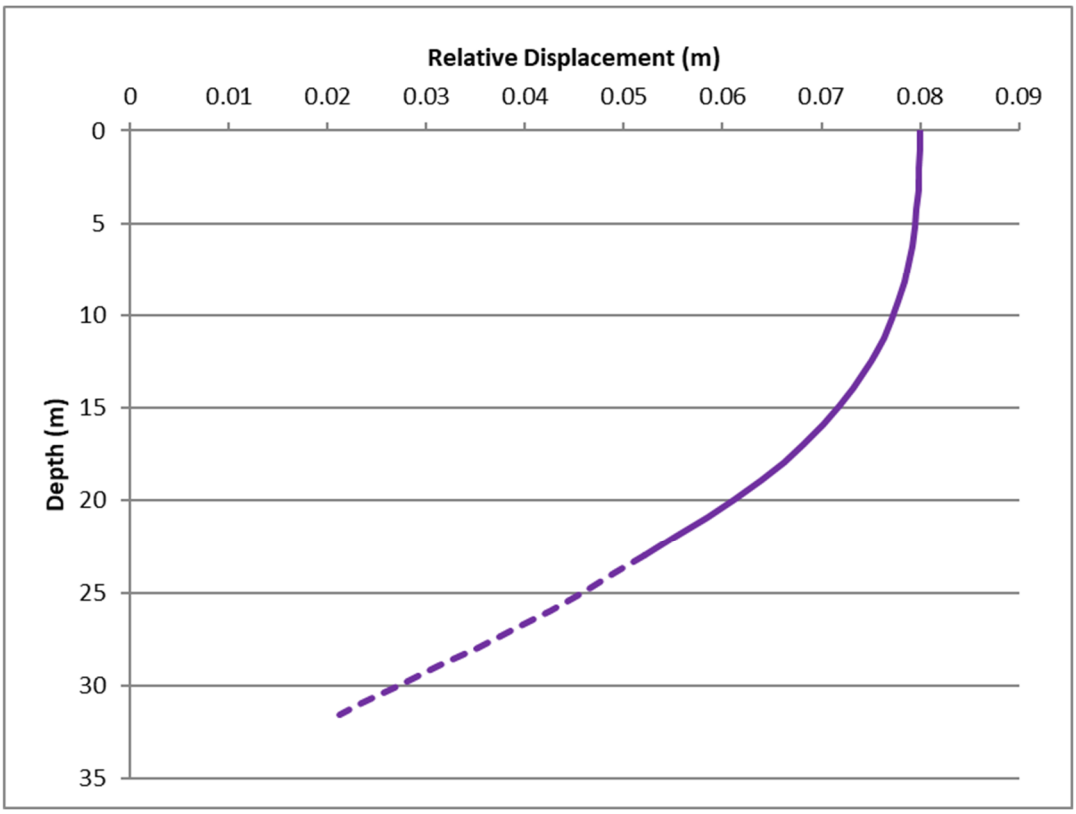

Figure 56: Trend of the displacements of the profile characterized by *Vs* = 360 m/s subjected to the Greece seismic input

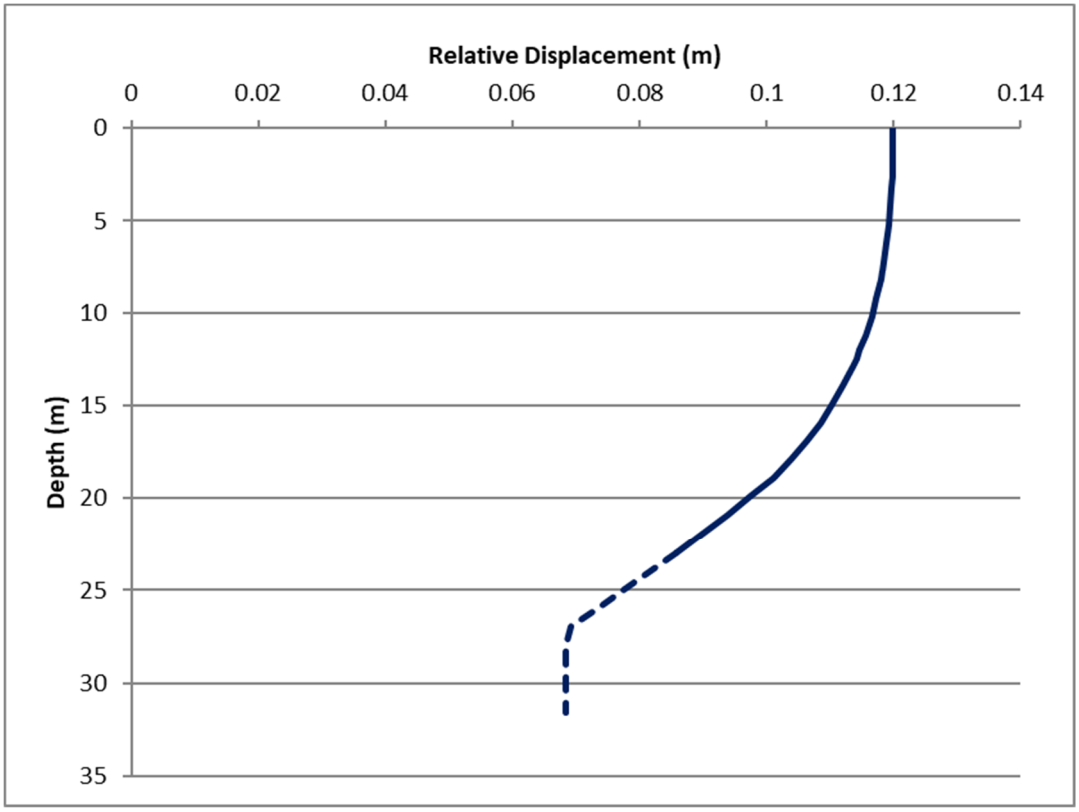

Figure 58: Trend of the displacements of the profile characterized by *Vs* = 360 m/s subjected to the Lima seismic input

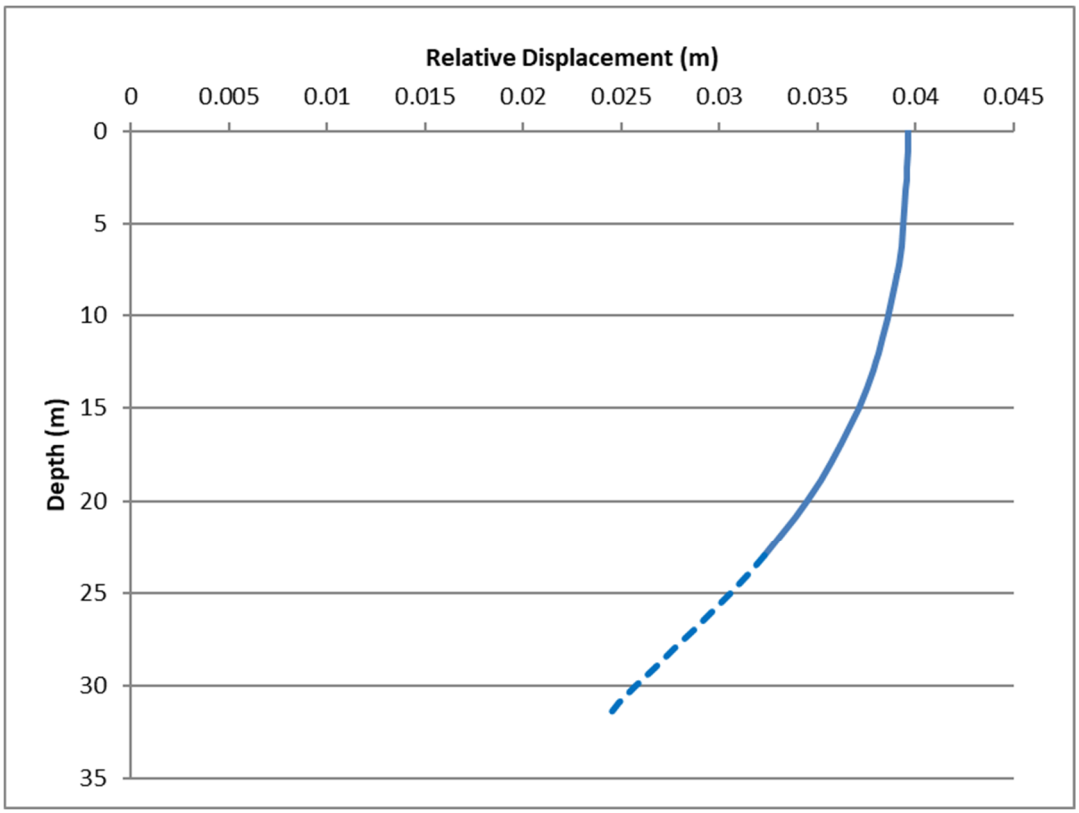

Figure 59: Trend of the displacements of the profile characterized by *Vs* = 450 m/s subjected to the Montenegro seismic input

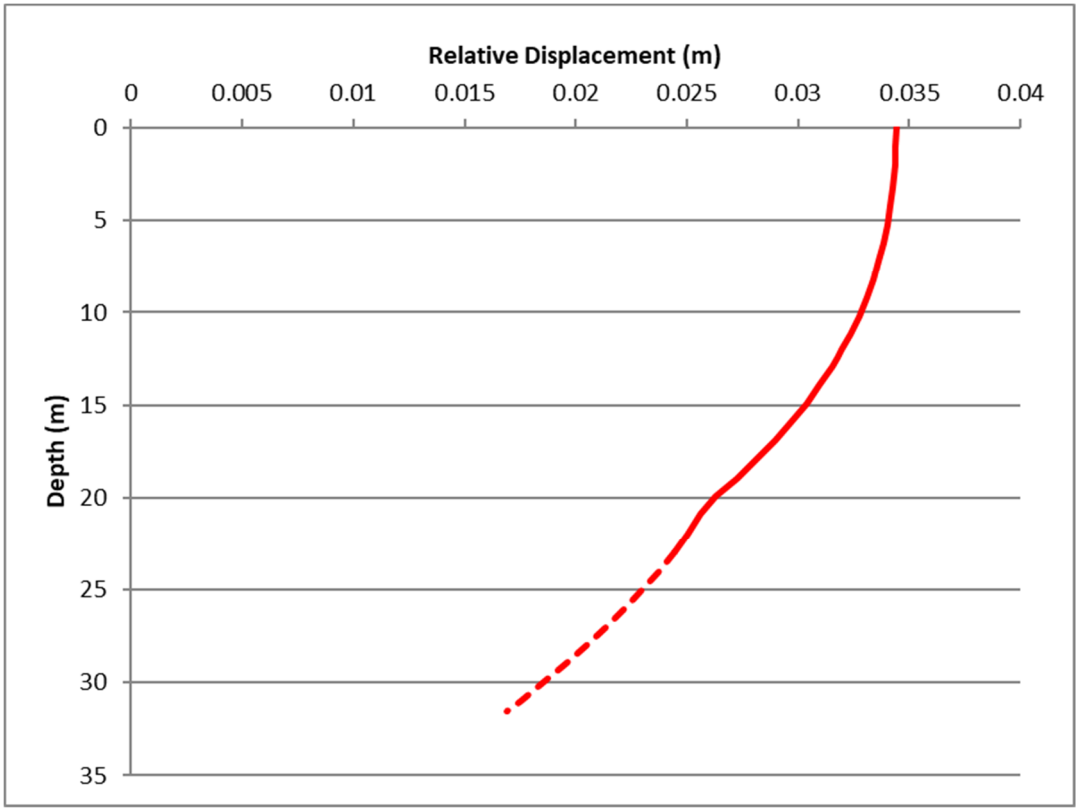

Figure 60: Trend of the displacements of the profile characterized by *Vs* = 450 m/s subjected to the Amatrice seismic input

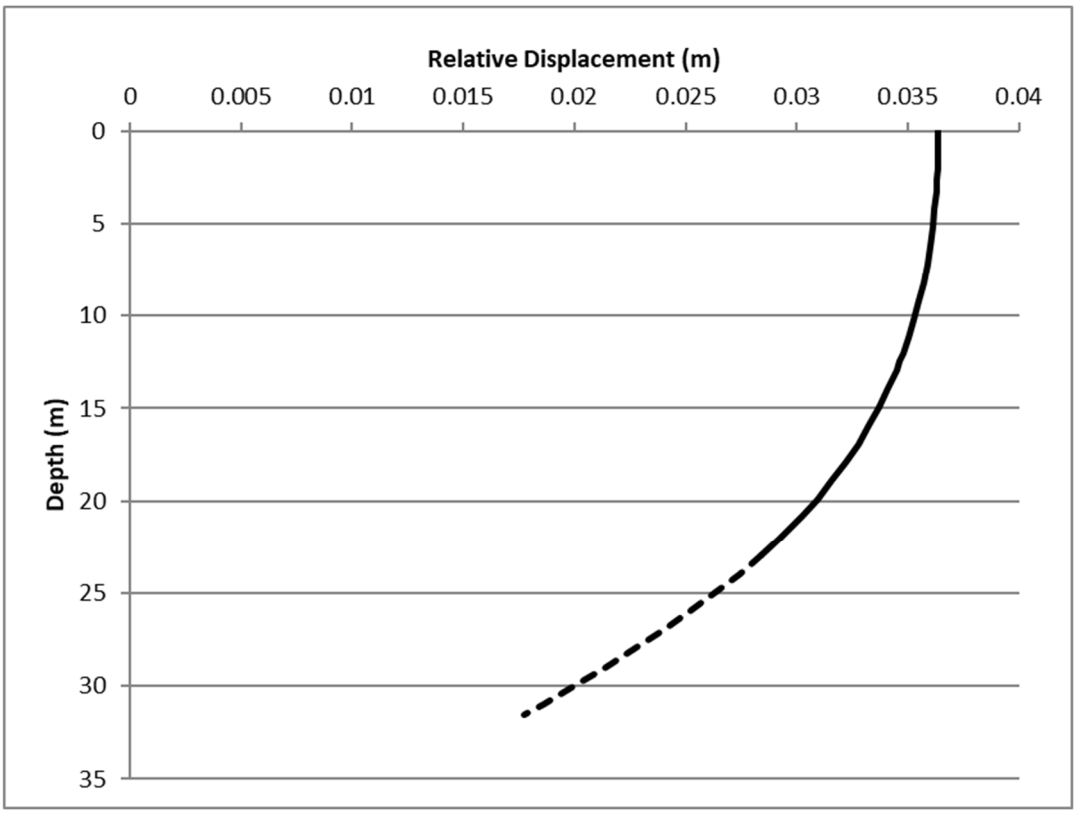

Figure 61: Trend of the displacements of the profile characterized by *Vs* = 450 m/s subjected to the L'Aquila seismic input

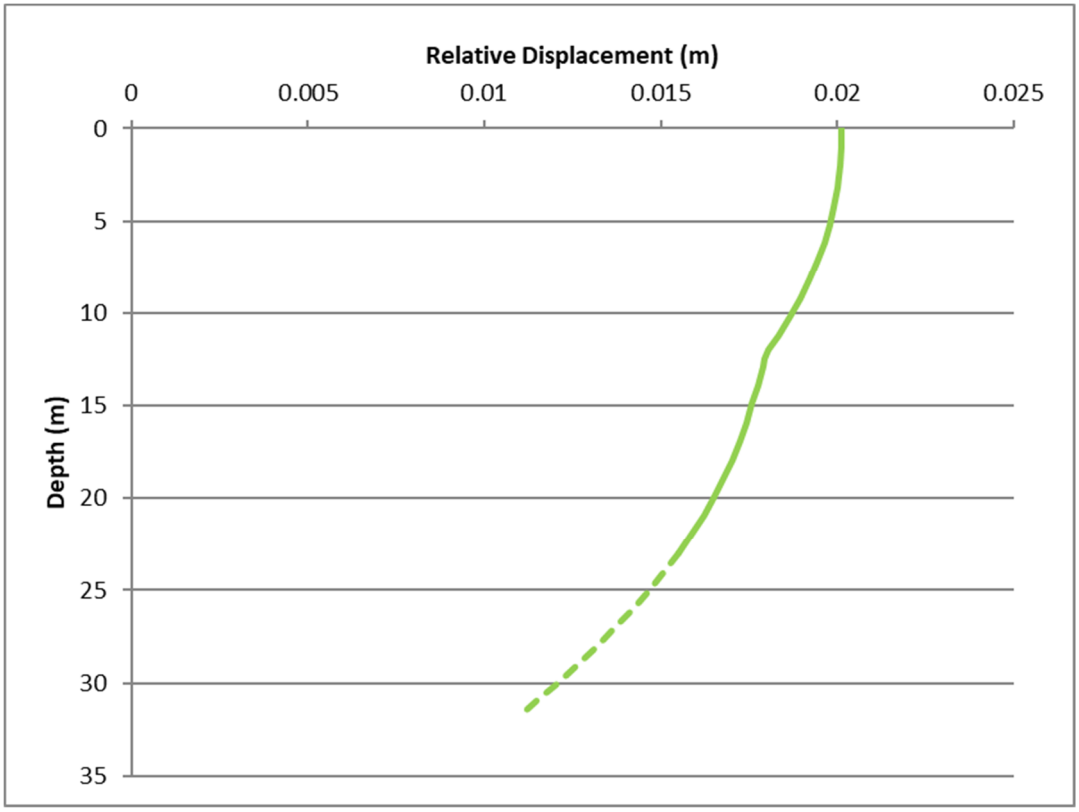

Figure 62: Trend of the displacements of the profile characterized by *Vs* = 450 m/s subjected to the Friuli seismic input

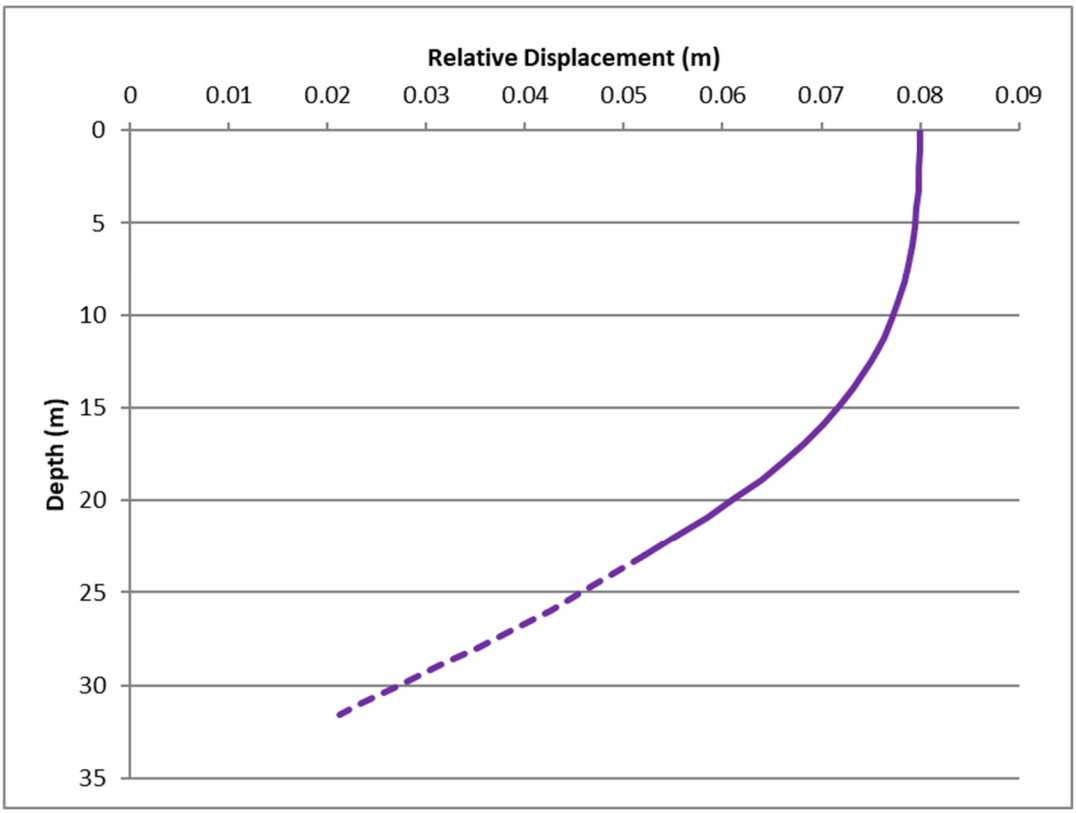

Figure 63: Trend of the displacements of the profile characterized by *Vs* = 450 m/s subjected to the Greece seismic input

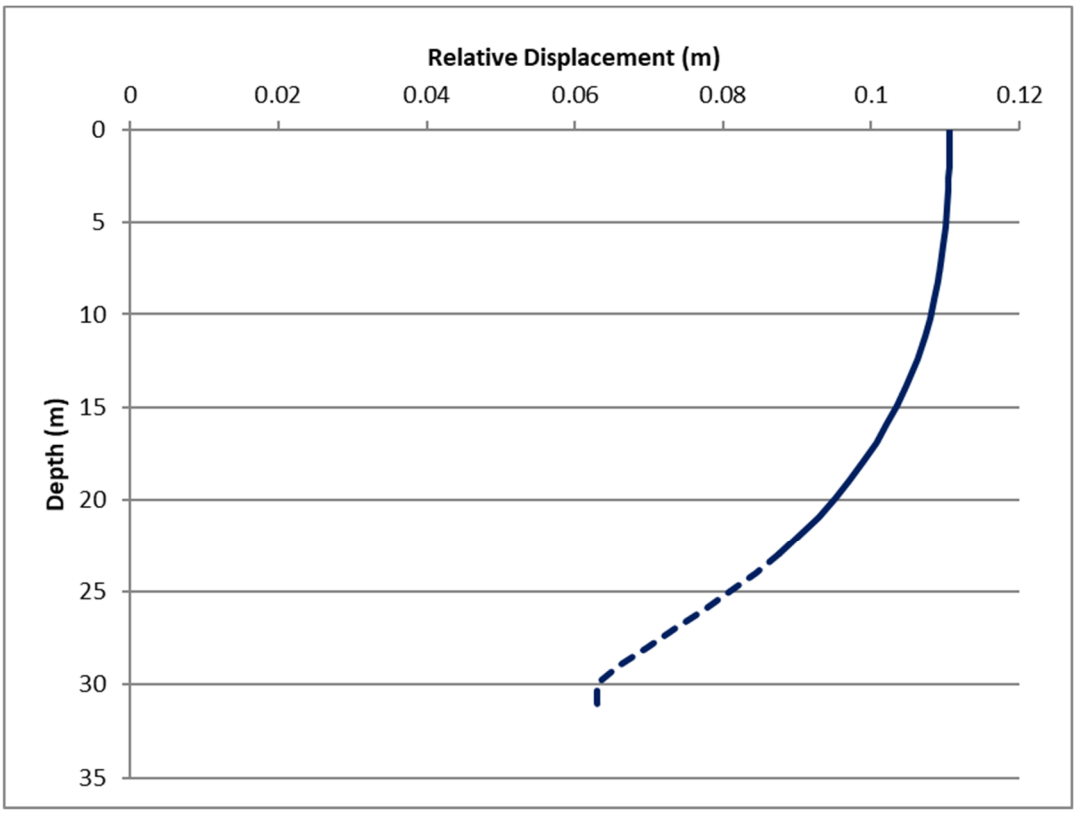

Figure 64: Trend of the displacements of the profile characterized by *Vs* = 450 m/s subjected to the Lima seismic input

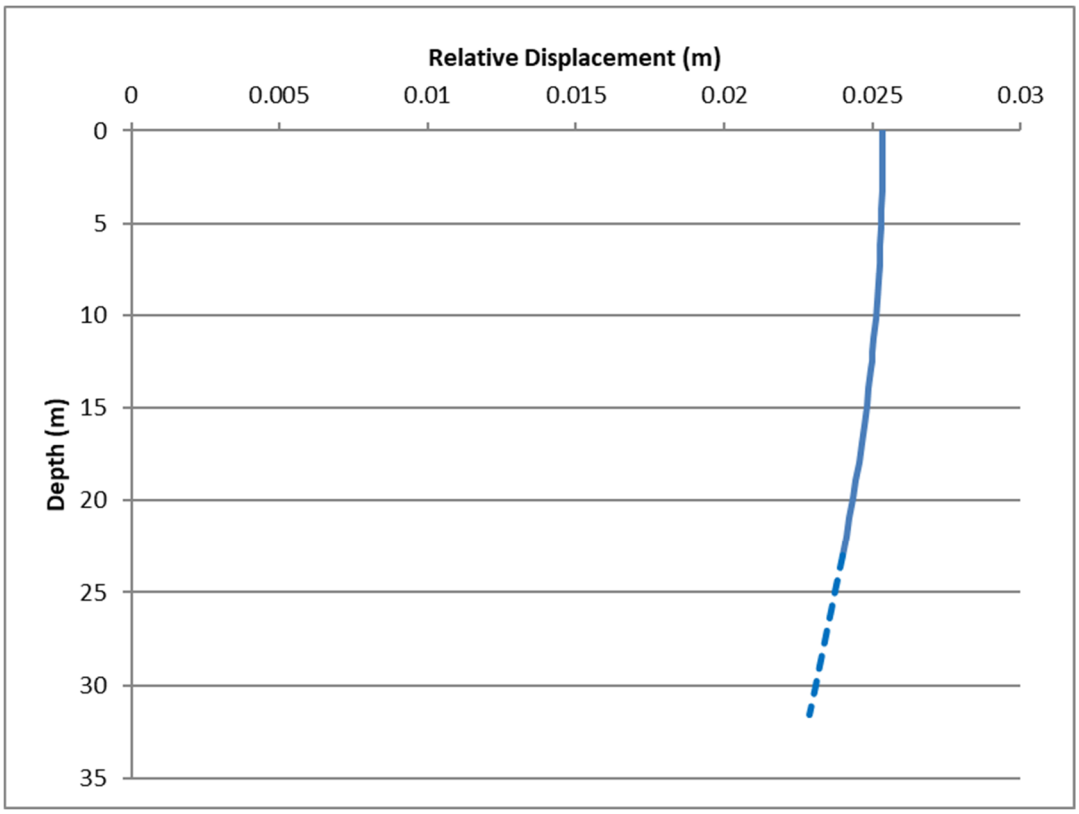

Figure 65: Trend of the displacements of the profile characterized by *Vs* = 600 m/s subjected to the Montenegro seismic input

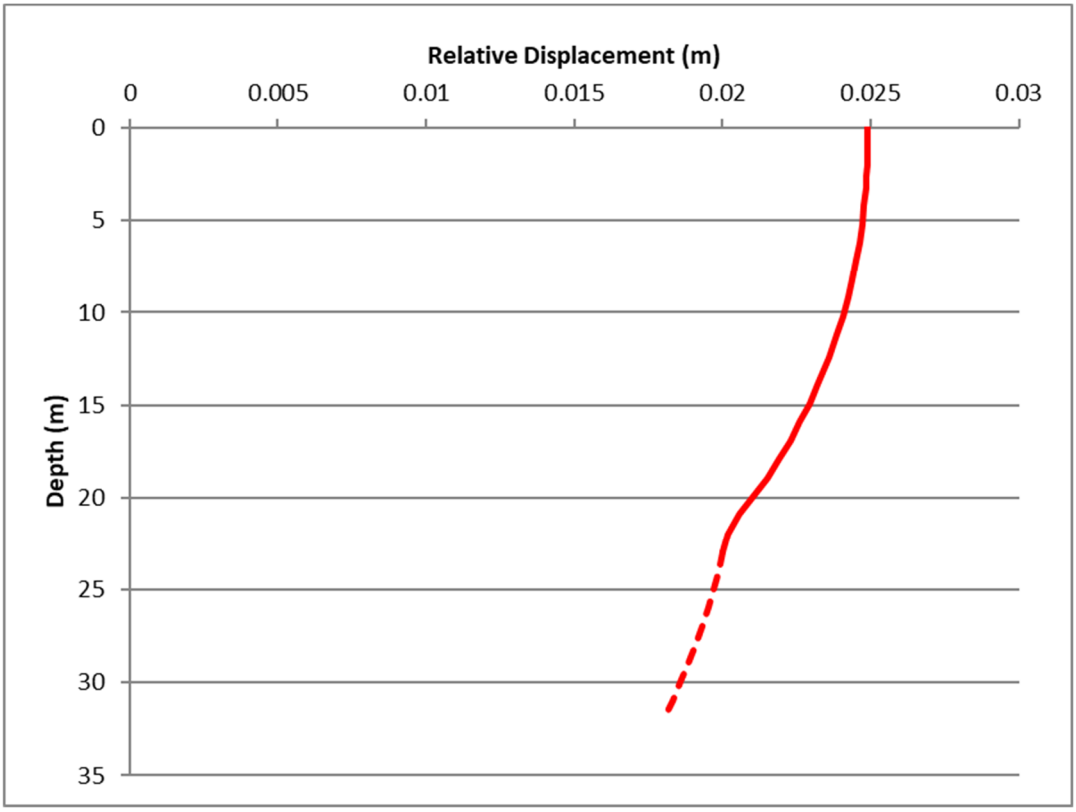

Figure 66: Trend of the displacements of the profile characterized by *Vs* = 600 m/s subjected to the Amatrice seismic input

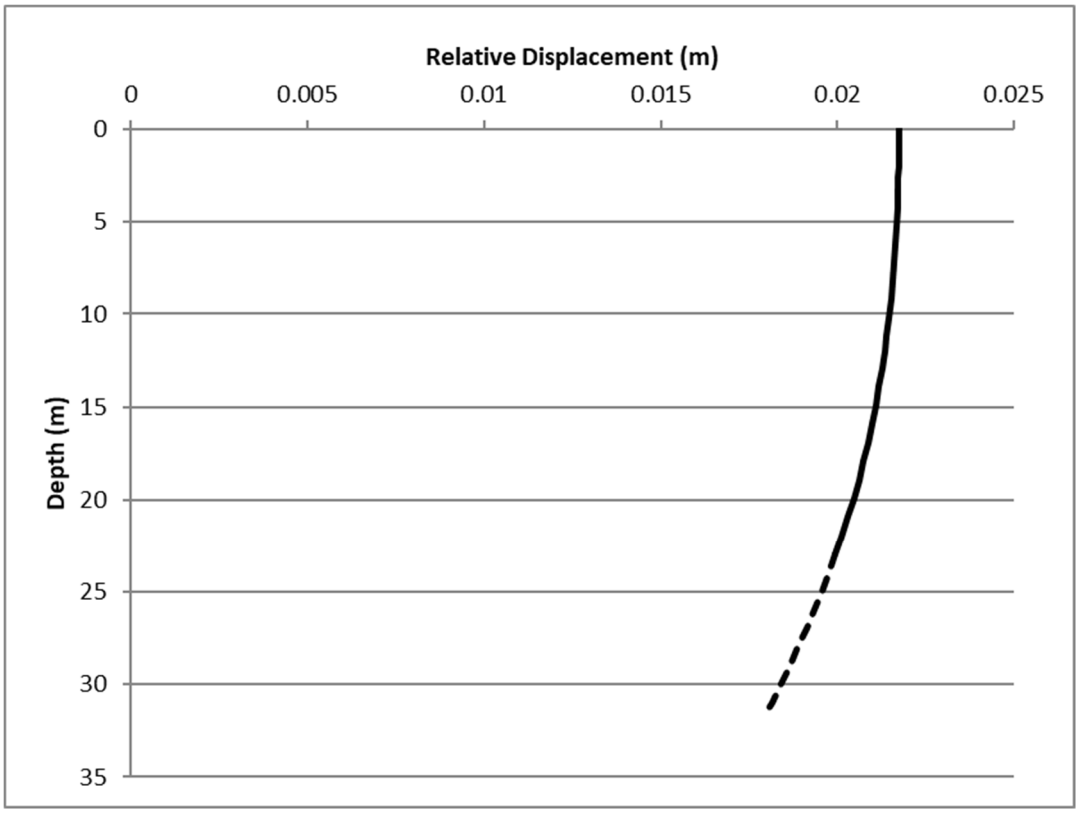

Figure 67: Trend of the displacements of the profile characterized by *Vs* = 600 m/s subjected to the L'Aquila seismic input

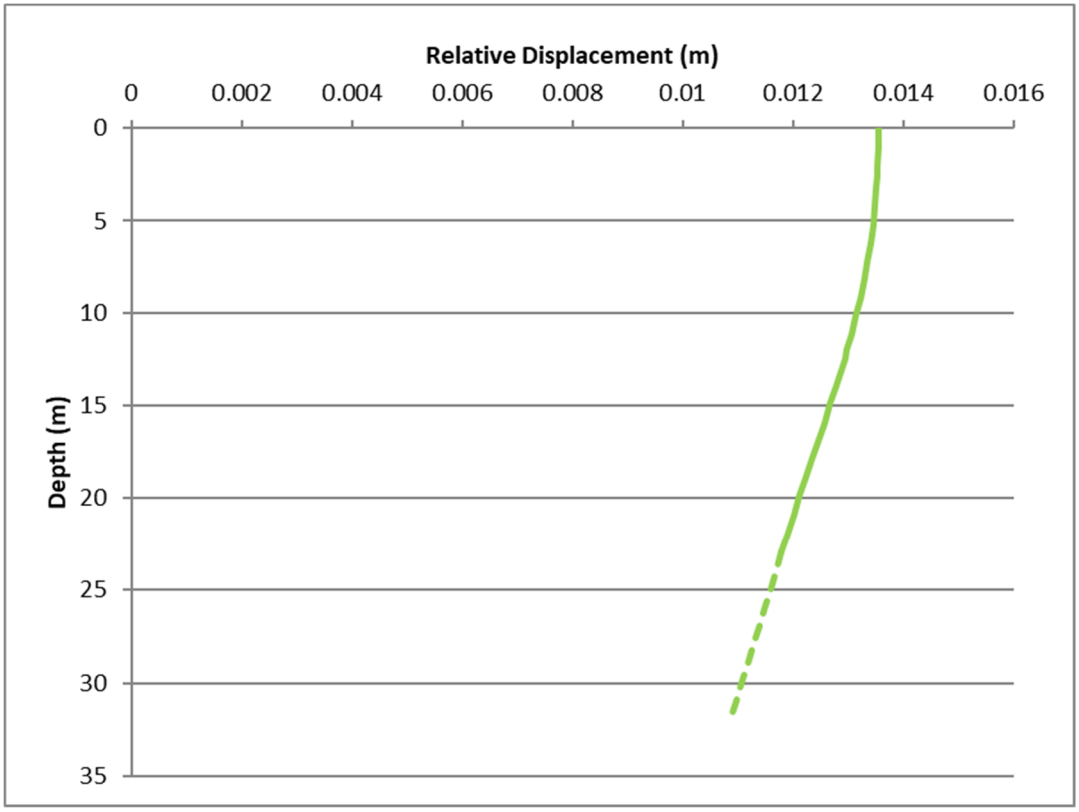

Figure 68: Trend of the displacements of the profile characterized by *Vs* = 600 m/s subjected to the Friuli seismic input

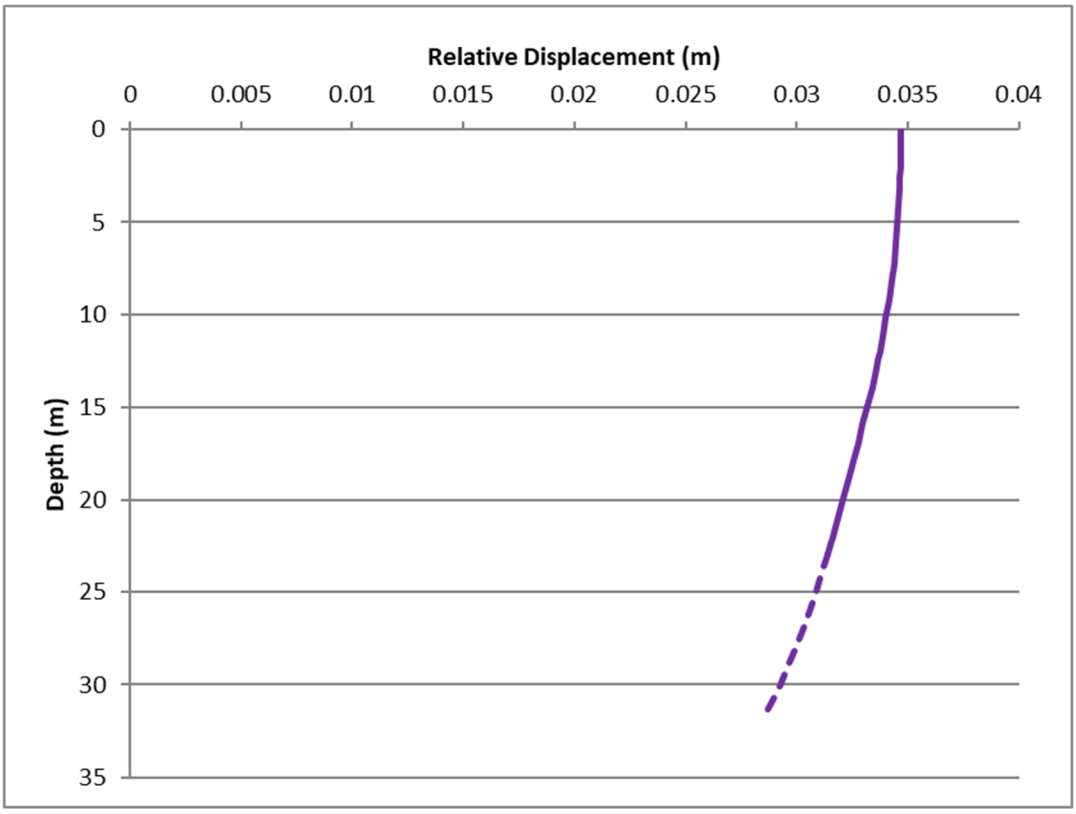

Figure 69: Trend of the displacements of the profile characterized by *Vs* = 600 m/s subjected to the Greece seismic input

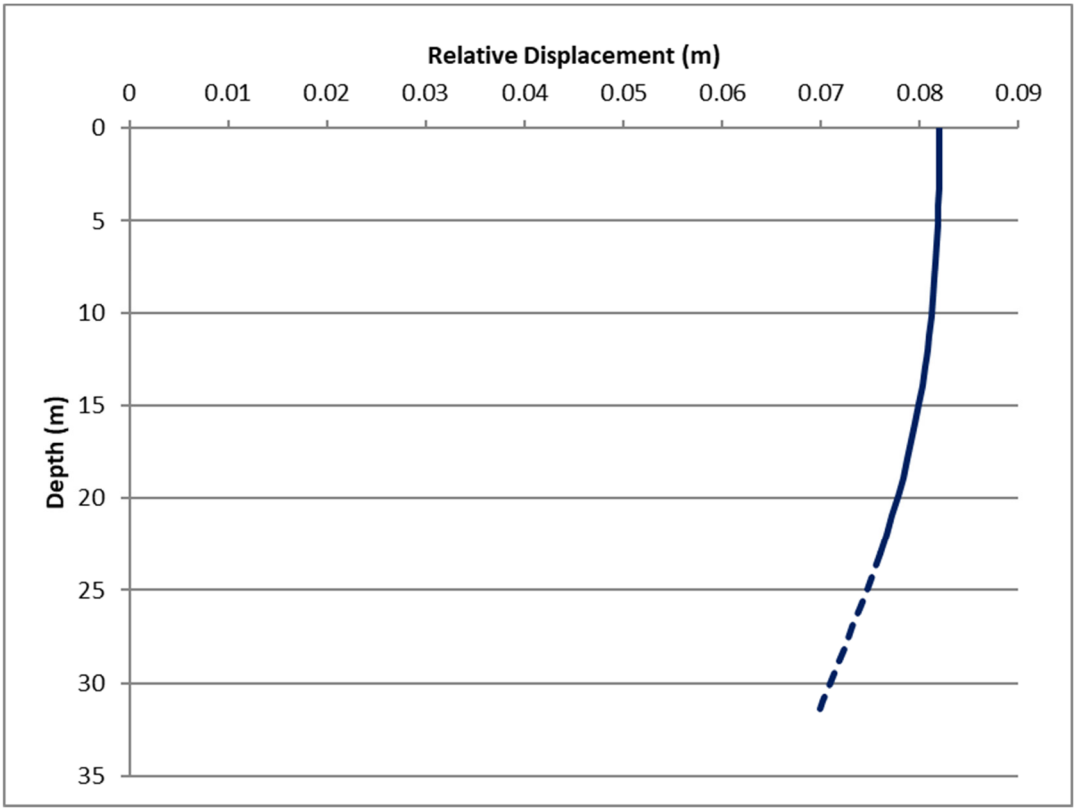

Figure 70: Trend of the displacements of the profile characterized by *Vs* = 600 m/s subjected to the Lima seismic input

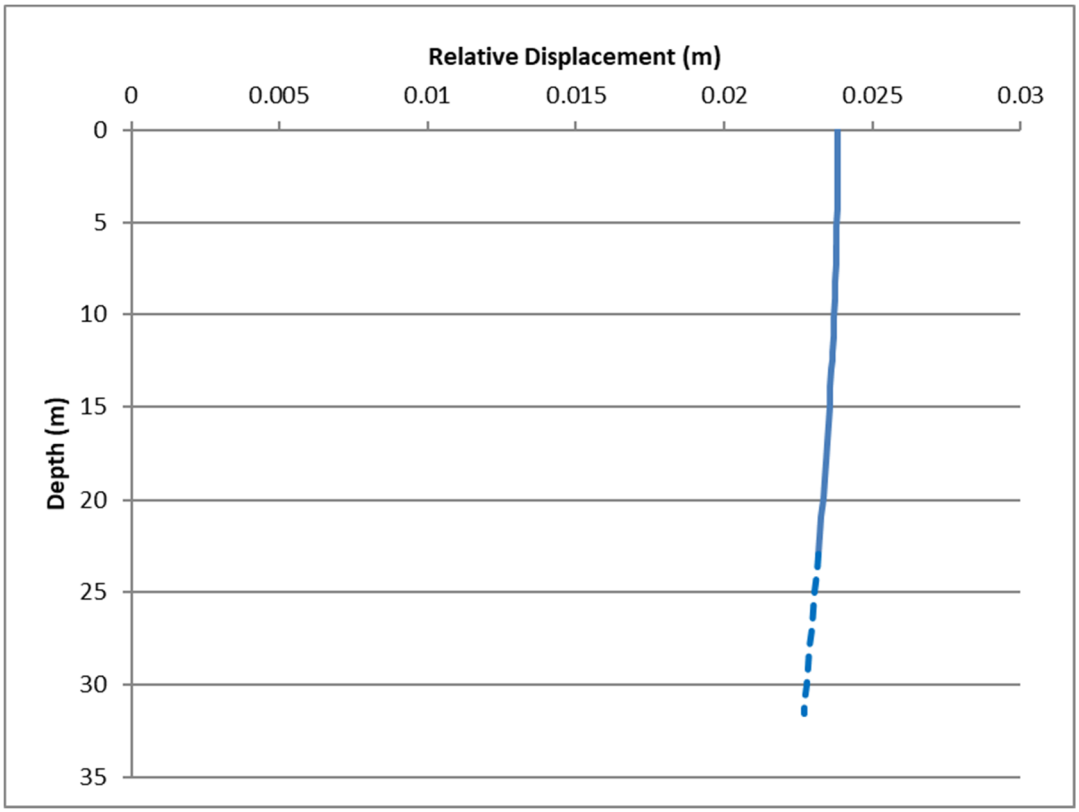

Figure 71: Trend of the displacements of the profile characterized by *Vs* = 750 m/s subjected to the Montenegro seismic input

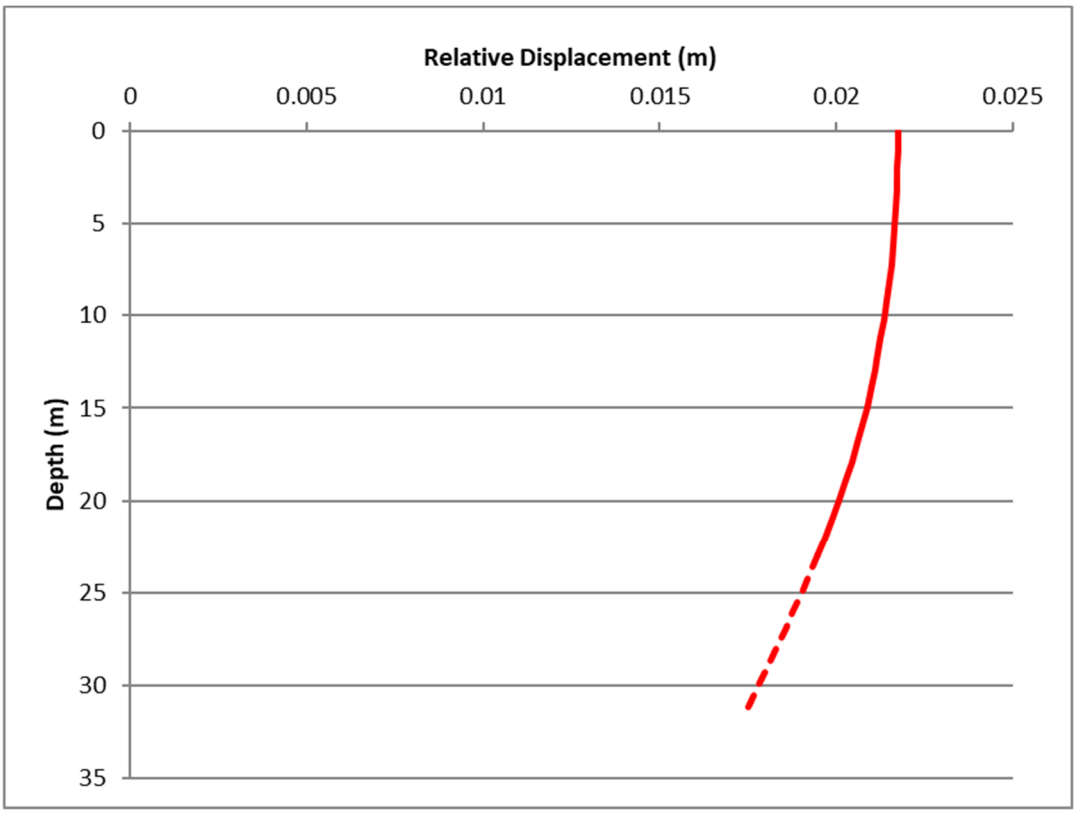

Figure 72: Trend of the displacements of the profile characterized by *Vs* = 750 m/s subjected to the Amatrice seismic input

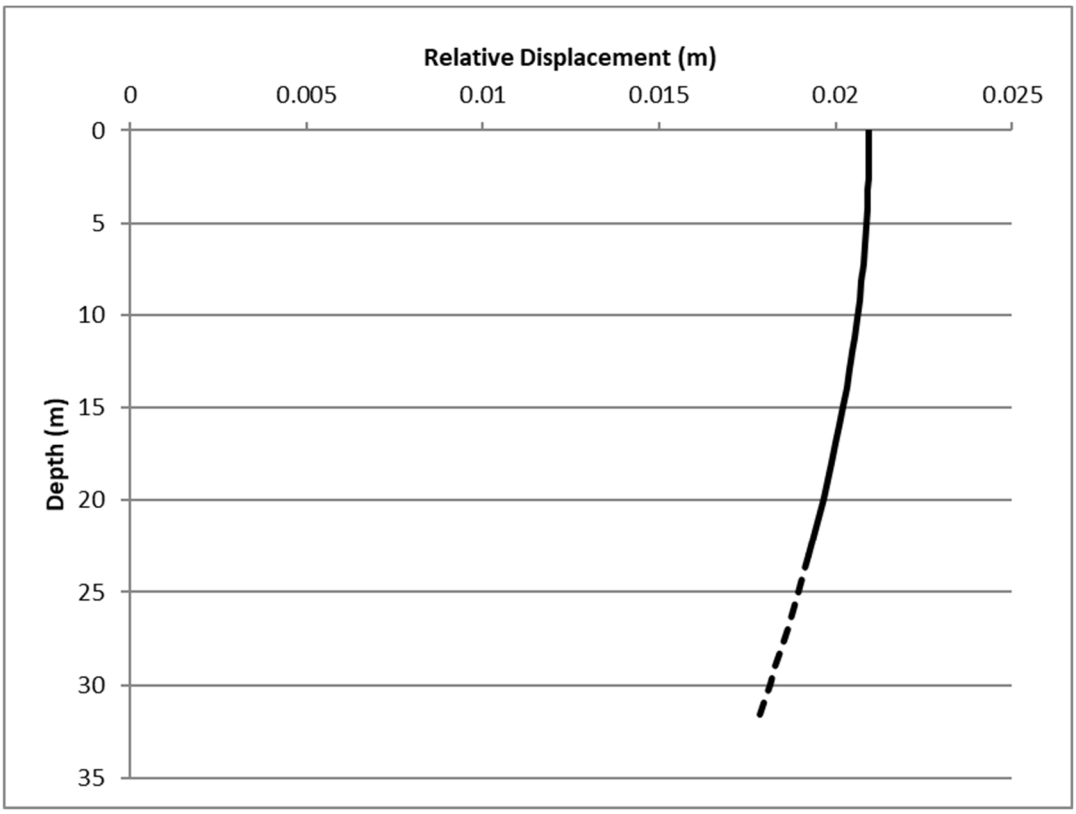

Figure 73: Trend of the displacements of the profile characterized by *Vs* = 750 m/s subjected to the L'Aquila seismic input

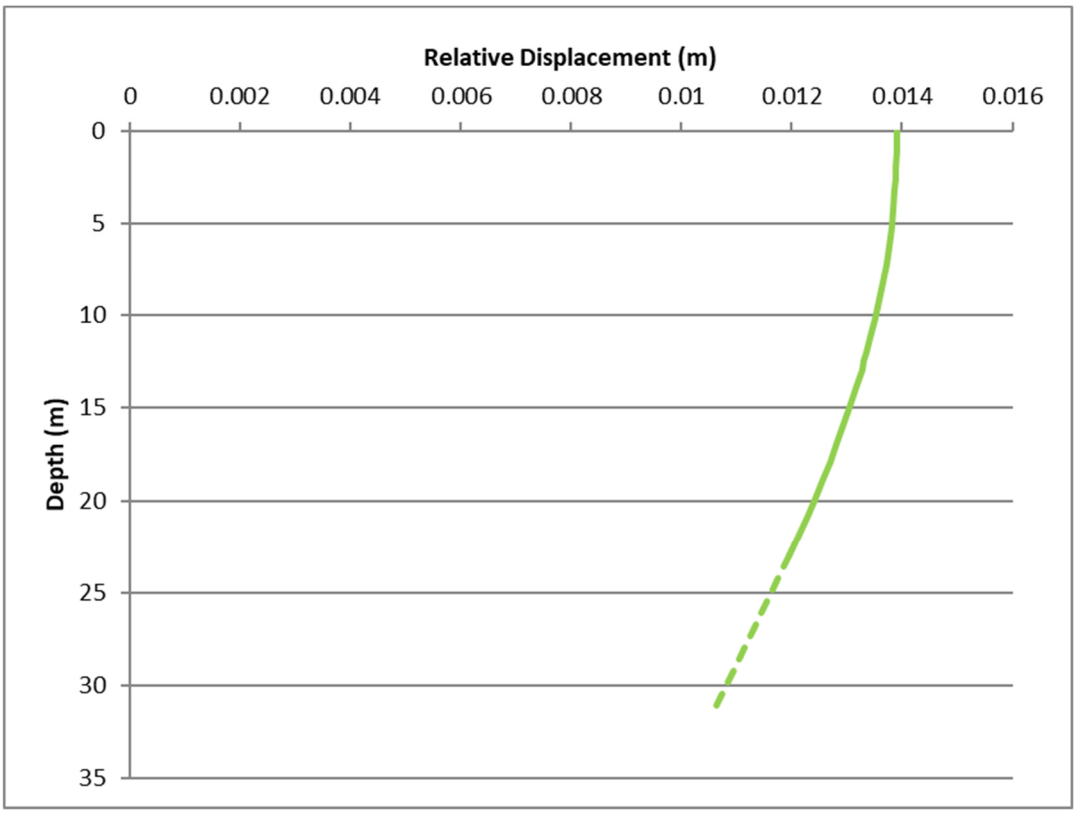

Figure 74: Trend of the displacements of the profile characterized by *Vs* = 750 m/s subjected to the Friuli seismic input

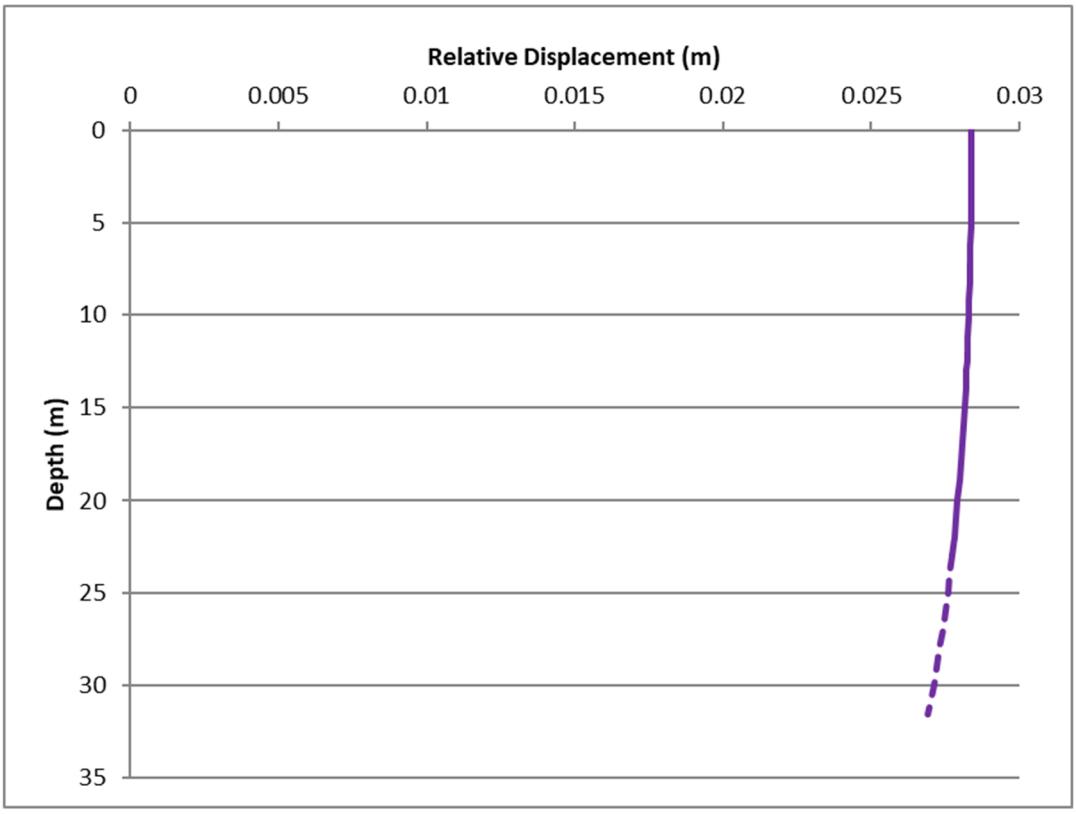

Figure 75: Trend of the displacements of the profile characterized by *Vs* = 750 m/s subjected to the Greece seismic input

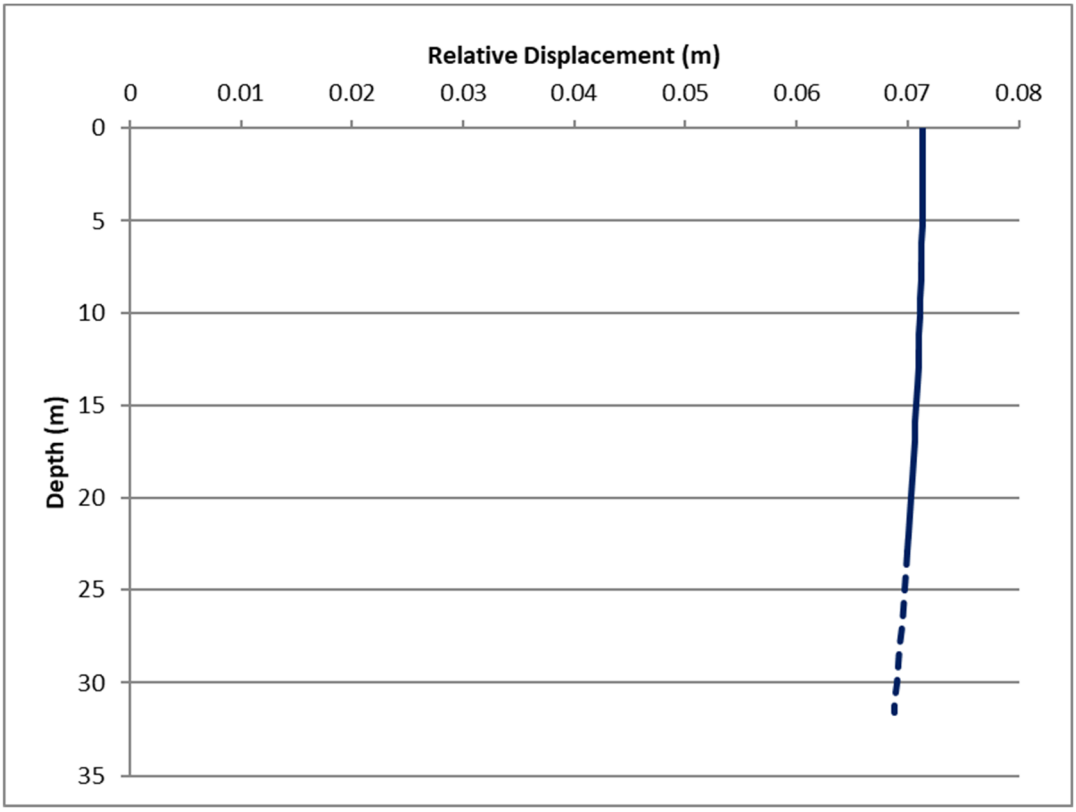

Figure 76: Trend of the displacements of the profile characterized by *Vs* = 750 m/s subjected to the Lima seismic input

In Table 11 a summary of the results of the equivalent linear analysis is reported. The relative displacements, as mentioned above, are obtained considering the difference between the displacement valued at the the depth corresponding at the top of the concrete retaining walls of the underground structure and the displacement valued at the depth corresponding at the base of the concrete retaining walls.

Table 11: Relative displacements

	Relative Displacement					
PROFILE V_S	AMATRICE	FRIULI	GREECE	MONTENEGRO	L'AQUILA	LIMA
[m/s]	[mm]	[mm]	[mm]	[mm]	[mm]	[mm]
360	13	8	28	37	15	34
450	11	5	27	7	8	23
600	5	2	3	2	2	6
750	2	2	1	1	2	1

Figures from 77 to 100 shown the results in terms of maximum envelope of bending moment acting on the concrete retaining walls.

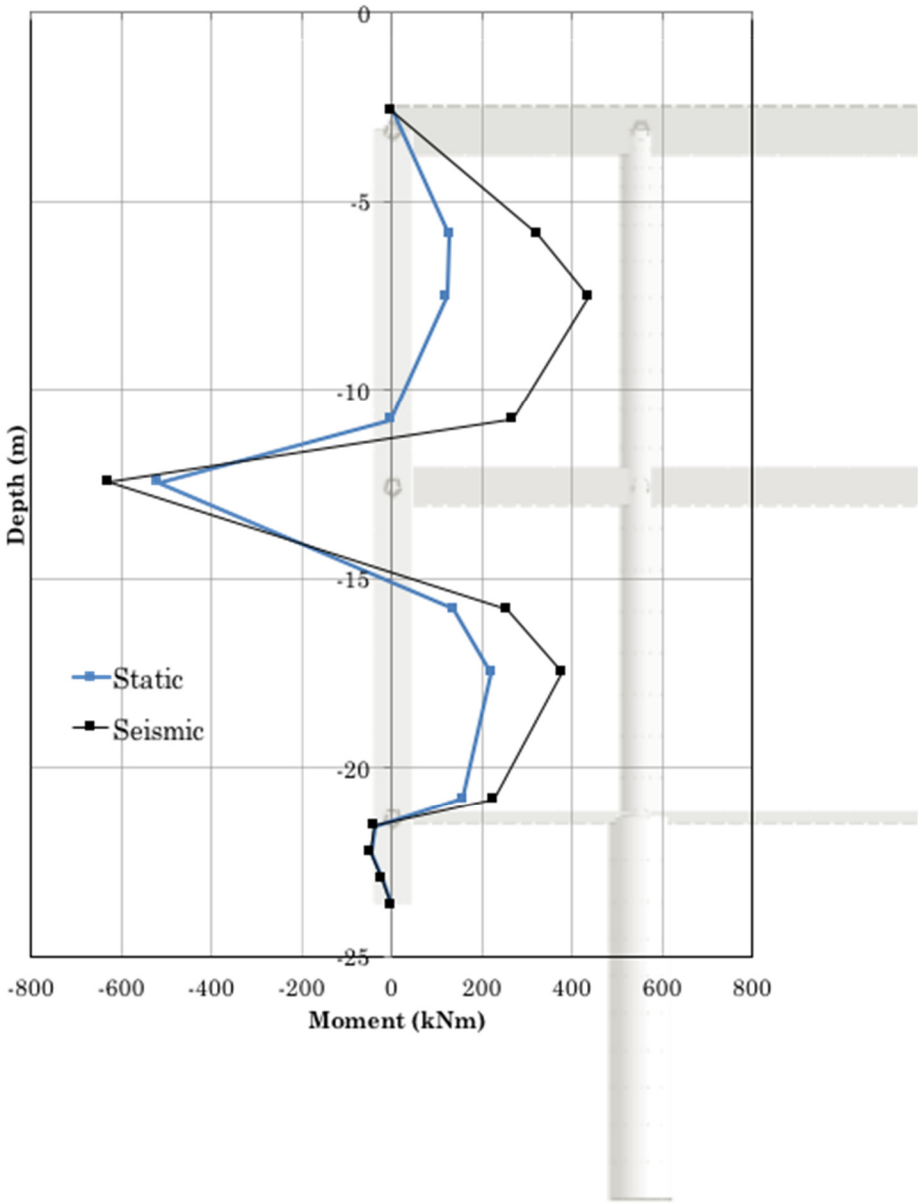

Figure 77: Equivalent linear analysis: bending moment acting on the concrete retaining walls - profile characterized by *Vs* = 360 m/s, input: MONTENEGRO

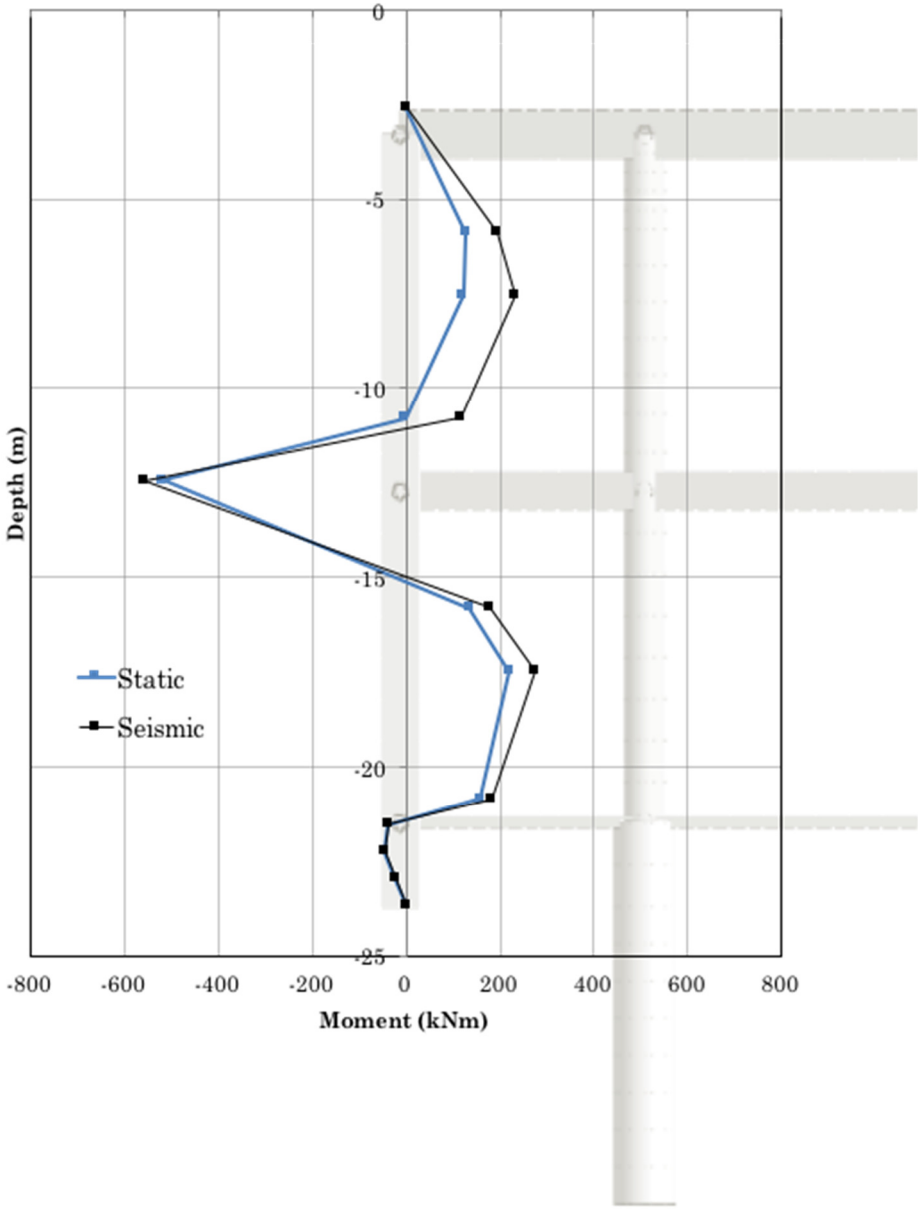

Figure 78: Equivalent linear analysis: bending moment acting on the concrete retaining walls - profile characterized by *Vs* = 360 m/s, input: AMATRICE

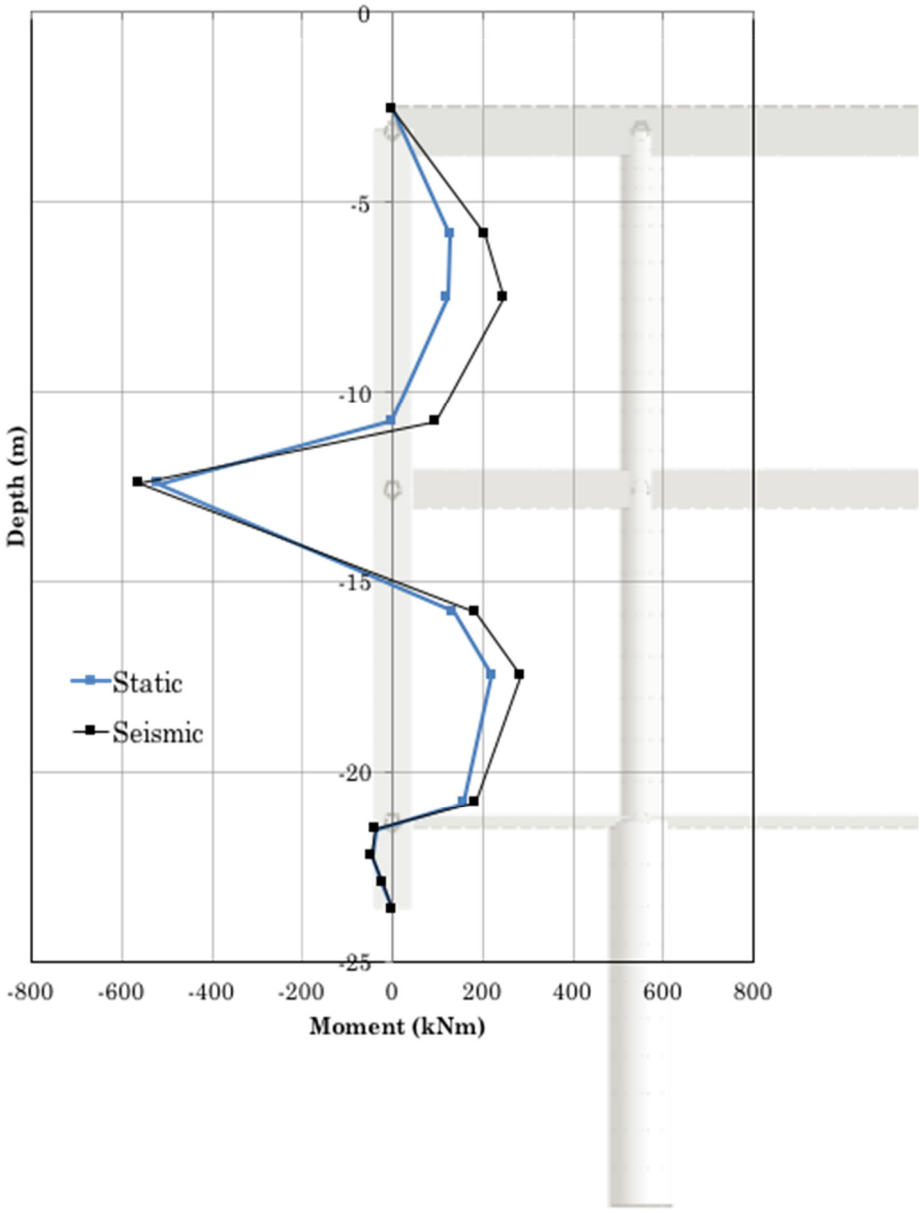

Figure 79: Equivalent linear analysis: bending moment acting on the concrete retaining walls - profile characterized by *Vs* = 360 m/s, input: L'AQUILA

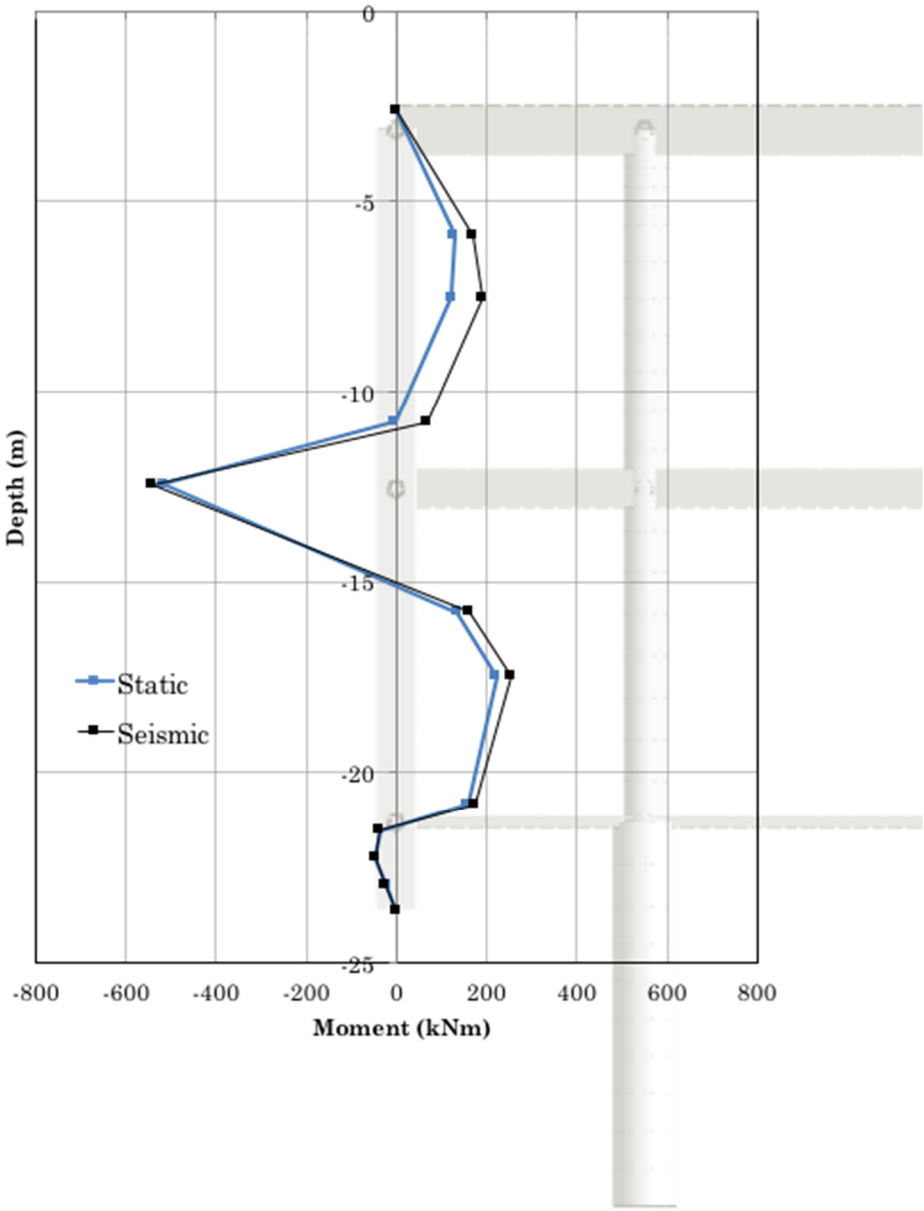

Figure 80: Equivalent linear analysis: bending moment acting on the concrete retaining walls - profile characterized by *Vs* = 360 m/s, input: FRIULI

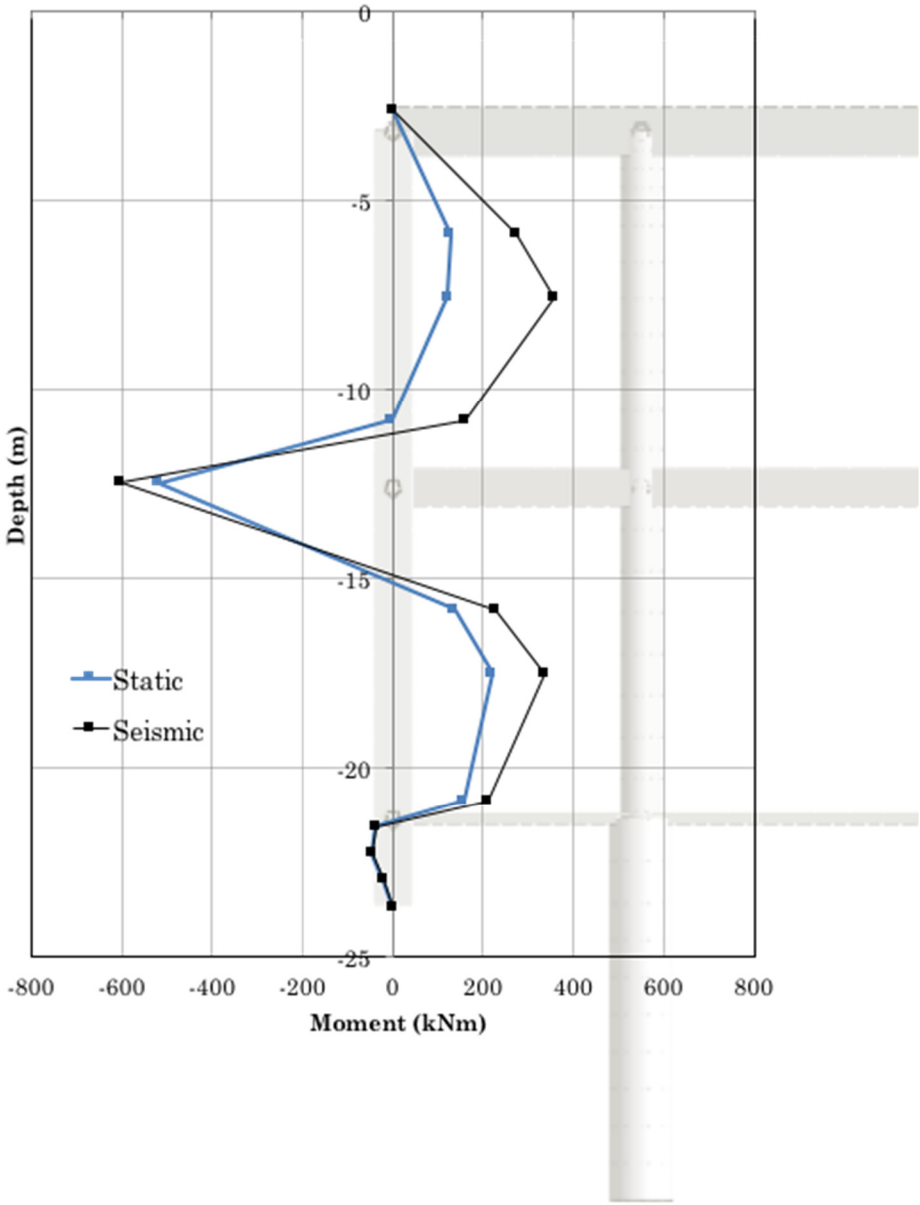

Figure 81: Equivalent linear analysis: bending moment acting on the concrete retaining walls - profile characterized by *Vs* = 360 m/s, input: GREECE

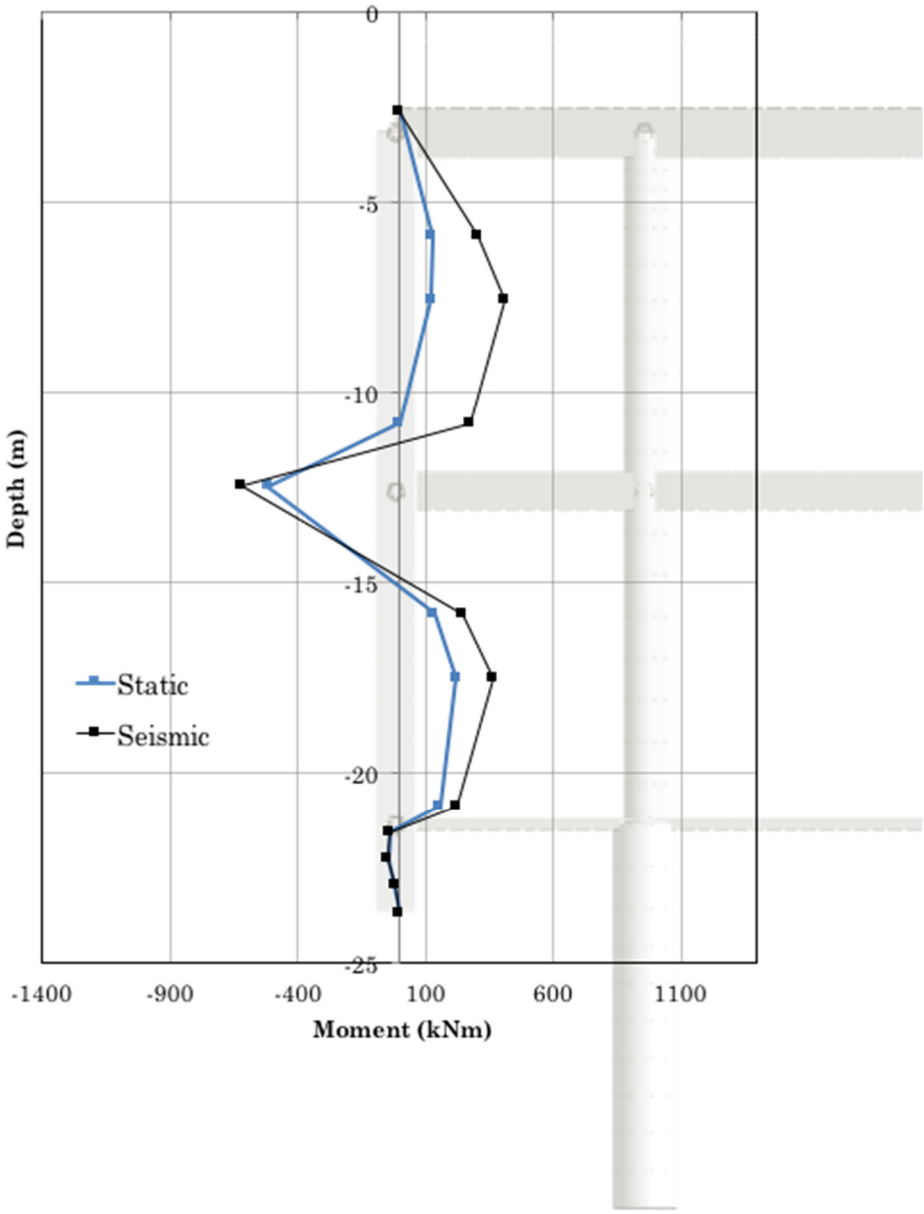

Figure 82: Equivalent linear analysis: bending moment acting on the concrete retaining walls - profile characterized by *Vs* = 360 m/s, input: LIMA

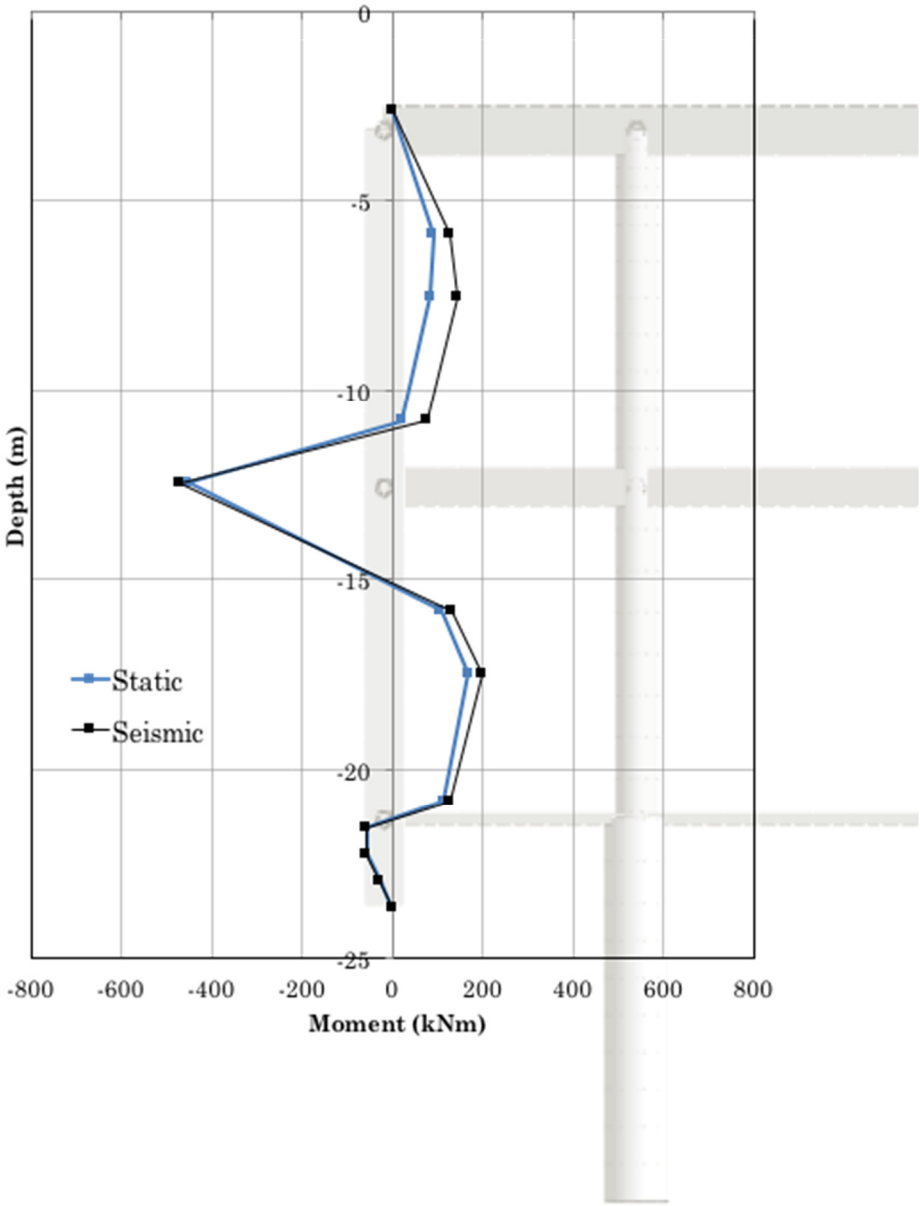

Figure 83: Equivalent linear analysis: bending moment acting on the concrete retaining walls - profile characterized by *Vs* = 450 m/s, input: MONTENEGRO

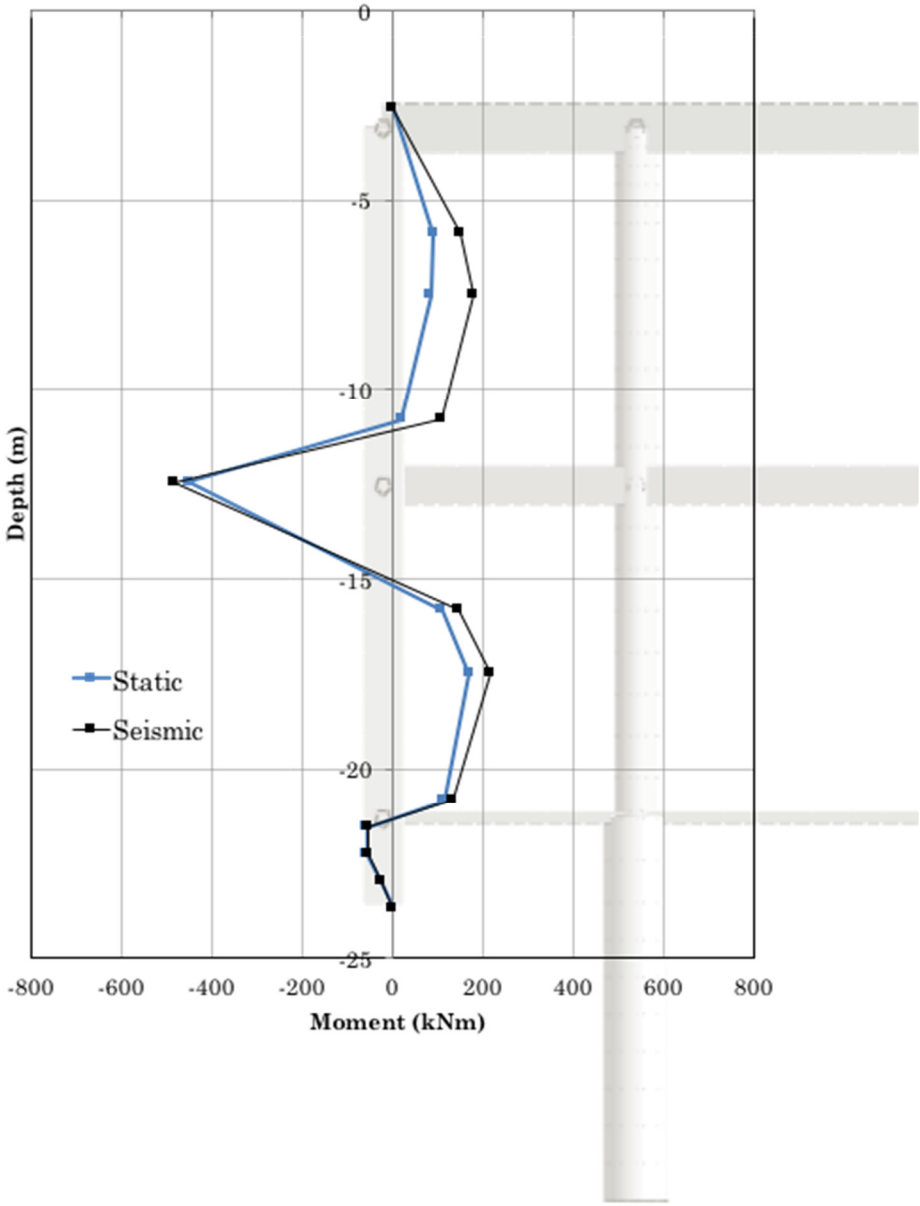

Figure 84: Equivalent linear analysis: bending moment acting on the concrete retaining walls - profile characterized by *Vs* = 450 m/s, input: AMATRICE

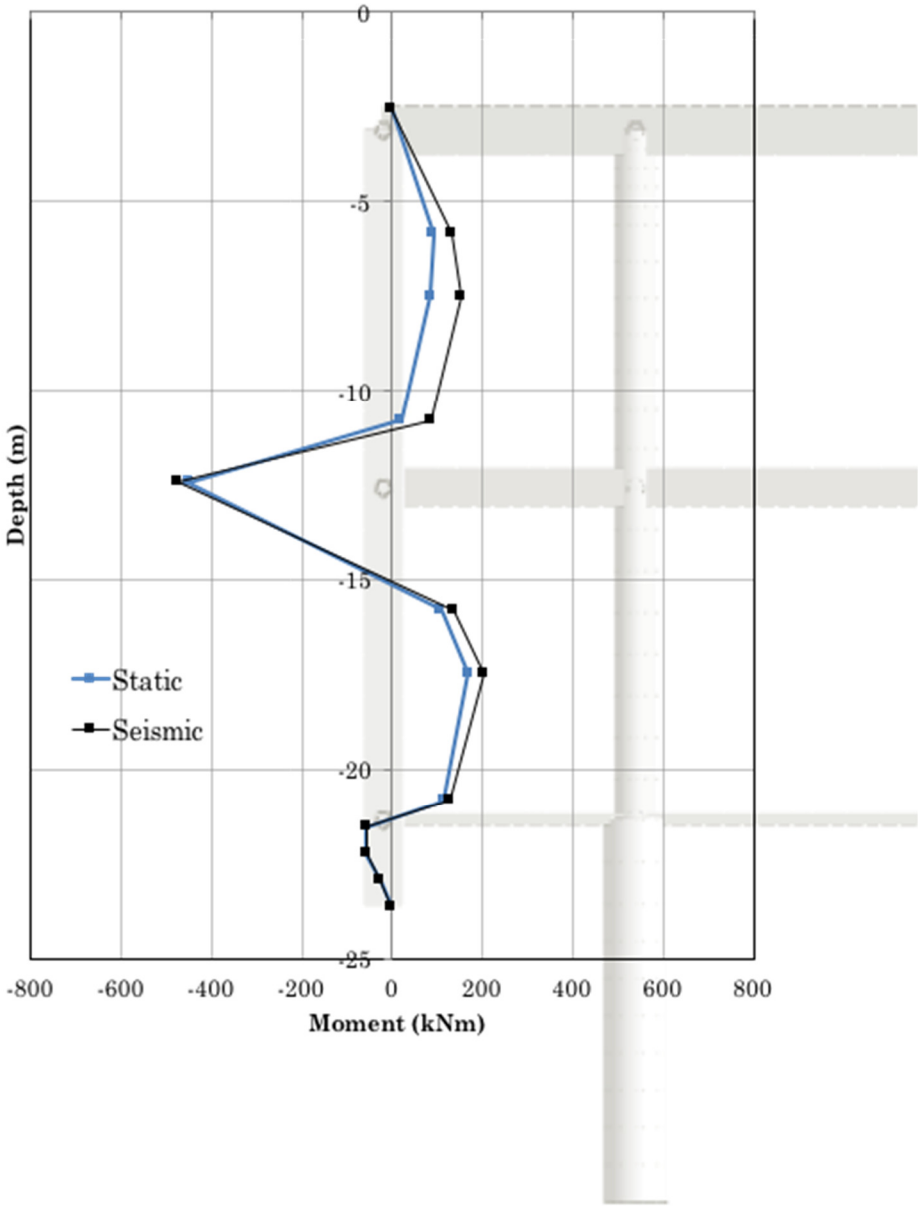

Figure 85: Equivalent linear analysis: bending moment acting on the concrete retaining walls - profile characterized by *Vs* = 450 m/s, input: L'AQUILA

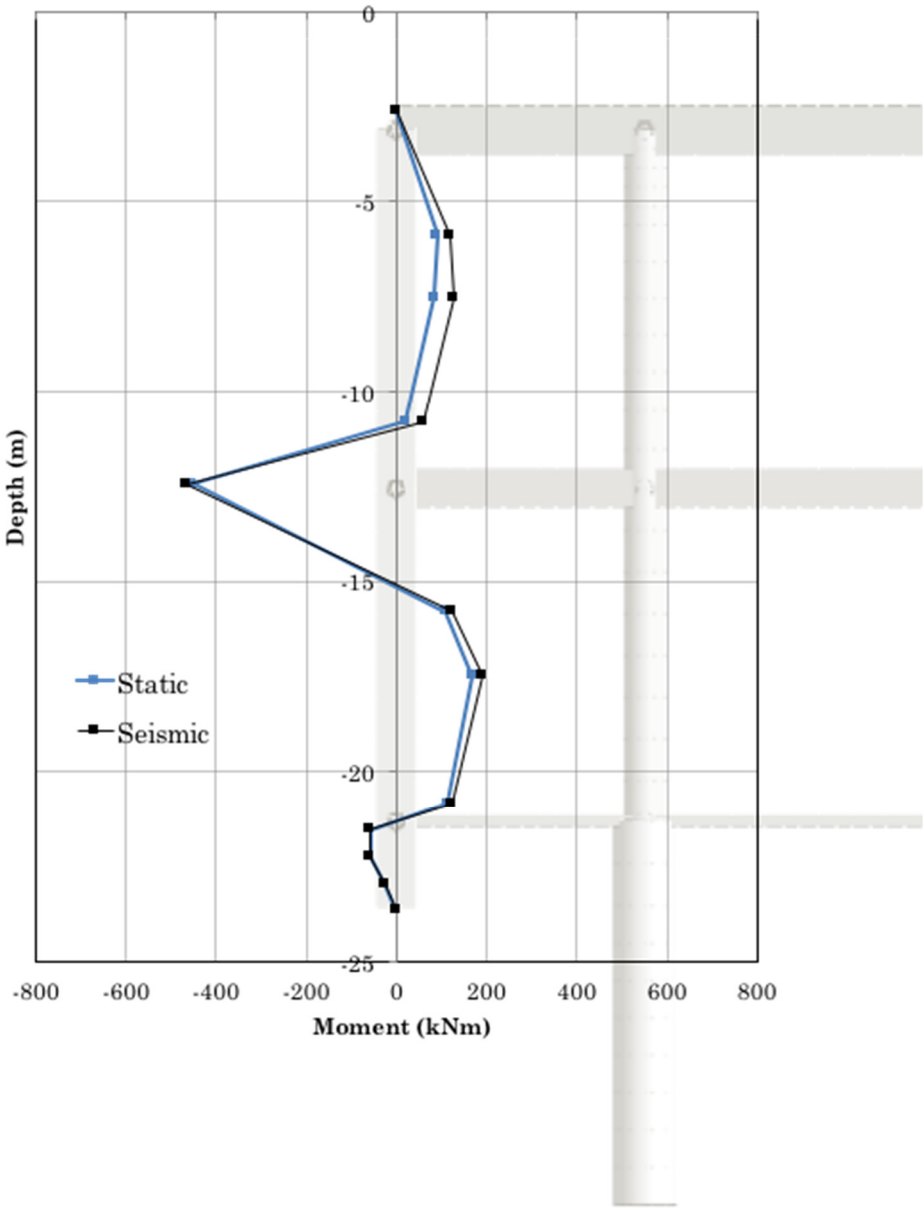

Figure 86: Equivalent linear analysis: bending moment acting on the concrete retaining walls - profile characterized by *Vs* = 450 m/s, input: FRIULI

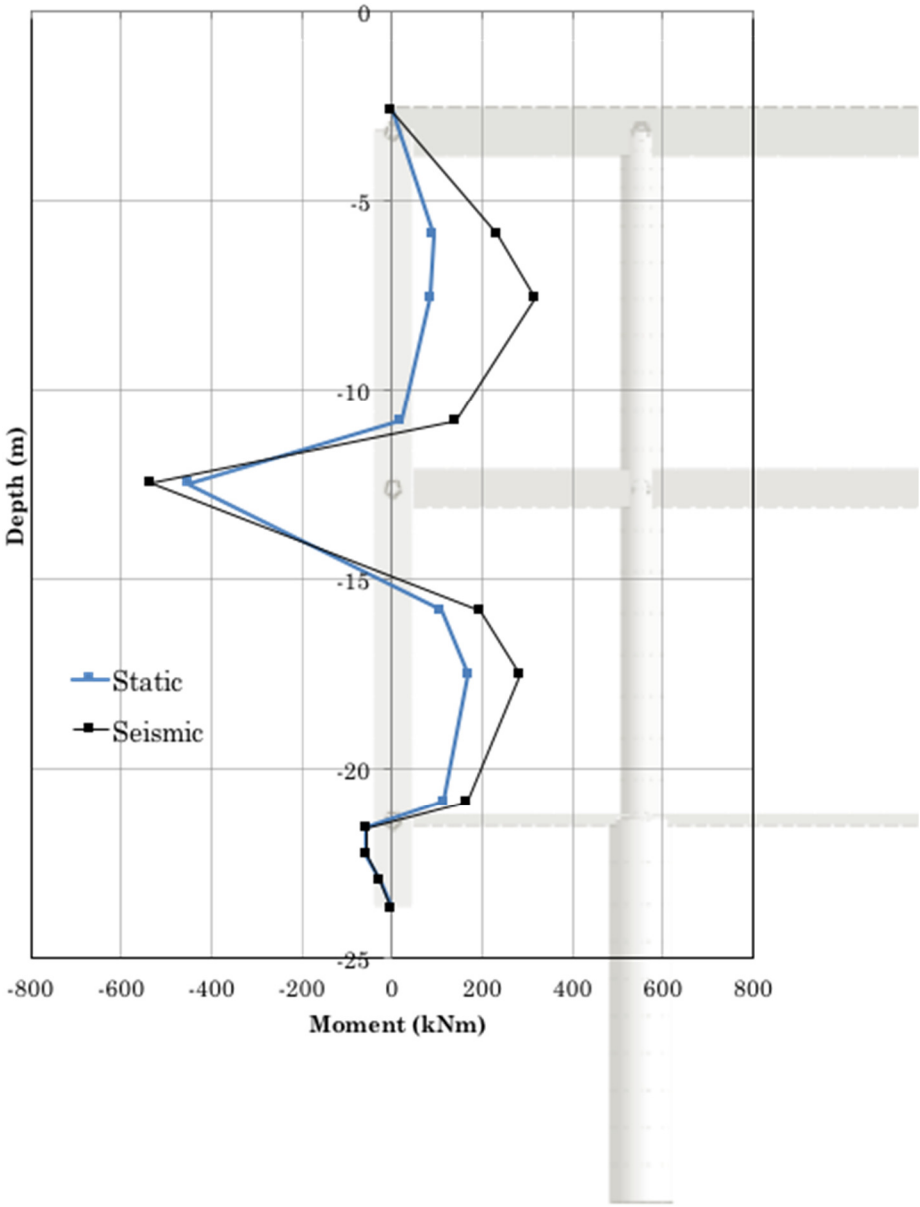

Figure 87: Equivalent linear analysis: bending moment acting on the concrete retaining walls - profile characterized by *Vs* = 450 m/s, input: GREECE

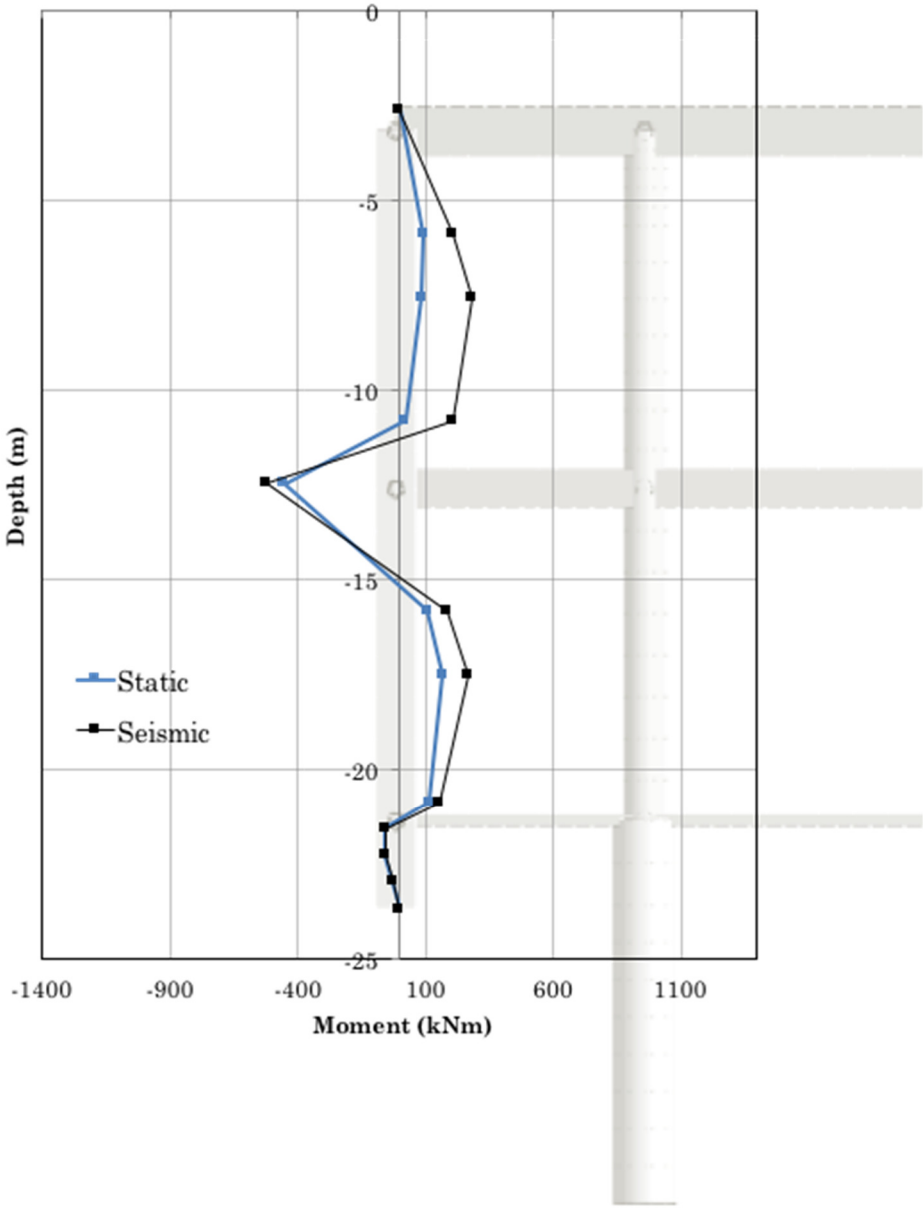

Figure 88: Equivalent linear analysis: bending moment acting on the concrete retaining walls - profile characterized by *Vs* = 450 m/s, input: LIMA

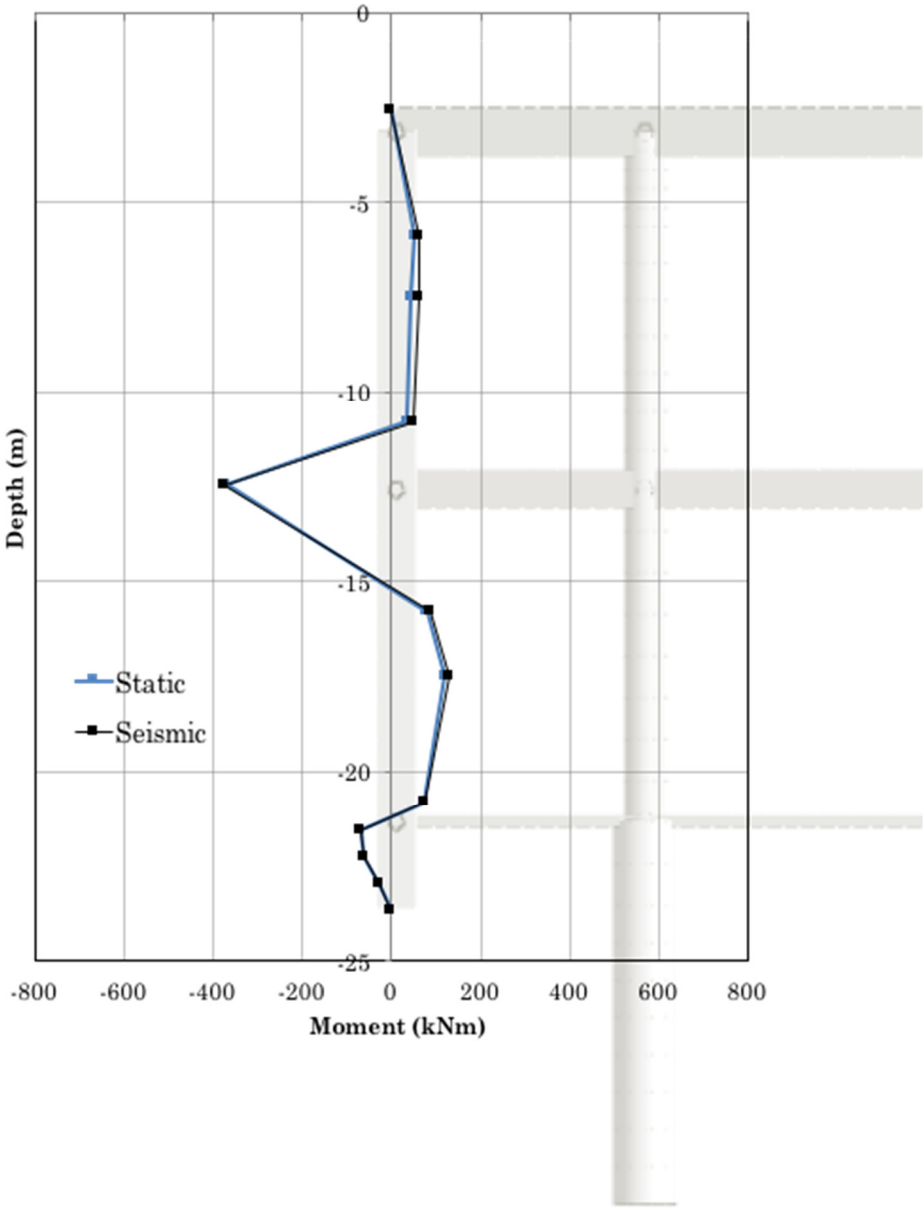

Figure 89: Equivalent linear analysis: bending moment acting on the concrete retaining walls - profile characterized by *Vs* = 600 m/s, input: MONTENEGRO

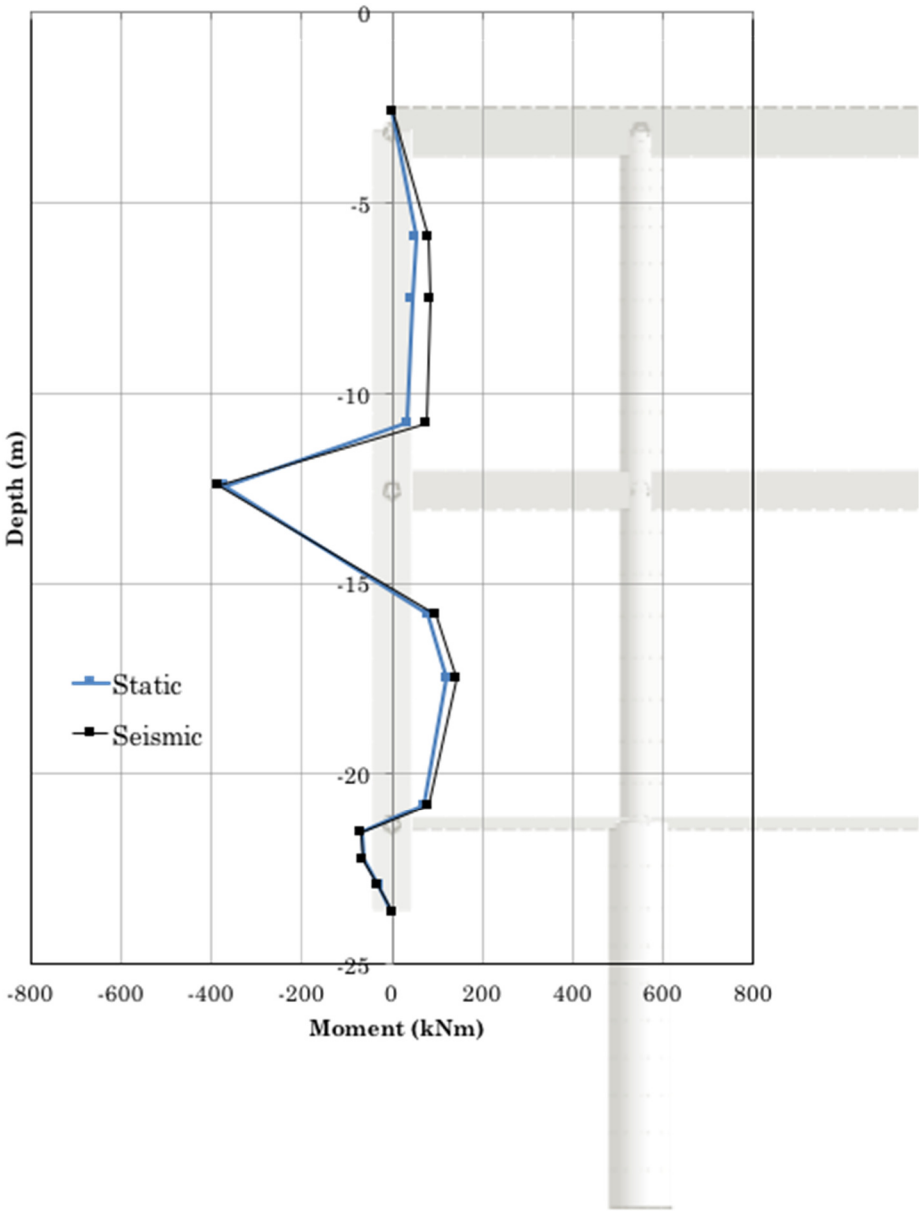

Figure 90: Equivalent linear analysis: bending moment acting on the concrete retaining walls - profile characterized by *Vs* = 600 m/s, input: AMATRICE

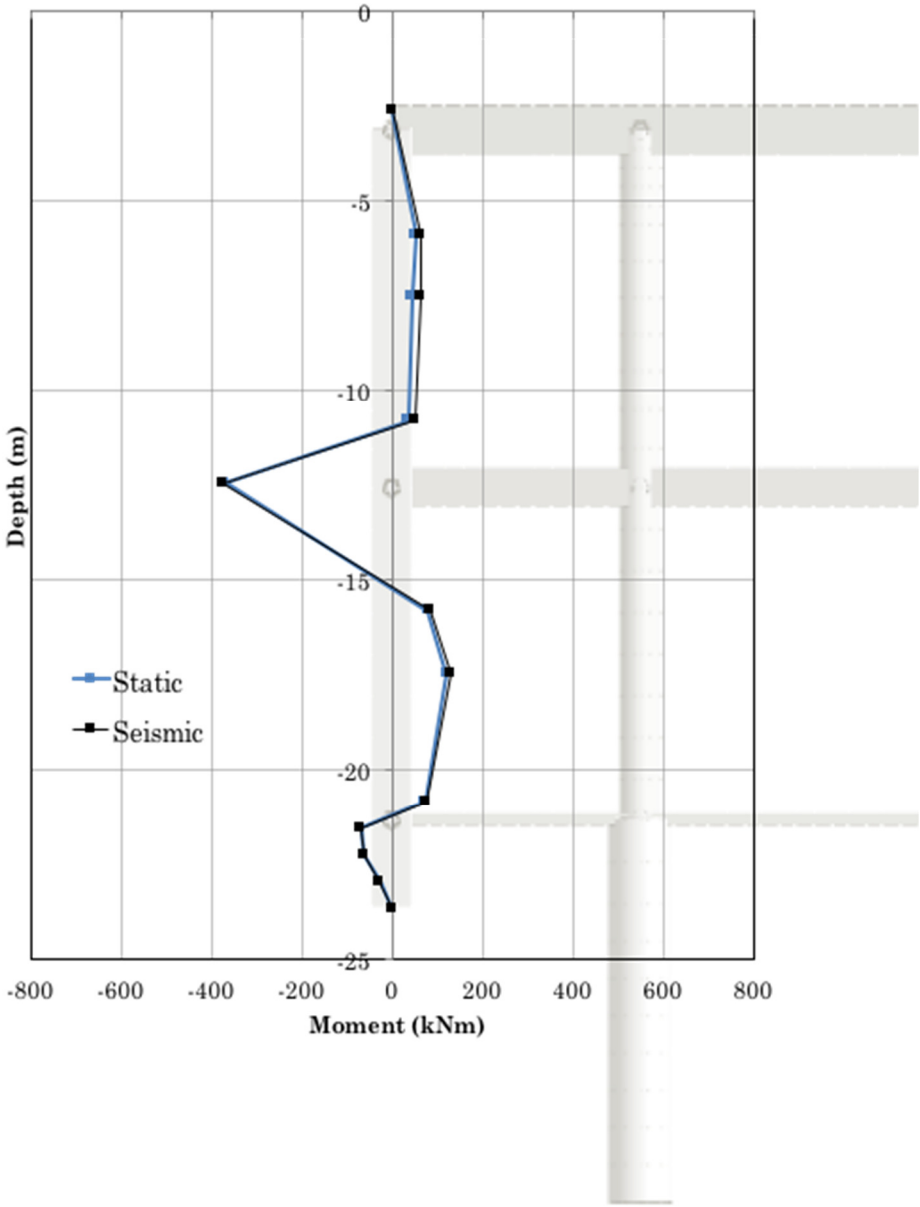

Figure 91: Equivalent linear analysis: bending moment acting on the concrete retaining walls - profile characterized by *Vs* = 600 m/s, input: L'AQUILA

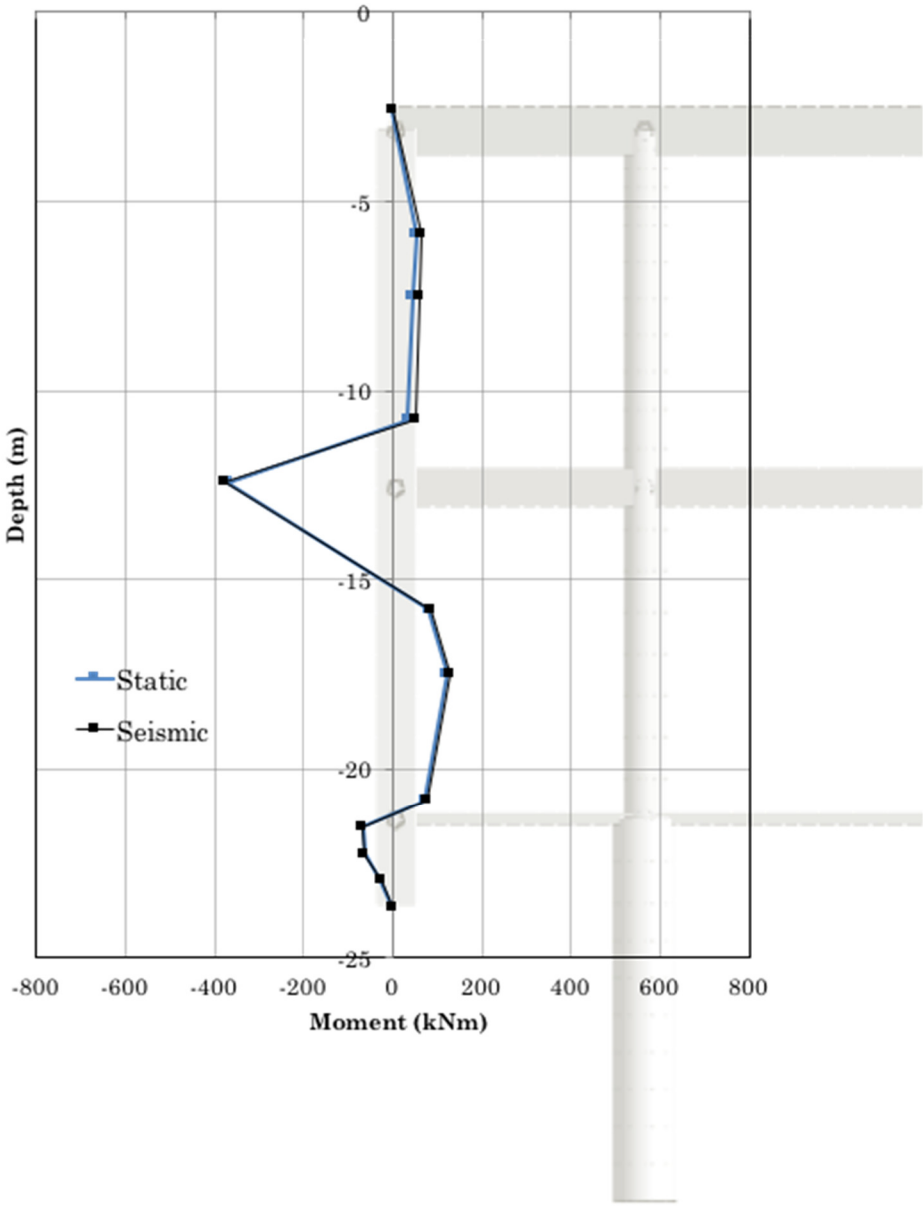

Figure 92: Equivalent linear analysis: bending moment acting on the concrete retaining walls - profile characterized by *Vs* = 600 m/s, input: FRIULI

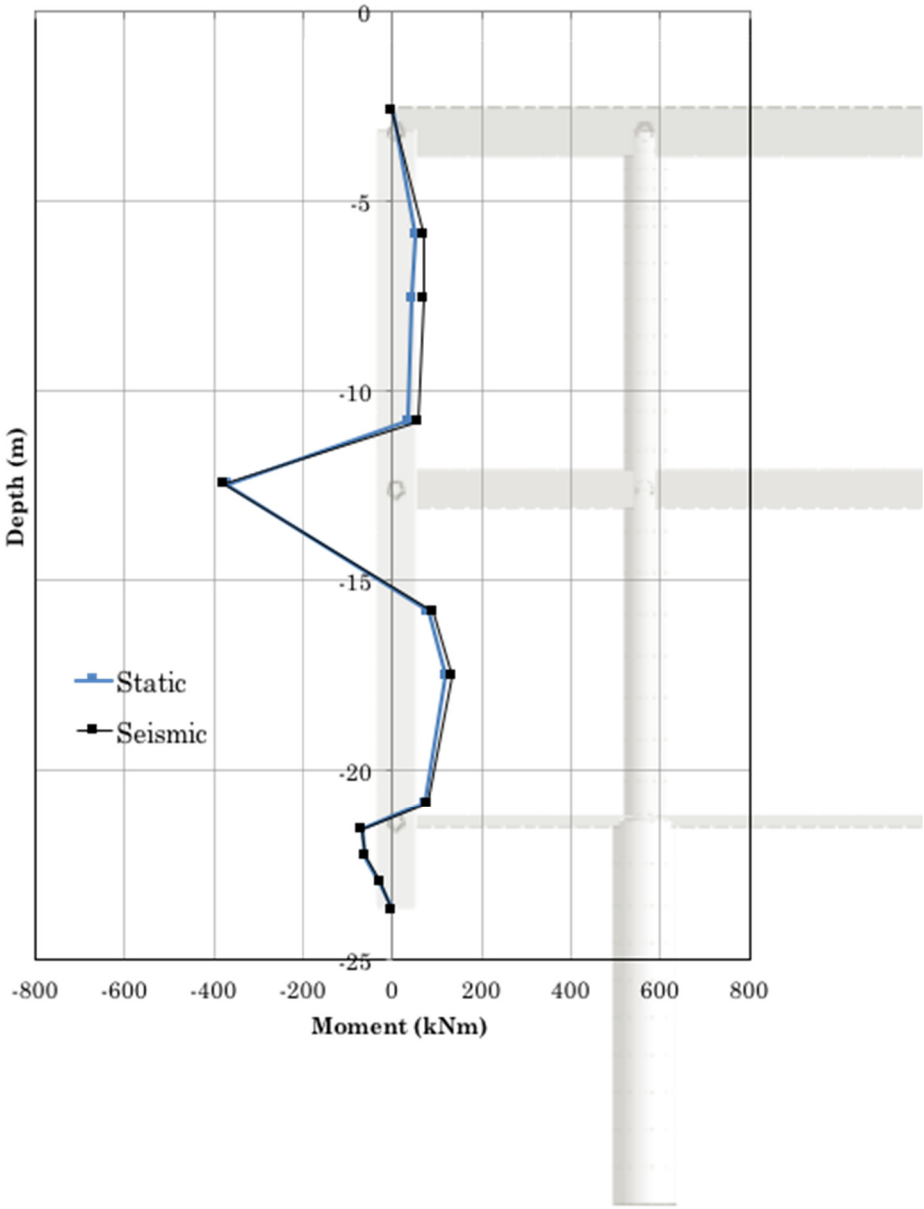

Figure 93: Equivalent linear analysis: bending moment acting on the concrete retaining walls - profile characterized by *Vs* = 600 m/s, input: GREECE

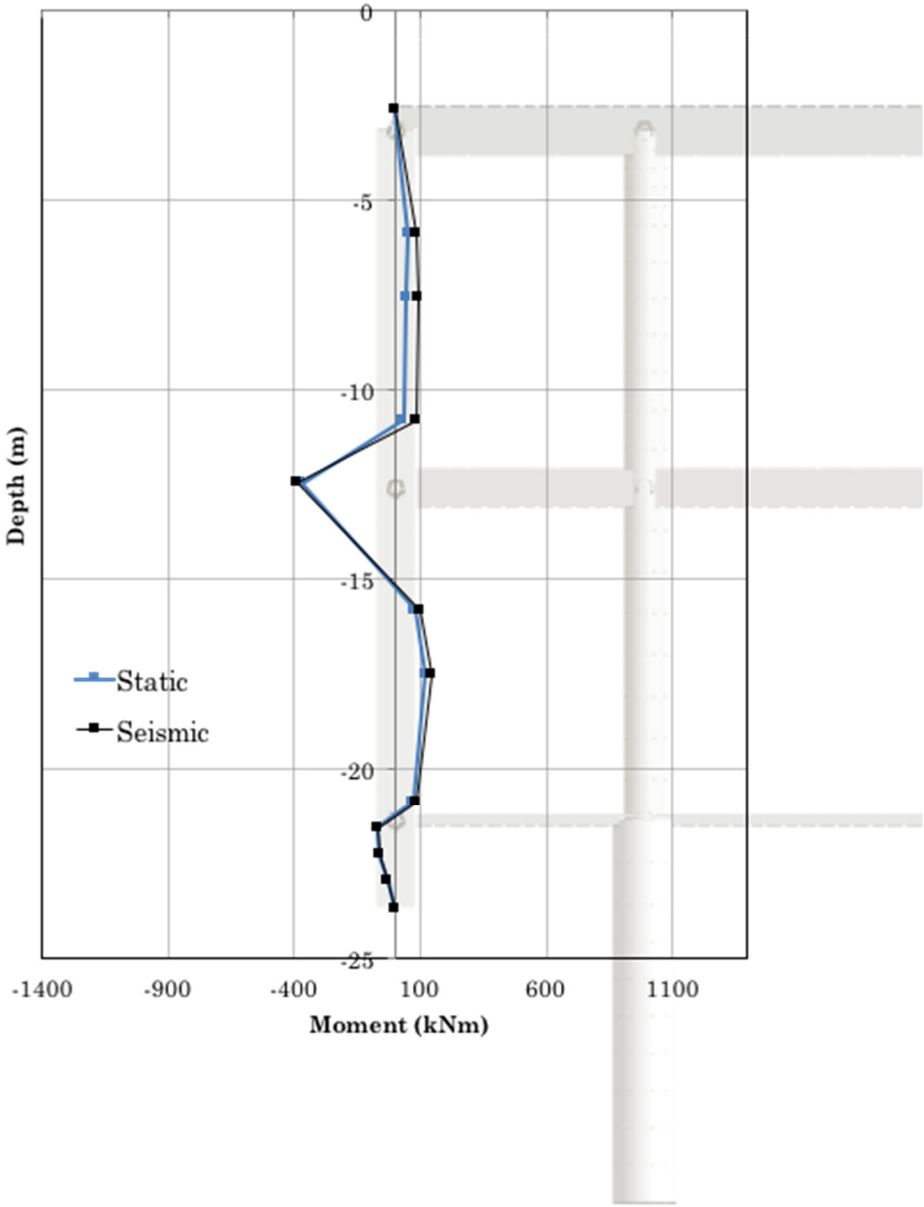

Figure 94: Equivalent linear analysis: bending moment acting on the concrete retaining walls - profile characterized by *Vs* = 600 m/s, input: LIMA

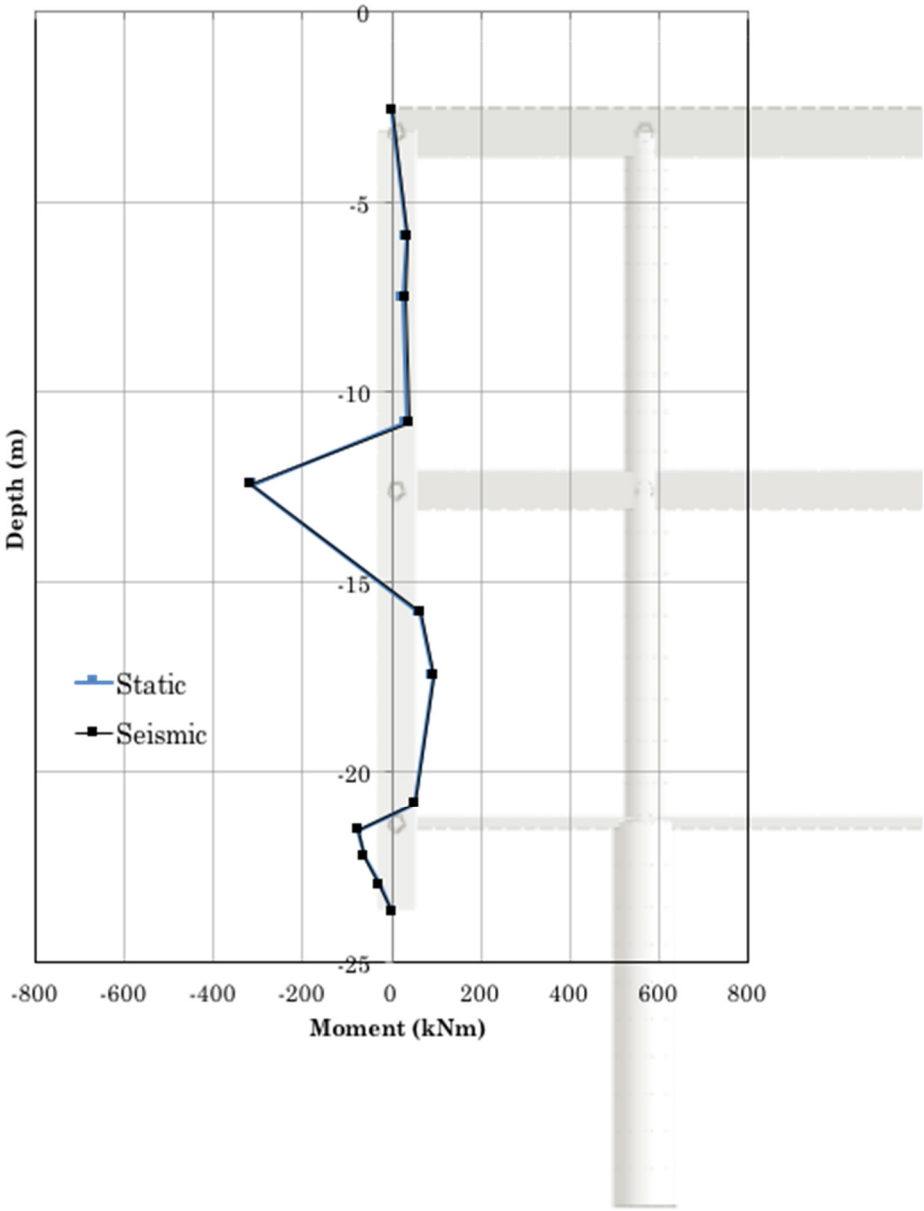

Figure 95: Equivalent linear analysis: bending moment acting on the concrete retaining walls - profile characterized by *Vs* = 750 m/s, input: MONTENEGRO

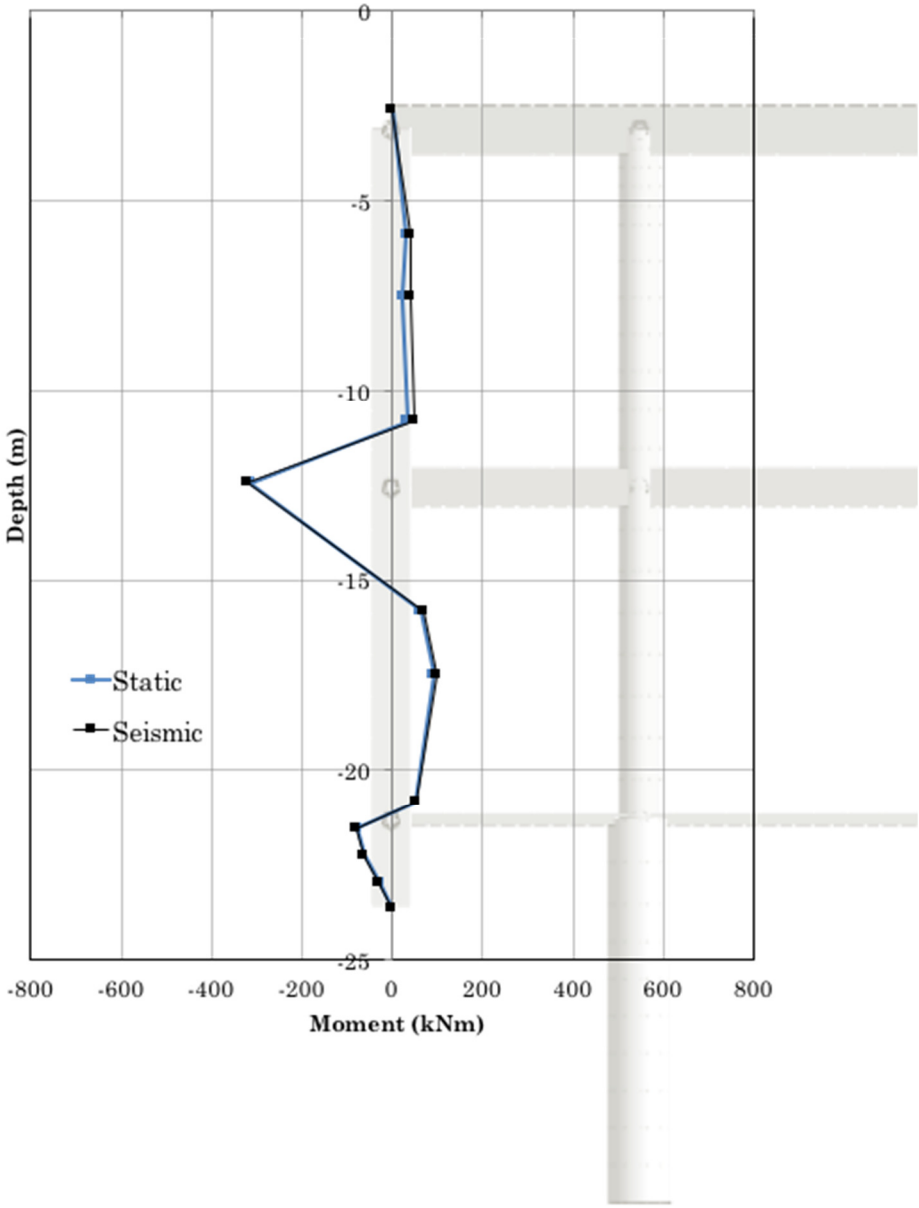

Figure 96: Equivalent linear analysis: bending moment acting on the concrete retaining walls - profile characterized by *Vs* = 750 m/s, input: AMATRICE

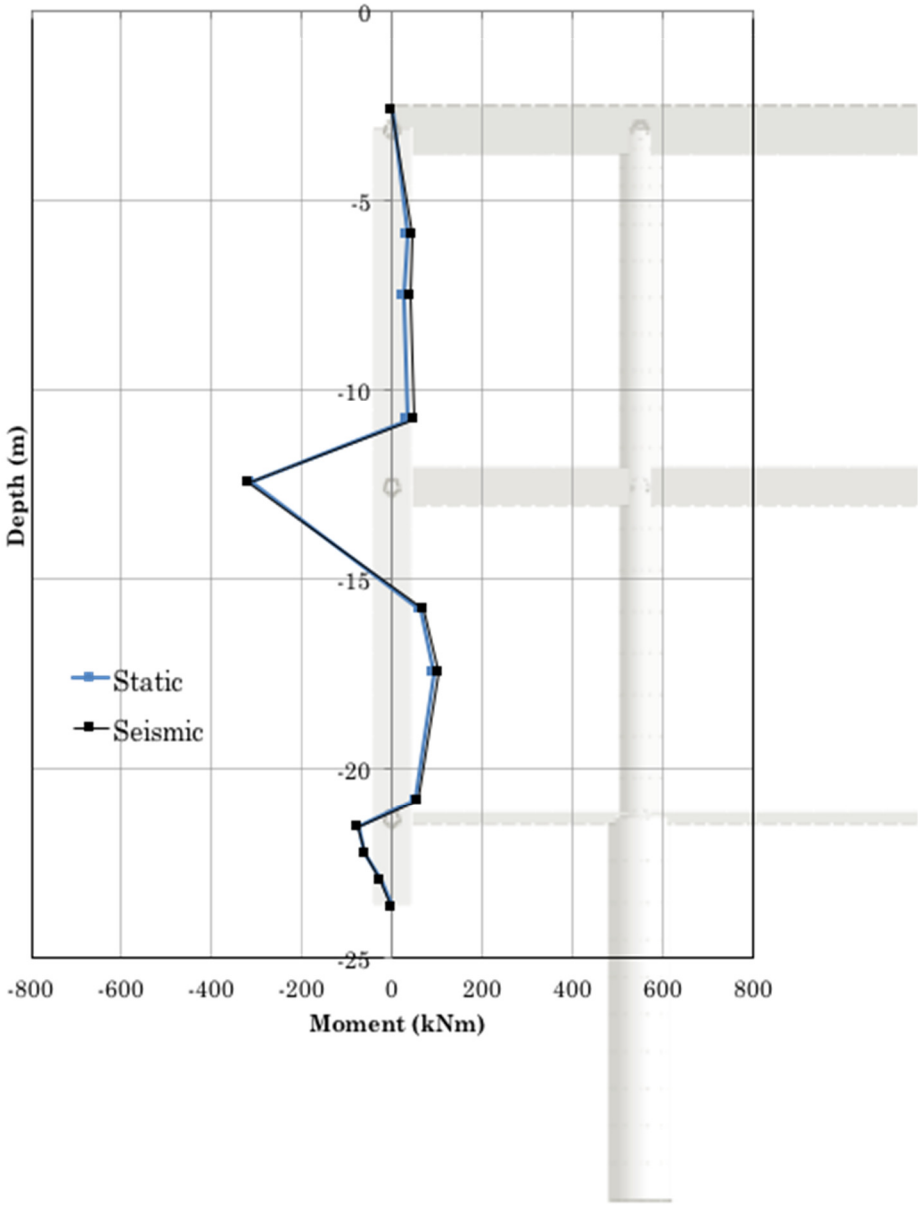

Figure 97: Equivalent linear analysis: bending moment acting on the concrete retaining walls - profile characterized by *Vs* = 750 m/s, input: L'AQUILA

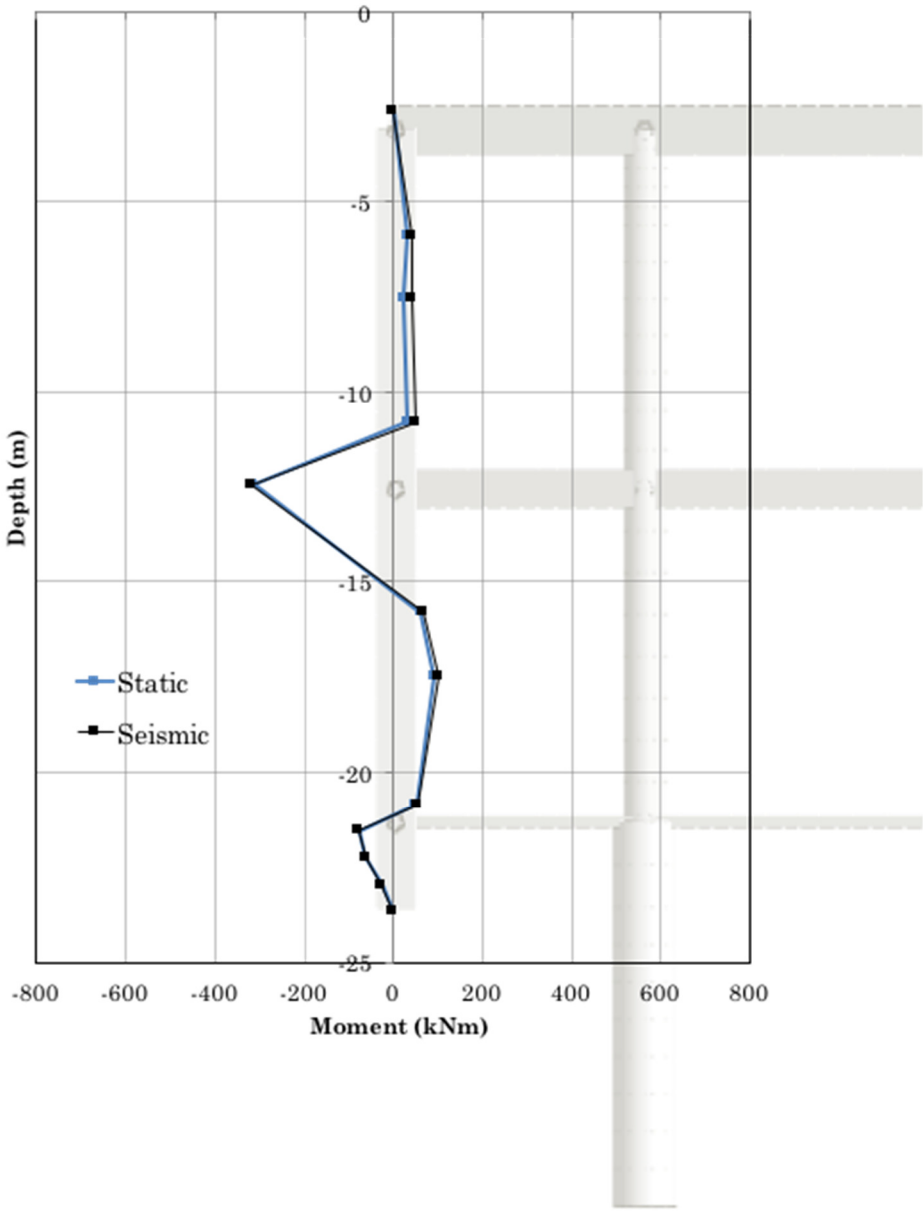

Figure 98: Equivalent linear analysis: bending moment acting on the concrete retaining walls - profile characterized by *Vs* = 750 m/s, input: FRIULI

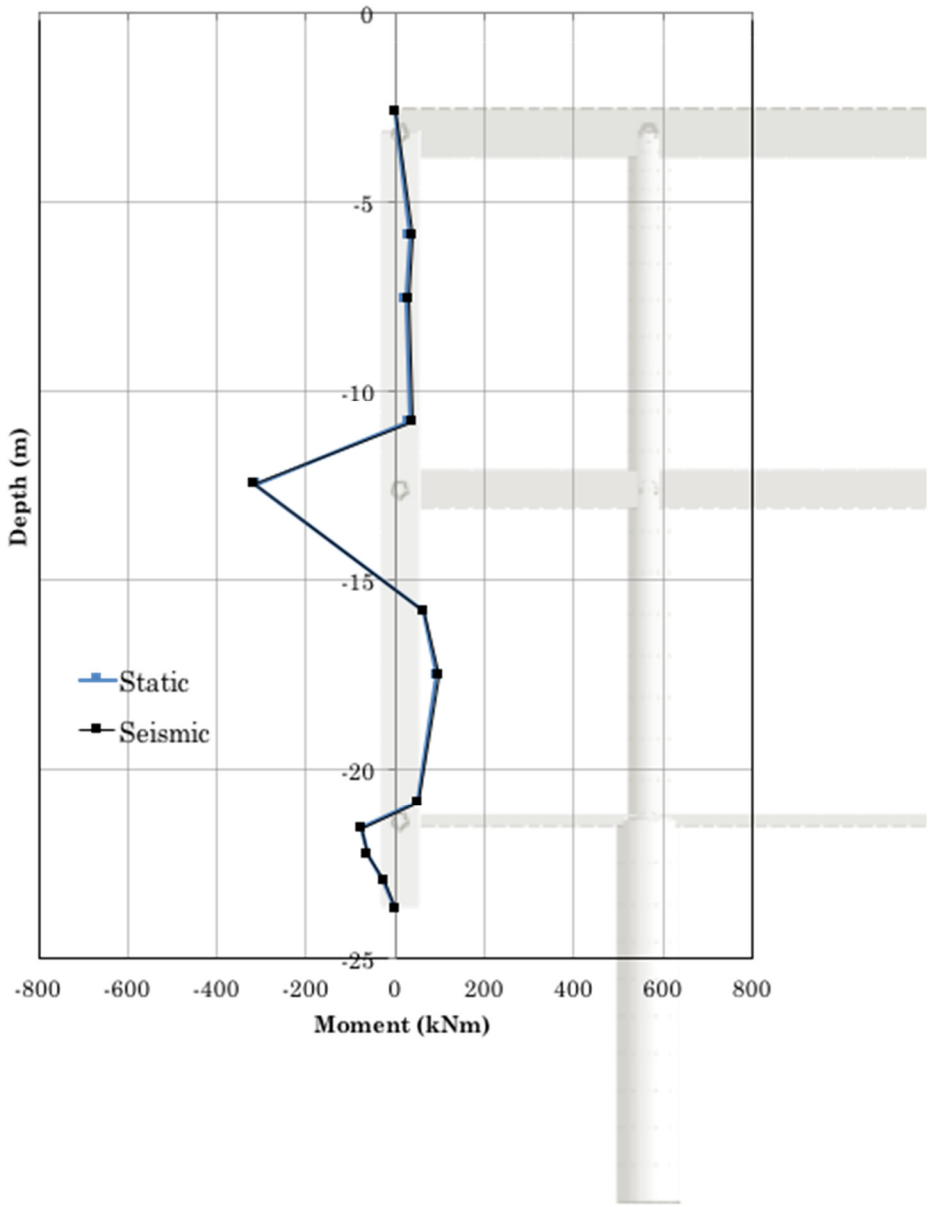

Figure 99: Equivalent linear analysis: bending moment acting on the concrete retaining walls - profile characterized by = 750 m/s, input: GREECE

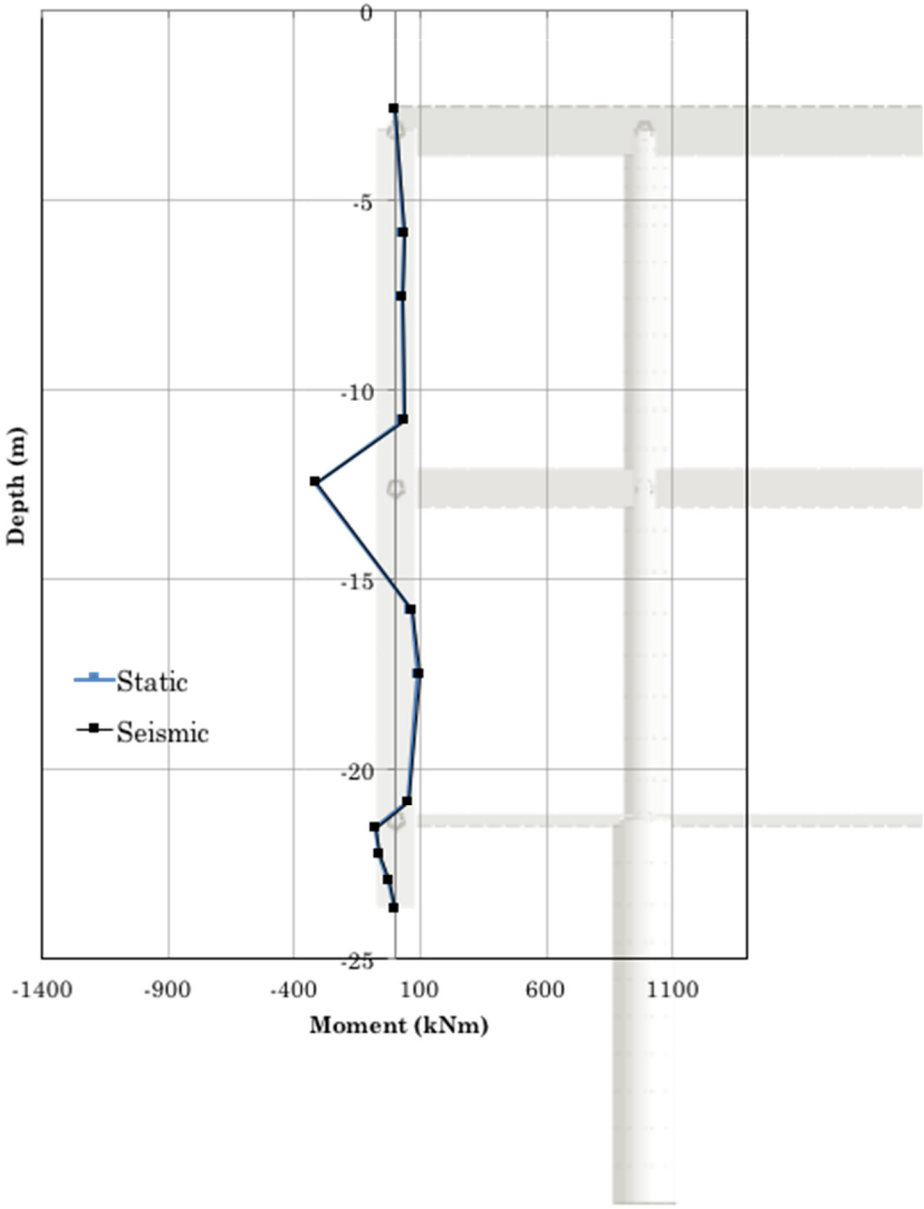

Figure 100: Equivalent linear analysis: bending moment acting on the concrete retaining walls - profile characterized by *Vs* = 750 m/s, input: LIMA

With reference to static case, the maximum increment of bending moment due to the seismic action is obtained. The maximum increase is verified for the profile characterized by a value of shear waves velocity equal to 360 m/s. In particular, the results of the equivalent linear analysis indicate that the maximum increase of bending moment is equal to 110 kNm, in the case of Montenegro earthquake while the increase of bending moment due to the seismic load is almost negligible in cases where the soil profile is characterized by high values of stiffness (V_S = 600 m/s and V_S = 750 m/s).

In any case, the results show that the maximum value of the bending moment acting on the retaining walls occurs in the section in correspondence of the central slab. Table 12 and Figures 101, 102, 103, 104, 105 and 106 show a summary of the results, in terms of bending moment acting on this section, obtained for the different four soil profiles.

Table 12: Bending moment acting on the section in correspondence of the central slab

MONTENEGRO			
Profile	**Moment**		
Vs	**Static**	**Seismic**	Δ
[m/s]	[kNm]	[kNm]	[%]
360	518	628	**21**
450	451	472	**5**
600	370	376	**2**
750	312	315	**1**

GREECE			
Profile	**Moment**		
Vs	**Static**	**Seismic**	Δ
[m/s]	[kNm]	[kNm]	[%]
360	518	601	**16**
450	451	532	**18**
600	370	379	**2**
750	312	315	**1**

AMATRICE			
Profile	**Moment**		
Vs	**Static**	**Seismic**	Δ
[m/s]	[kNm]	[kNm]	[%]
360	518	557	**7**
450	451	484	**7**
600	370	385	**4**
750	312	318	**2**

L'AQUILA			
Profile	**Moment**		
Vs	**Static**	**Seismic**	Δ
[m/s]	[kNm]	[kNm]	[%]
360	518	562	**9**
450	451	475	**5**
600	370	376	**2**
750	312	318	**2**

FRIULI			
Profile	**Moment**		
Vs	**Static**	**Seismic**	Δ
[m/s]	[kNm]	[kNm]	[%]
360	518	542	**5**
450	451	466	**3**
600	370	376	**2**
750	312	318	**2**

LIMA			
Profile	**Moment**		
Vs	**Static**	**Seismic**	Δ
[m/s]	[kNm]	[kNm]	[%]
360	518	619	**20**
450	451	520	**15**
600	370	387	**5**
750	312	315	**1**

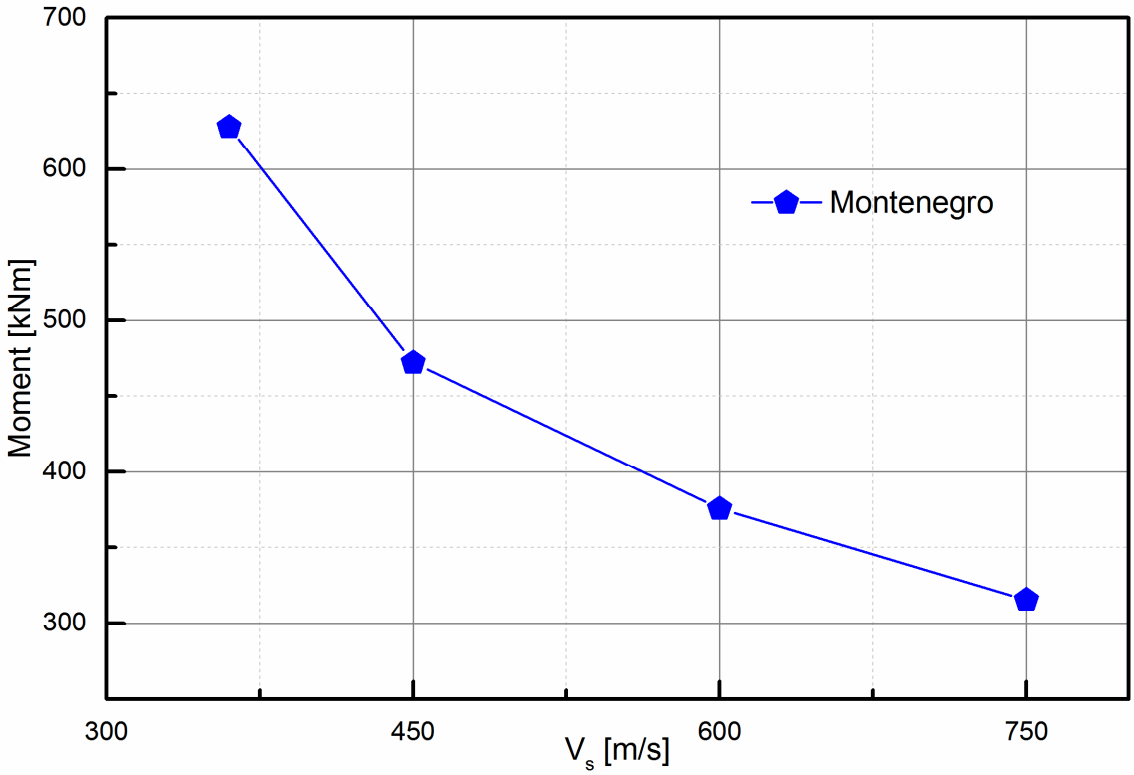

Figure 101: Equivalent linear analysis: maximum bending moment acting on the section in correspondence to the central slab

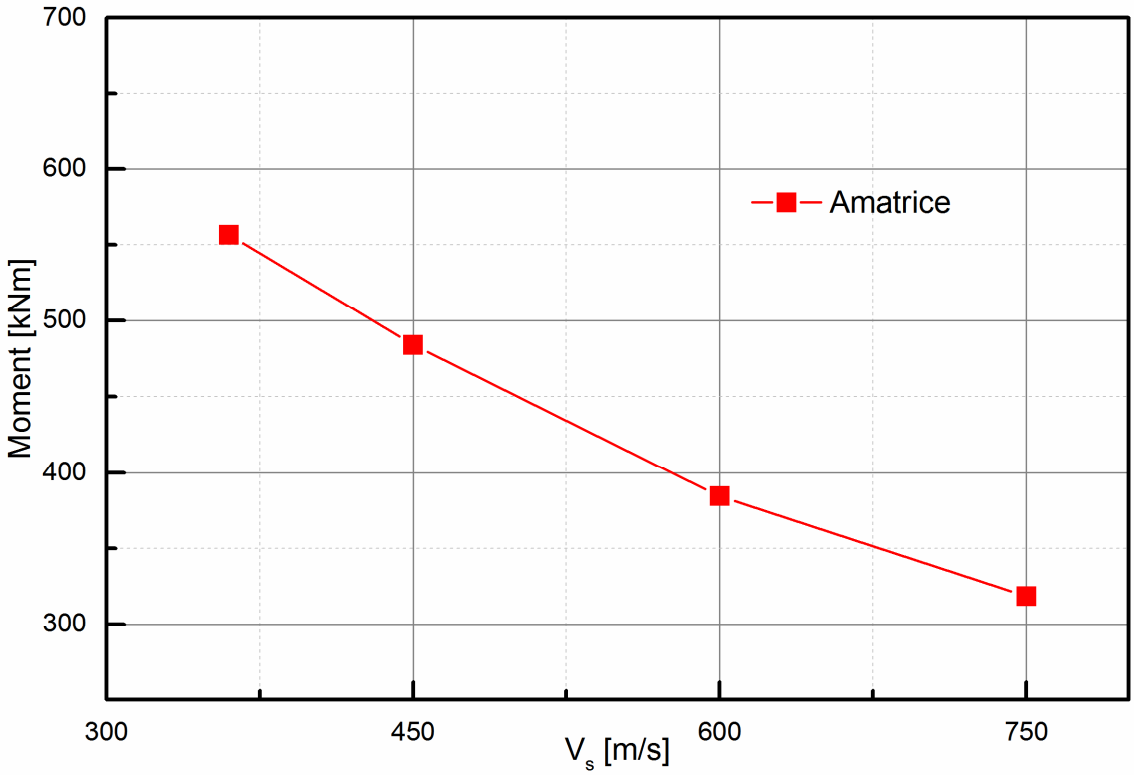

Figure 102: Equivalent linear analysis: maximum bending moment acting on the section in correspondence to the central slab

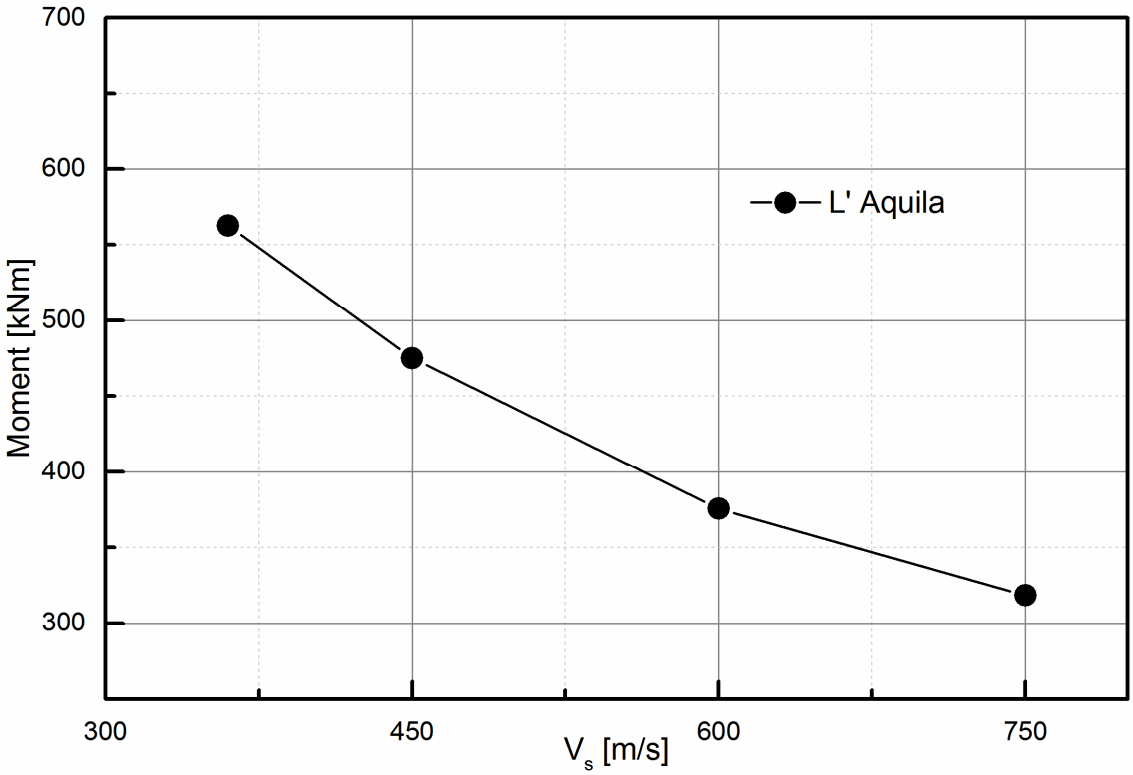

Figure 103: Equivalent linear analysis: maximum bending moment acting on the section in correspondence to the central slab

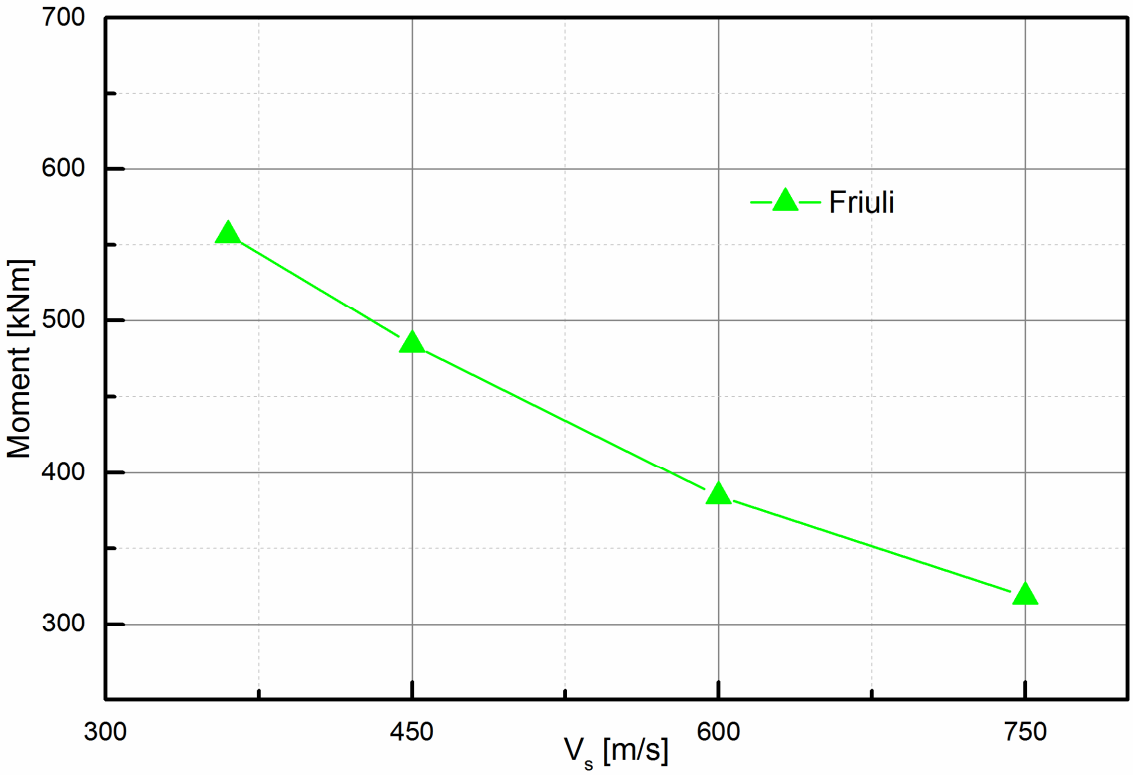

Figure 104: Equivalent linear analysis: maximum bending moment acting on the section in correspondence to the central slab

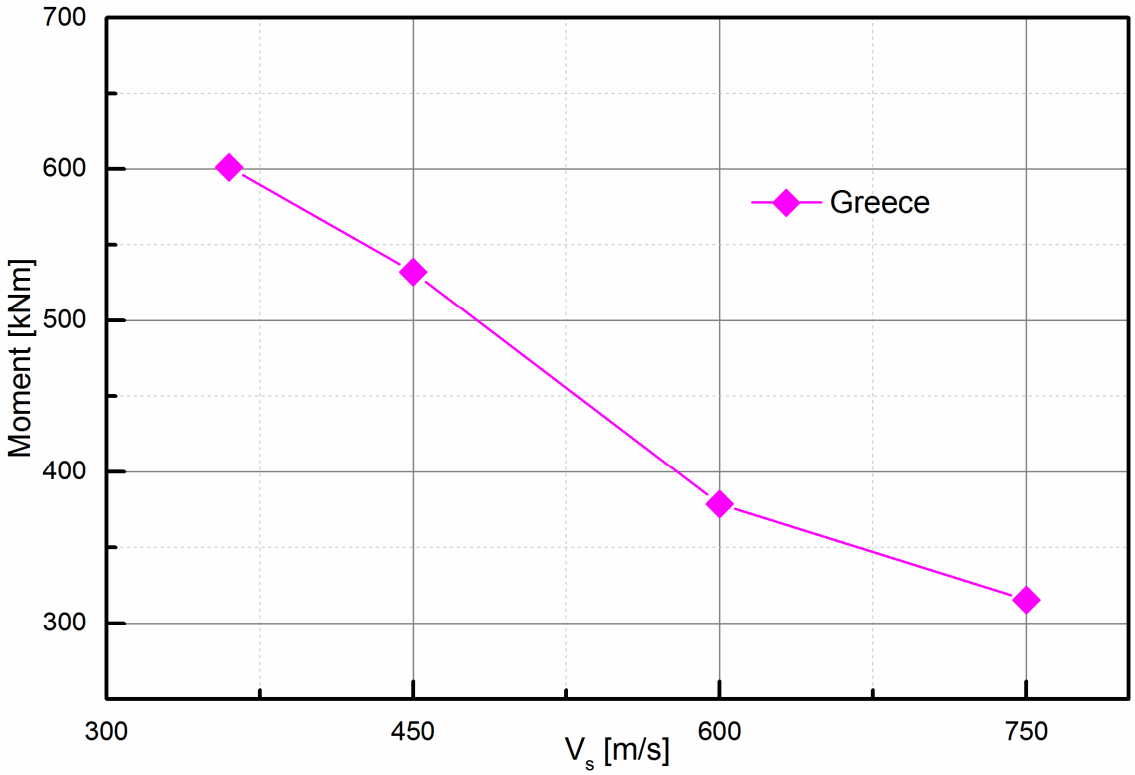

Figure 105: Equivalent linear analysis: maximum bending moment acting on the section in correspondence to the central slab

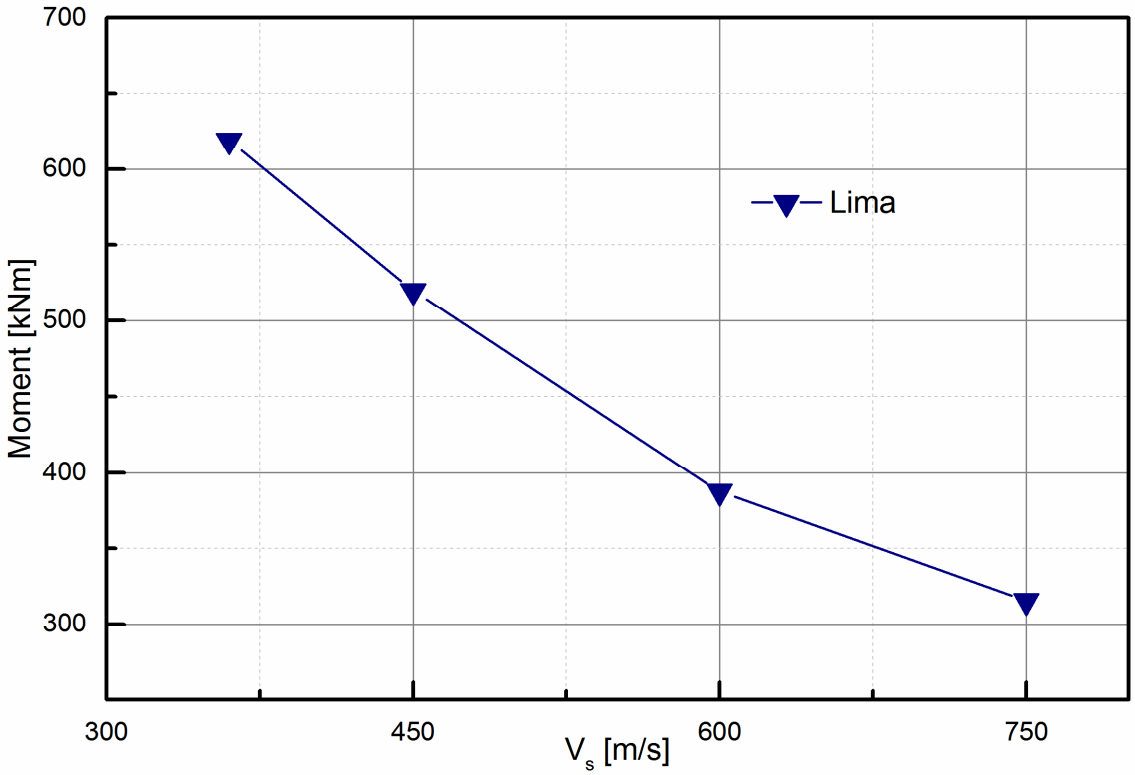

Figure 106: Equivalent linear analysis: maximum bending moment acting on the section in correspondence to the central slab

The second approach, used to obtain the displacements at the depth of the base and at the roof of the underground structure, is to consider the free-field displacements resulting from the numerical model, described in the previous paragraph 3.3, through the execution of a fully dynamic non-linear analysis. This type of analysis follows the evolution of the non-linear behavior of the soil gradually in the time domain and, for this reason, it is necessary to define the law that characterizes the stress-strain behavior of the soil. The nonlinearity of stress-strain behavior of the soil implies which the soil shear modulus is constantly decreasing and the inelasticity implies that the soil unloads along a different path than its loading path, thereby dissipanting enegy at the points of contact between particles. Contrary to the equivalent linear analysis, the non linear behavior in the stress-strain law is followed directly by all the elements as the solution marches on in time. On condition that one suitable non-linear law is chosen, the dependence of damping and apparent modulus on the level of the strain is automatically implemented. The elato-plastic behavior taking into consideration the elementary necessary plastic mechanism such as progressive friction mobilization, Coulomb type failure, critical state and dilatancy/contractance flow rule, is used. Consider an elasto-plastic behavior with a constant shear modulus, G_0, and a constant yield stress, τ_m, under a cyclic shear strain of amplitude, γ.
Below yield, the secant shear modulus G is simply equa to G_0. Under cyclic action which involves yield, the value of the secant shear modulus is equal to.

$$G = \frac{\tau_m}{\gamma}$$

The maximum stored energy, W, during the cycle and the dissipated energy, A_{loop}, are obtained by the following relations:

$$W = \frac{\tau_m \gamma}{2}$$

$$\Delta W = 4\tau_m(\gamma - \gamma_m)$$

with:

$$\gamma_m = \frac{\tau_m}{G_0}$$

Consequently:

$$\frac{\Delta W}{W} = \frac{8(\gamma - \gamma_m)}{\gamma}$$

Considering the damping ratio D and that (Kolsky, 1963):

$$4\pi D \approx \frac{\Delta W}{W}$$

for small value of damping ratio:

$$D = \frac{2(\gamma - \gamma_m)}{\pi\gamma}$$

In Table 13 a summary of the results of the non-linear analysis is reported. In this case, the relative displacements are obtained considering the difference between the displacement valued at the depth corresponding at the top of the concrete retaining walls of the underground structure and the displacement valued at the depth corresponding at the base of the concrete retaining walls.

Table 13: Relative displacements

	Relative Displacement					
PROFILE V_s	AMATRICE	FRIULI	GREECE	MONTENEGRO	L'AQUILA	LIMA
[m/s]	[mm]	[mm]	[mm]	[mm]	[mm]	[mm]
360	18	12	33	42	19	120
450	16	8	30	13	10	107
600	8	4	7	4	4	36
750	5	3	2	2	4	23

Figures from 107 to 130 shown the results in terms of bending moment acting on the concrete retaining walls.

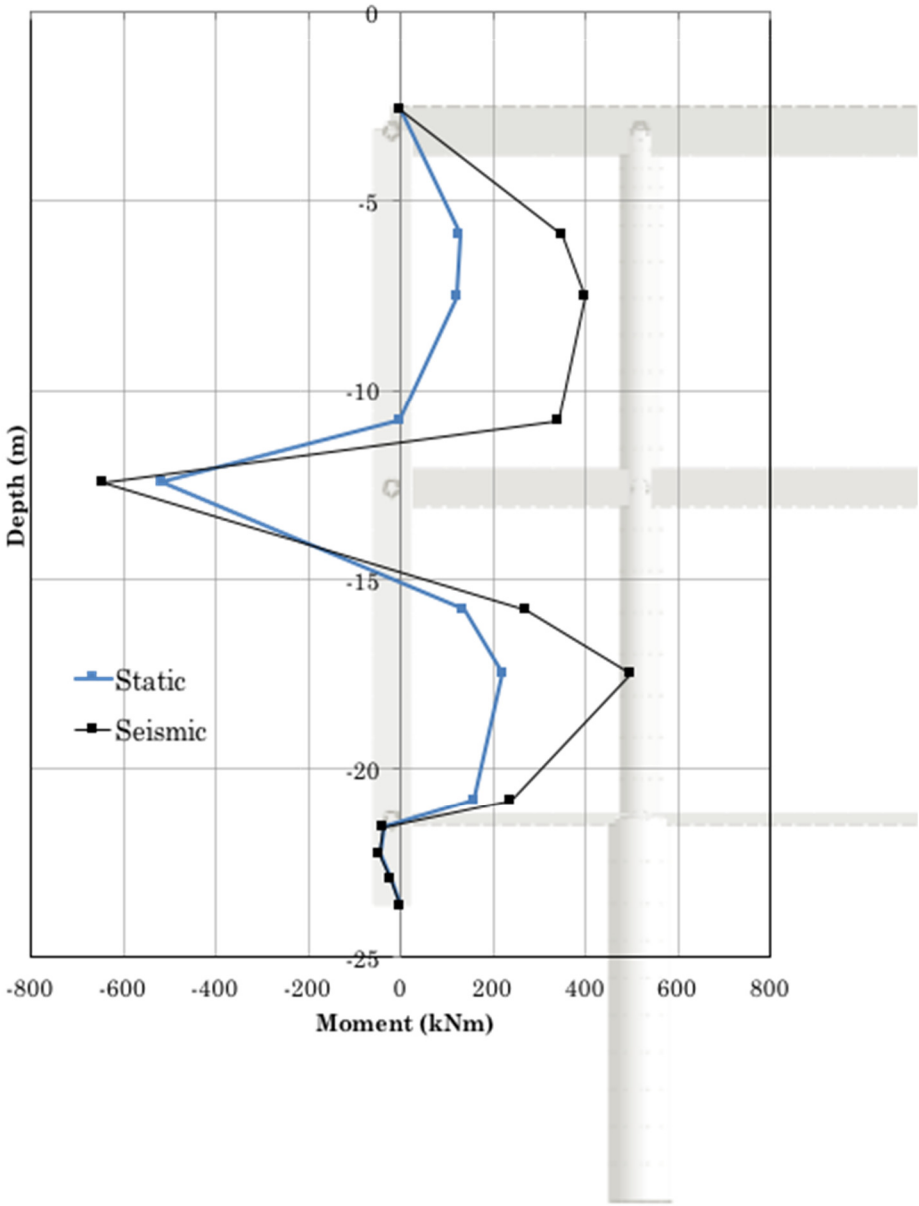

Figure 107: Non-linear analysis: bending moment acting on the concrete retaining walls - profile characterized by *Vs* = 360 m/s, input: MONTENEGRO

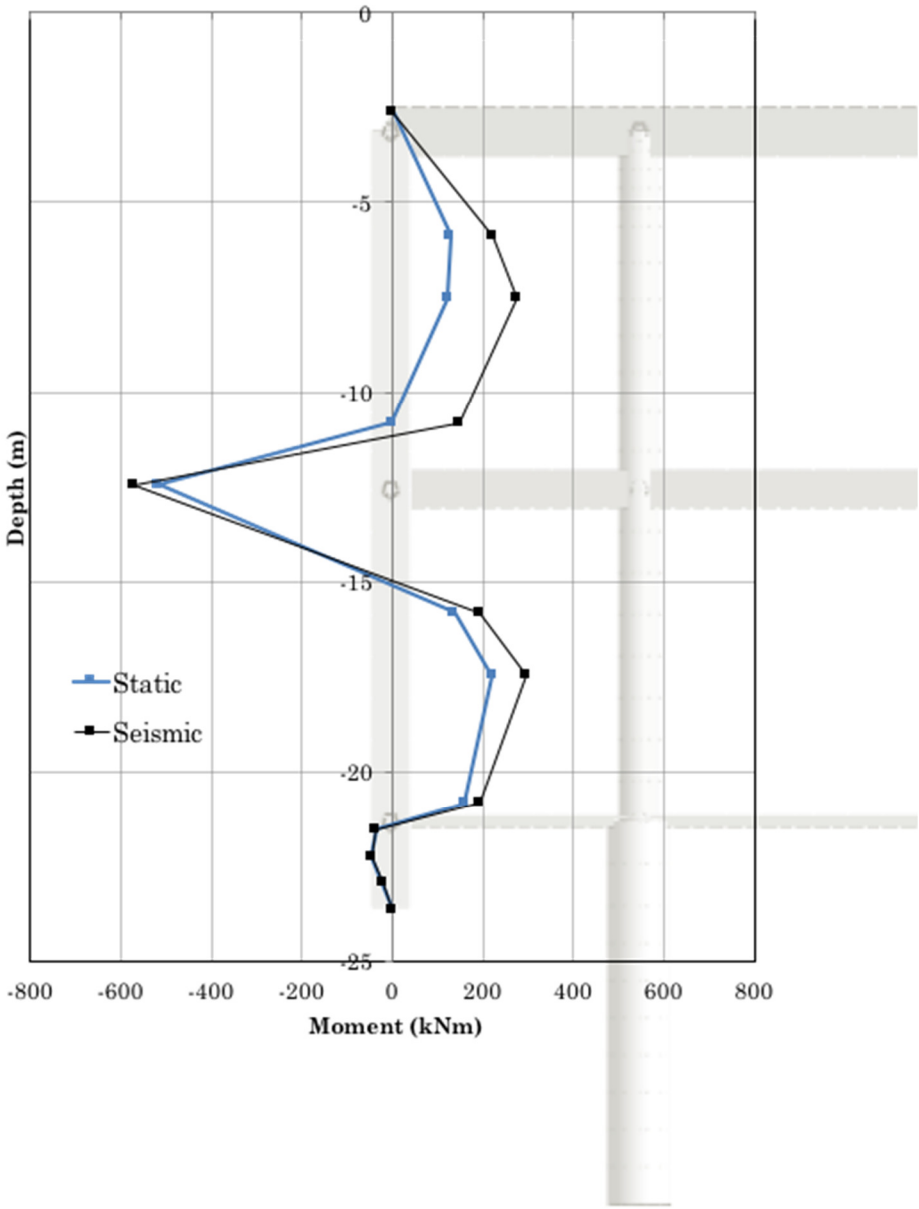

Figure 108: Non-linear analysis: bending moment acting on the concrete retaining walls - profile characterized by *Vs* = 360 m/s, input: AMATRICE

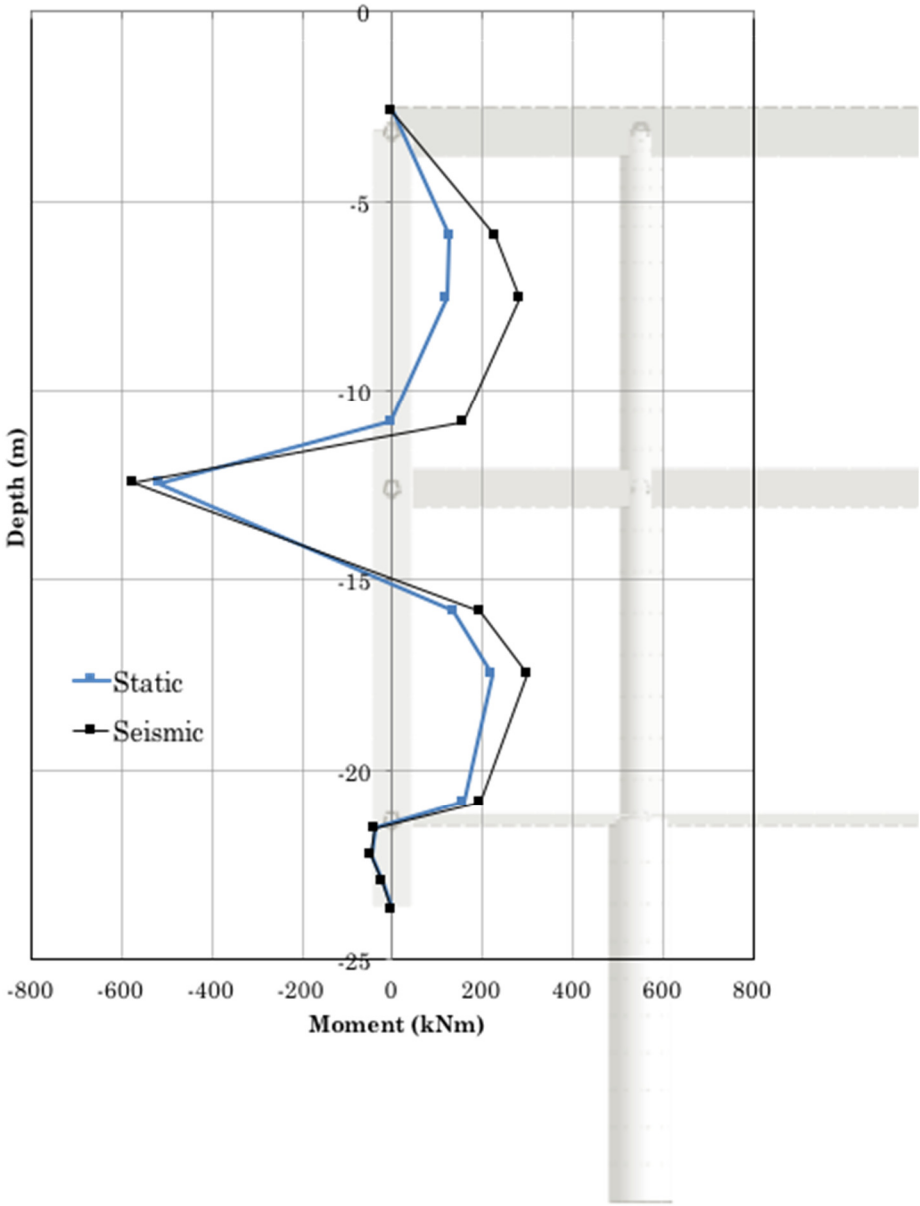

Figure 109: Non-linear analysis: bending moment acting on the concrete retaining walls - profile characterized by *Vs* = 360 m/s, input: L'AQUILA

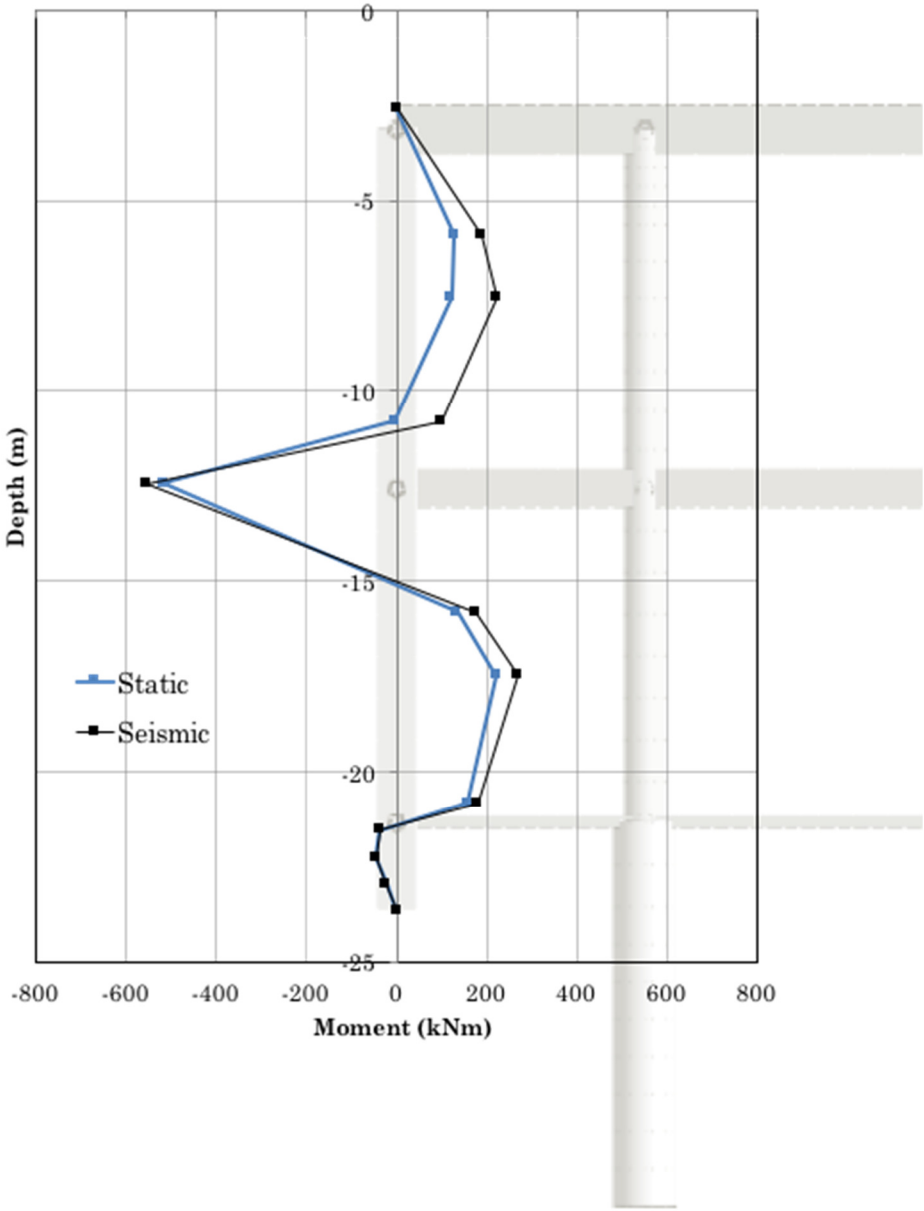

Figure 110: Non-linear analysis: bending moment acting on the concrete retaining walls - profile characterized by *Vs* = 360 m/s, input: FRIULI

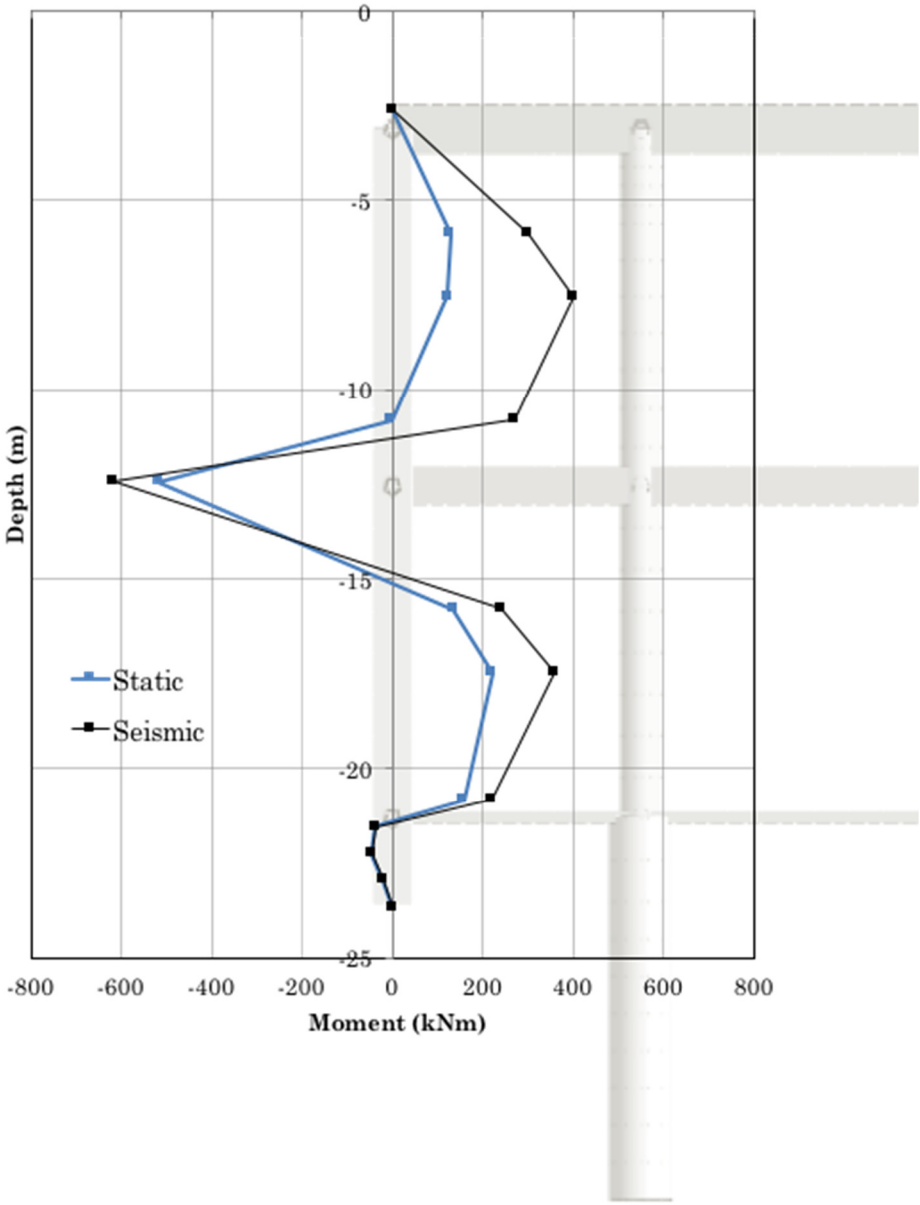

Figure 111: Non-linear analysis: bending moment acting on the concrete retaining walls - profile characterized by *Vs* = 360 m/s, input: GREECE

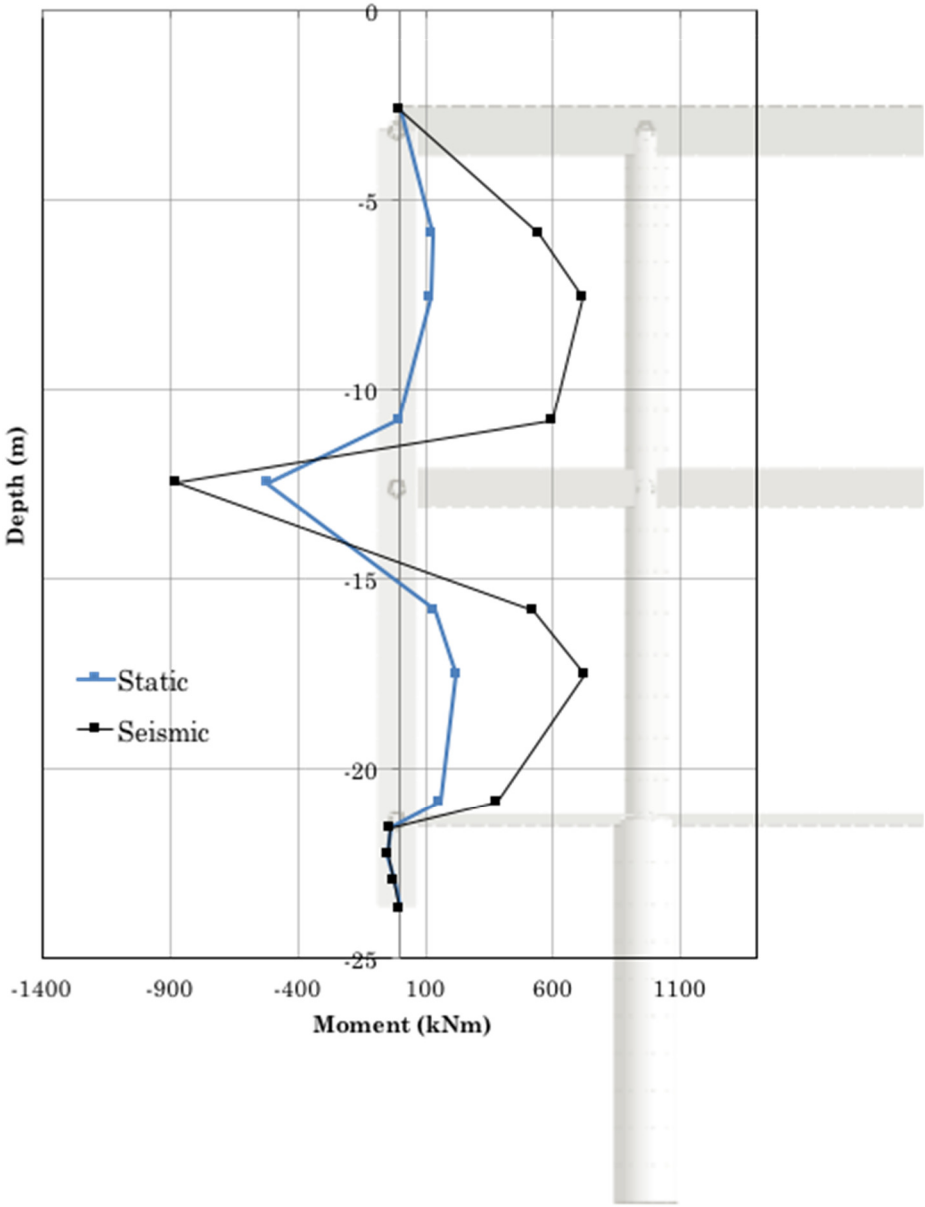

Figure 112: Non-linear analysis: bending moment acting on the concrete retaining walls - profile characterized by *Vs* = 360 m/s, input: LIMA

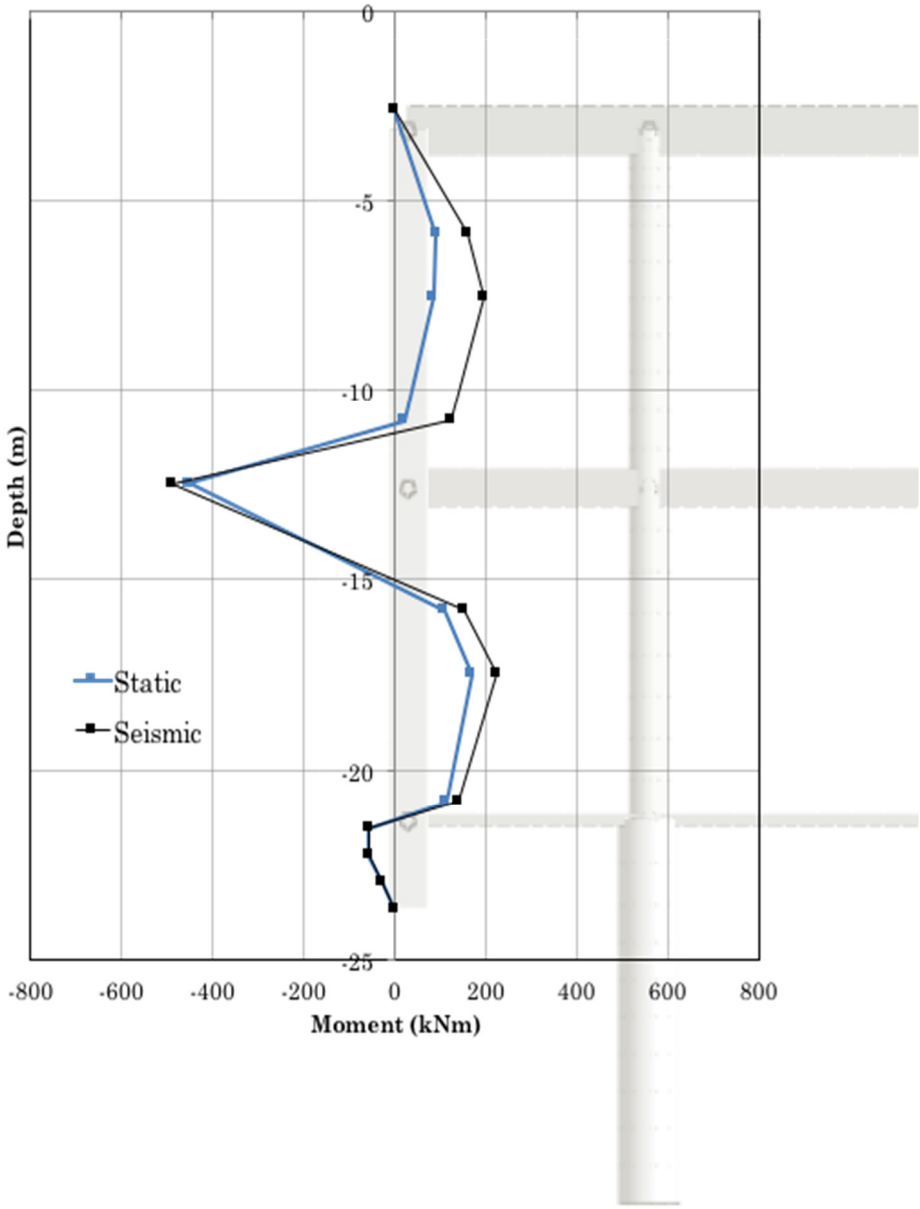

Figure 113: Non-linear analysis: bending moment acting on the concrete retaining walls - profile characterized by *Vs* = 450 m/s, input: MONTENEGRO

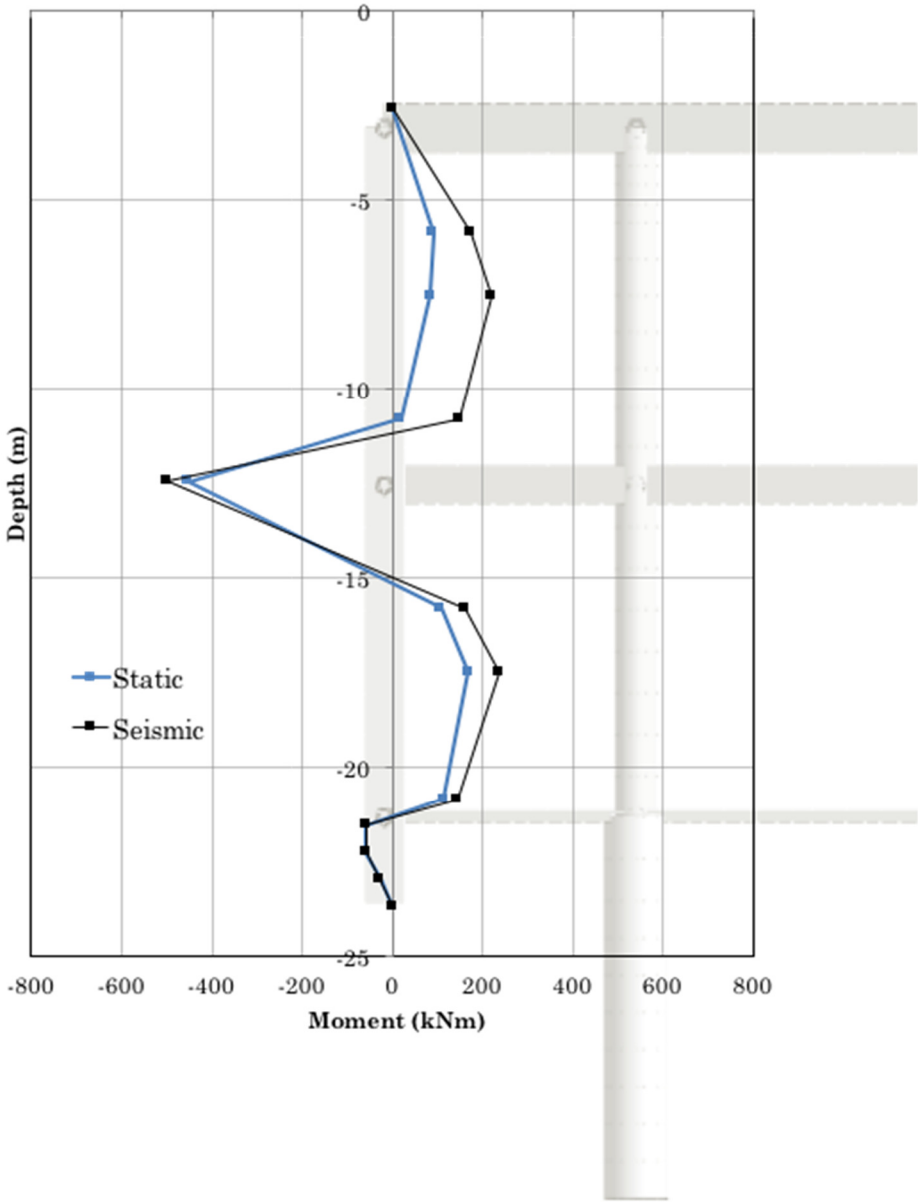

Figure 114: Non-linear analysis: bending moment acting on the concrete retaining walls - profile characterized by *Vs* = 450 m/s, input: AMATRICE

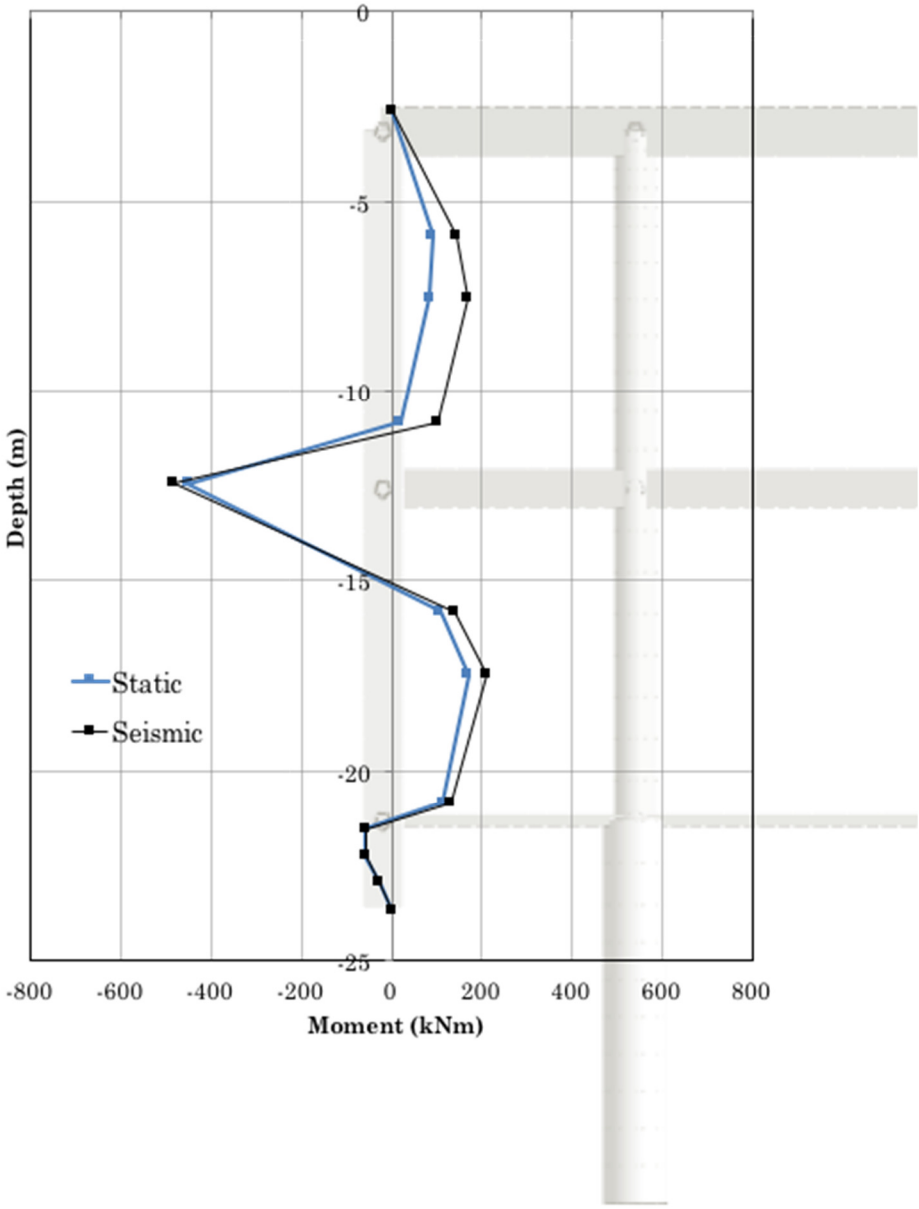

Figure 115: Non-linear analysis: bending moment acting on the concrete retaining walls - profile characterized by *Vs* = 450 m/s, input: L'AQUILA

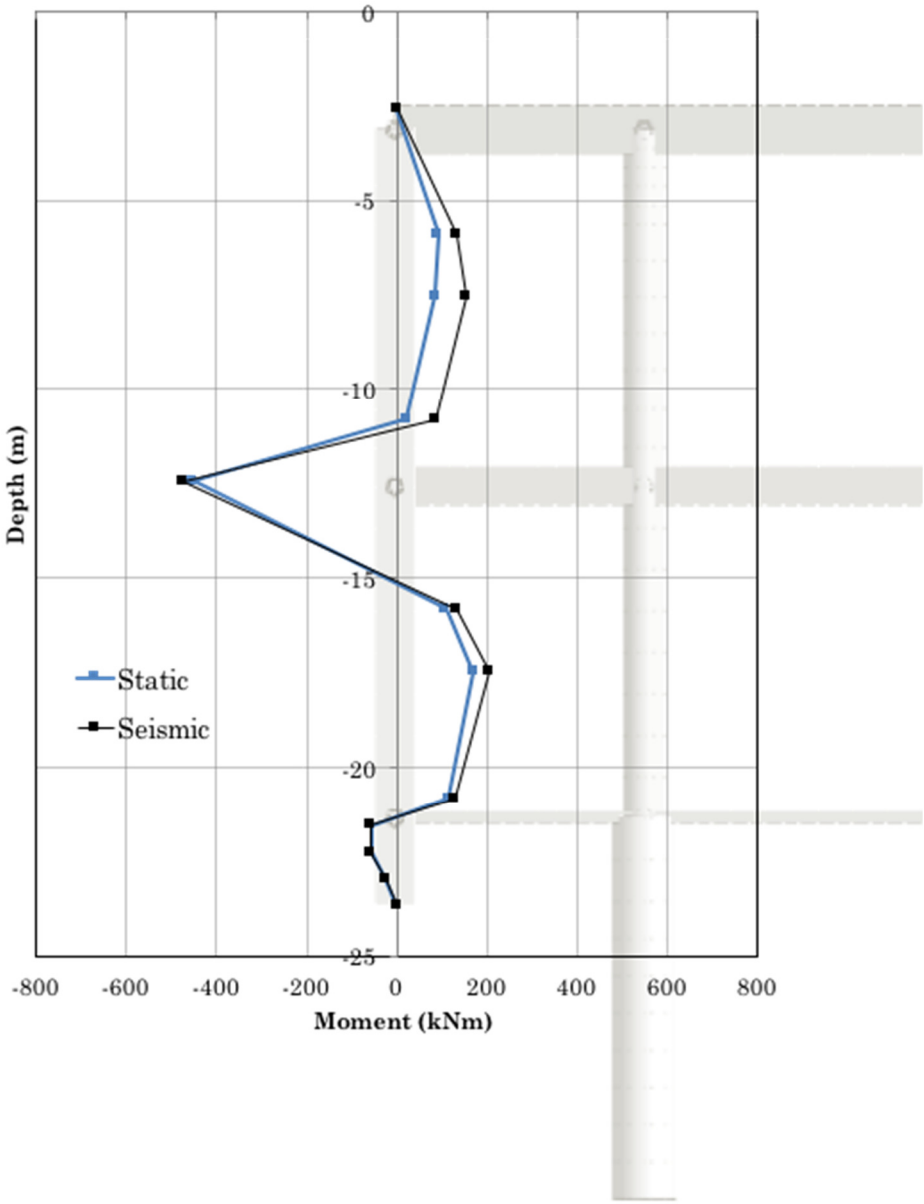

Figure 116: Non-linear analysis: bending moment acting on the concrete retaining walls - profile characterized by *Vs* = 450 m/s, input: FRIULI

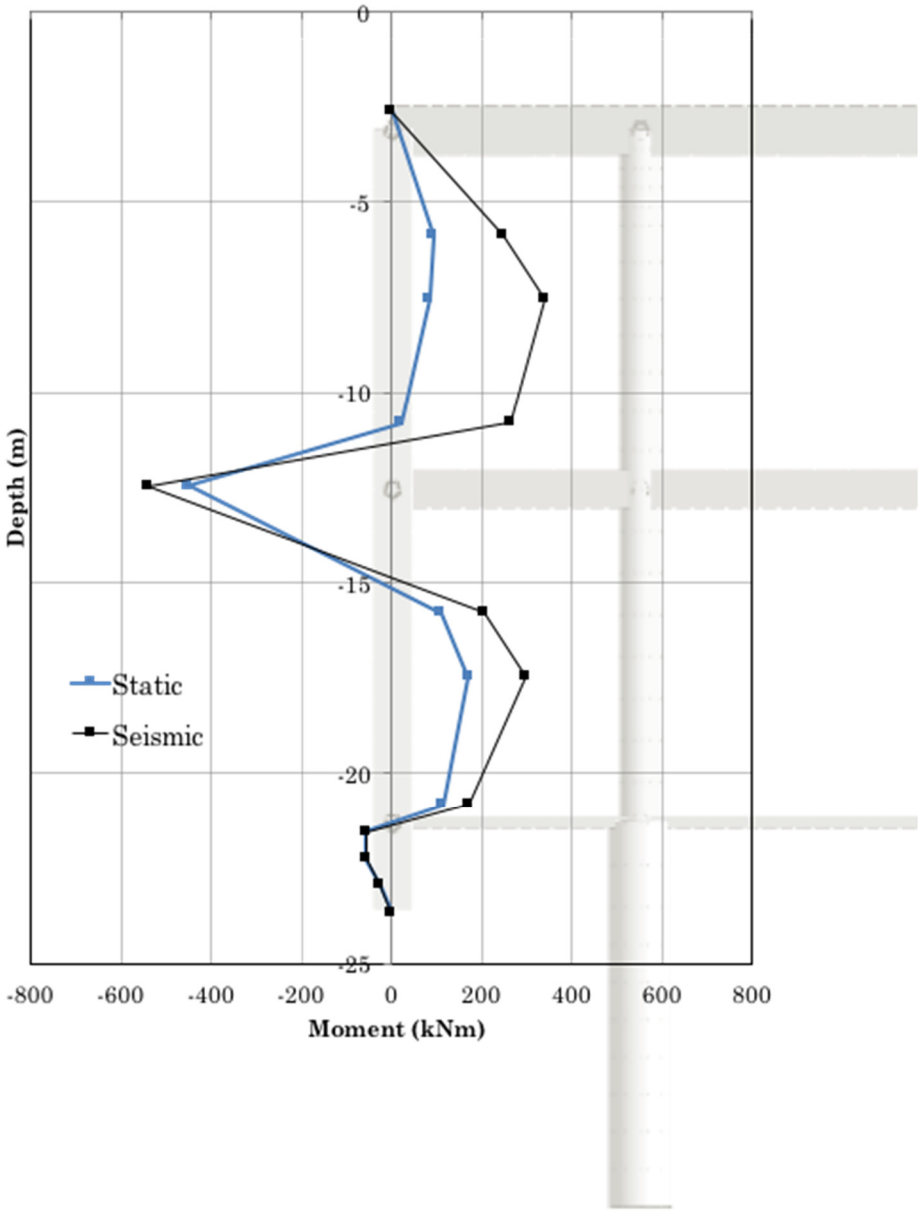

Figure 117: Non-linear analysis: bending moment acting on the concrete retaining walls - profile characterized by *Vs* = 450 m/s, input: GREECE

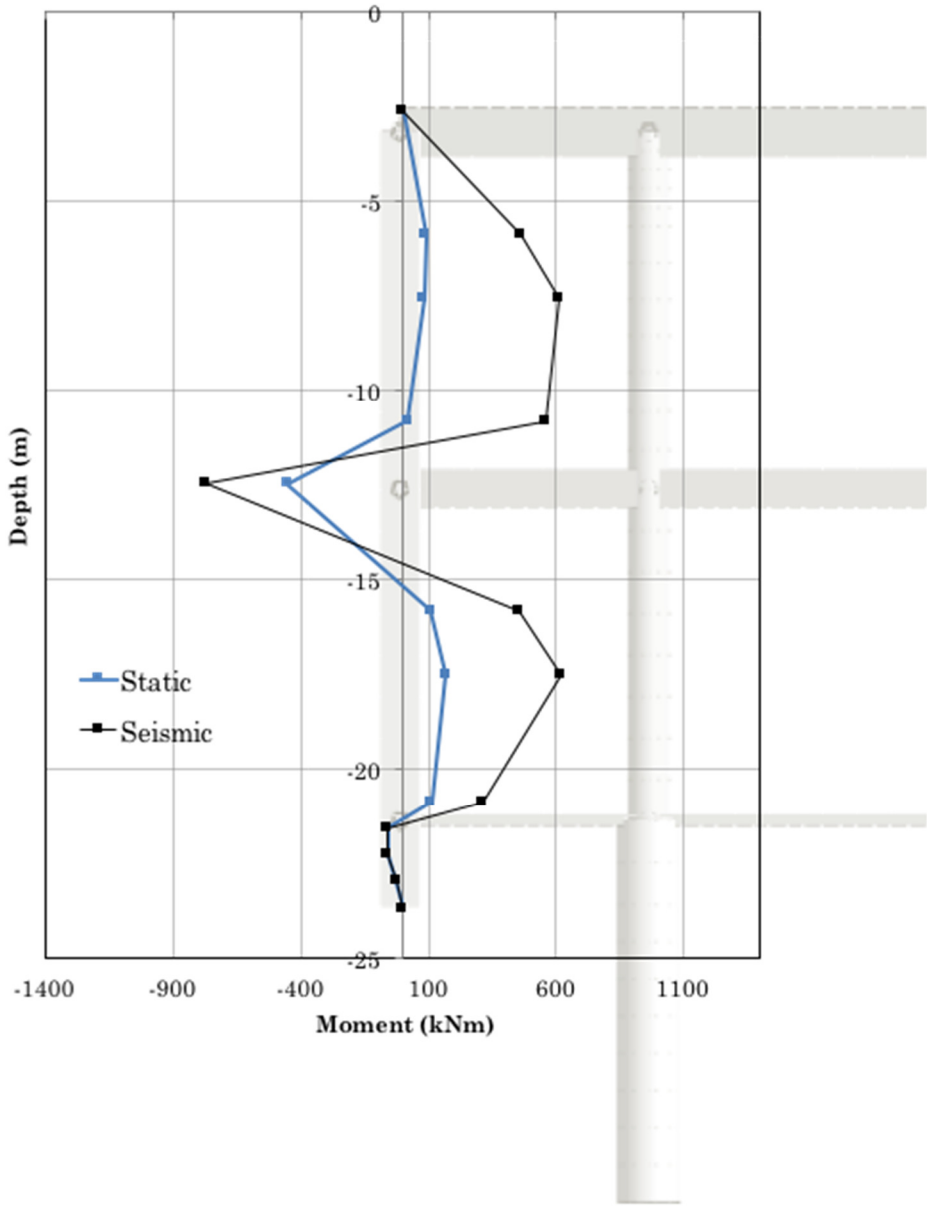

Figure 118: Non-linear analysis: bending moment acting on the concrete retaining walls - profile characterized by *Vs* = 450 m/s, input: LIMA

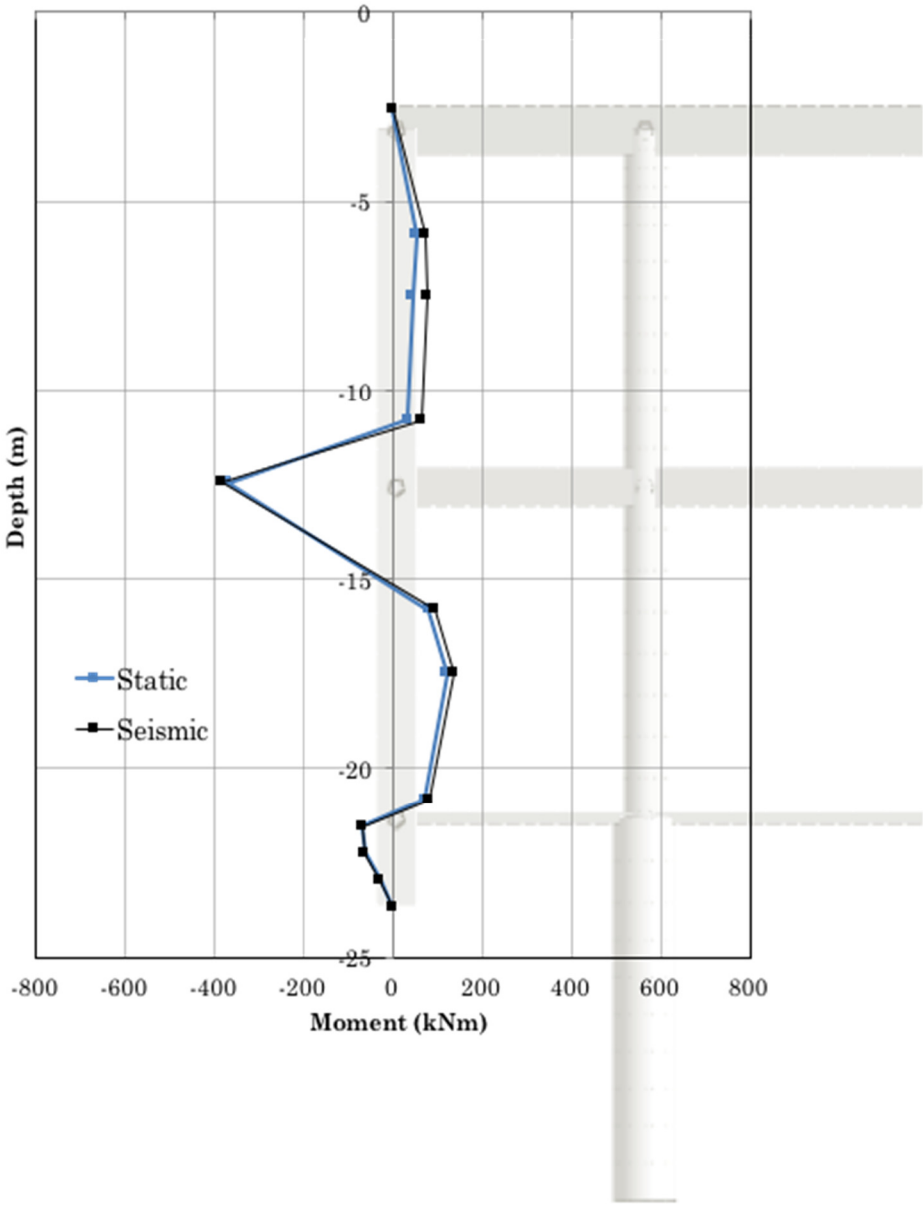

Figure 119: Non-linear analysis: bending moment acting on the concrete retaining walls - profile characterized by *Vs* = 600 m/s, input: MONTENEGRO

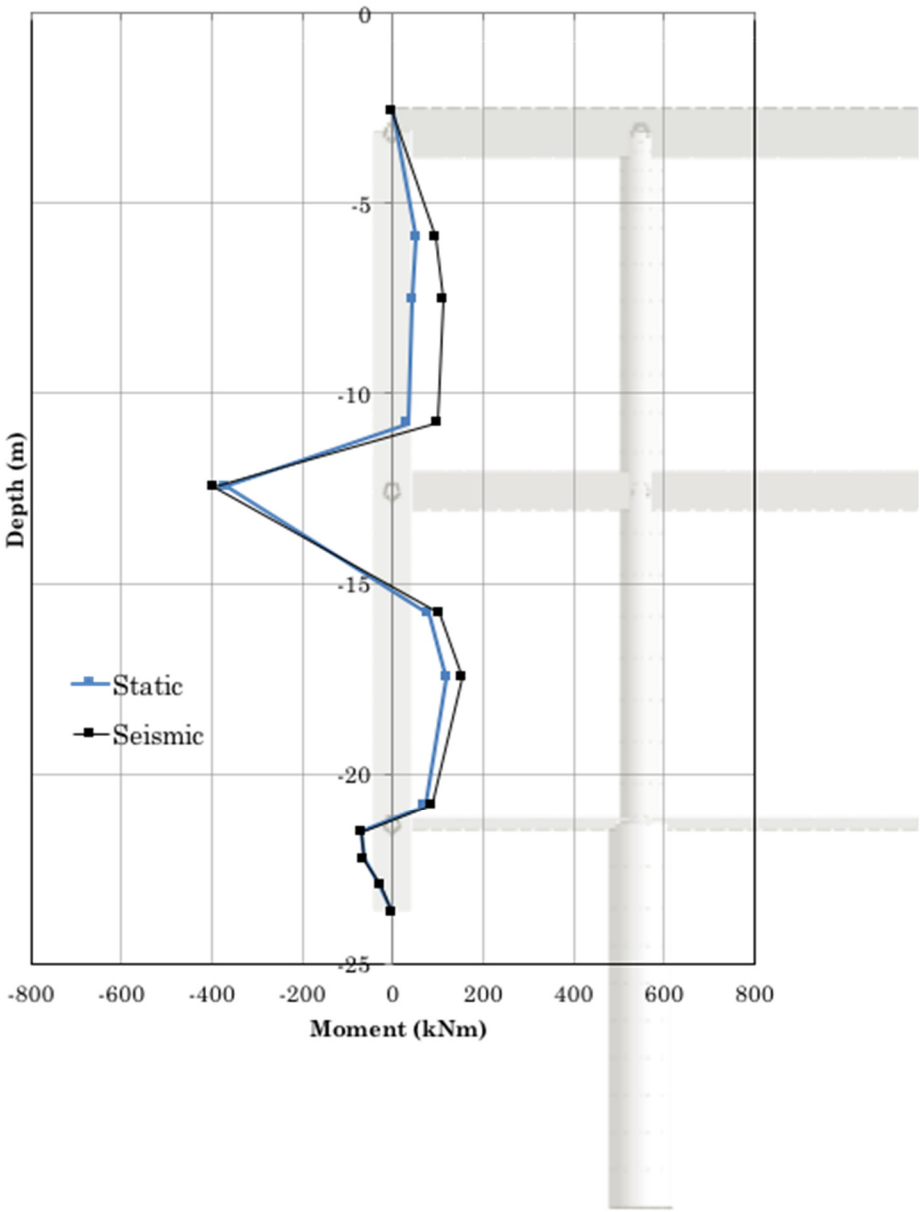

Figure 120: Non-linear analysis: bending moment acting on the concrete retaining walls - profile characterized by *Vs* = 600 m/s, input: AMATRICE

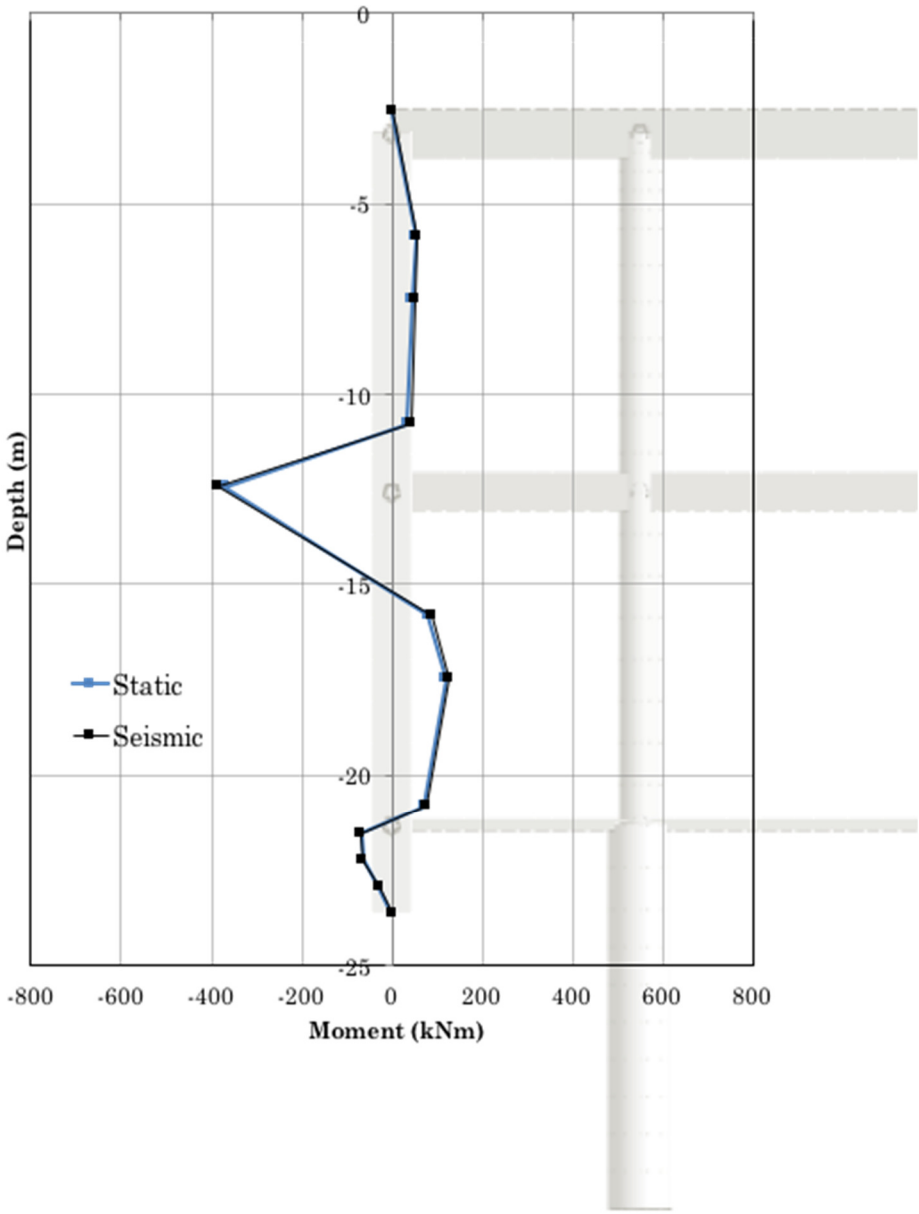

Figure 121: Non-linear analysis: bending moment acting on the concrete retaining walls - profile characterized by *Vs* = 600 m/s, input: L'AQUILA

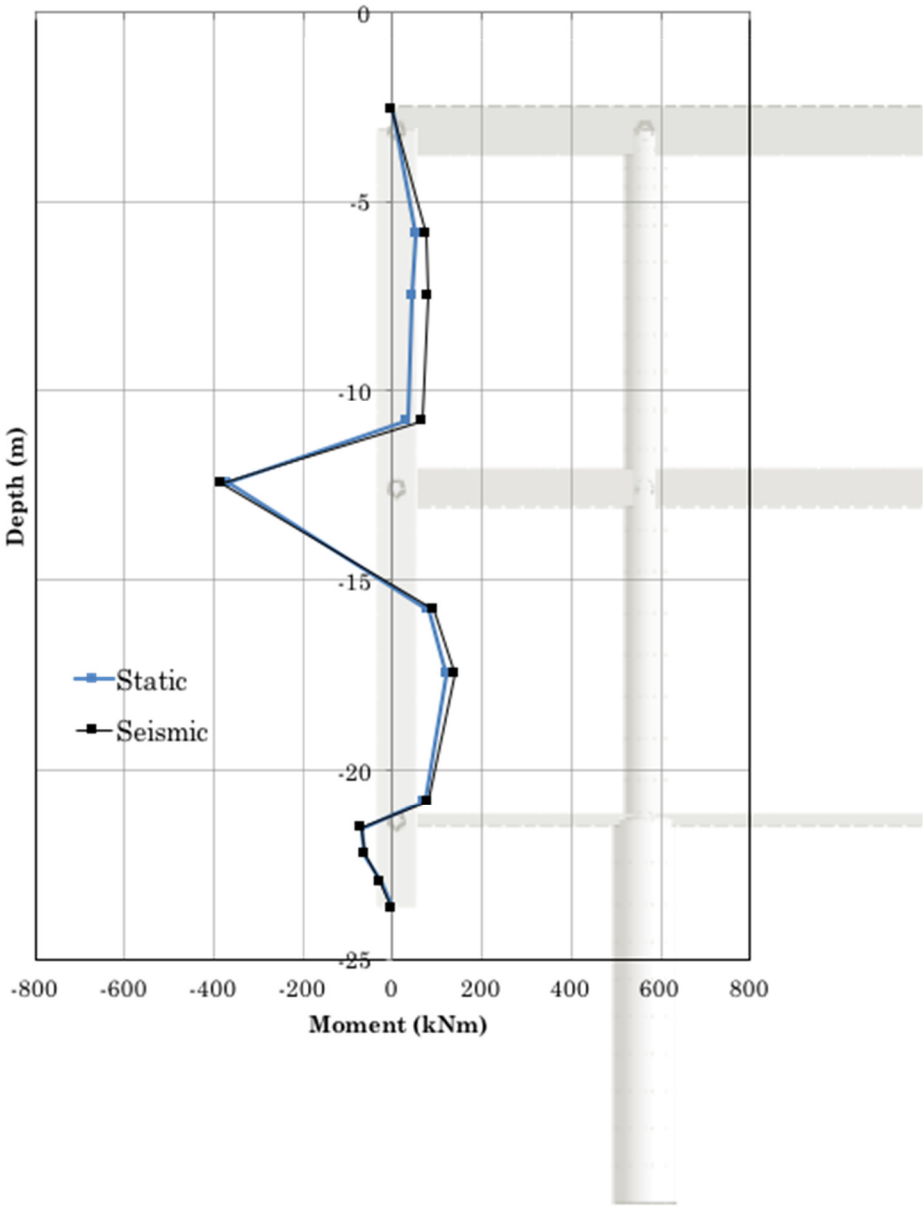

Figure 122: Non-linear analysis: bending moment acting on the concrete retaining walls - profile characterized by *Vs* = 600 m/s, input: FRIULI

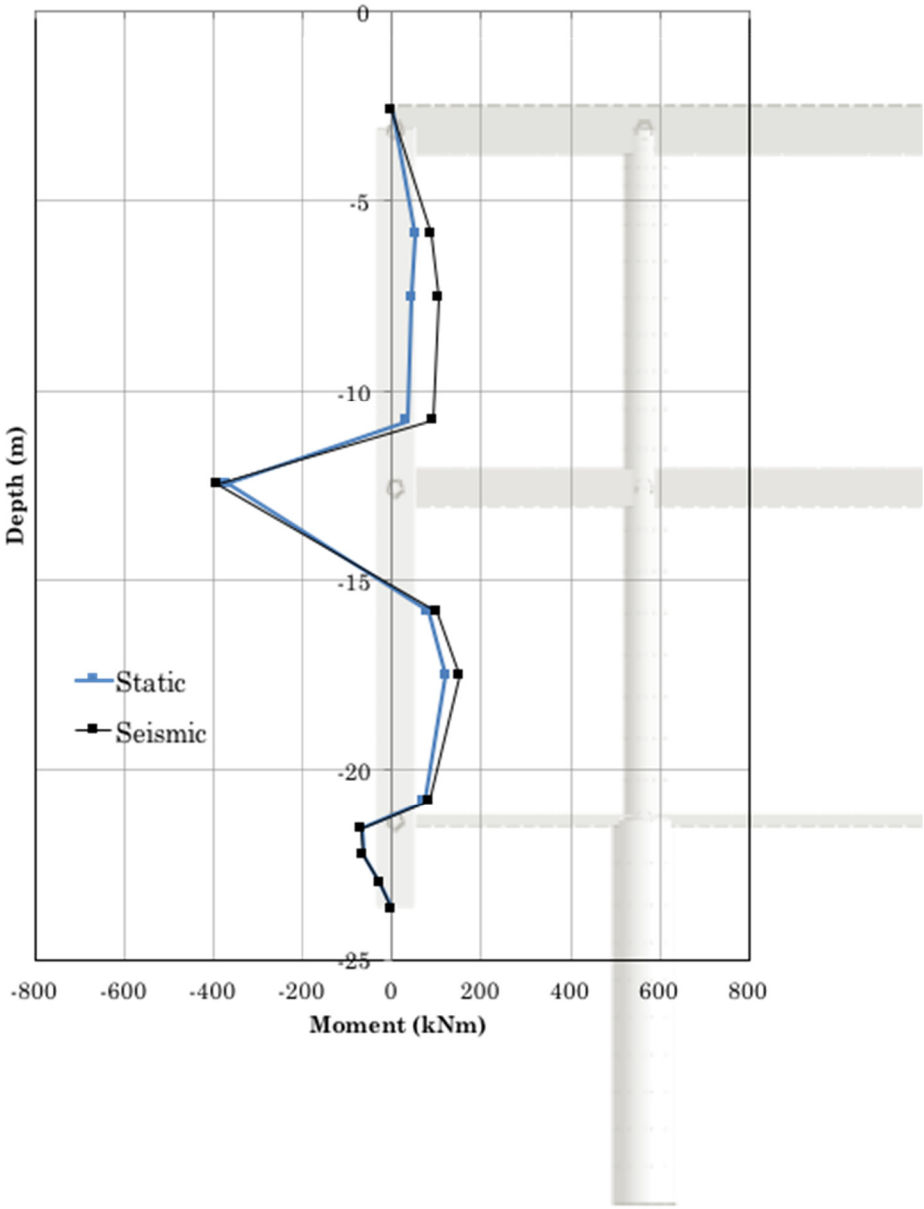

Figure 123: Non-linear analysis: bending moment acting on the concrete retaining walls - profile characterized by *Vs* = 600 m/s, input: GREECE

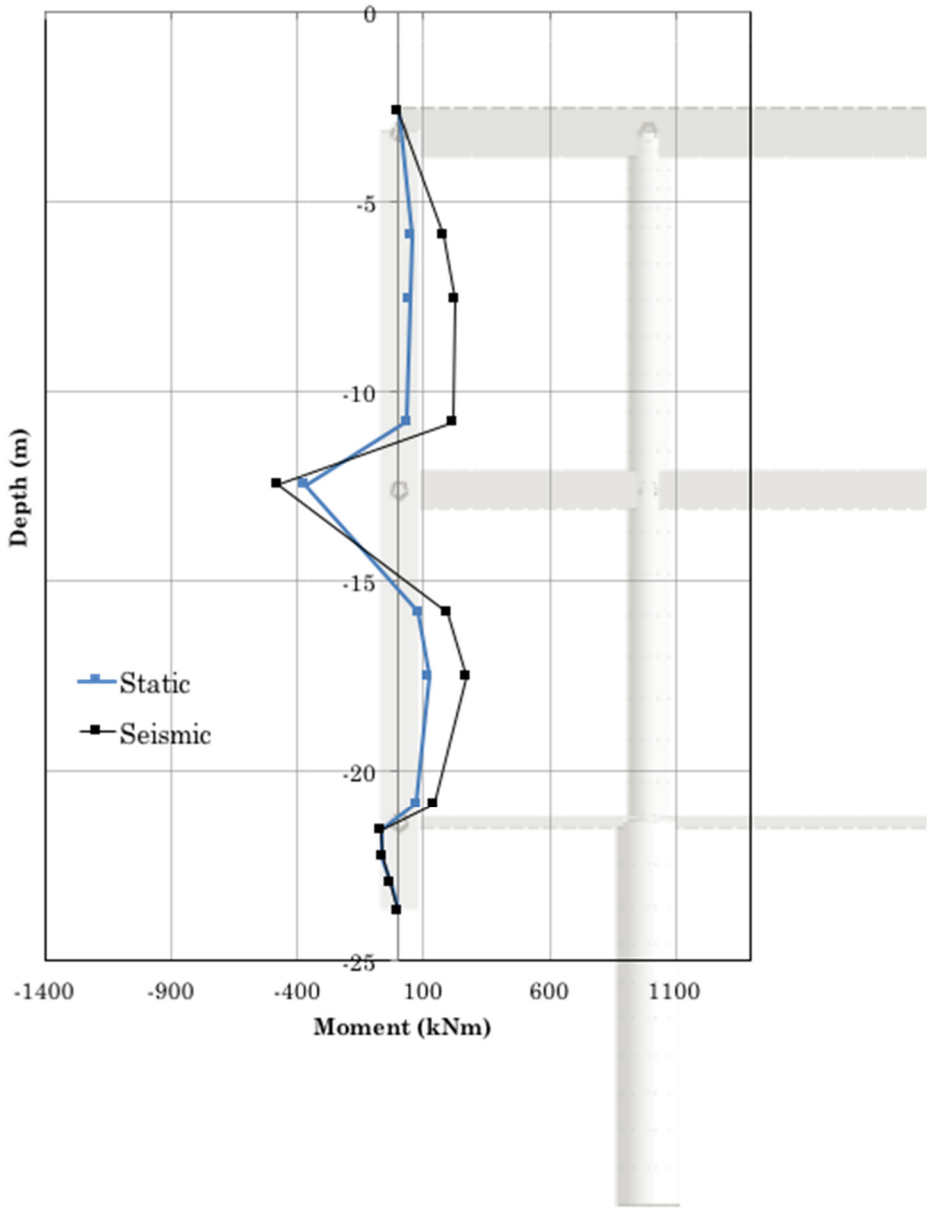

Figure 124: Non-linear analysis: bending moment acting on the concrete retaining walls - profile characterized by *Vs* = 600 m/s, input: LIMA

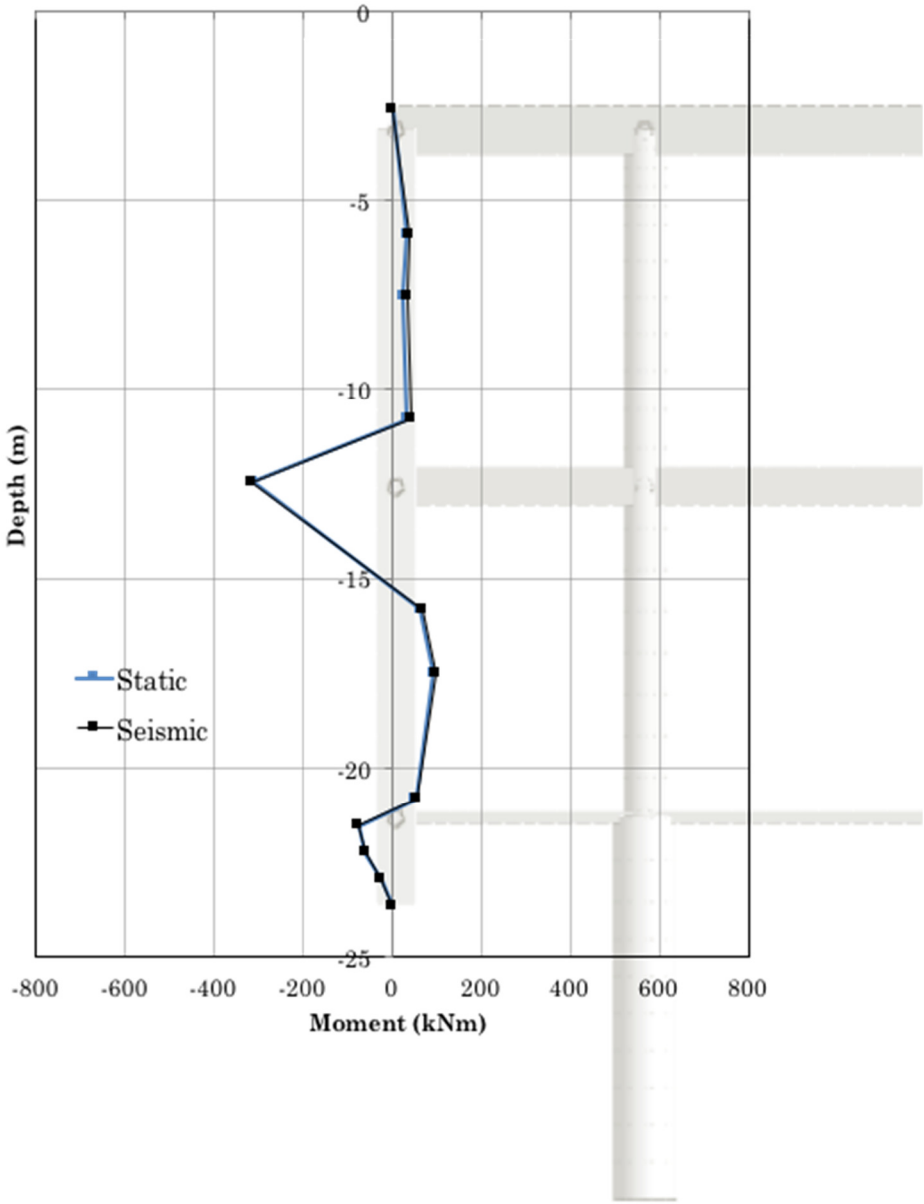

Figure 125: Non-linear analysis: bending moment acting on the concrete retaining walls - profile characterized by *Vs* = 750 m/s, input: MONTENEGRO

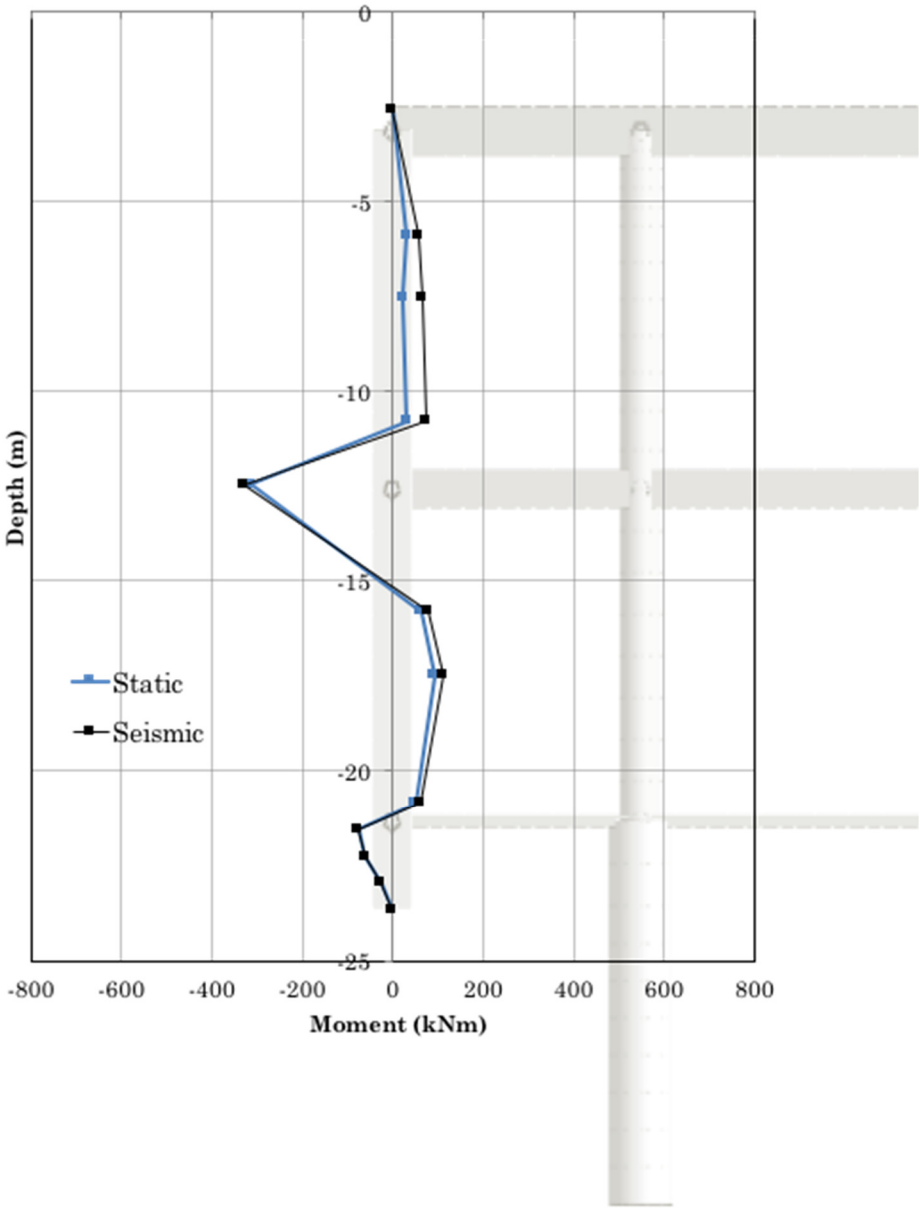

Figure 126: Non-linear analysis: bending moment acting on the concrete retaining walls - profile characterized by *Vs* = 750 m/s, input: AMATRICE

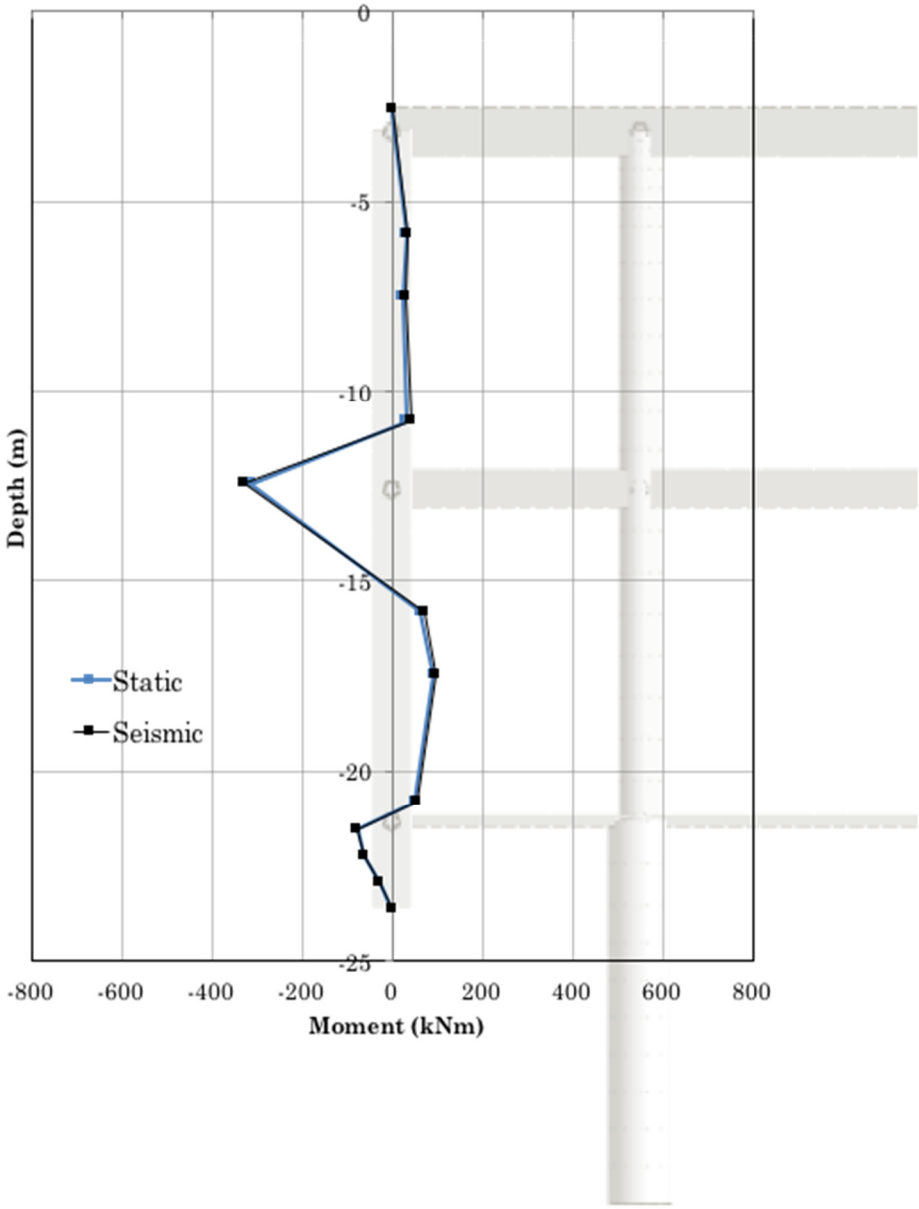

Figure 127: Non-linear analysis: bending moment acting on the concrete retaining walls - profile characterized by *Vs* = 750 m/s, input: L'AQUILA

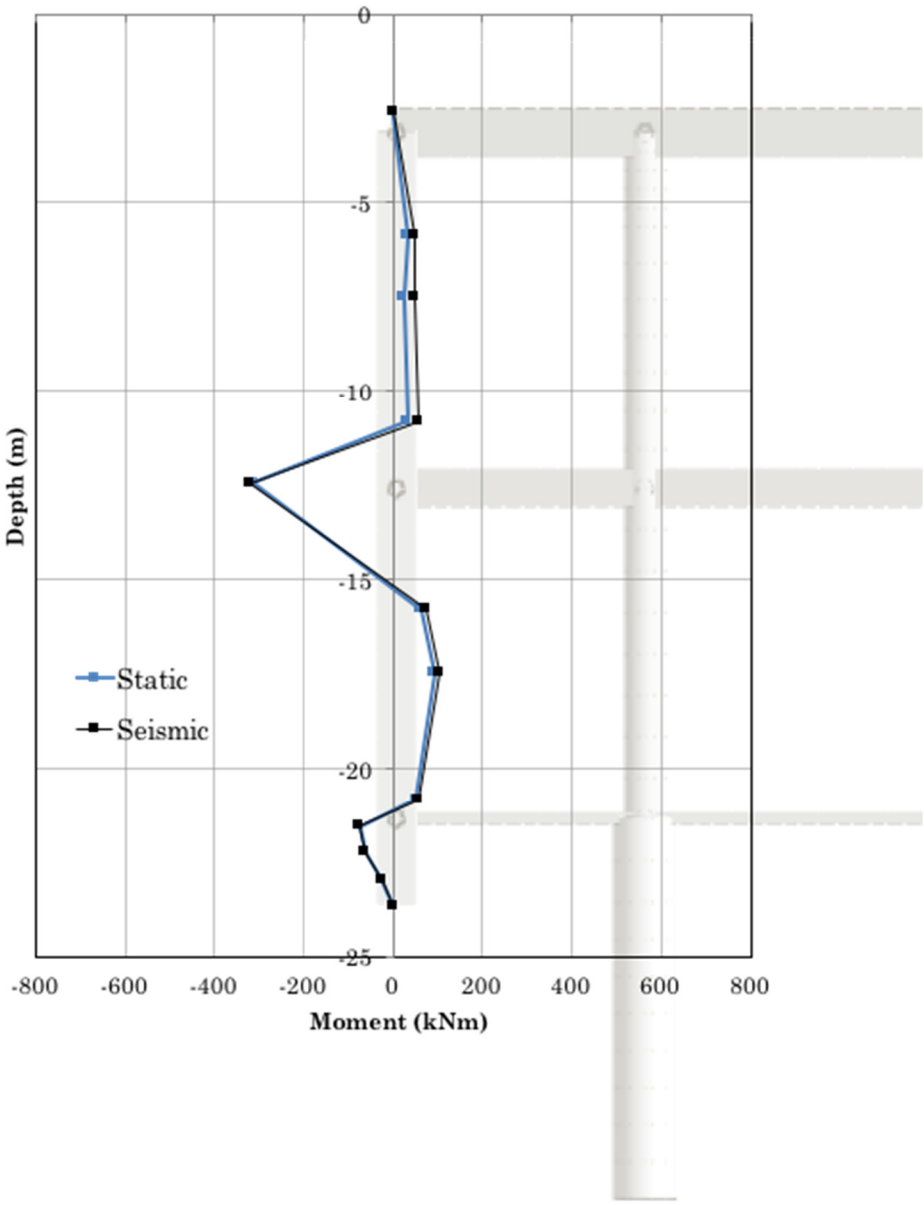

Figure 128: Non-linear analysis: bending moment acting on the concrete retaining walls - profile characterized by *Vs* = 750 m/s, input: FRIULI

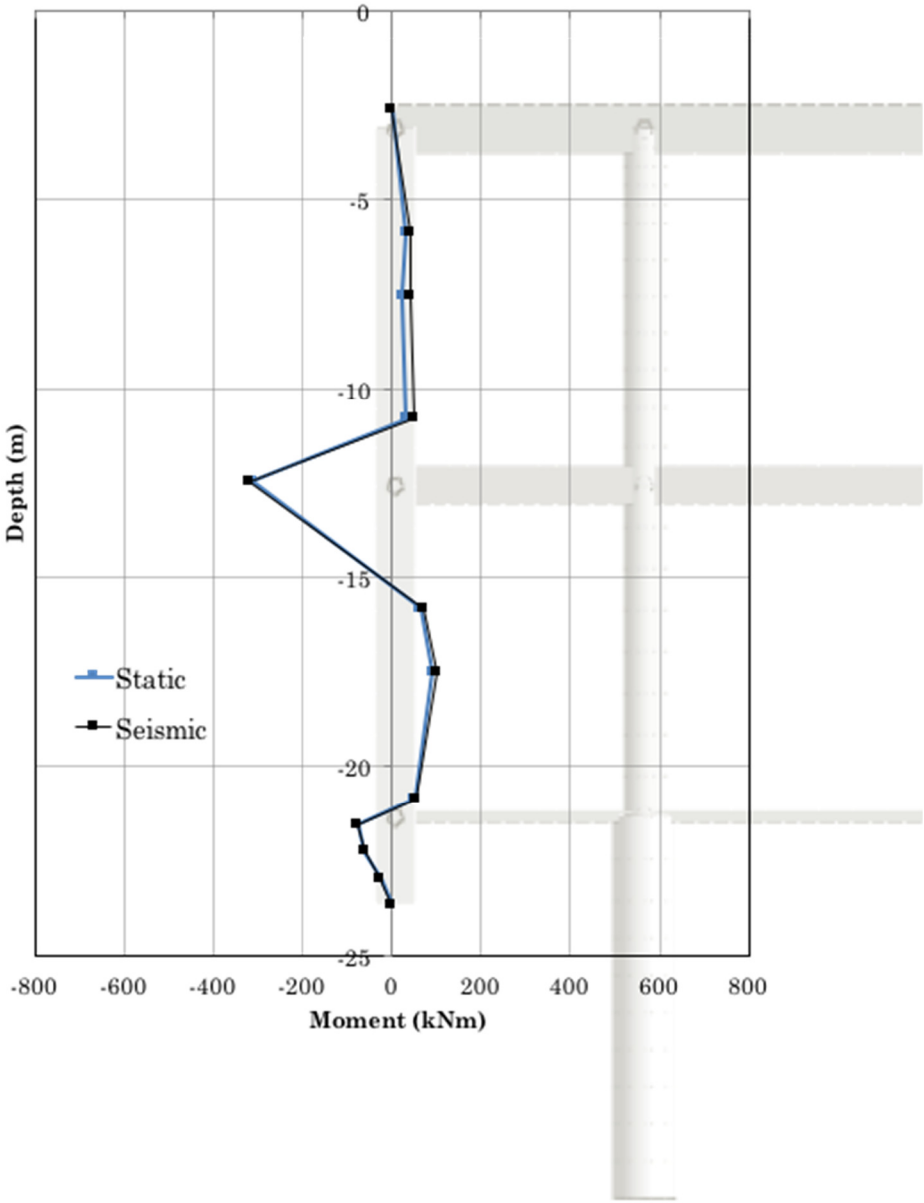

Figure 129: Non-linear analysis: bending moment acting on the concrete retaining walls - profile characterized by *Vs* = 750 m/s, input: GREECE

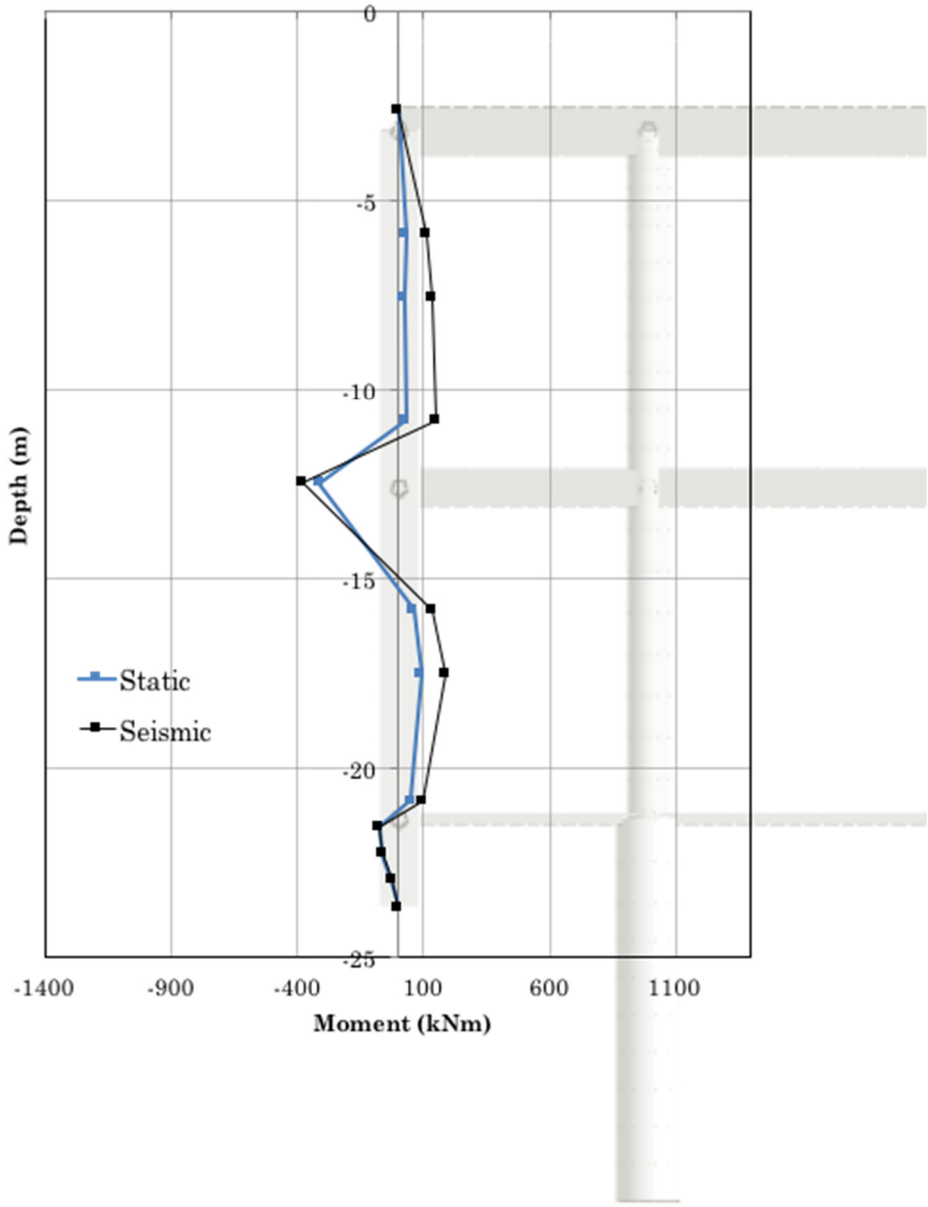

Figure 130: Non-linear analysis: bending moment acting on the concrete retaining walls - profile characterized by *Vs* = 750 m/s, input: LIMA

In this case the maximum increment of bending moment due to the seismic action occurs in the profile characterized by low values of shear waves velocity (V_s = 360 m/s and 450 m/s). The maximum increase of bending moment is equal to 125 kNm always in the case of Montenegro earthquake.
Table 14 and Figures 131, 132, 133, 134, 135 and 136 show a summary of the results, in terms of bending moment acting on the section in correspondence of the central slab, obtained for the different four soil profiles.

Table 14: Bending moment acting on the section in correspondence of the central slab

MONTENEGRO			
Profile	**Moment**		
Vs	**Static**	**Seismic**	Δ
[m/s]	[kNm]	[kNm]	[%]
360	518	643	**24**
450	451	490	**9**
600	370	382	**3**
750	312	315	**1**

GREECE			
Profile	**Moment**		
Vs	**Static**	**Seismic**	Δ
[m/s]	[kNm]	[kNm]	[%]
360	518	616	**19**
450	451	541	**20**
600	370	390	**6**
750	312	318	**2**

AMATRICE			
Profile	**Moment**		
Vs	**Static**	**Seismic**	Δ
[m/s]	[kNm]	[kNm]	[%]
360	518	571	**10**
450	451	499	**11**
600	370	393	**6**
750	312	327	**5**

L'AQUILA			
Profile	**Moment**		
Vs	**Static**	**Seismic**	Δ
[m/s]	[kNm]	[kNm]	[%]
360	518	574	**11**
450	451	481	**7**
600	370	384	**4**
750	312	327	**5**

FRIULI			
Profile	**Moment**		
Vs	**Static**	**Seismic**	Δ
[m/s]	[kNm]	[kNm]	[%]
360	518	554	**7**
450	451	475	**5**
600	370	382	**3**
750	312	321	**3**

LIMA			
Profile	**Moment**		
Vs	**Static**	**Seismic**	Δ
[m/s]	[kNm]	[kNm]	[%]
360	518	875	**69**
450	451	769	**71**
600	370	477	**29**
750	312	381	**22**

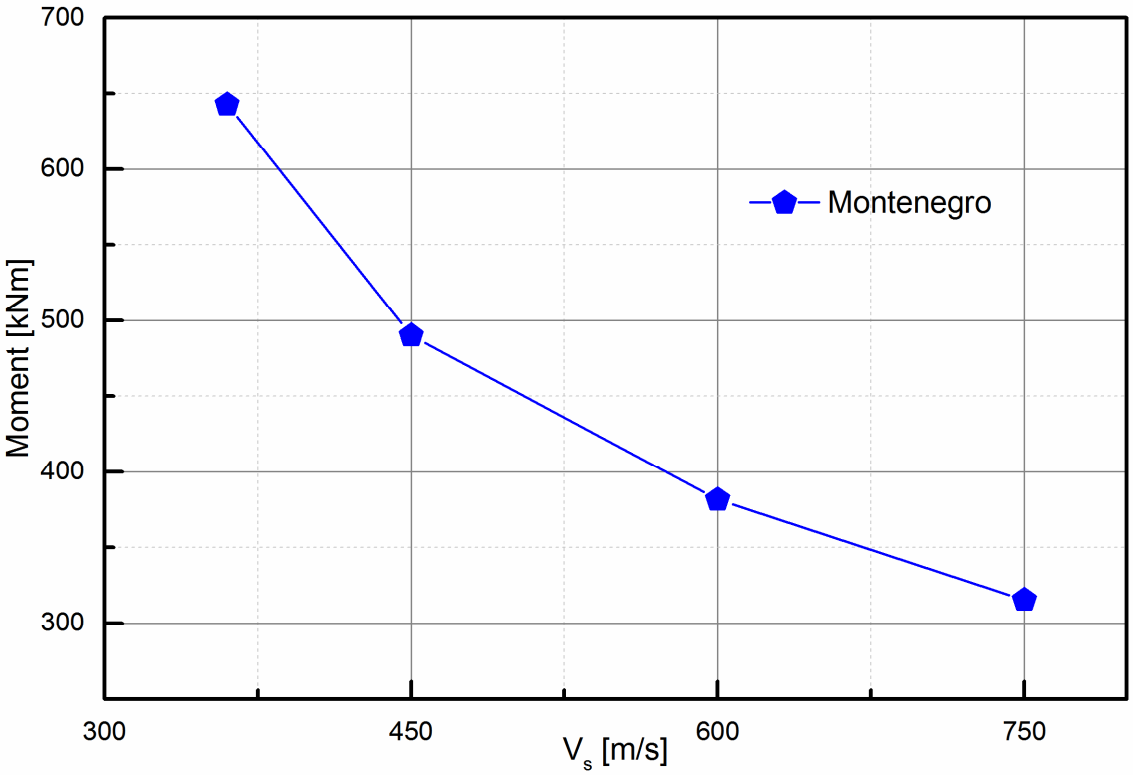

Figure 131: Non-linear analysis: maximum bending moment acting on the section in correspondence to the central slab

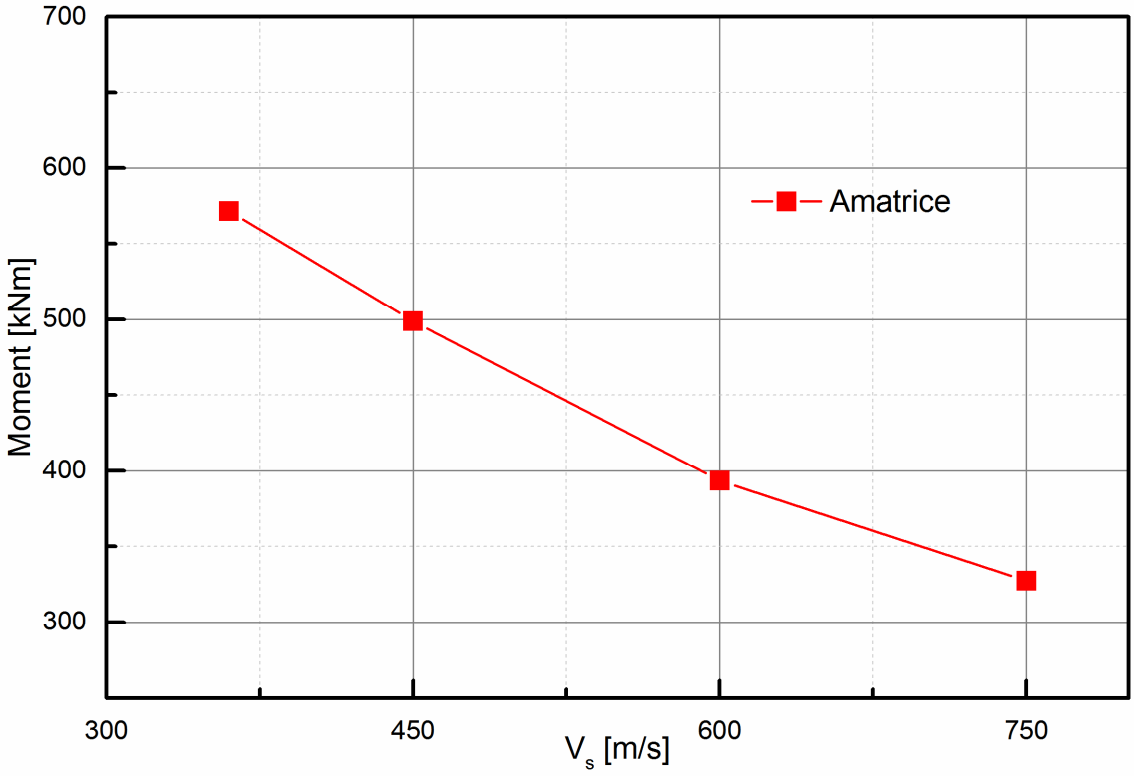

Figure 132: Non-linear analysis: maximum bending moment acting on the section in correspondence to the central slab

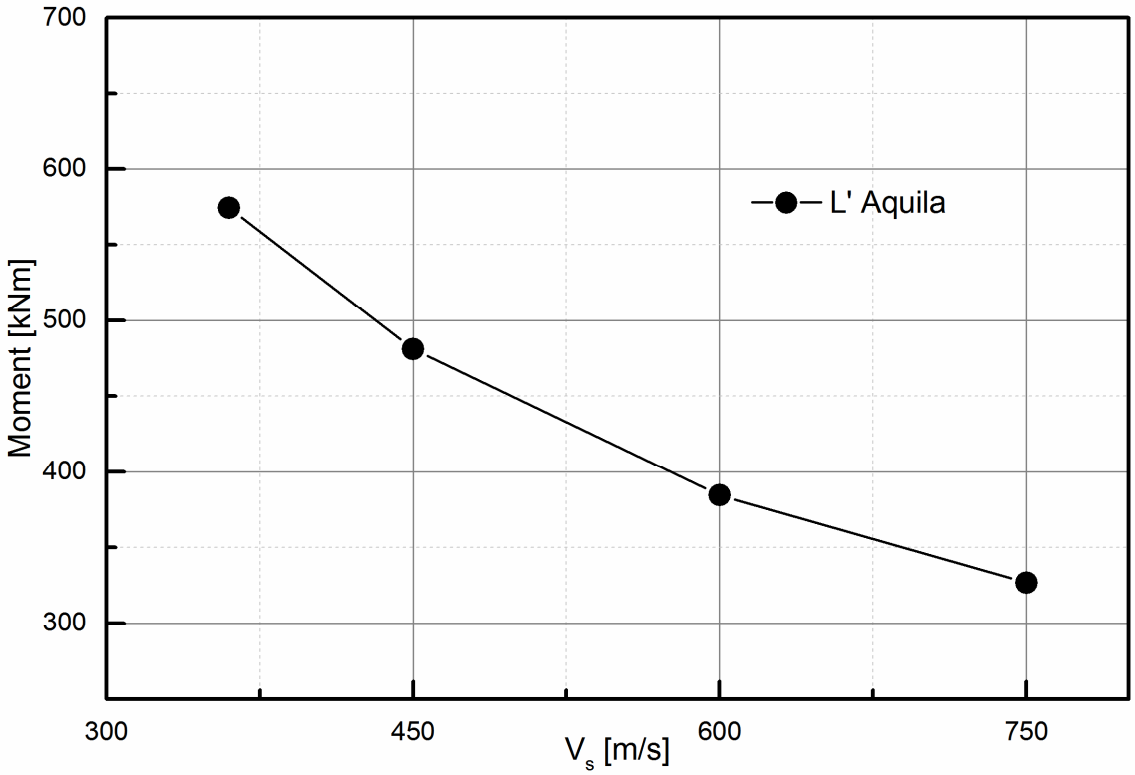

Figure 133: Non-linear analysis: maximum bending moment acting on the section in correspondence to the central slab

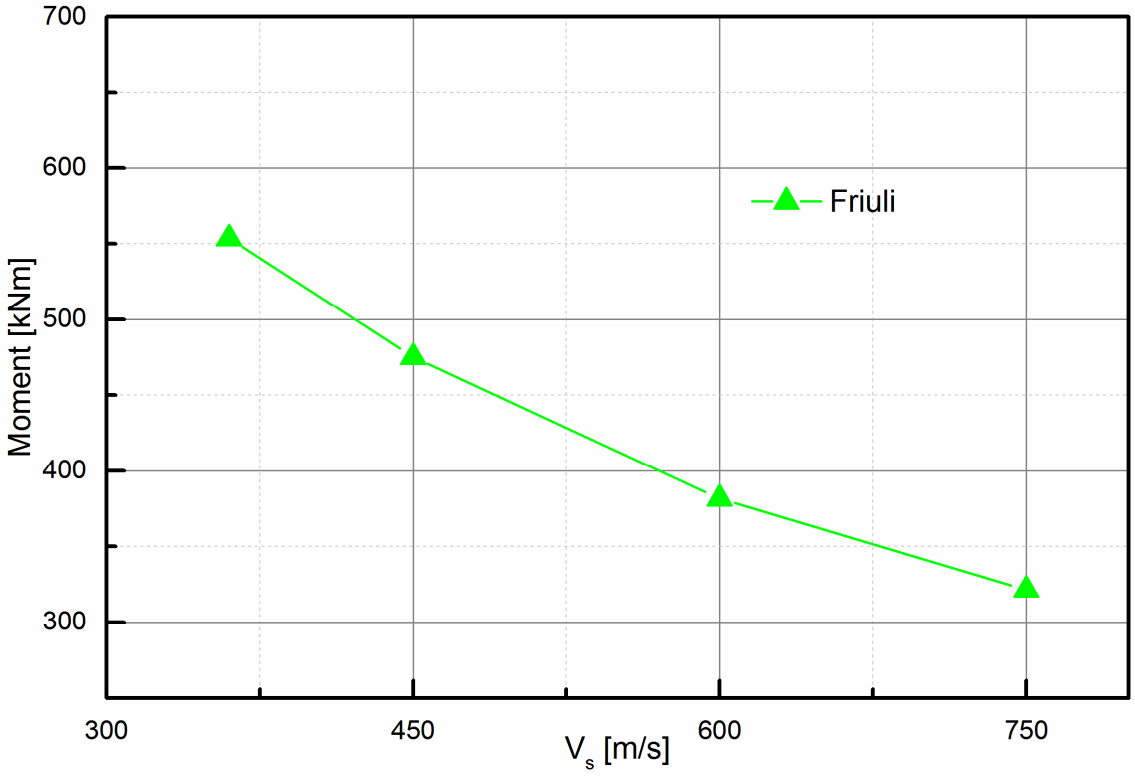

Figure 134: Non-linear analysis: maximum bending moment acting on the section in correspondence to the central slab

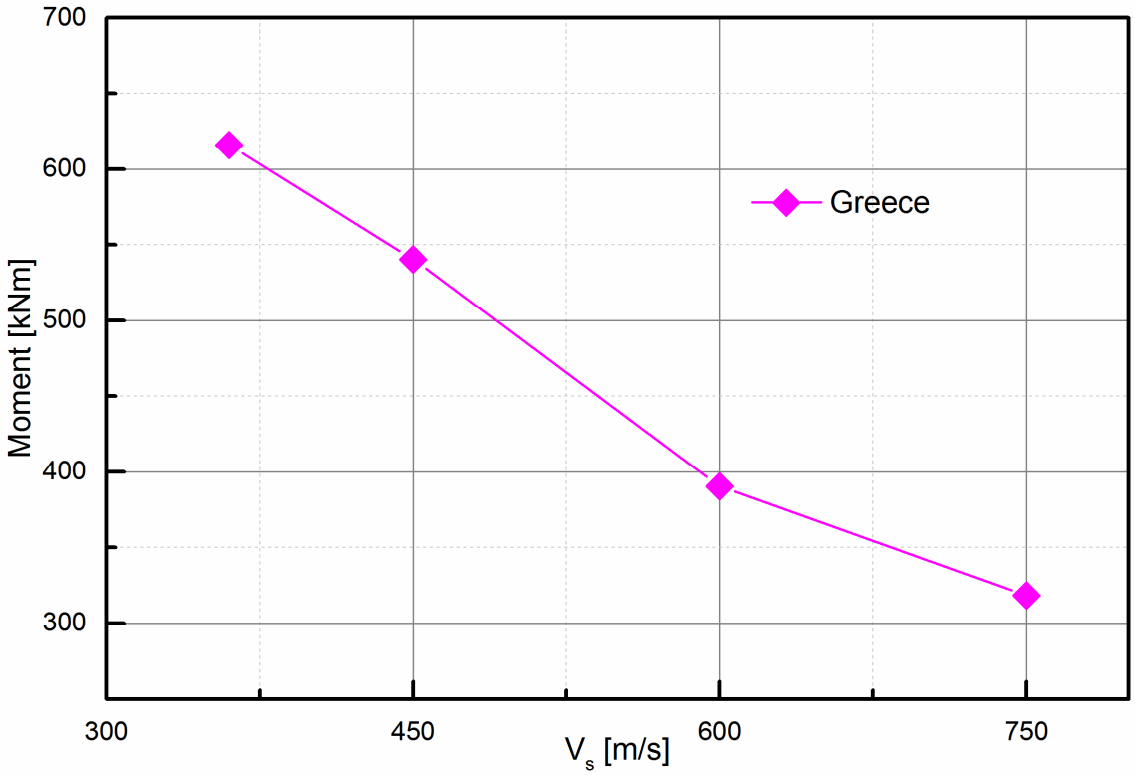

Figure 135: Non-linear analysis: maximum bending moment acting on the section in correspondence to the central slab

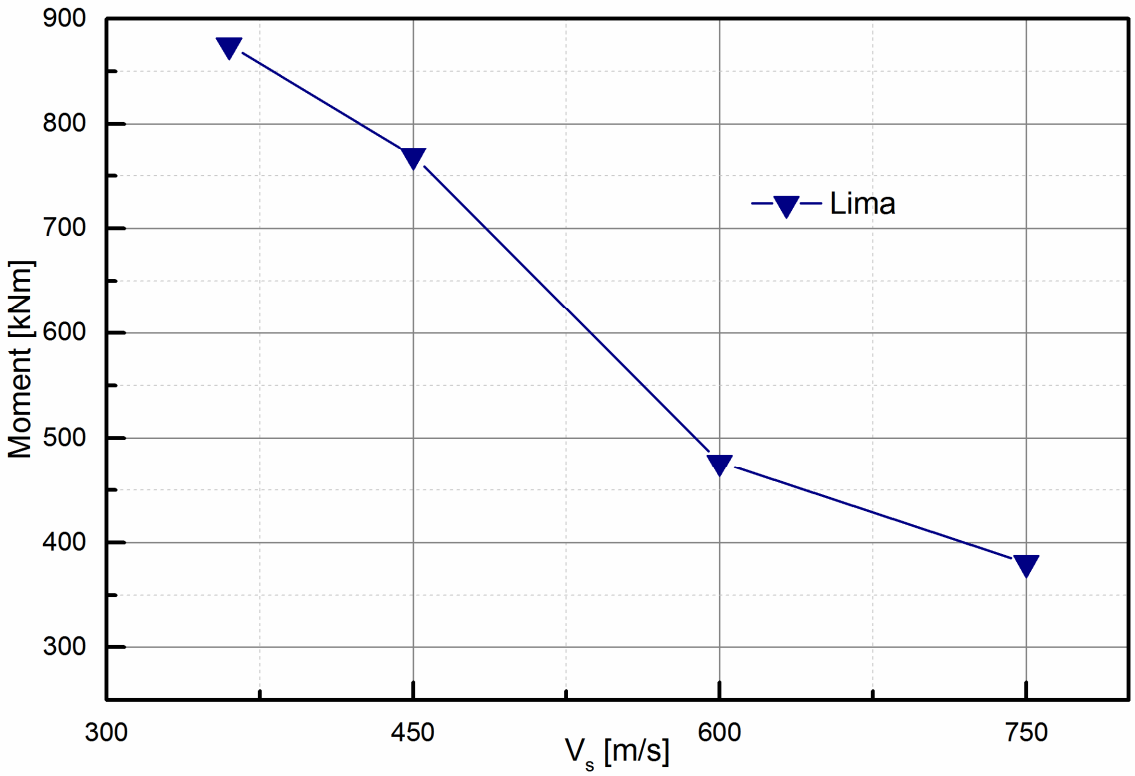

Figure 136: Non-linear analysis: maximum bending moment acting on the section in correspondence to the central slab

The comparison of the results of the two different methods showed that the relative displacements obtained by the non-linear analysis are greater than the relative displacements obtained by the equivalent linear analysis. Consequently, also the increase of the bending moment acting on the retaining walls follows this trend (Table 15).

Table 15: Comparison of the results in terms of bending moment acting on the section in correspondence of the central slab

MONTENEGRO			
Profile	**Moment**		
Vs	**EL**	**NL**	Δ
[m/s]	[kNm]	[kNm]	[%]
360	628	643	**2**
450	472	490	**4**
600	376	382	**2**
750	315	315	**0**

GREECE			
Profile	**Moment**		
Vs	**EL**	**NL**	Δ
[m/s]	[kNm]	[kNm]	[%]
360	601	616	**2**
450	532	541	**2**
600	379	390	**3**
750	315	318	**1**

AMATRICE			
Profile	**Moment**		
Vs	**EL**	**NL**	Δ
[m/s]	[kNm]	[kNm]	[%]
360	557	571	**3**
450	484	499	**3**
600	385	393	**2**
750	318	327	**3**

L'AQUILA			
Profile	**Moment**		
Vs	**EL**	**NL**	Δ
[m/s]	[kNm]	[kNm]	[%]
360	562	574	**2**
450	475	481	**1**
600	376	384	**2**
750	318	327	**3**

FRIULI			
Profile	**Moment**		
Vs	**EL**	**NL**	Δ
[m/s]	[kNm]	[kNm]	[%]
360	542	554	**2**
450	466	475	**2**
600	376	382	**2**
750	318	321	**1**

LIMA			
Profile	**Moment**		
Vs	**EL**	**NL**	Δ
[m/s]	[kNm]	[kNm]	[%]
360	619	875	**41**
450	520	769	**48**
600	387	477	**23**
750	315	381	**21**

The results summarized in Table 15 show that the difference Δ of the values of the bending moment acting on the section in correspondence to the central slab obtained by non-linear analysis, NL, and that obtained by equivalent linear analysis, EL, referred to EL, lies between 2% and 4% for all the natural accelerograms. This limited value is due to the incidence of the value of the moment obtained under static conditions on the value of the final moment compared to the increment due to the seismic action.
The same situation does not accur for the syntethic accelerogram (Lima) where the value of Δ is greater than 40% for the soil profiles characterized by V_S = 360 m/s and 450 m/s and almost 20% for the soil profiles characterized by V_S = 600 m/s and 750 m/s.

3.6. Coupled Approach

The coupled approach is performed through one Finite Difference Model (FDM), implemented by FLAC 7.0 (Itasca, 2007) software, representing both structure and soil (Figure 137). The model characteristics are described in the previous paragraph 3.3.
The evaluation of the seismic behavior of the underground structure described above is carried out considering static and dynamic loads.
As mentioned before, the FDM is characterized by plane strain element while for the structure linear beam elements are used.
In the static phase, the boundary conditions are the following (Zucca et al., 2017):

- vertical supports in the base nodes to restrain the vertical displacements;
- horizontal supports in the lateral nodes of the mesh to permit vertical soil settlements,

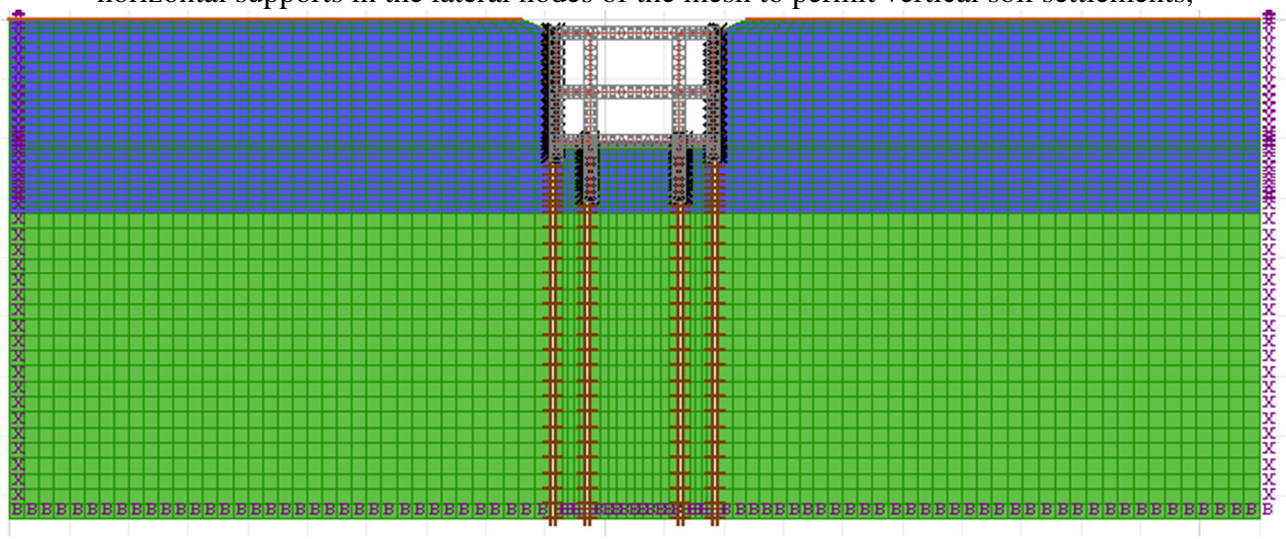

Figure 137: Finite Difference Model computation grid

while the loads considered are:

- dead load on the on the sides of the station equal to 50 kN/m^2 due to the presence of existing buildings and streets;
- dead load in correspondence to the station equal to 20 kN/m^2 due to the presence of the streets;
- self-weight of the structure and the soil.

The static condition is determined by performing a construction stage analysis, accounting for all the main phases involved in the construction of the structure. The sequence of the construction phases is summarized as follow:

- the realization of an excavation, characterized by a provisional slope 1H : 5V, to create a first entrance ramp;
- the realization of the vertical structural elements of the underground structure;
- the realization of the top cover slab made from reinforced concrete and 1.2 m thick;
- the execution of a second excavation until depth 12.60 m;
- the realization of the intermediate slab made from reinforced concrete and 0.9 m thick;
- the execution of a third excavation until depth 20.66 m;
- the realization of the concrete bottom slab 0.25 m thick;
- the road surface restoration.

The dynamic analysis is performed, after the final step of the construction stage, by using fully non-linear dynamic analysis in time domain considering the six different seismic inputs.
Figures from 138 to 161 show the results in terms of bending moment acting on the concrete retaining walls where the initial moment due to the static loads, the value of the bending moment when occurs its maximum value in the section in correspondence to the central slab during the seismic action and the bending moment at the end of the seismic event (residual moment) are reported.
During the main shaking stage, the loads distribution on the retaining walls appears slightly asymmetric, while at the end to the seismic event (residual moment) it tends to balance. This consideration is valid only for the five natural accelerograms because in the case of Lima seismic input the loads distribution on the retaining walls remains asymmetric also at the end of the seismic event.
Taking as a reference the static state, the increment due to the seismic action is reported for all the signals considering the section in correspondence to the central slab (Table 16).

Table 16: Bending moment acting on the section in correspondence of the central slab (maximum value of the two retaining walls)

MONTENEGRO			
Profile	**Moment**		
Vs	**Static**	**Seismic**	Δ
[m/s]	[kNm]	[kNm]	[%]
360	518	665	**28**
450	451	600	**33**
600	370	518	**40**
750	312	458	**47**

GREECE			
Profile	**Moment**		
Vs	**Static**	**Seismic**	Δ
[m/s]	[kNm]	[kNm]	[%]
360	518	652	**26**
450	451	593	**31**
600	370	513	**37**
750	312	454	**46**

AMATRICE			
Profile	**Moment**		
Vs	**Static**	**Seismic**	Δ
[m/s]	[kNm]	[kNm]	[%]
360	518	647	**25**
450	451	587	**30**
600	370	504	**36**
750	312	447	**43**

L'AQUILA			
Profile	**Moment**		
Vs	**Static**	**Seismic**	Δ
[m/s]	[kNm]	[kNm]	[%]
360	518	659	**27**
450	451	589	**31**
600	370	506	**37**
750	312	451	**45**

FRIULI			
Profile	**Moment**		
Vs	**Static**	**Seismic**	Δ
[m/s]	[kNm]	[kNm]	[%]
360	518	639	**23**
450	451	579	**28**
600	370	500	**35**
750	312	438	**40**

LIMA			
Profile	**Moment**		
Vs	**Static**	**Seismic**	Δ
[m/s]	[kNm]	[kNm]	[%]
360	518	1967	**279**
450	451	1977	**338**
600	370	1890	**411**
750	312	1805	**479**

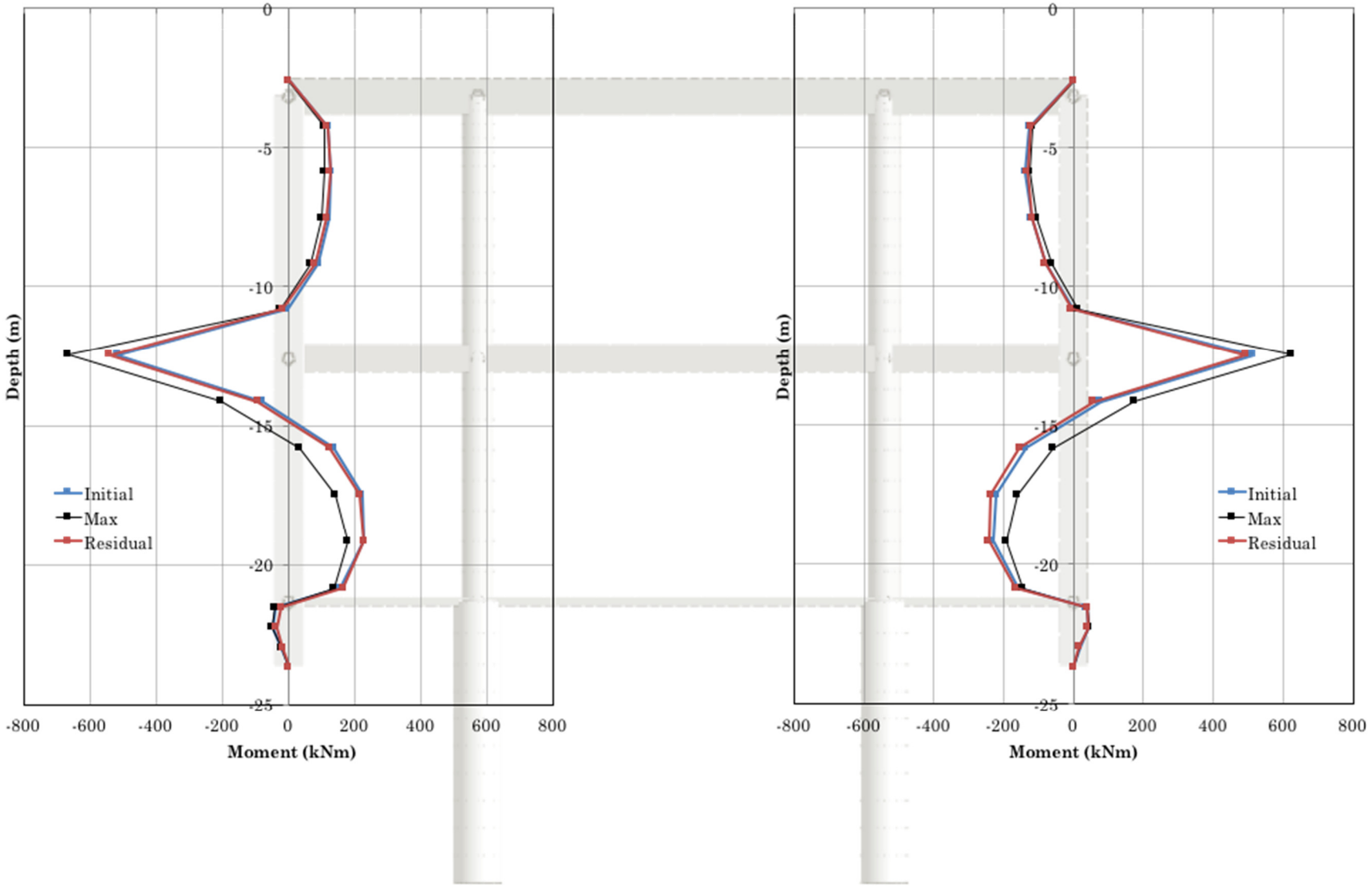

Figure 138: Bending moment acting on the concrete retaining walls - profile characterized by *Vs* = 360 m/s, input: MONTENEGRO

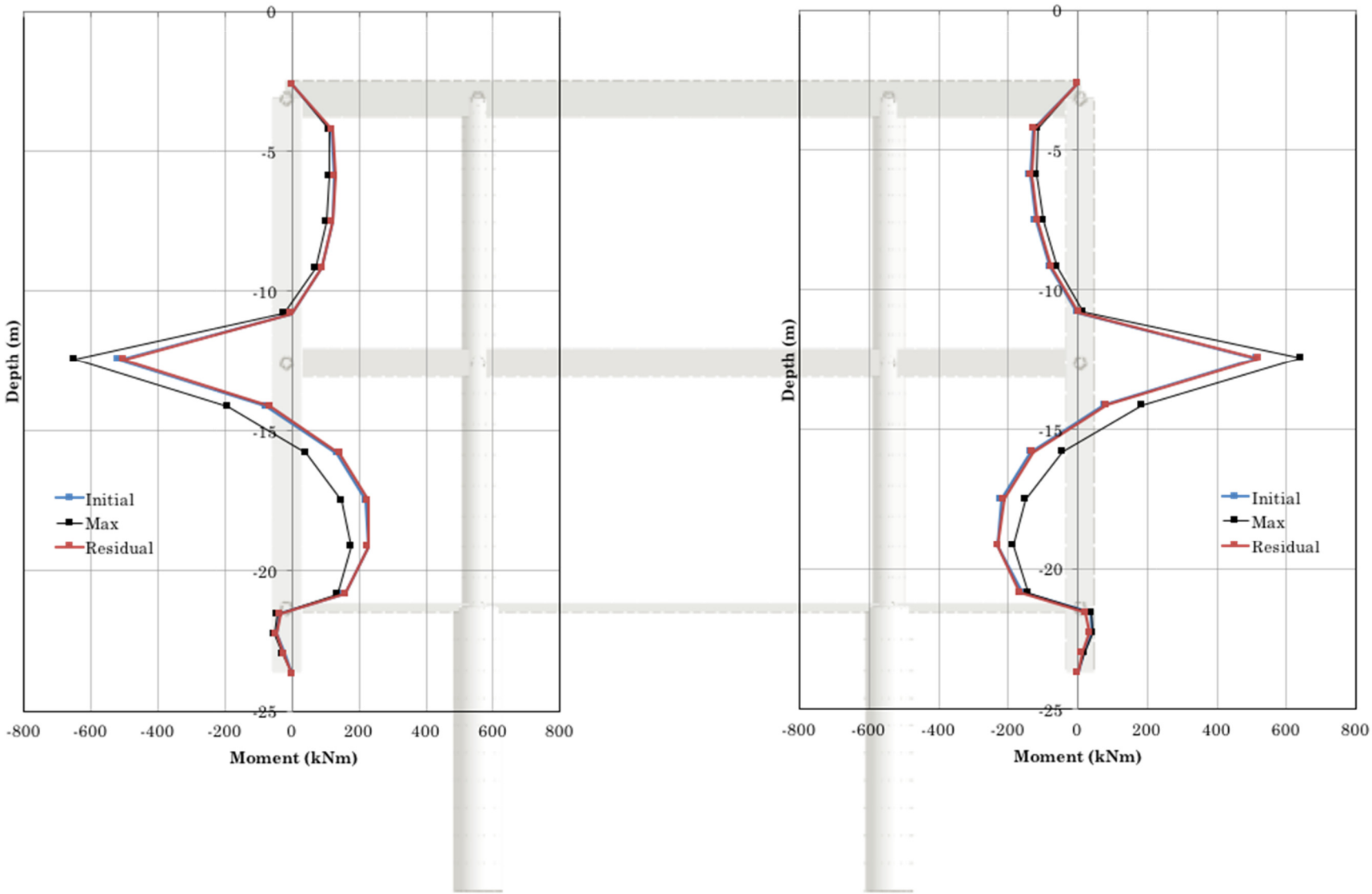

Figure 139: Bending moment acting on the concrete retaining walls - profile characterized by *Vs* = 360 m/s, input: AMATRICE

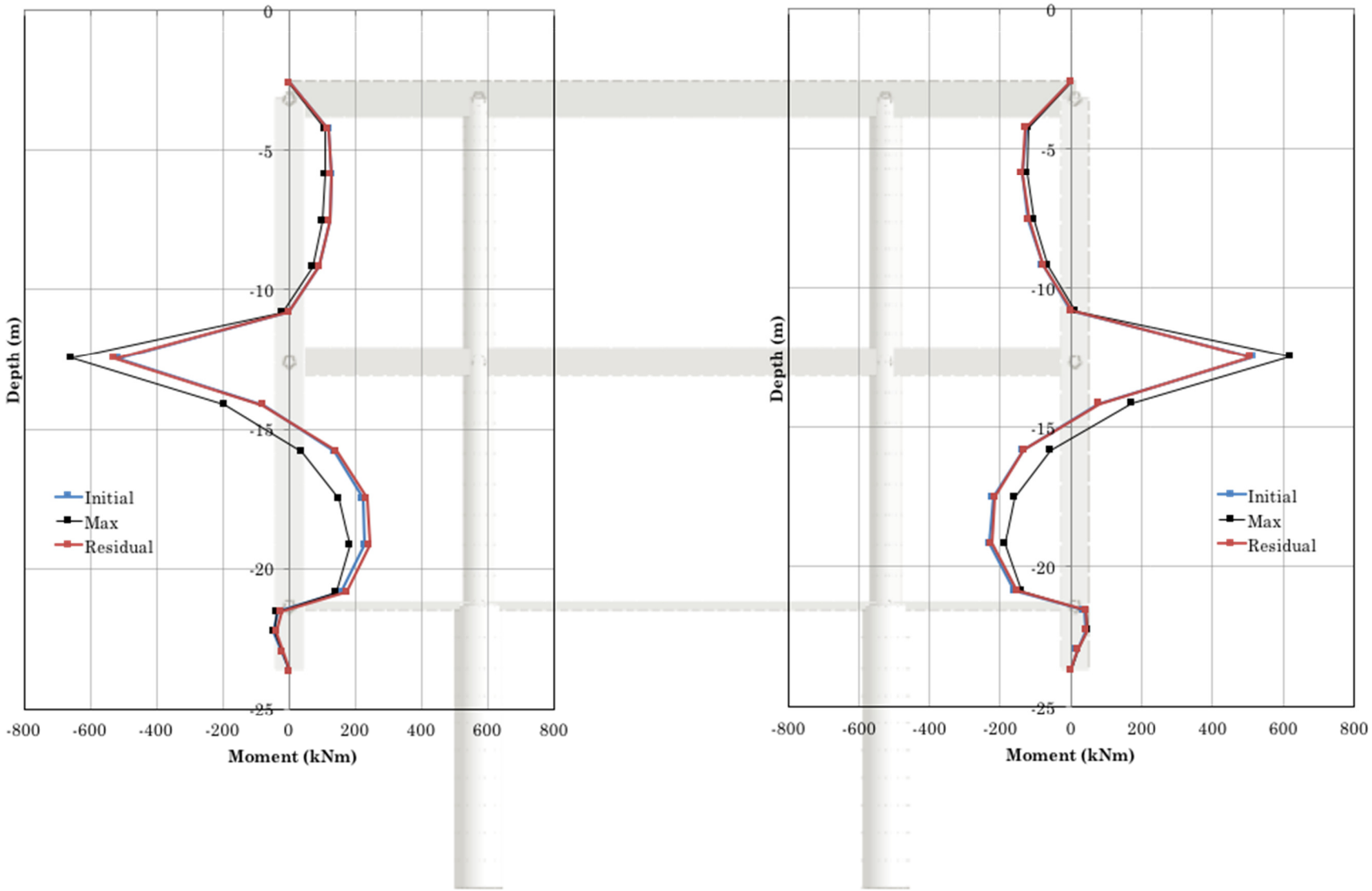

Figure 140: Bending moment acting on the concrete retaining walls - profile characterized by *Vs* = 360 m/s, input: L'AQUILA

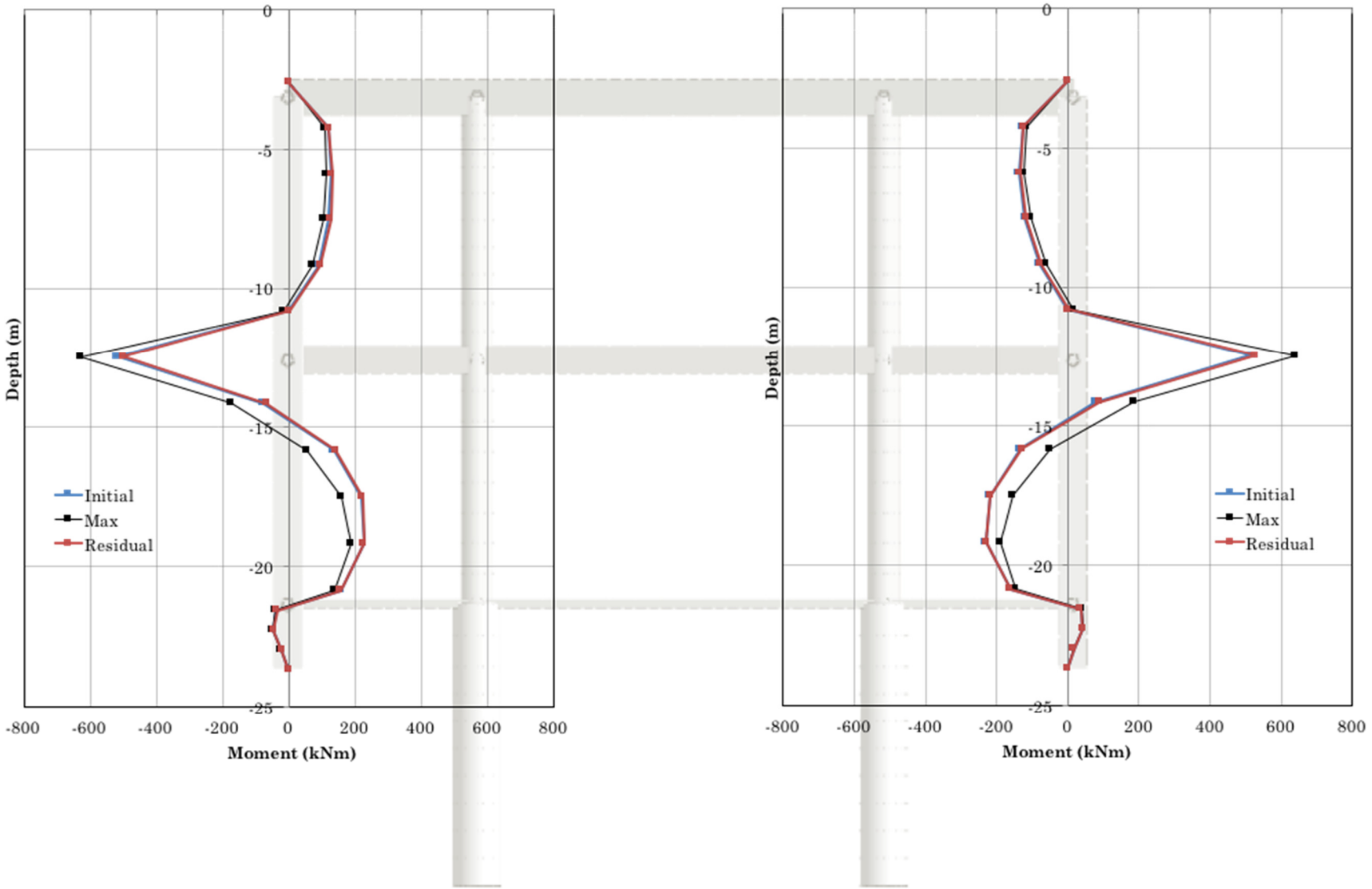

Figure 141: Bending moment acting on the concrete retaining walls - profile characterized by *Vs* = 360 m/s, input: FRIULI

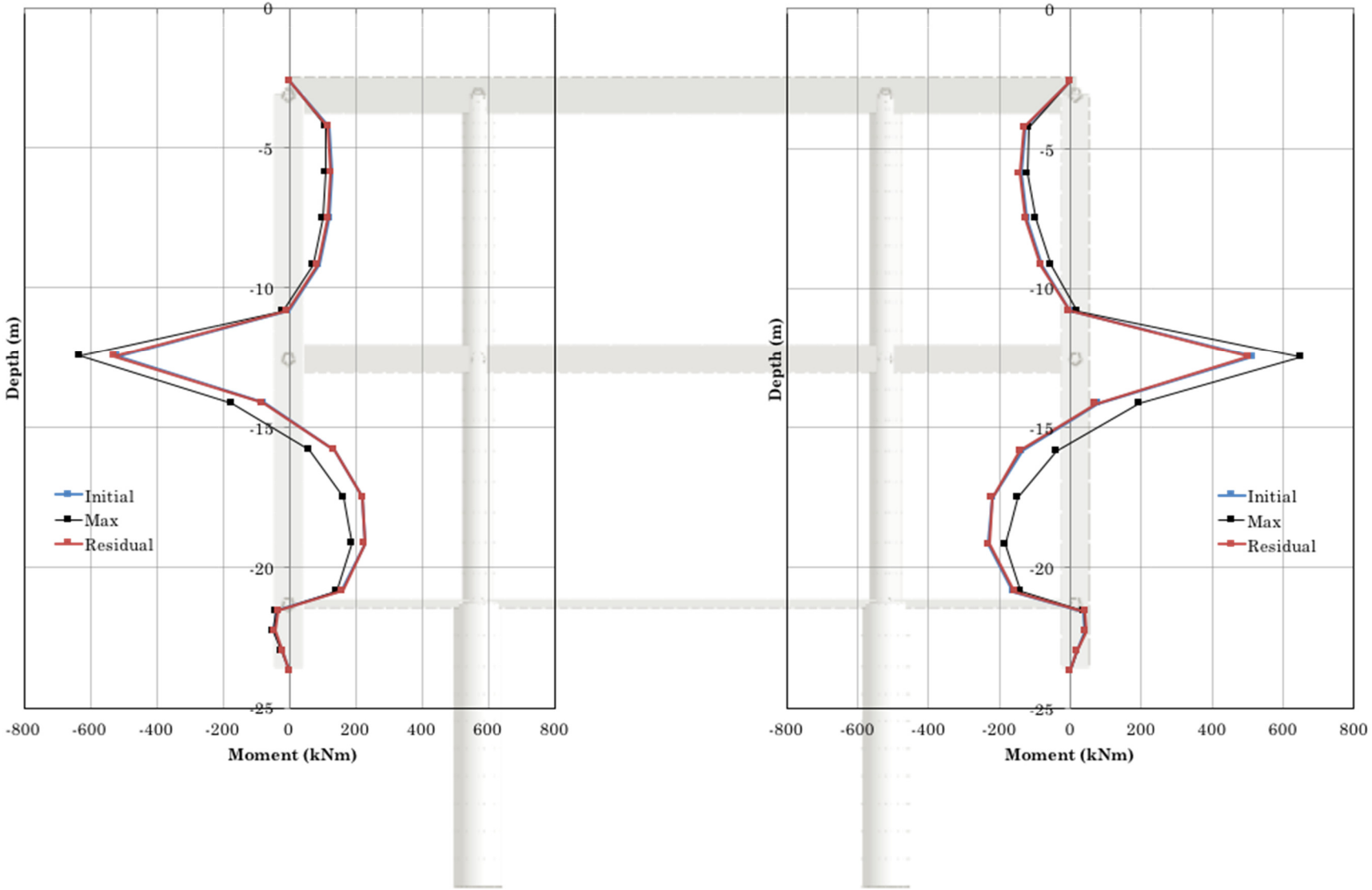

Figure 142: Bending moment acting on the concrete retaining walls - profile characterized by *Vs* = 360 m/s, input: GREECE

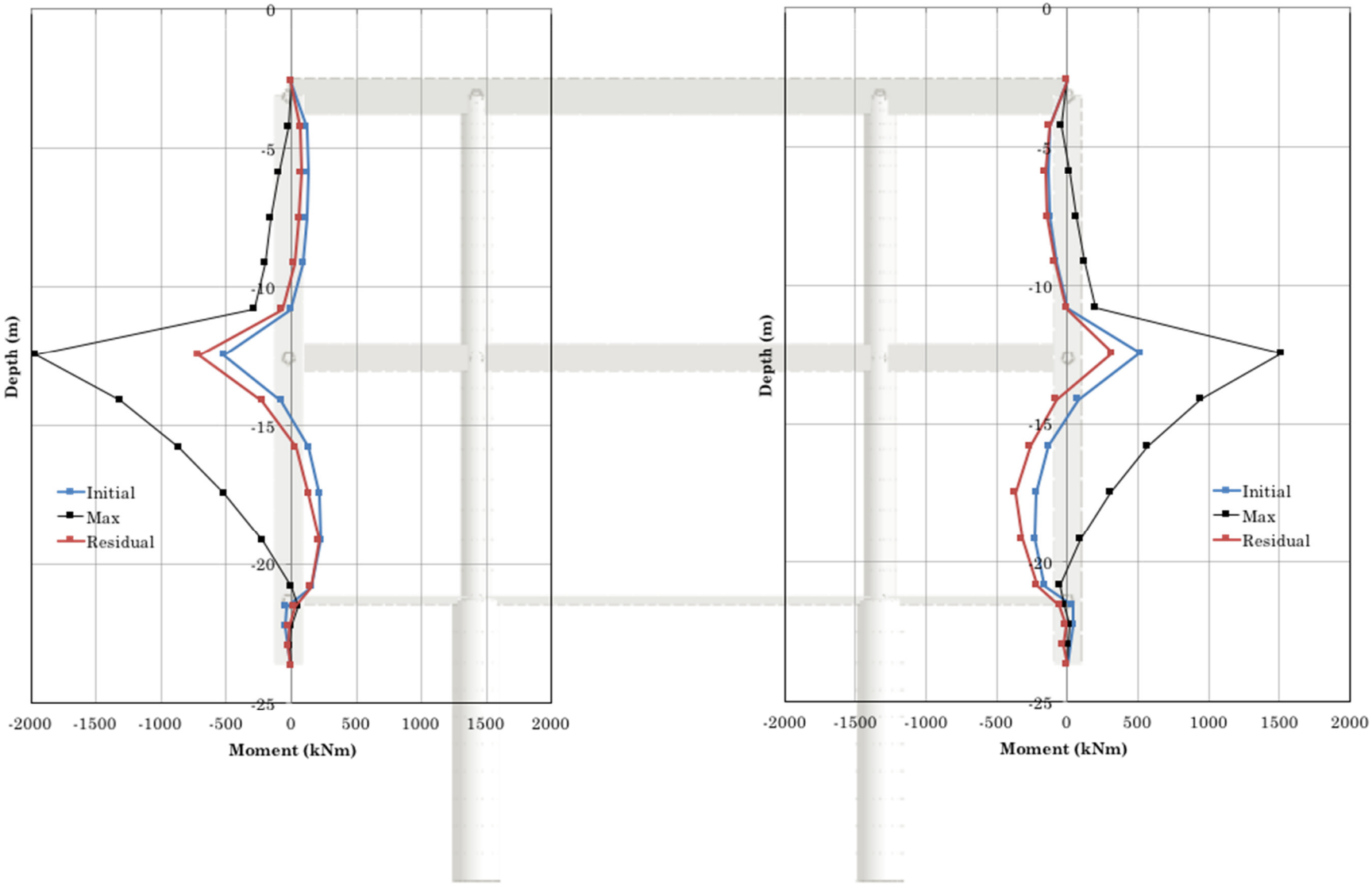

Figure 143: Bending moment acting on the concrete retaining walls - profile characterized by *Vs* = 360 m/s, input: LIMA

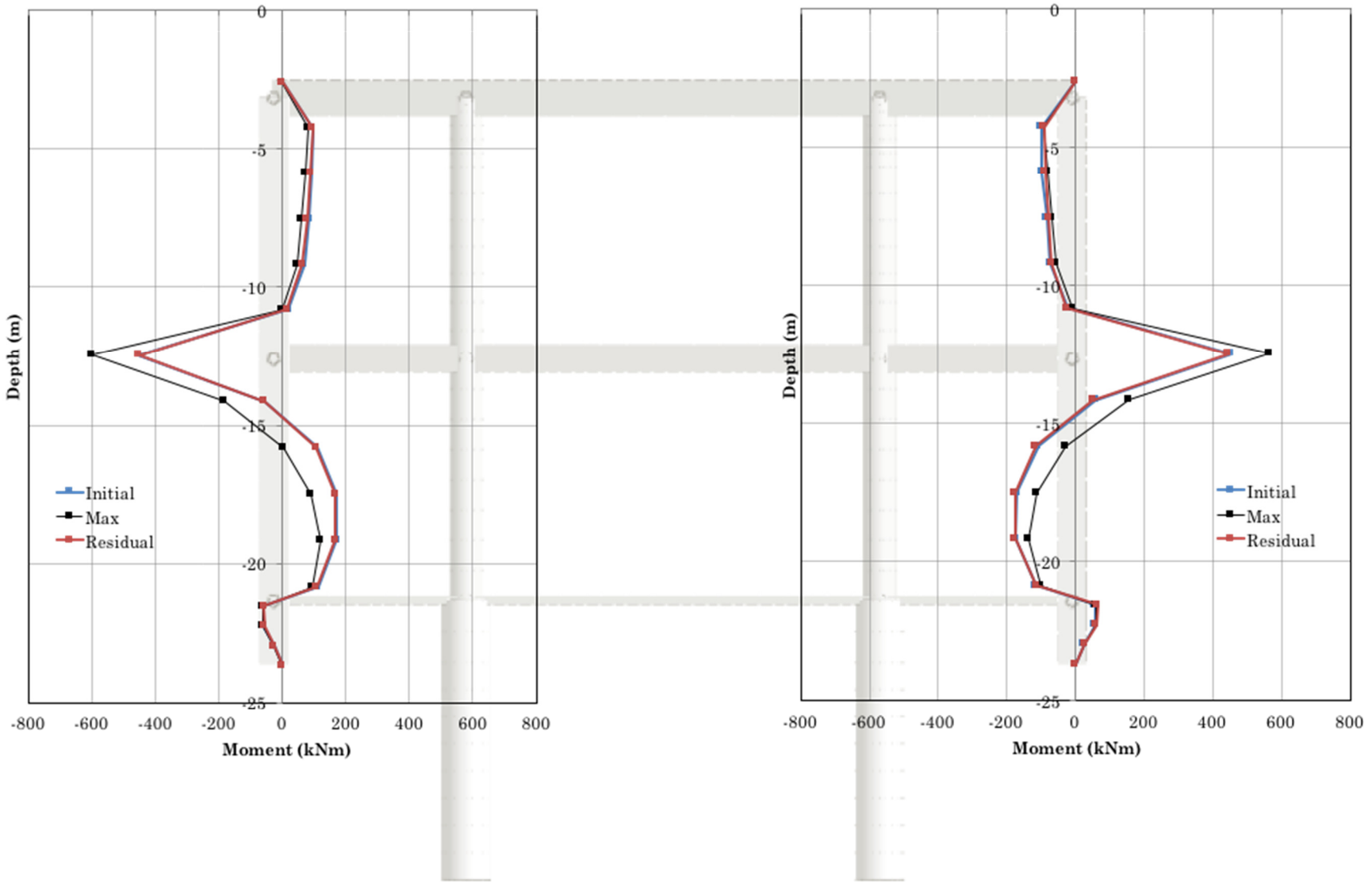

Figure 144: Bending moment acting on the concrete retaining walls - profile characterized by *Vs* = 450 m/s, input: MONTENEGRO

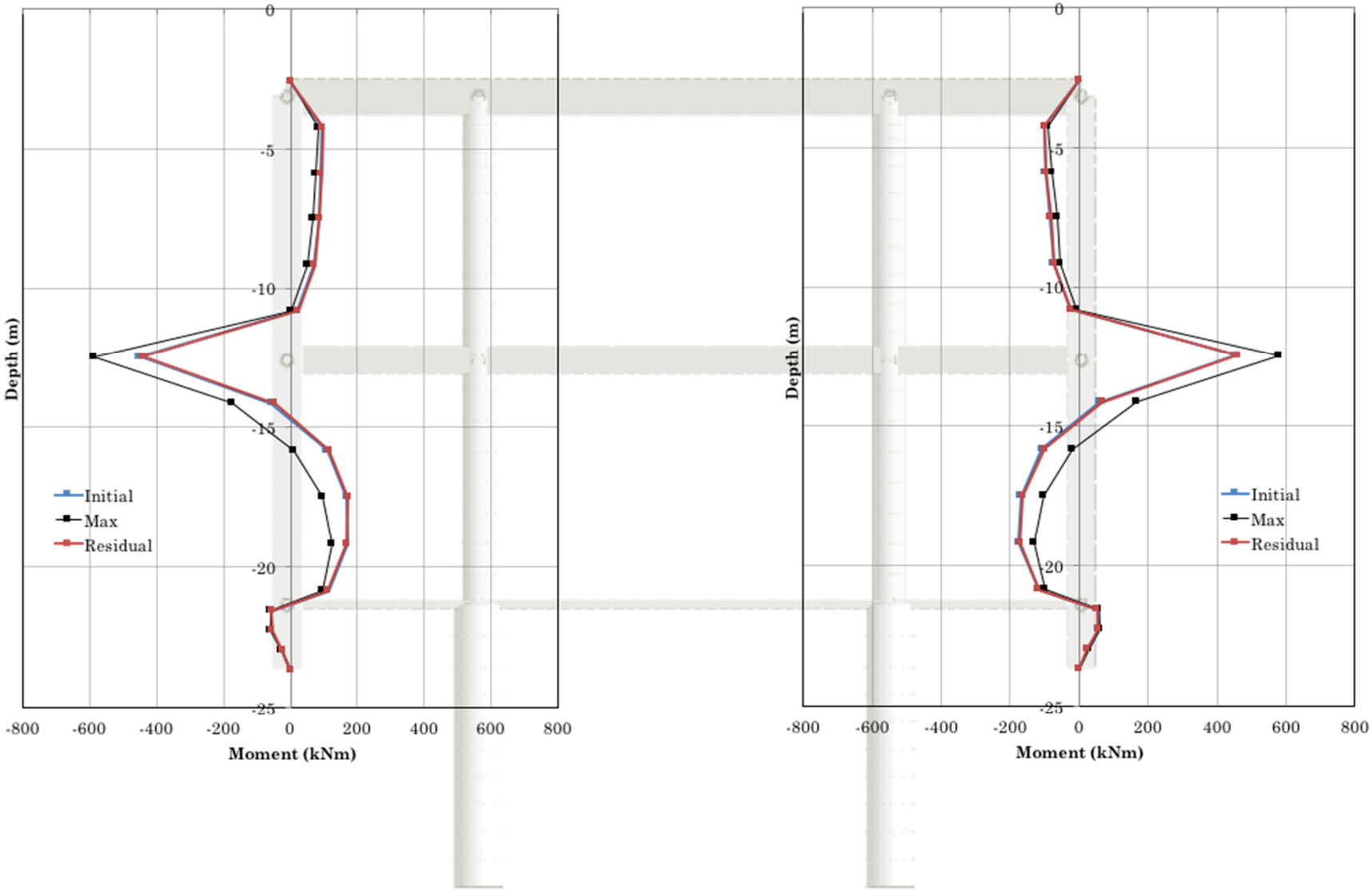

Figure 145: Bending moment acting on the concrete retaining walls - profile characterized by *Vs* = 450 m/s, input: AMATRICE

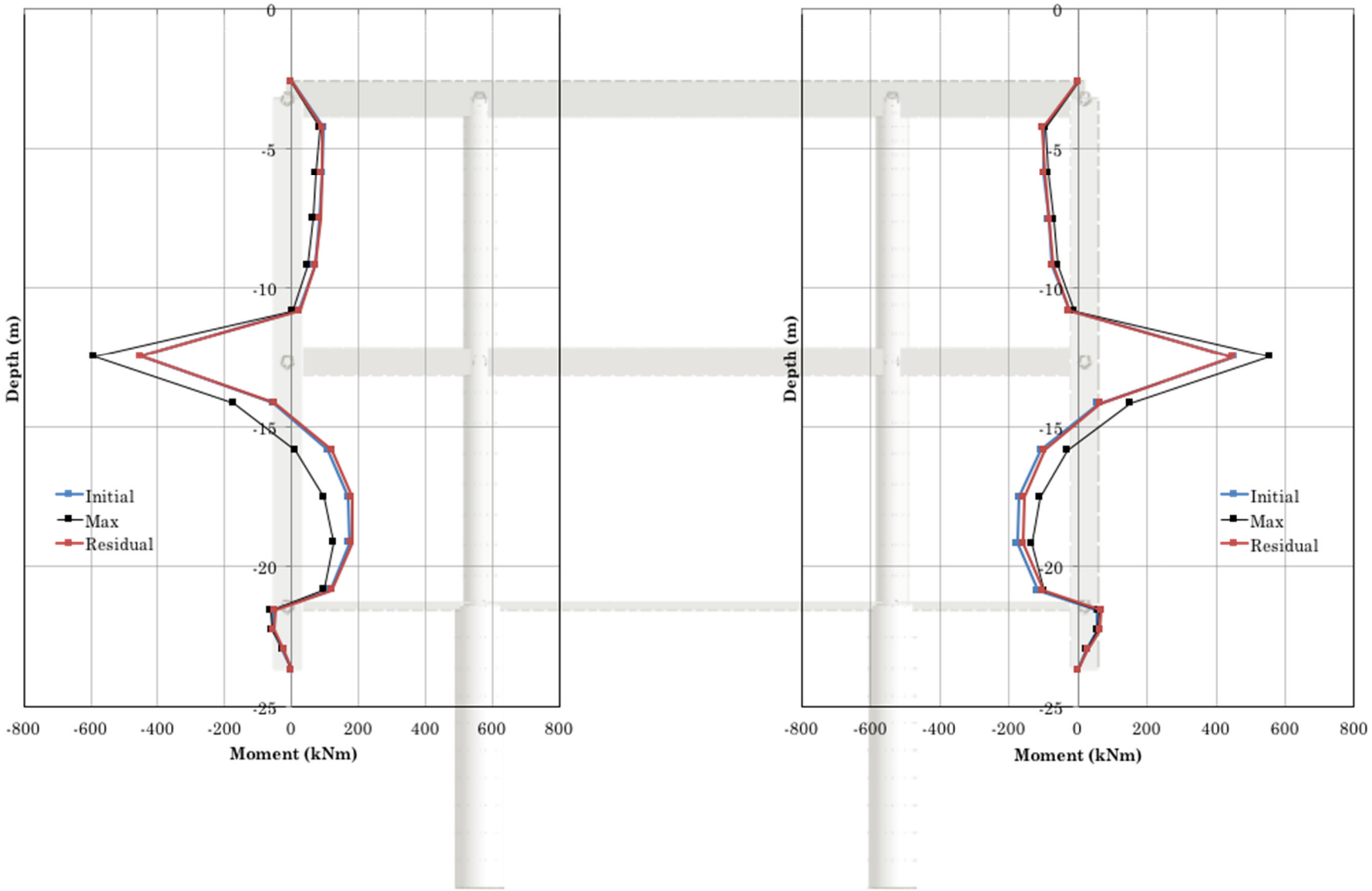

Figure 146: Bending moment acting on the concrete retaining walls - profile characterized by *Vs* = 450 m/s, input: L'AQUILA

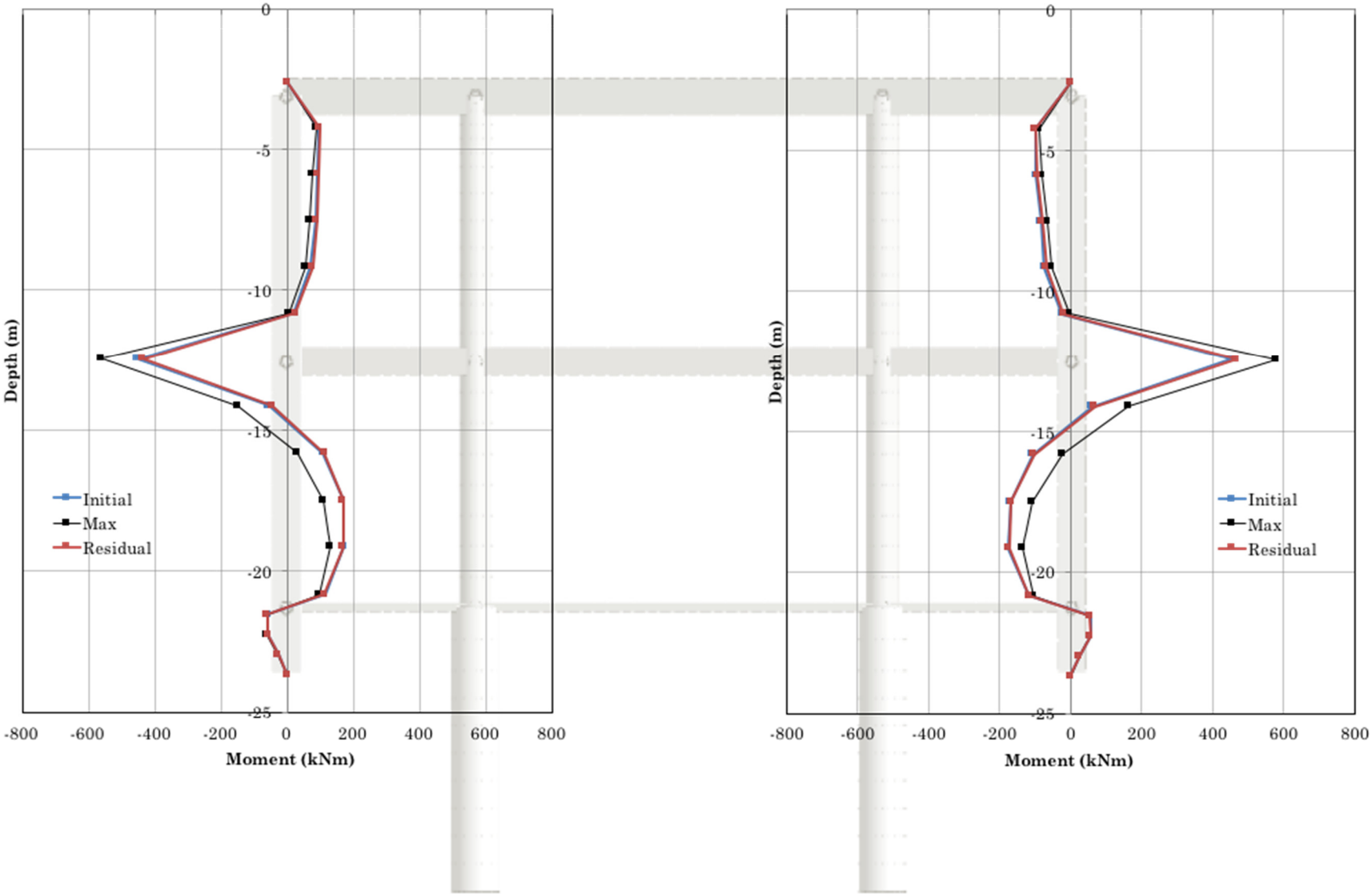

Figure 147: Bending moment acting on the concrete retaining walls - profile characterized by *Vs* = 450 m/s, input: FRIULI

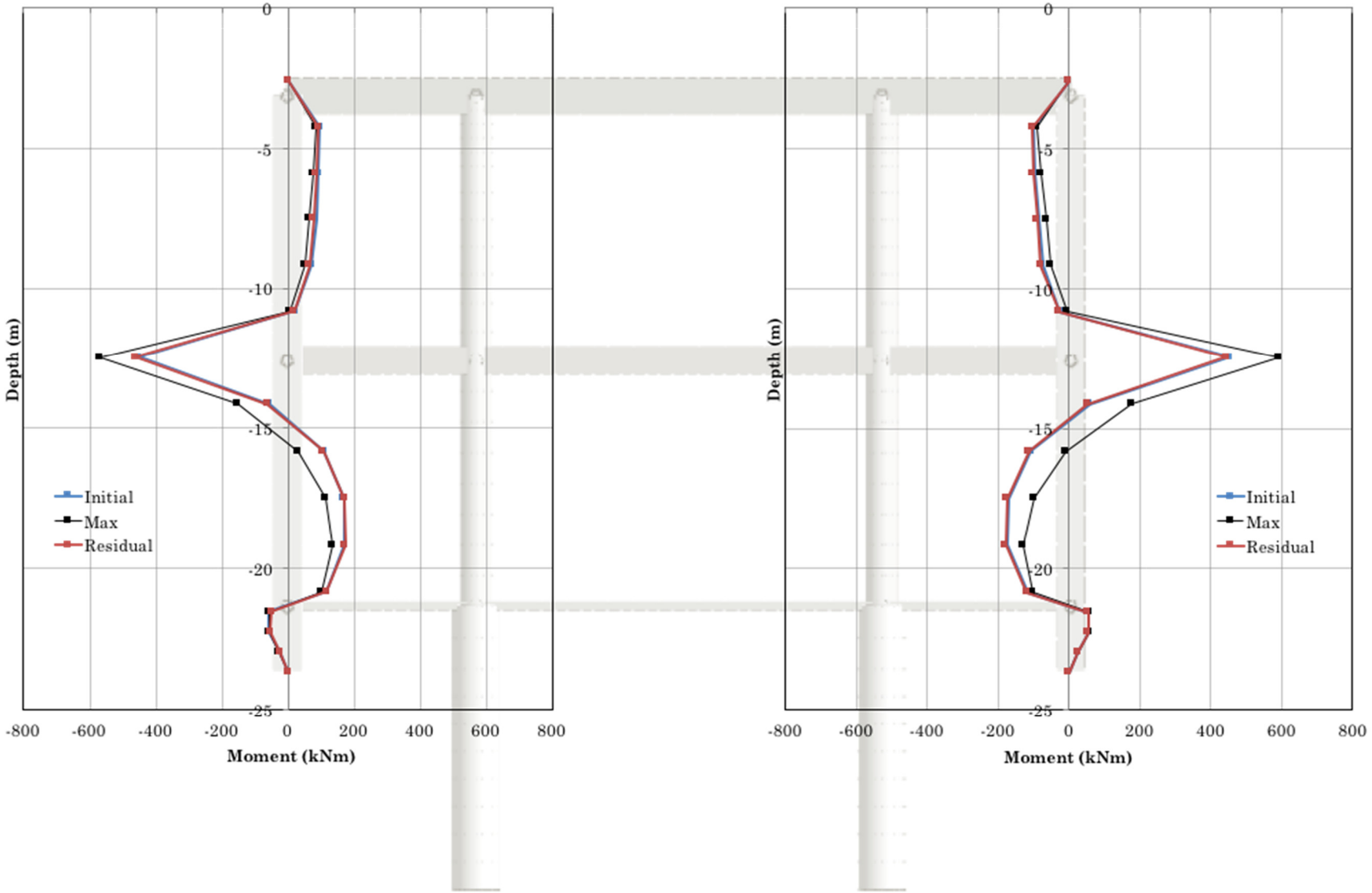

Figure 148: Bending moment acting on the concrete retaining walls - profile characterized by *Vs* = 450 m/s, input: GREECE

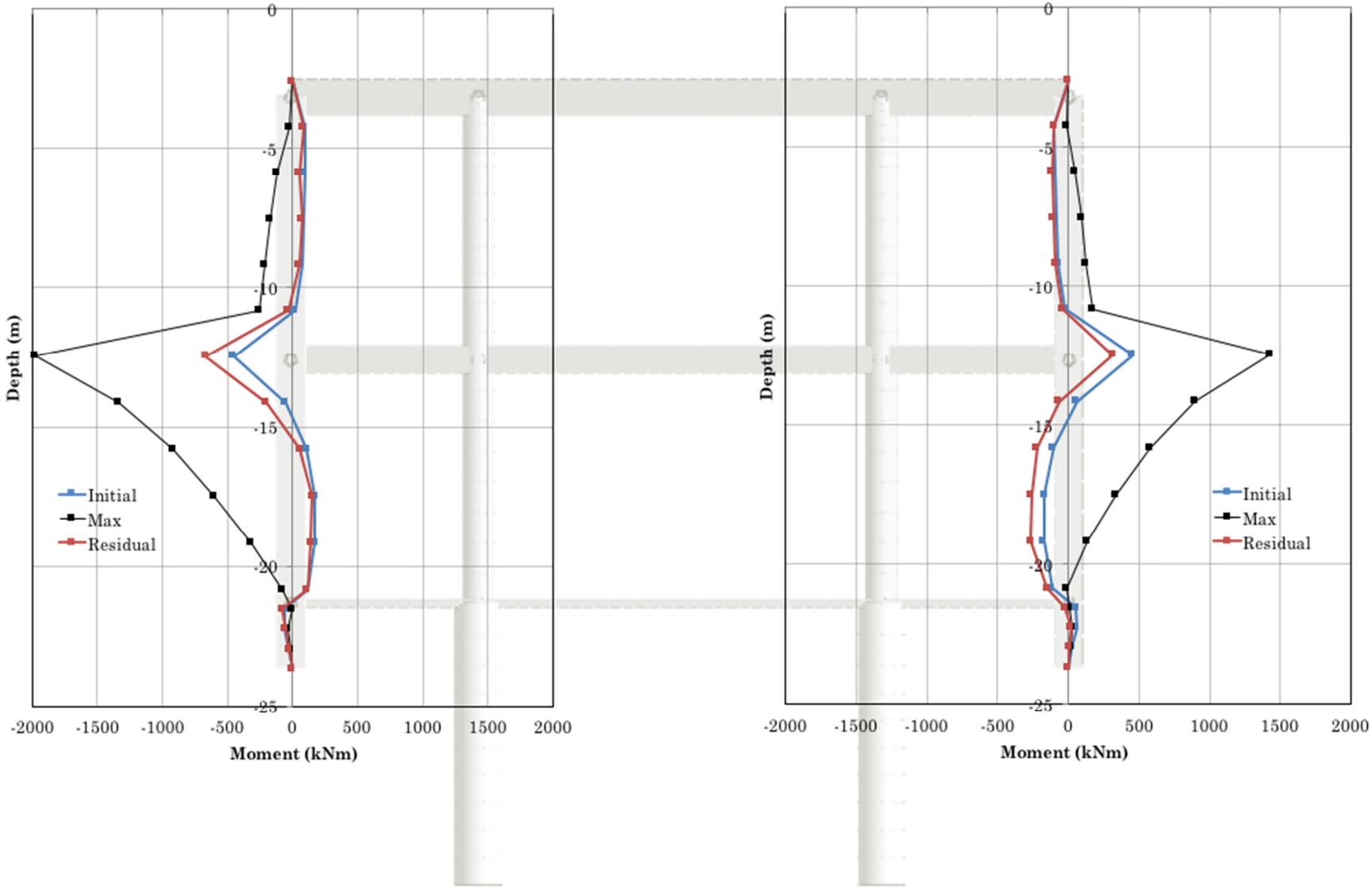

Figure 149: Bending moment acting on the concrete retaining walls - profile characterized by *Vs* = 450 m/s, input: LIMA

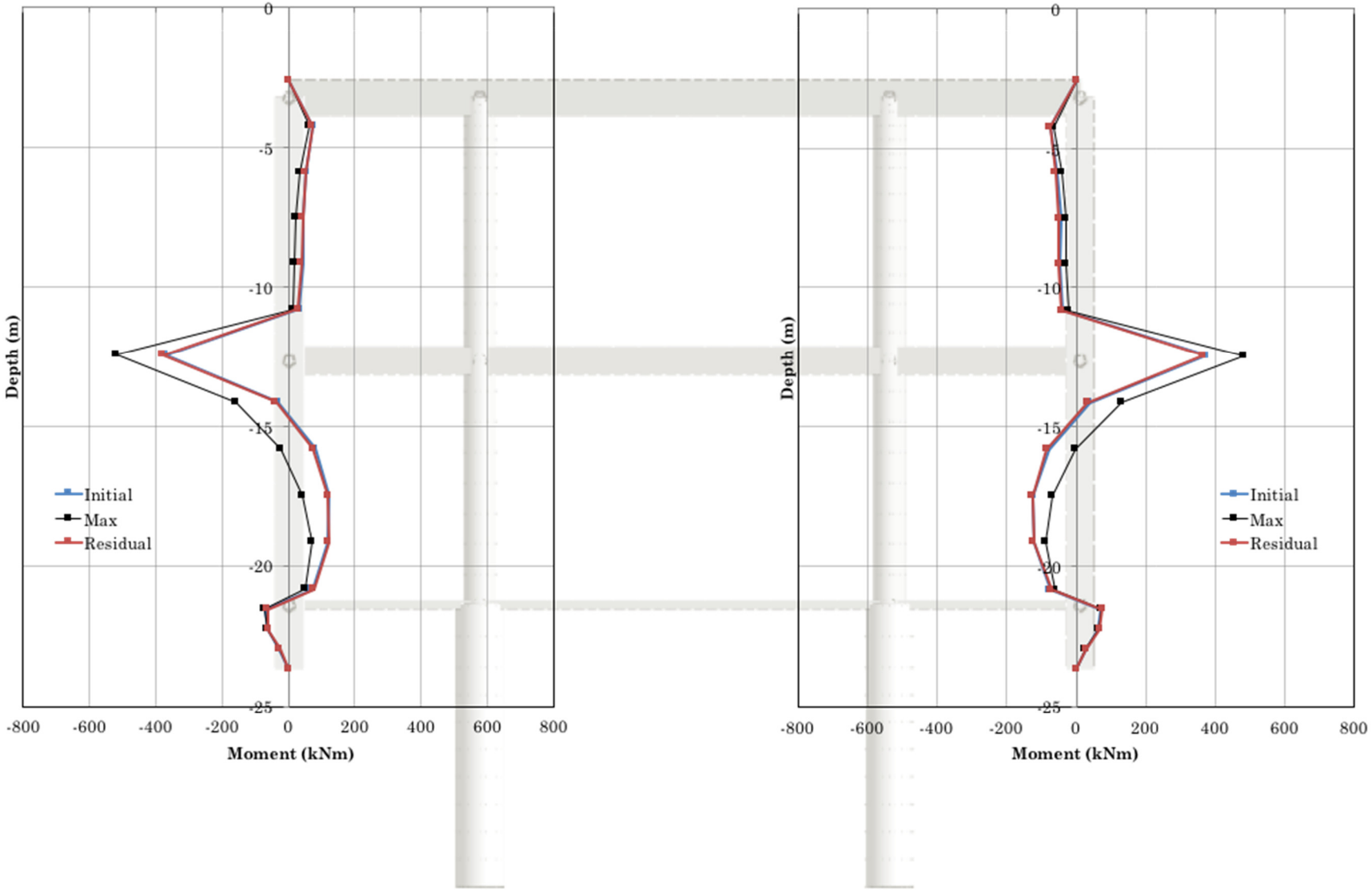

Figure 150: Bending moment acting on the concrete retaining walls - profile characterized by *Vs* = 600 m/s, input: MONTENEGRO

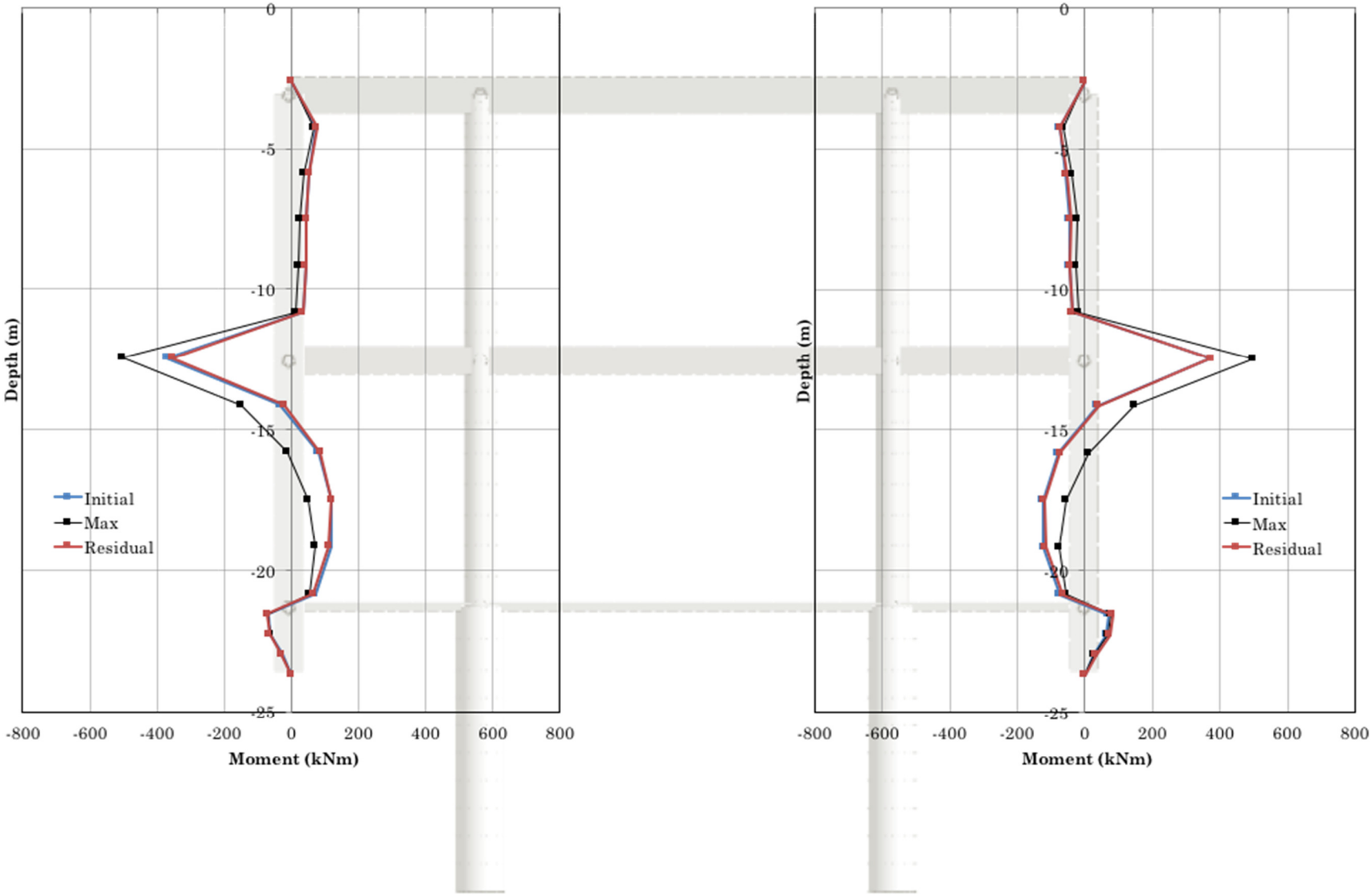

Figure 151: Bending moment acting on the concrete retaining walls - profile characterized by *Vs* = 600 m/s, input: AMATRICE

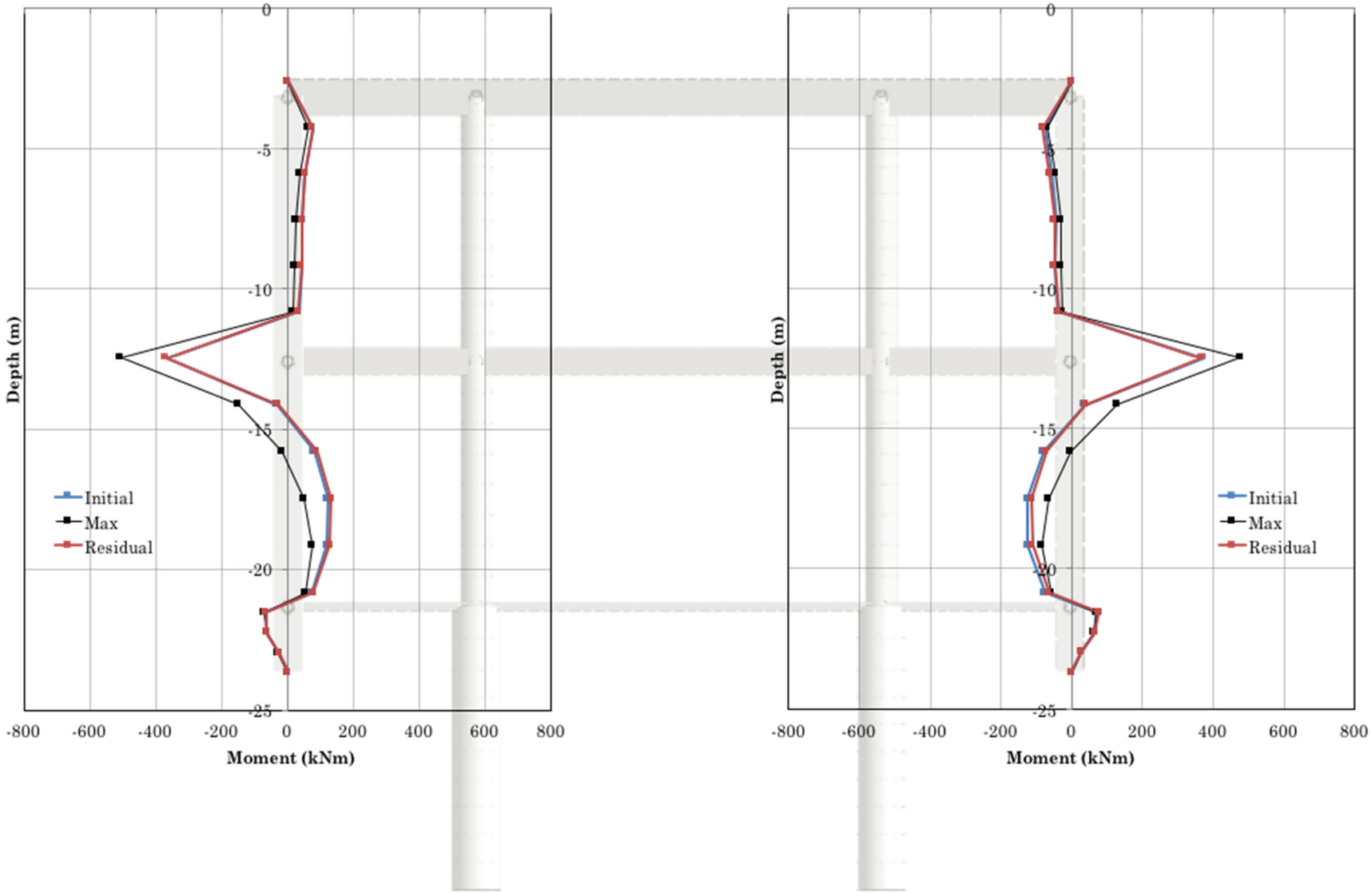

Figure 152: Bending moment acting on the concrete retaining walls - profile characterized by *Vs* = 600 m/s, input: L'AQUILA

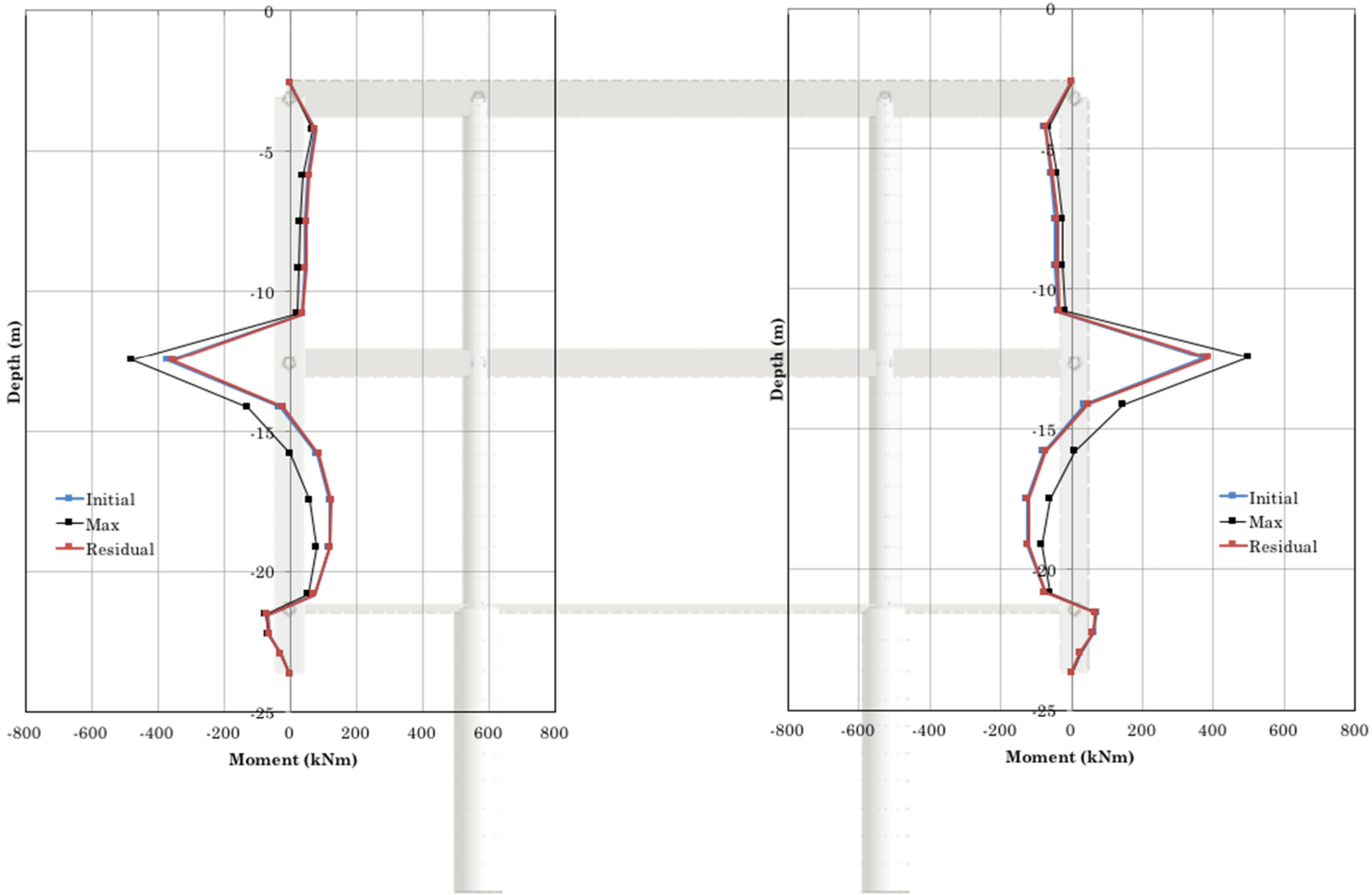

Figure 153: Bending moment acting on the concrete retaining walls - profile characterized by *Vs* = 600 m/s, input: FRIULI

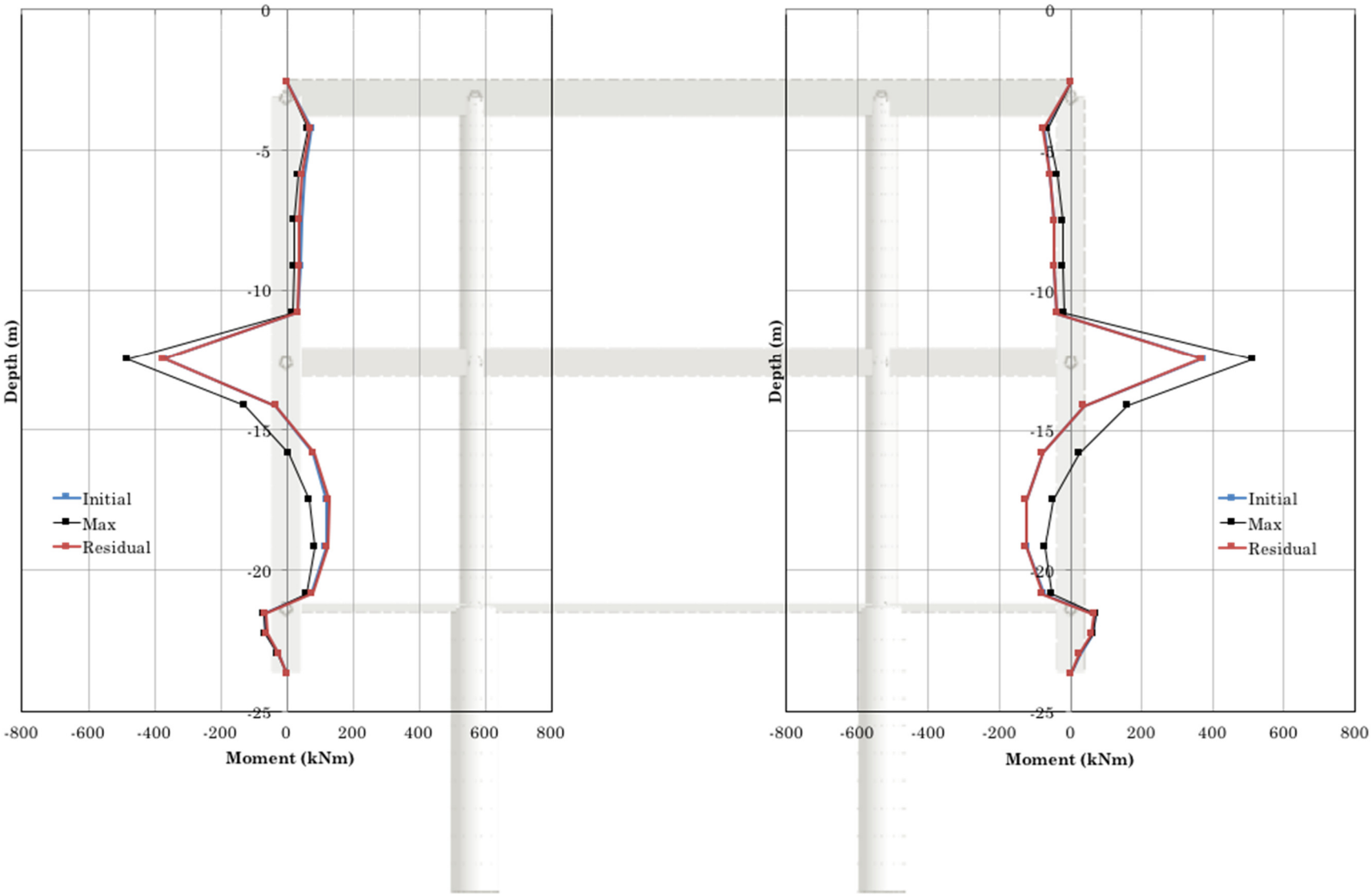

Figure 154: Bending moment acting on the concrete retaining walls - profile characterized by *Vs* = 600 m/s, input: GREECE

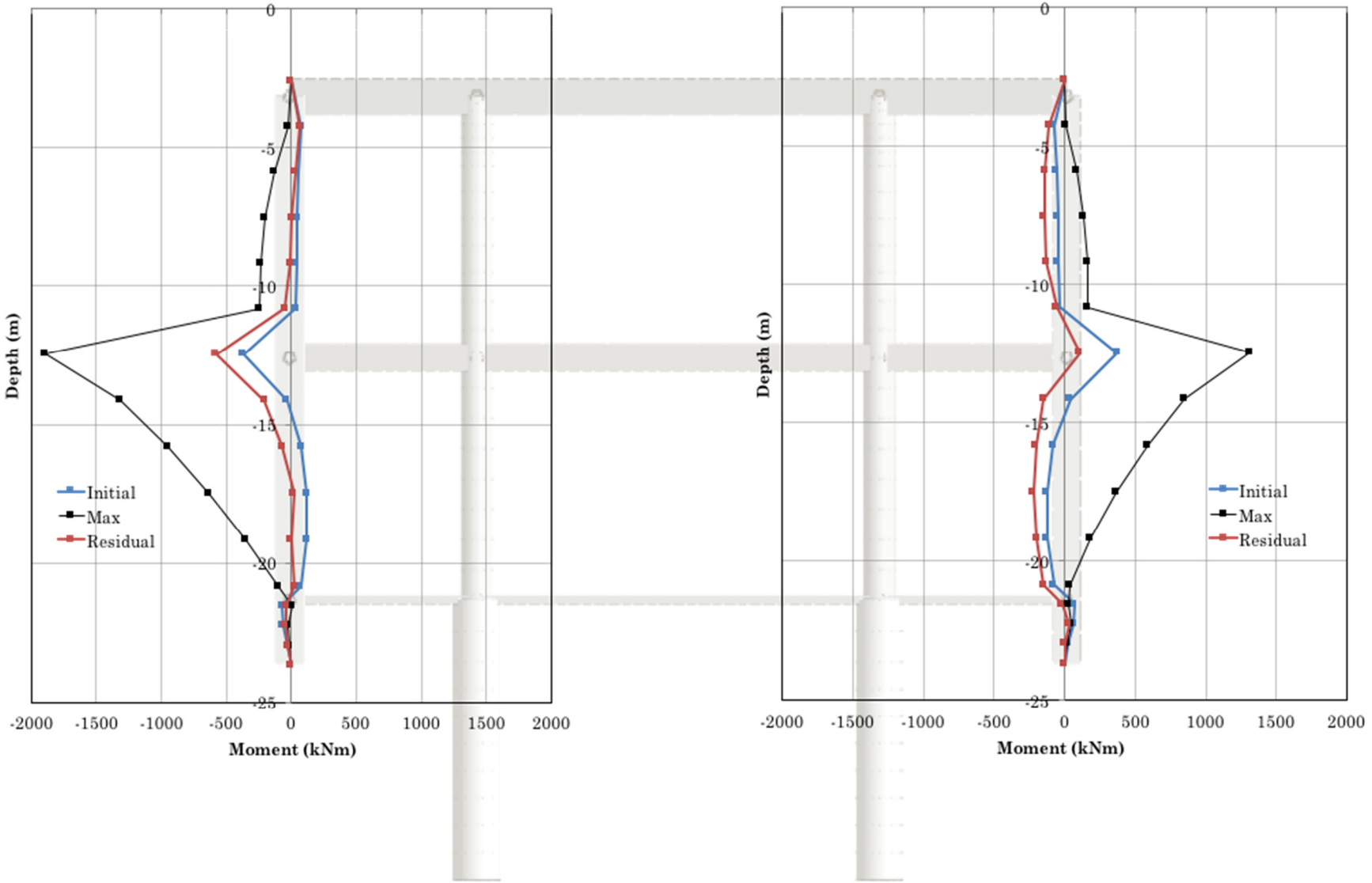

Figure 155: Bending moment acting on the concrete retaining walls - profile characterized by *Vs* = 600 m/s, input: LIMA

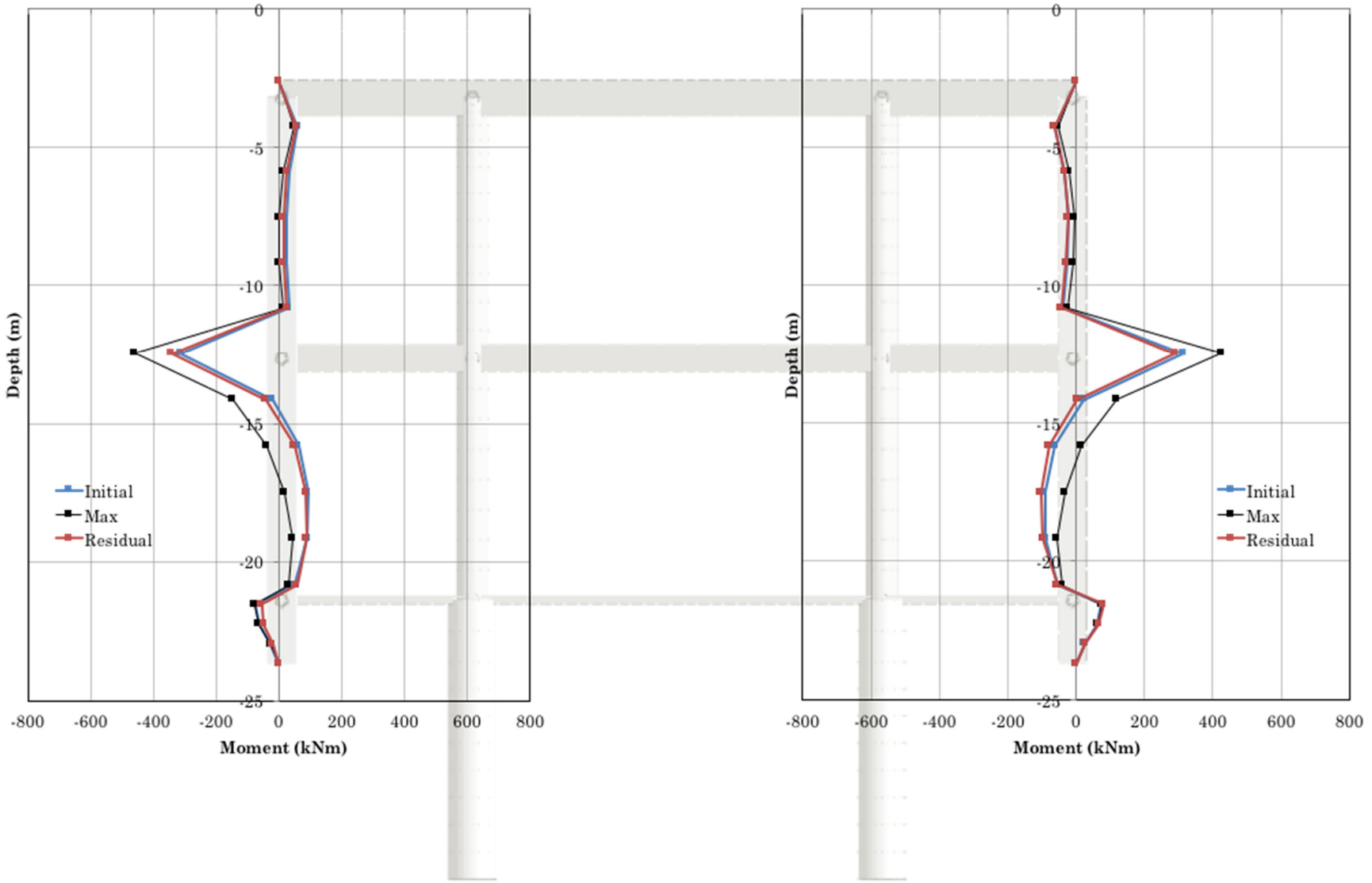

Figure 156: Bending moment acting on the concrete retaining walls - profile characterized by *Vs* = 750 m/s, input: MONTENEGRO

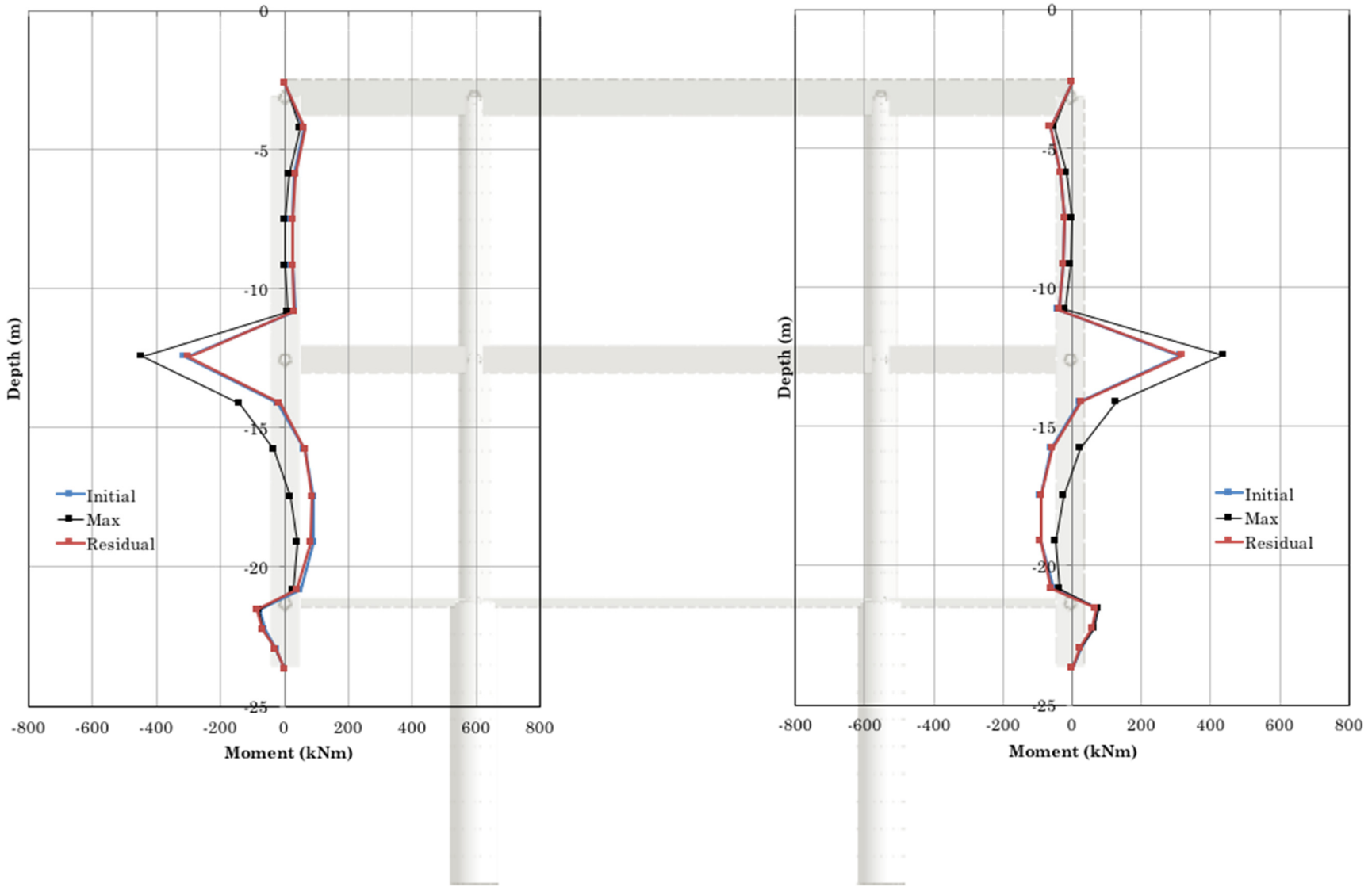

Figure 157: Bending moment acting on the concrete retaining walls - profile characterized by *Vs* = 750 m/s, input: AMATRICE

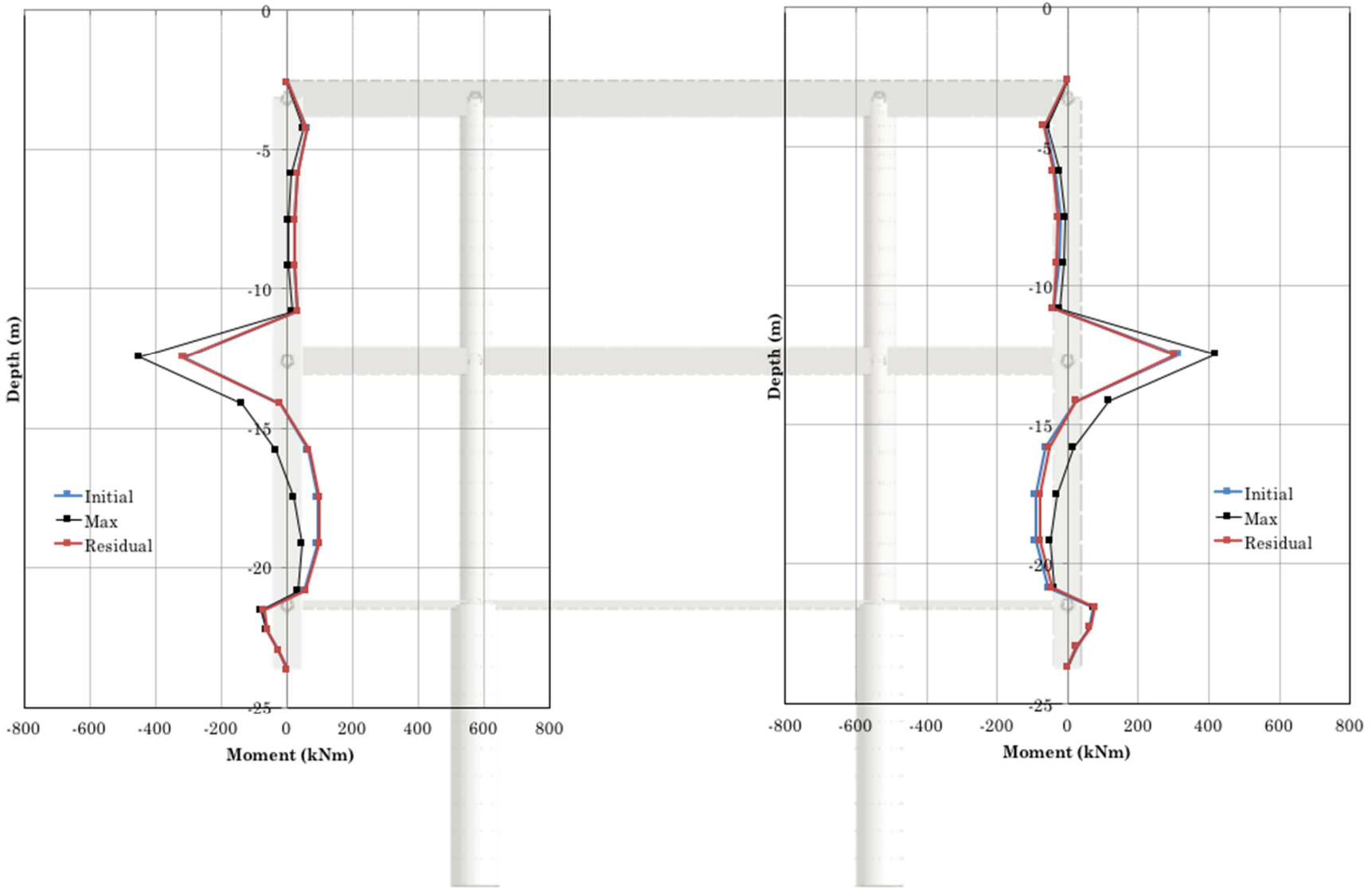

Figure 158: Bending moment acting on the concrete retaining walls - profile characterized by *Vs* = 750 m/s, input: L'AQUILA

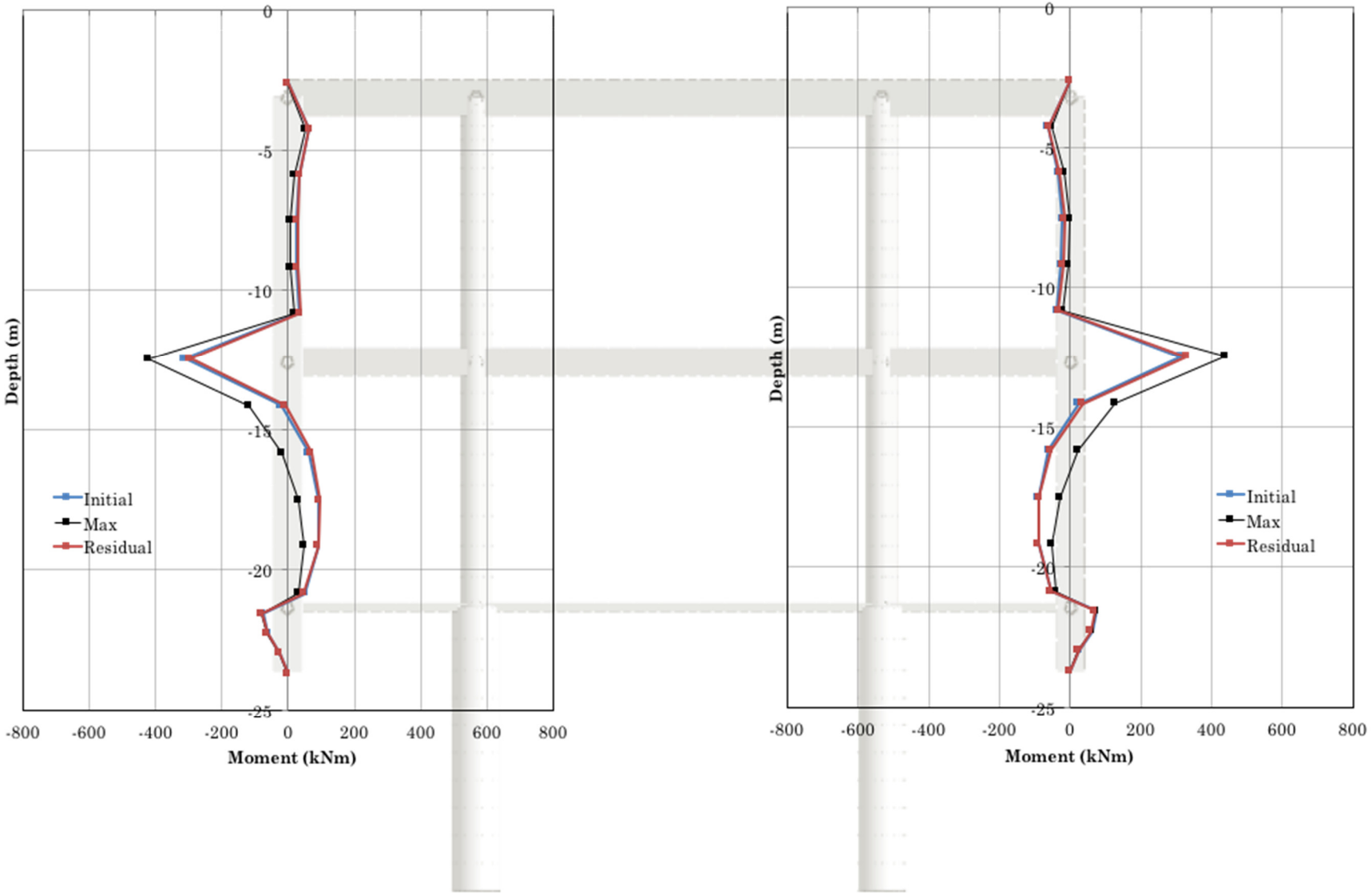

Figure 159: Bending moment acting on the concrete retaining walls - profile characterized by *Vs* = 750 m/s, input: FRIULI

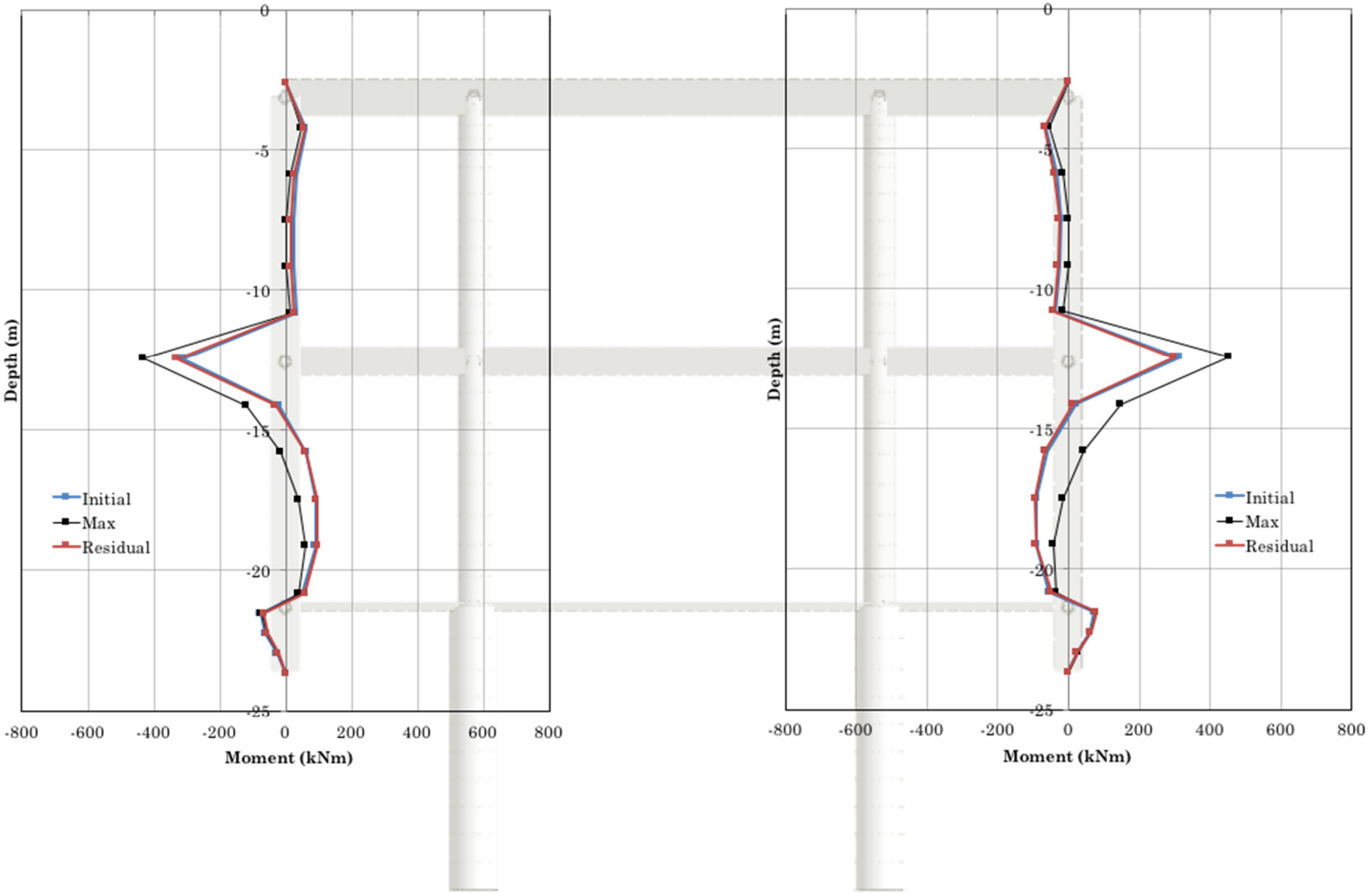

Figure 160: Bending moment acting on the concrete retaining walls - profile characterized by *Vs* = 750 m/s, input: GREECE

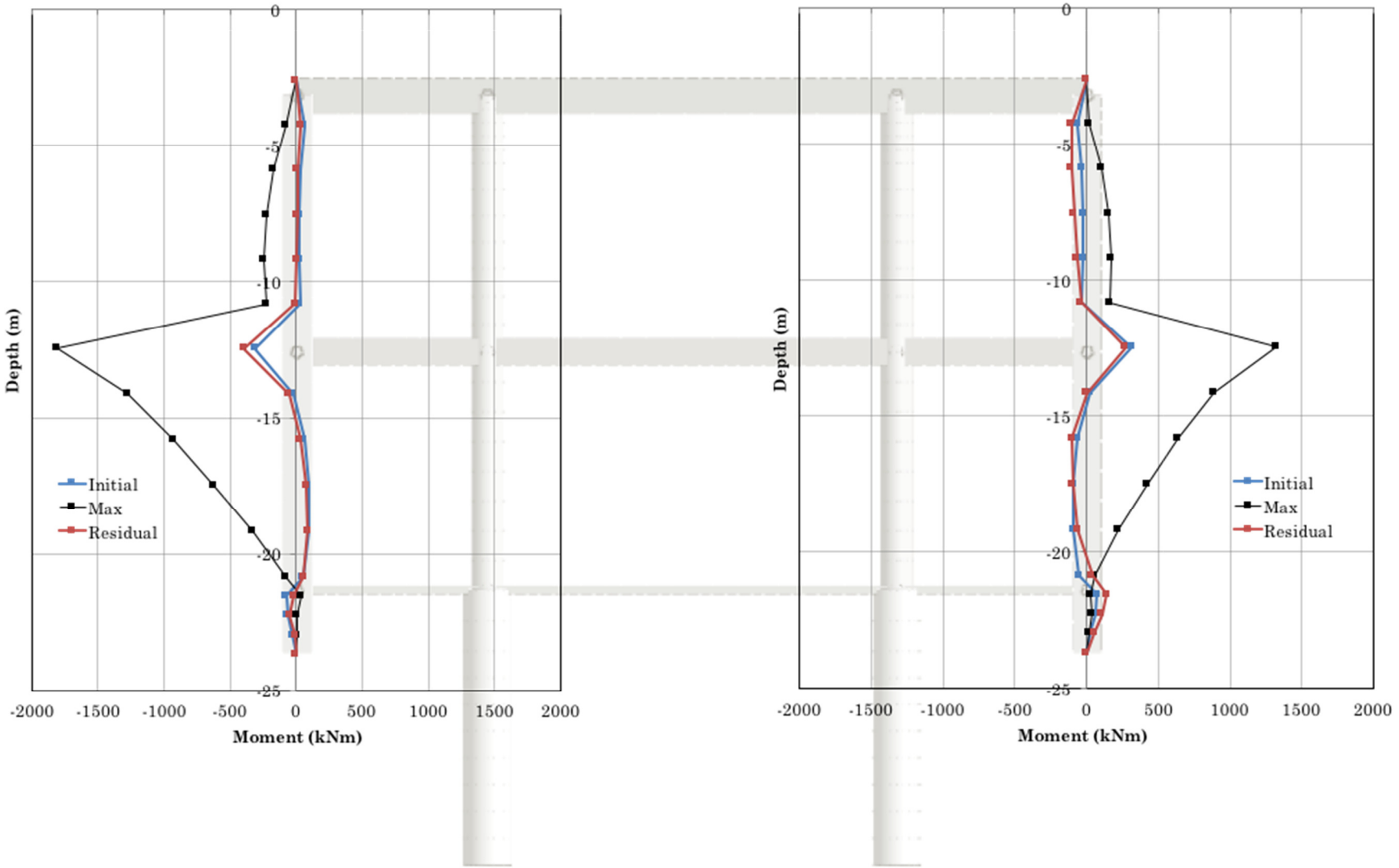

Figure 161: Bending moment acting on the concrete retaining walls - profile characterized by *Vs* = 750 m/s, input: LIMA

For all the accelerograms, the increment due to the seismic action is higher for the soil profiles characterized by V_S = 600 m/s and 750 m/s, in contrast to the decoupled approach results. The maximum increment, also in this case, occurs under Lima seismic signal and is equal to 1493 kNm for the soil profile characterized by V_S = 750 m/s, that is about 4.75 times the value obtained by the static condition. For the natural accelerograms, instead, the maximum increment is about 150 kNm and occurs for Montenegro seismic input.
The trend of the maximum value of the bending moment, obtained during the seismic event, acting on the section in correspondence to the central slab is reported in the Figures 162, 163, 164, 165, 166 and 167 and show a decrease of the maximum value when the soil column stiffness increases. Only for the Lima seismic input the maximum value of the bending moment is obtained for the soil profile characterized by V_S = 450 m/s according to the resonance effects highlighted by the previous Figure 28.
Figures from 168 to 215 show the evolution of the ratio between the value of the bending moment obtained by the static condition and the value of the bending moment acting on the left and right retaining walls occurs during the different sesmic events for the four soil profiles. The results point out a behavior similar to a frame effect of the underground structure under seismic action highlighted by the occurrence of increases and decreases of the internal actions acting on the concrete retaining walls. The maximum ratio happens for the Lima seismic input and it is equal to 5.5 for the left retaining wall considering the soil profile characterized by V_S = 750 m/s (Figure 214), in accordance with the previous considerations. Furthemore, analysing the trend of the moment due to the Lima seismic action, the high frequencies appear almost over-damped; this fact could be due to the use of Rayleigh damping in the numerical model.
For the Amatrice seismic input, the maximum ratio occurs for the soil profile characterized by V_S = 750 m/s and it is equal to 1.4 (Figure 206). For the same soil profile, the other natural accelerograms (Friuli, L'Aquila and Grecce) show similar values while for the Montenegro seismic input the ratio reaches a greater value equal to 1.5.
Table 17 summarises the increment (or the decrese) of the residual moment compared to the initial value of the bending moment, Δ, acting in the section in correspondence to the central slab, obtained by the static analysis for the left and right retaining wall. For all the natural accelerograms, the value of Δ is included between 1% and 9%. This variation of the value of the internal action acting on the structural elements is due to the non-linear behavior of the soil described above. The synthetic seismic input (Lima) indicates significantly higher values for all the soil profiles which also reaches values higher than 50%. Moreover, it is more evident the asymmetric distribution of the internal action on both the retaining walls at the end of the motion. These differences in values are due to the particular characterstics of the Lima seismic input.

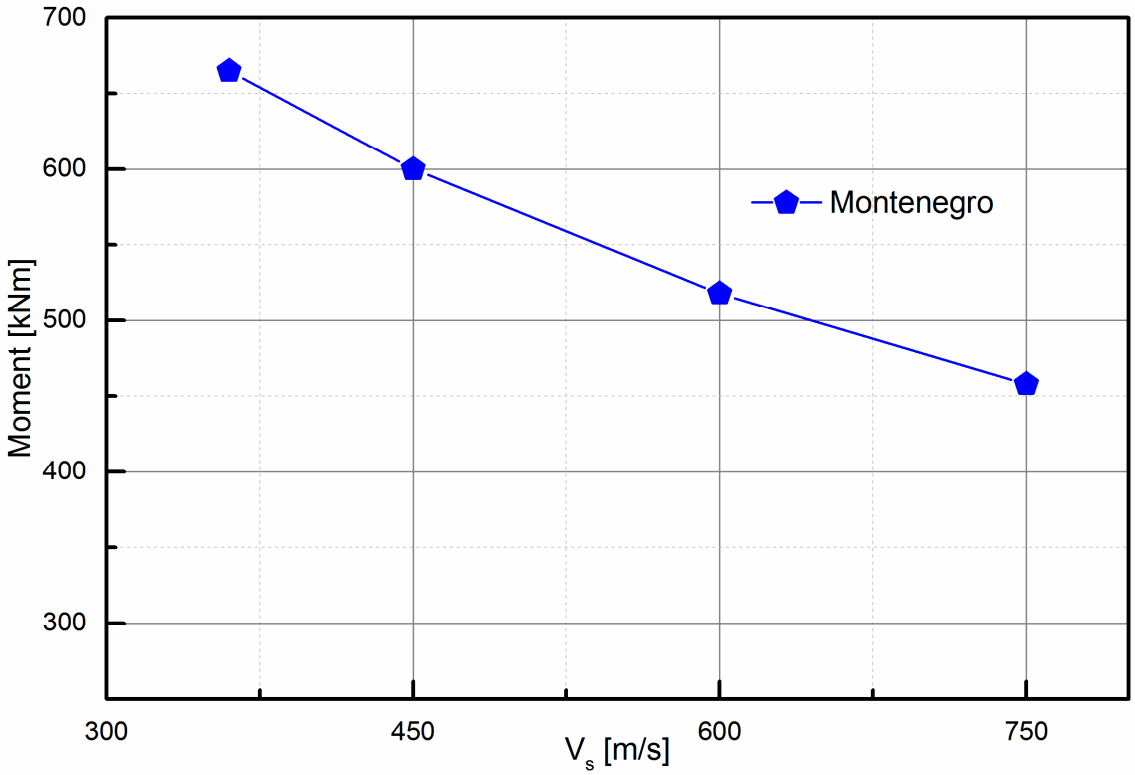

Figure 162: Coupled approach: maximum bending moment acting on the section in correspondence to the central slab

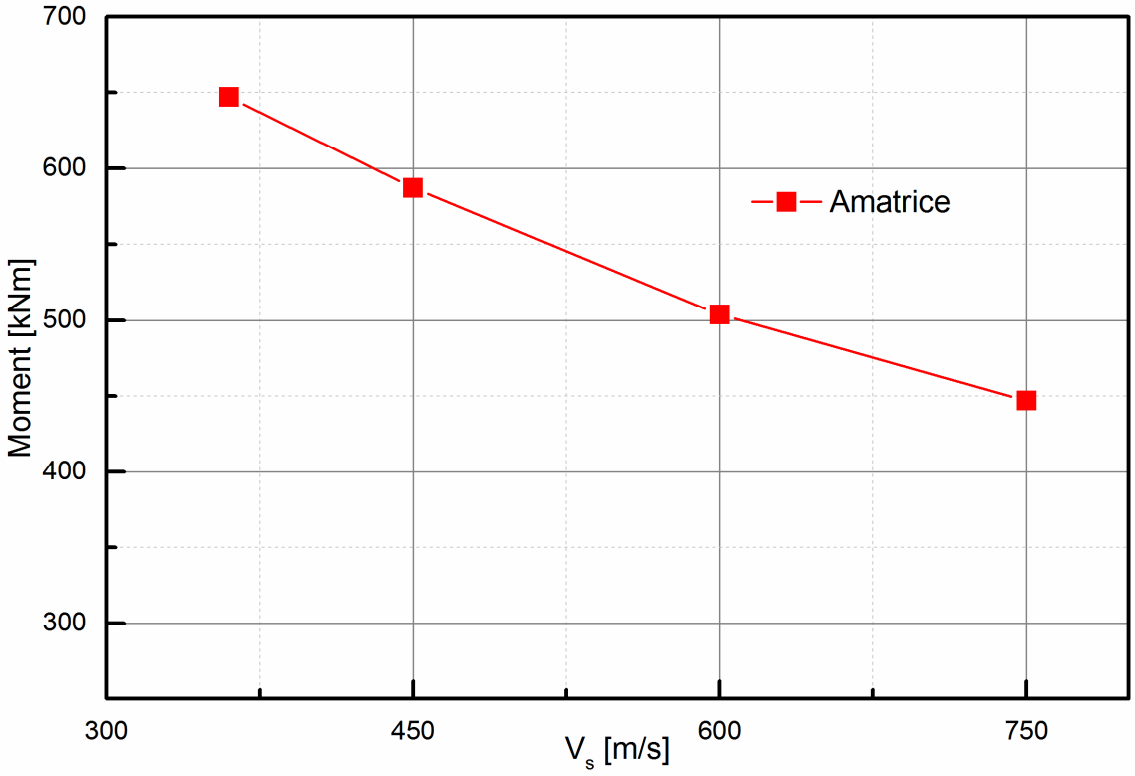

Figure 163: Coupled approach: maximum bending moment acting on the section in correspondence to the central slab

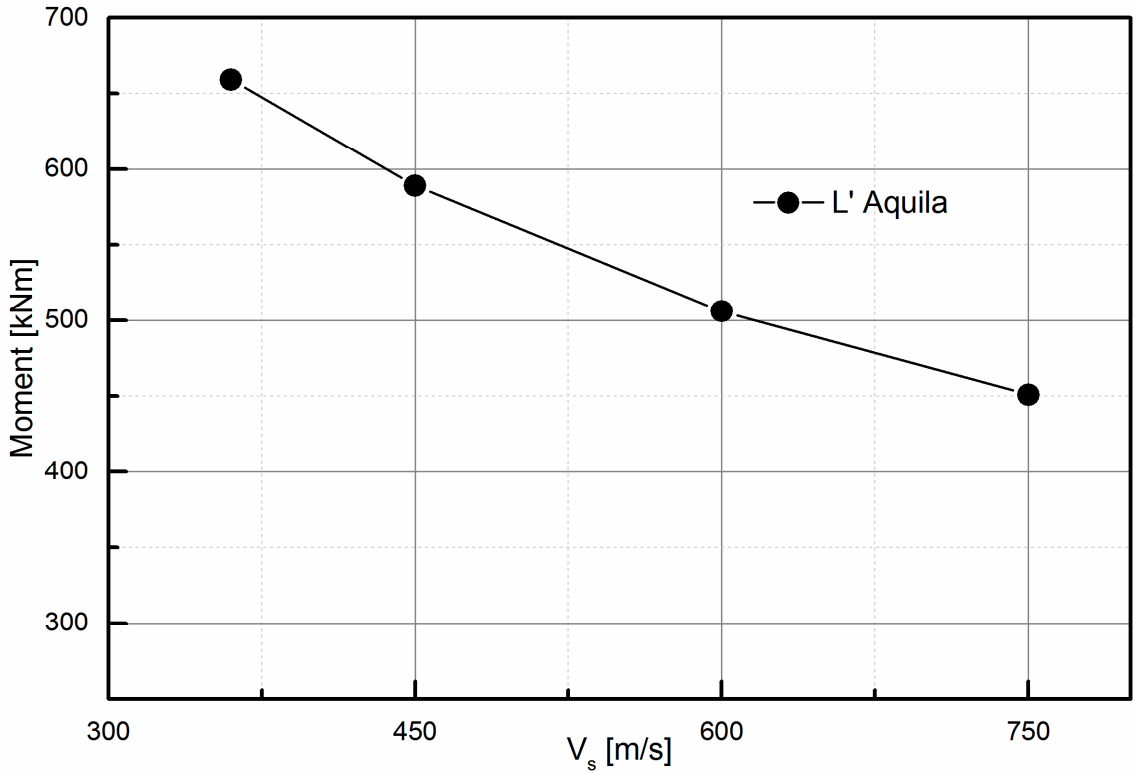

Figure 164: Coupled approach: maximum bending moment acting on the section in correspondence to the central slab

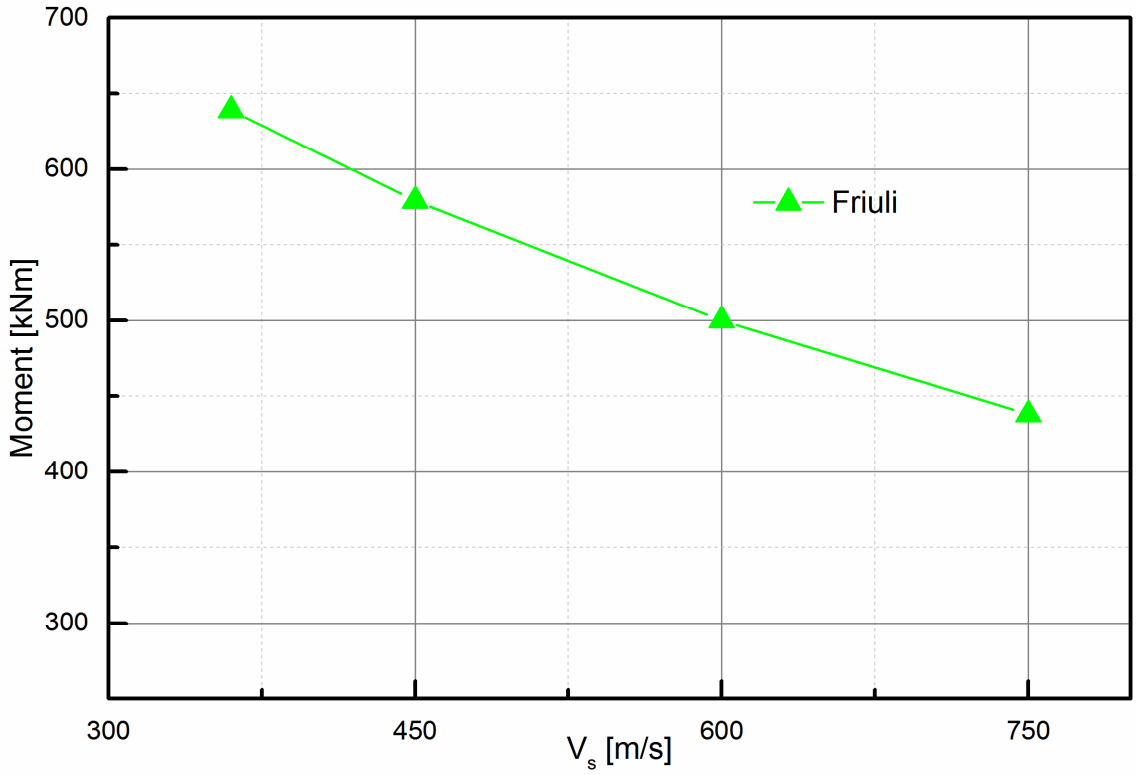

Figure 165: Coupled approach: maximum bending moment acting on the section in correspondence to the central slab

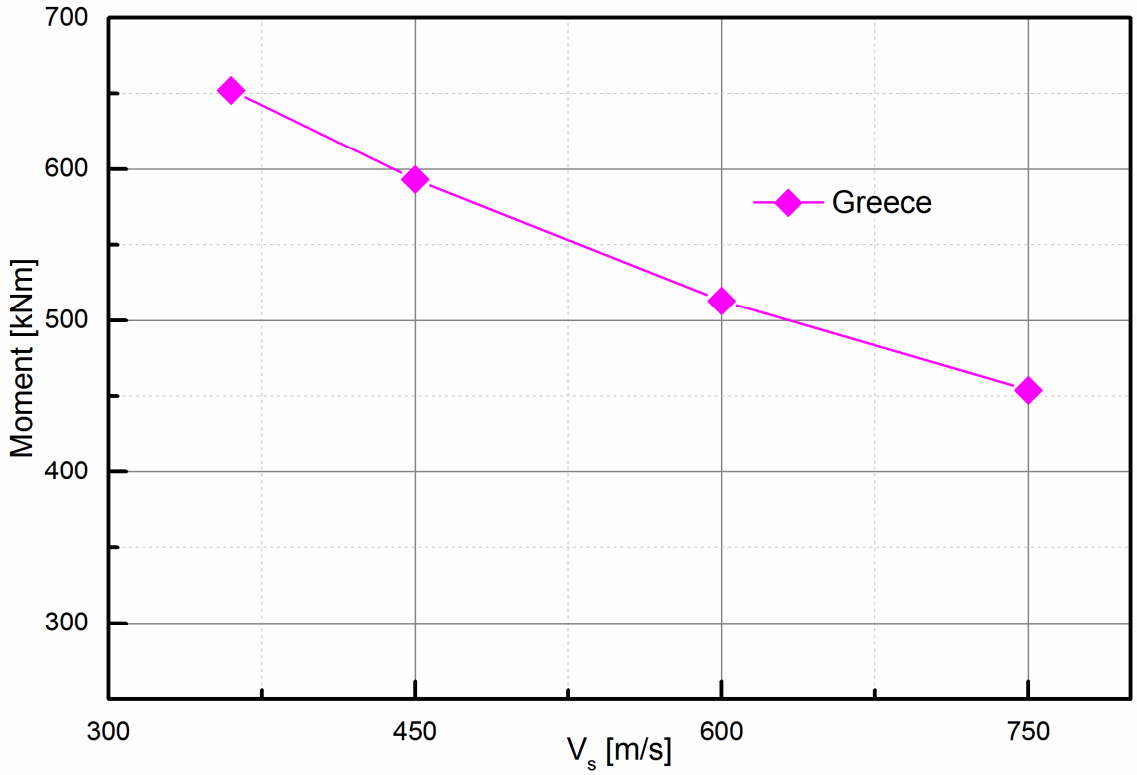

Figure 166: Coupled approach: maximum bending moment acting on the section in correspondence to the central slab

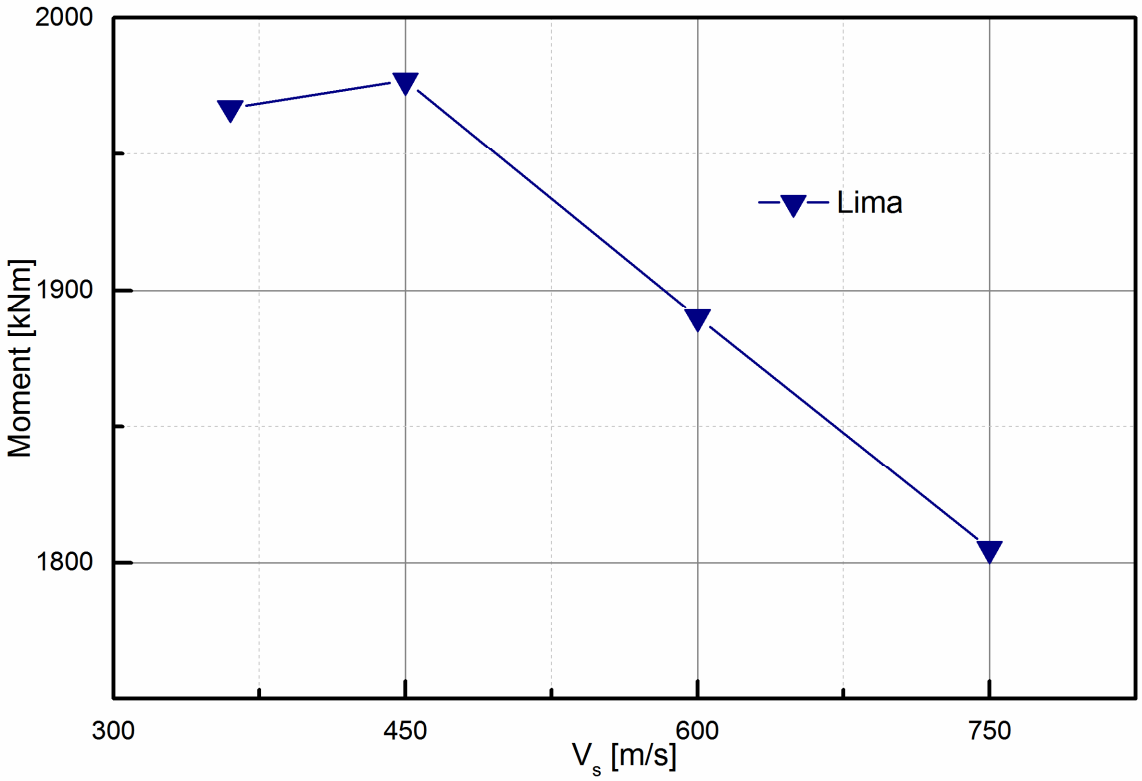

Figure 167: Coupled approach: maximum bending moment acting on the section in correspondence to the central slab

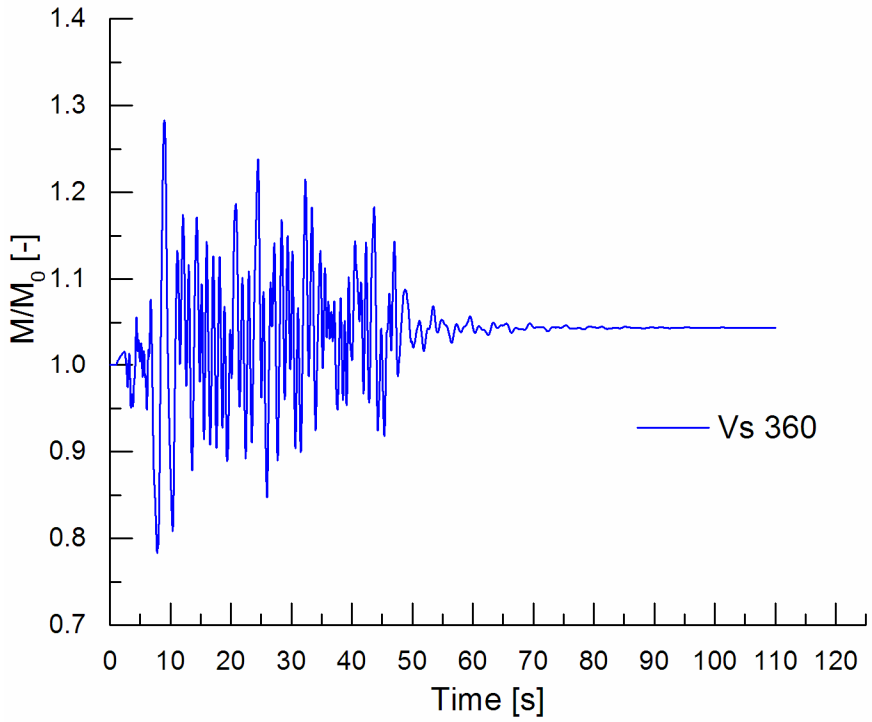

Figure 168: Coupled approach: ratio between the value of the initial bending moment and the value of the bending moment during the Montenegro seismic event acting on the section in correspondence to the central slab in the left retaining wall

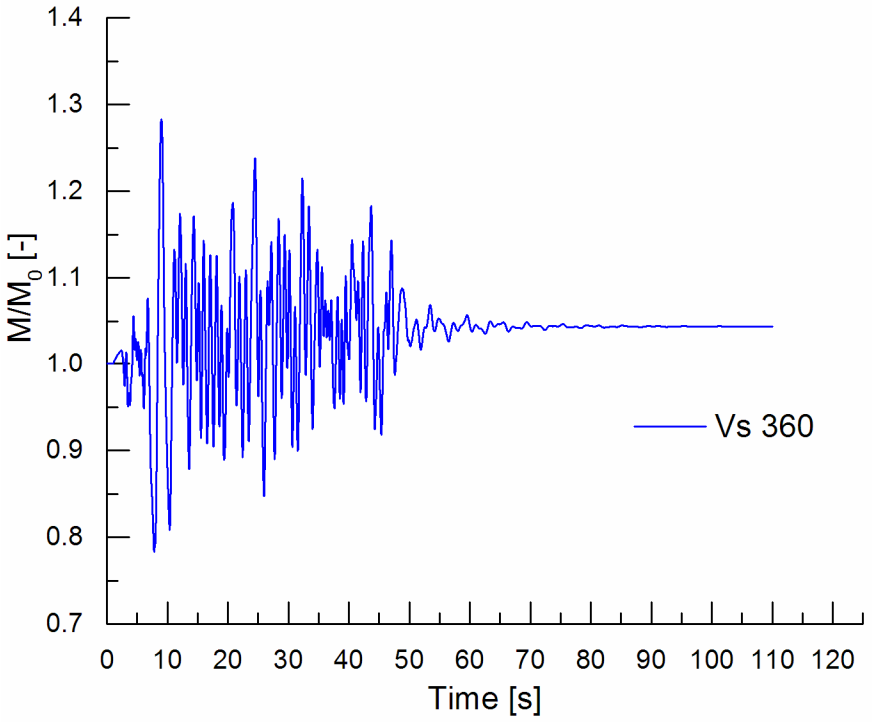

Figure 169: Coupled approach: ratio between the value of the initial bending moment and the value of the bending moment during the Montenegro seismic event acting on the section in correspondence to the central slab in the right retaining wall

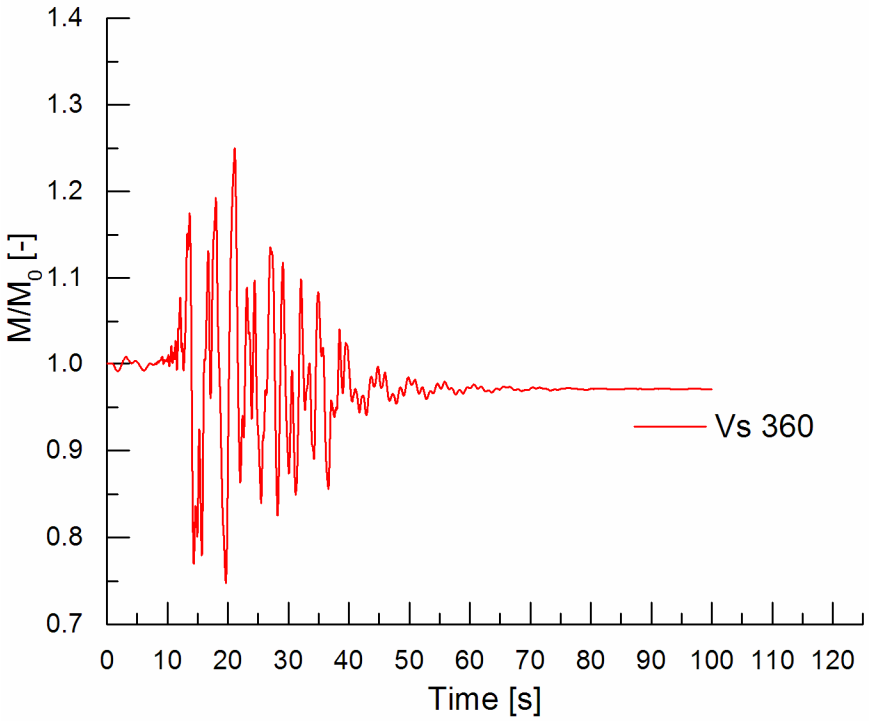

Figure 170: Coupled approach: ratio between the value of the initial bending moment and the value of the bending moment during the Amatrice seismic event acting on the section in correspondence to the central slab in the left retaining wall

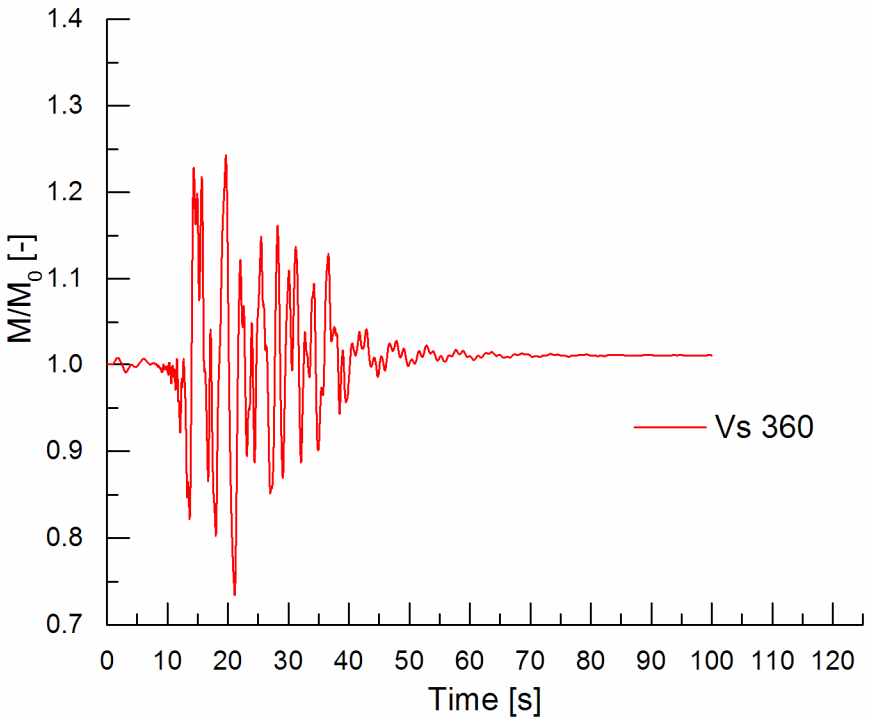

Figure 171: Coupled approach: ratio between the value of the initial bending moment and the value of the bending moment during the Amatrice seismic event acting on the section in correspondence to the central slab in the right retaining wall

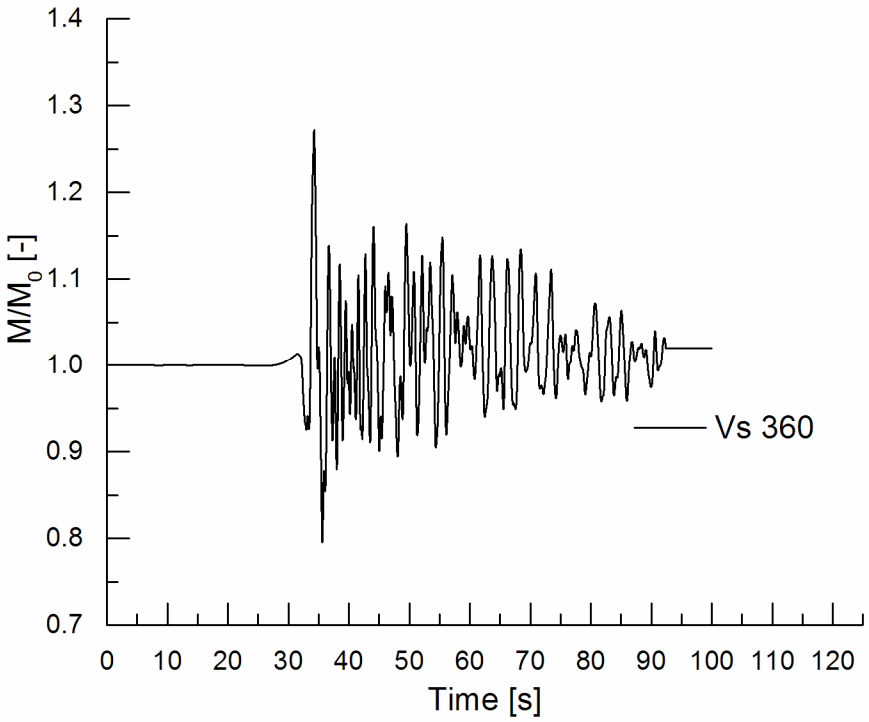

Figure 172: Coupled approach: ratio between the value of the initial bending moment and the value of the bending moment during the L'Aquila seismic event acting on the section in correspondence to the central slab in the left retaining wall

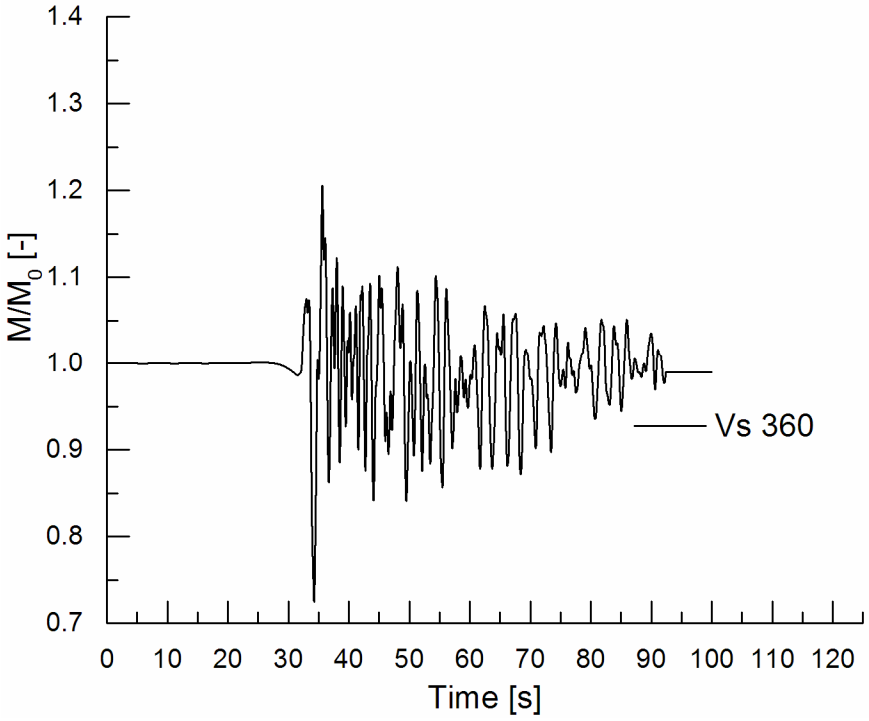

Figure 173: Coupled approach: ratio between the value of the initial bending moment and the value of the bending moment during the L'Aquila seismic event acting on the section in correspondence to the central slab in the right retaining wall

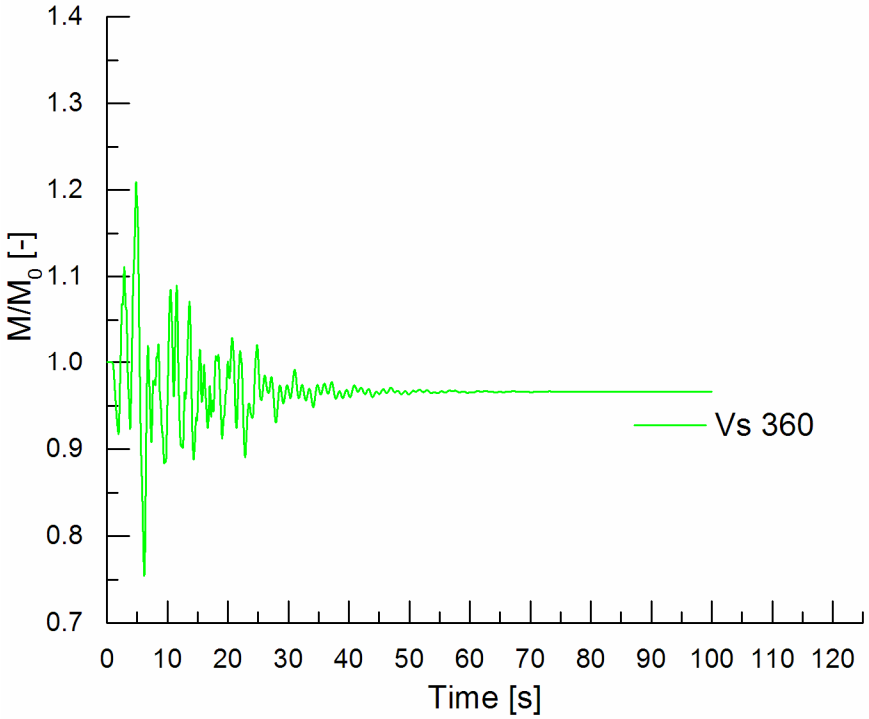

Figure 174: Coupled approach: ratio between the value of the initial bending moment and the value of the bending moment during the Friuli seismic event acting on the section in correspondence to the central slab in the left retaining wall

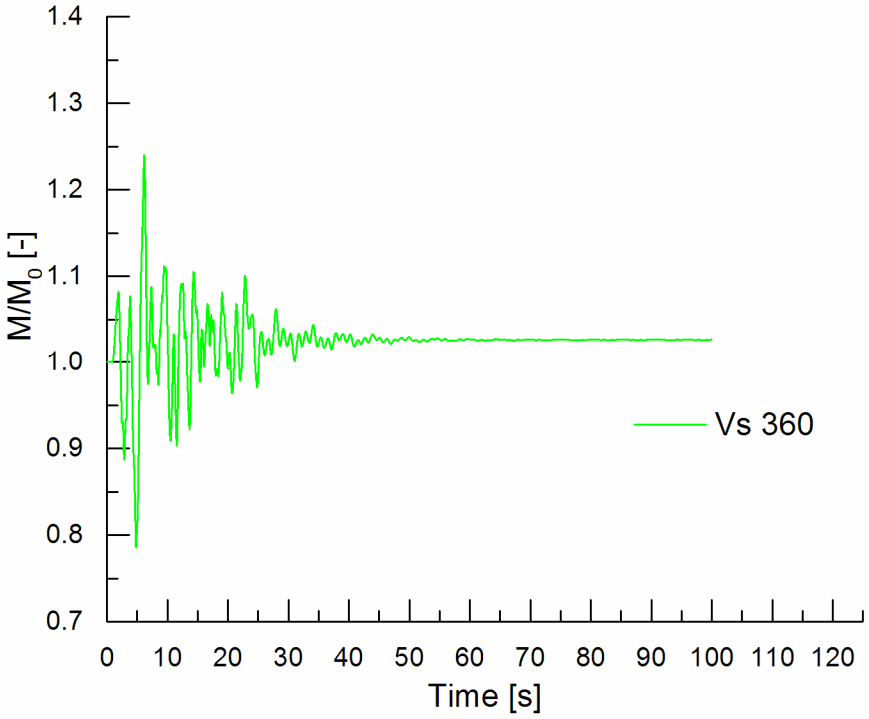

Figure 175: Coupled approach: ratio between the value of the initial bending moment and the value of the bending moment during the Friuli seismic event acting on the section in correspondence to the central slab in the right retaining wall

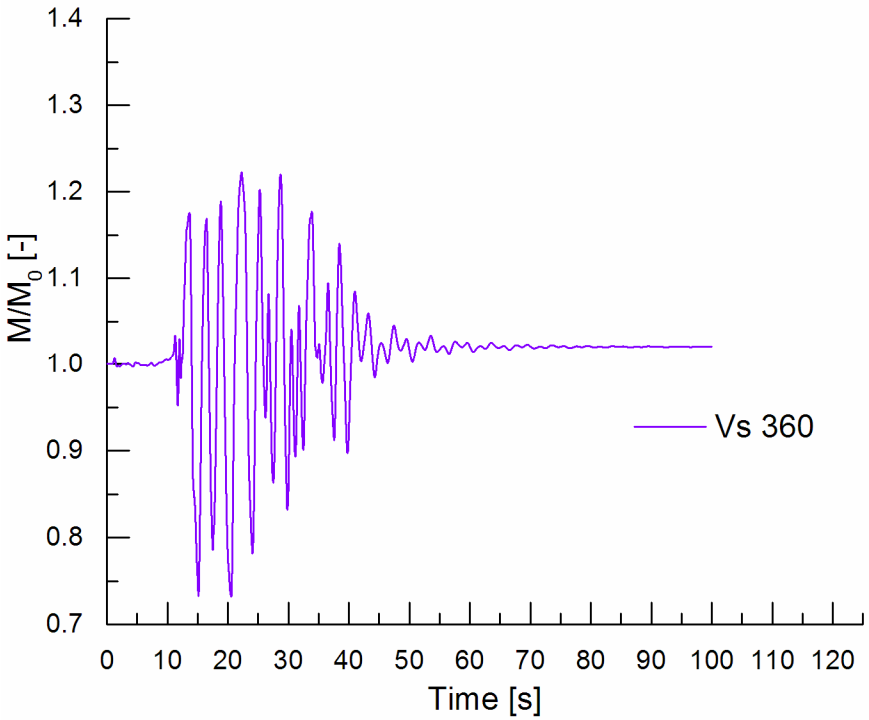

Figure 176: Coupled approach: ratio between the value of the initial bending moment and the value of the bending moment during the Greece seismic event acting on the section in correspondence to the central slab in the left retaining wall

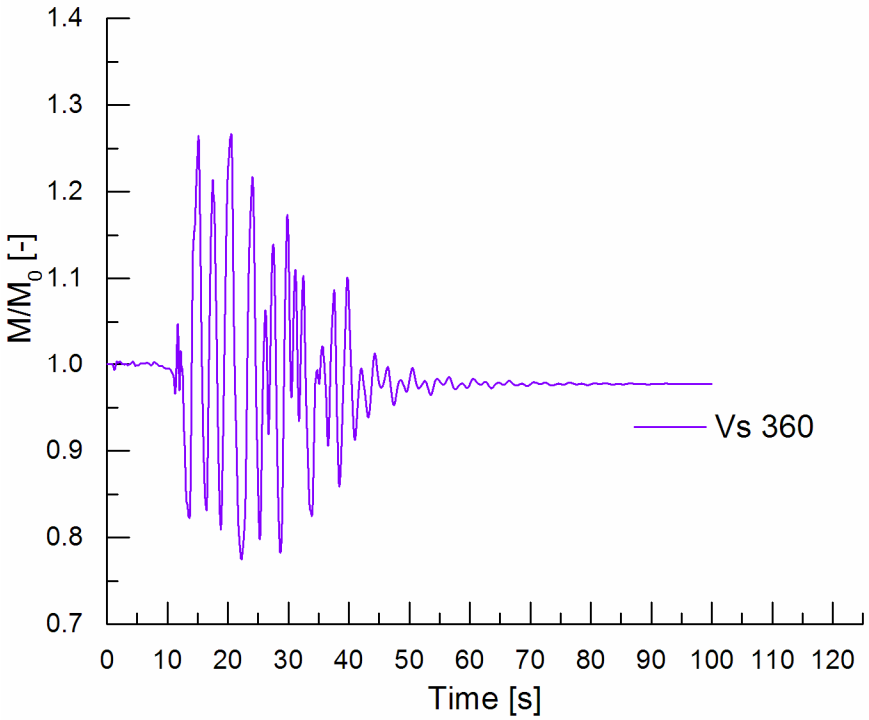

Figure 177: Coupled approach: ratio between the value of the initial bending moment and the value of the bending moment during the Greece seismic event acting on the section in correspondence to the central slab in the right retaining wall

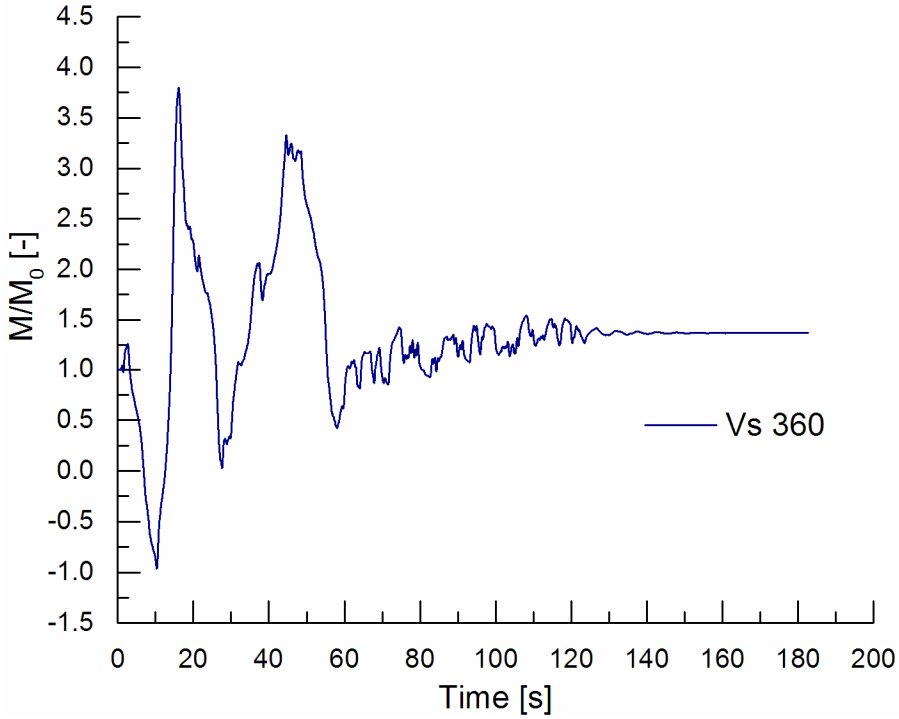

Figure 178: Coupled approach: ratio between the value of the initial bending moment and the value of the bending moment during the Lima seismic event acting on the section in correspondence to the central slab in the left retaining wall

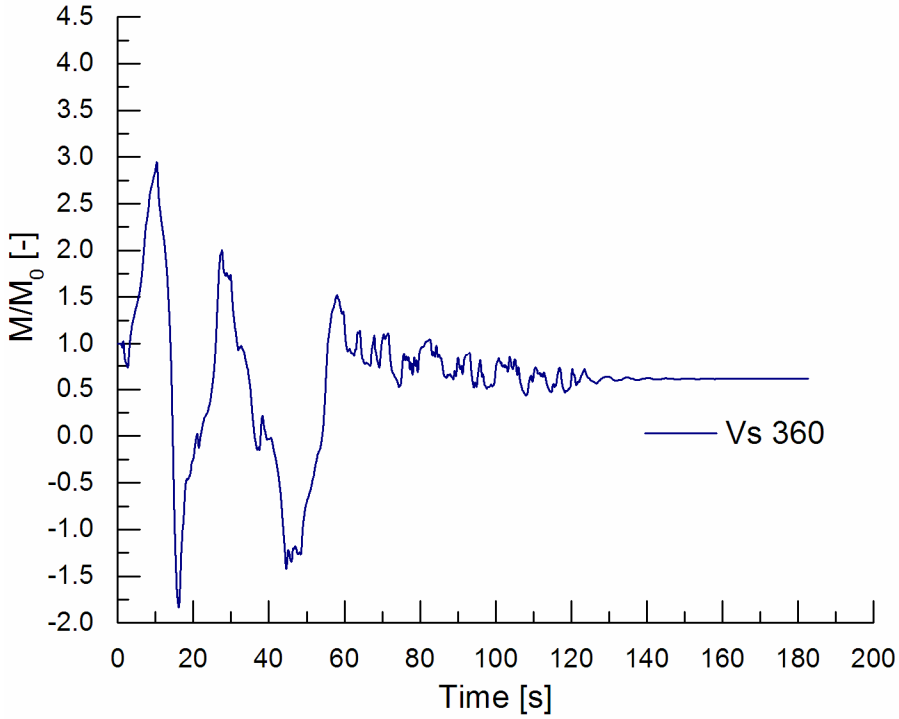

Figure 179: Coupled approach: ratio between the value of the initial bending moment and the value of the bending moment during the Lima seismic event acting on the section in correspondence to the central slab in the right retaining wall

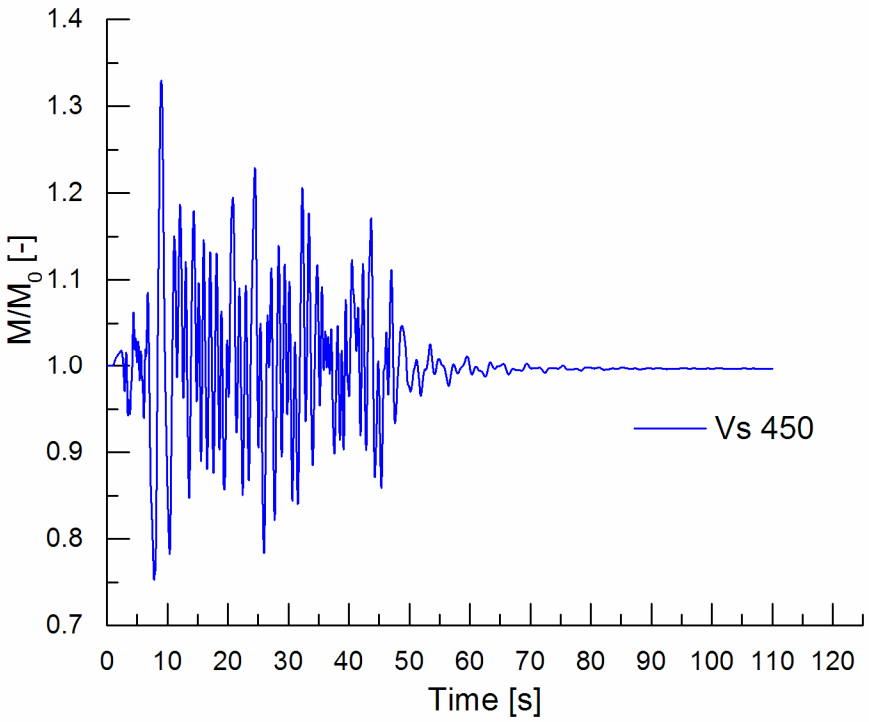

Figure 180: Coupled approach: ratio between the value of the initial bending moment and the value of the bending moment during the Montenegro seismic event acting on the section in correspondence to the central slab in the left retaining wall

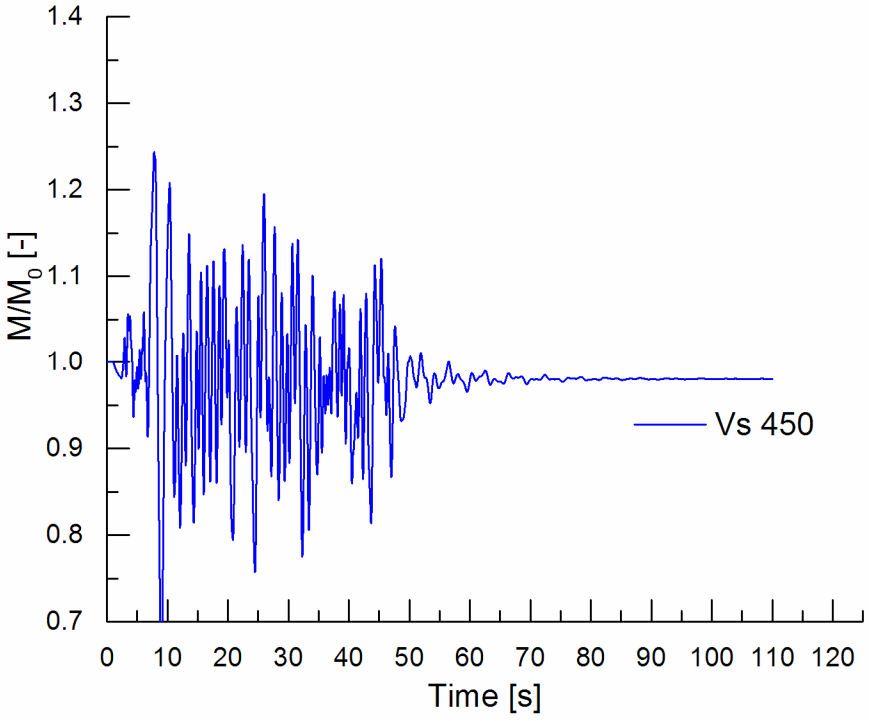

Figure 181: Coupled approach: ratio between the value of the initial bending moment and the value of the bending moment during the Montenegro seismic event acting on the section in correspondence to the central slab in the right retaining wall

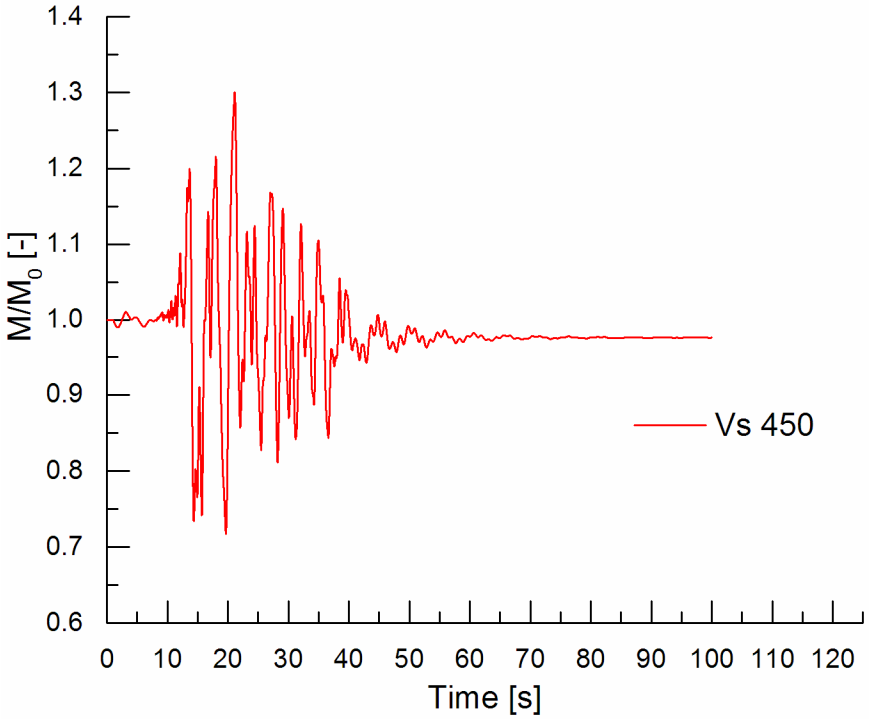

Figure 182: Coupled approach: ratio between the value of the initial bending moment and the value of the bending moment during the Amatrice seismic event acting on the section in correspondence to the central slab in the left retaining wall

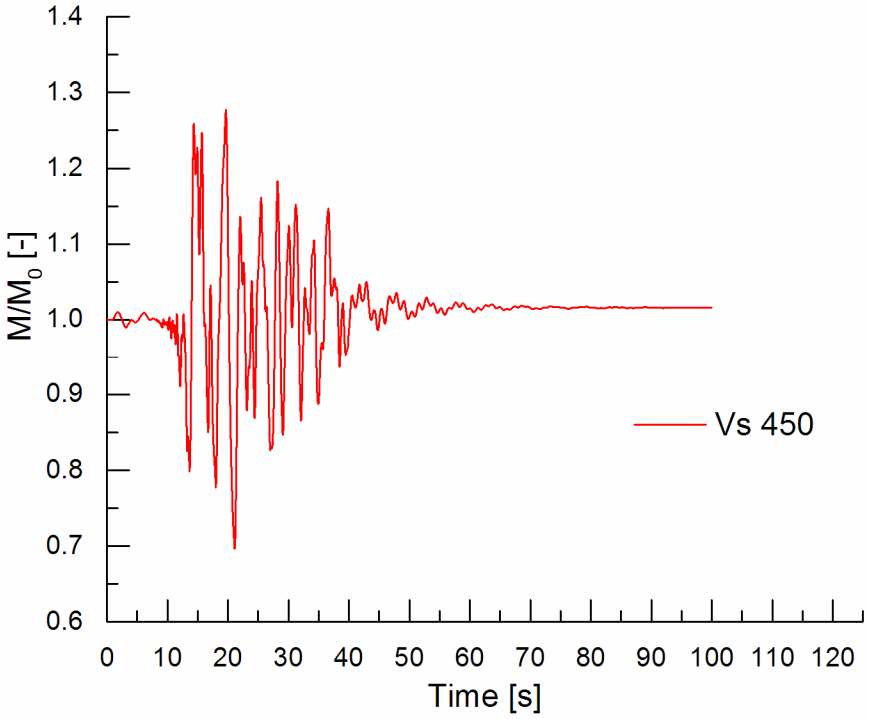

Figure 183: Coupled approach: ratio between the value of the initial bending moment and the value of the bending moment during the Amatrice seismic event acting on the section in correspondence to the central slab in the right retaining wall

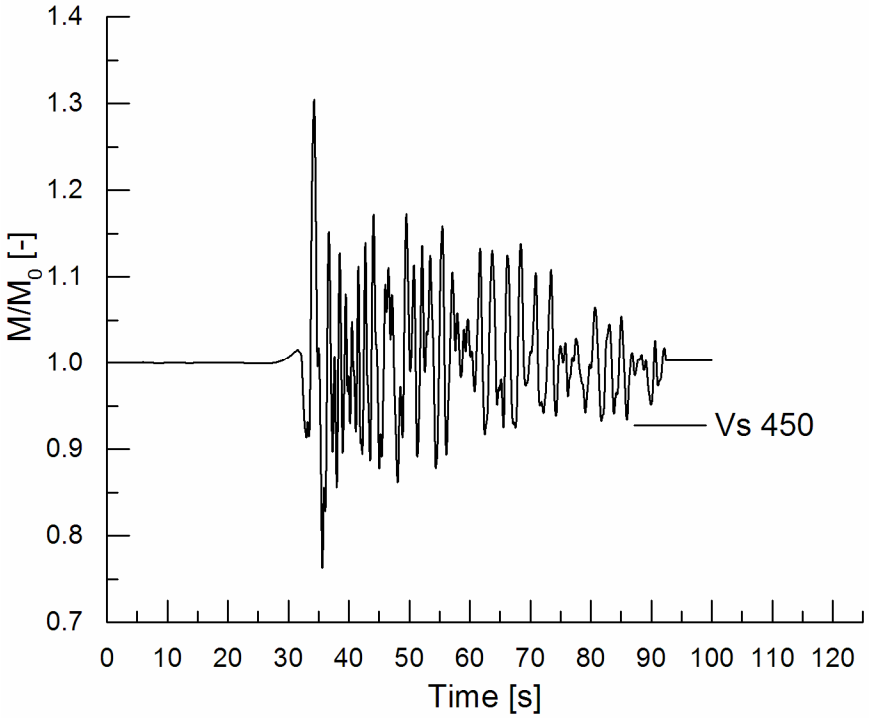

Figure 184: Coupled approach: ratio between the value of the initial bending moment and the value of the bending moment during the L'Aquila seismic event acting on the section in correspondence to the central slab in the left retaining wall

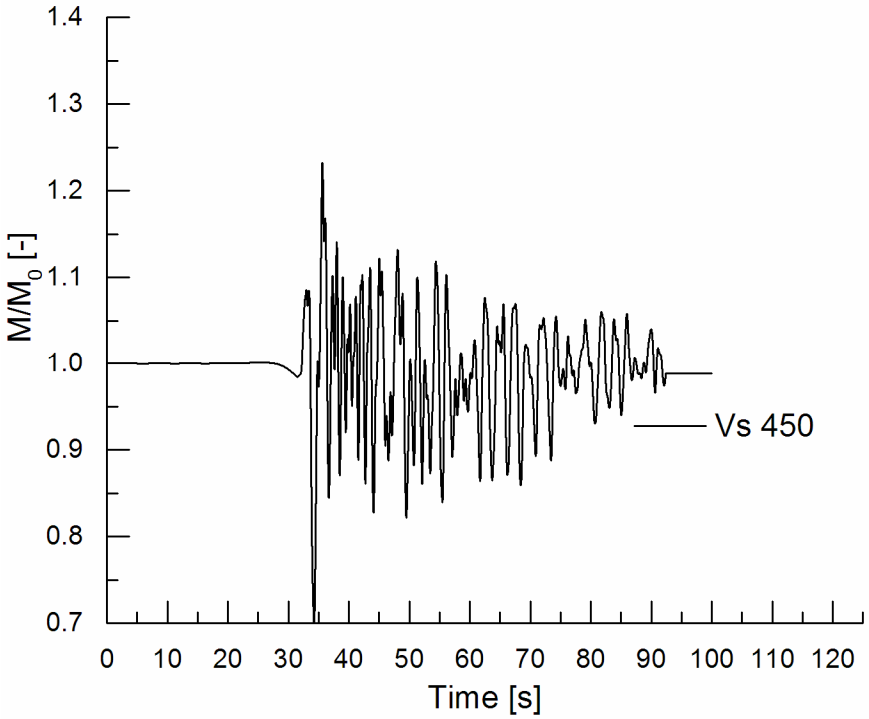

Figure 185: Coupled approach: ratio between the value of the initial bending moment and the value of the bending moment during the L'Aquila seismic event acting on the section in correspondence to the central slab in the right retaining wall

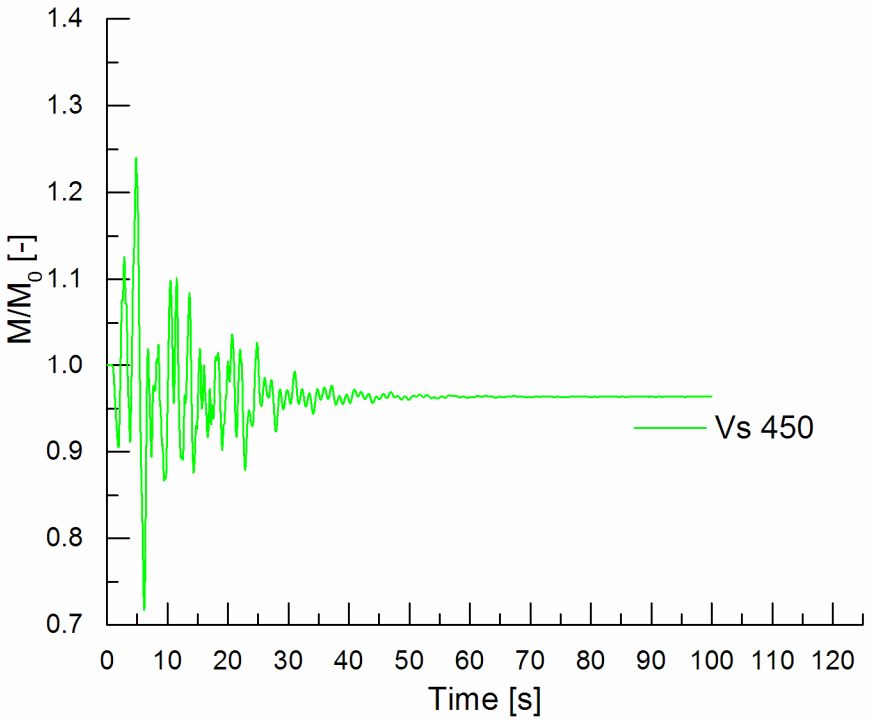

Figure 186: Coupled approach: ratio between the value of the initial bending moment and the value of the bending moment during the Friuli seismic event acting on the section in correspondence to the central slab in the left retaining wall

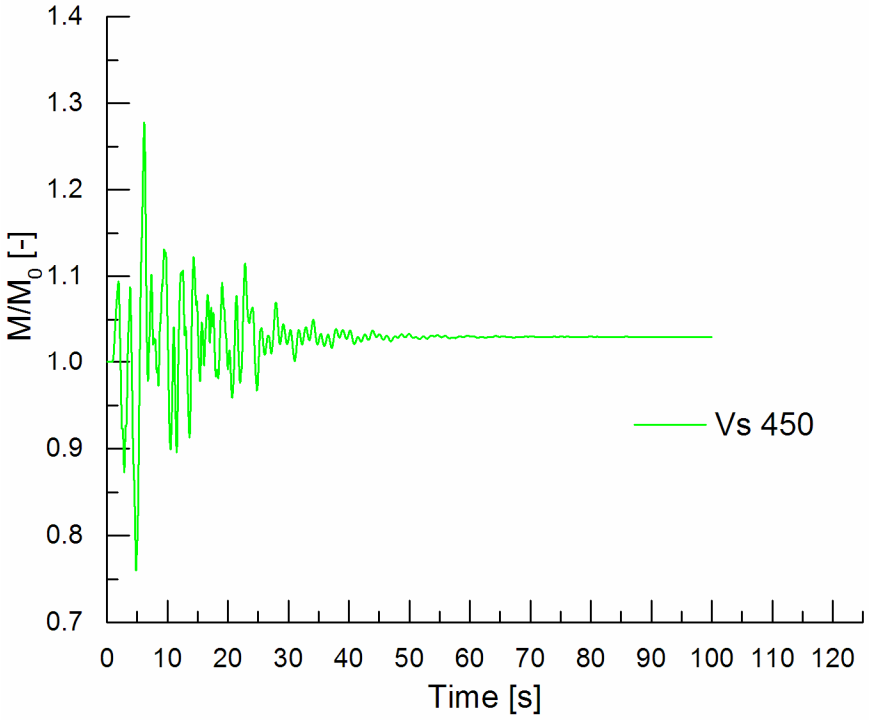

Figure 187: Coupled approach: ratio between the value of the initial bending moment and the value of the bending moment during the Friuli seismic event acting on the section in correspondence to the central slab in the right retaining wall

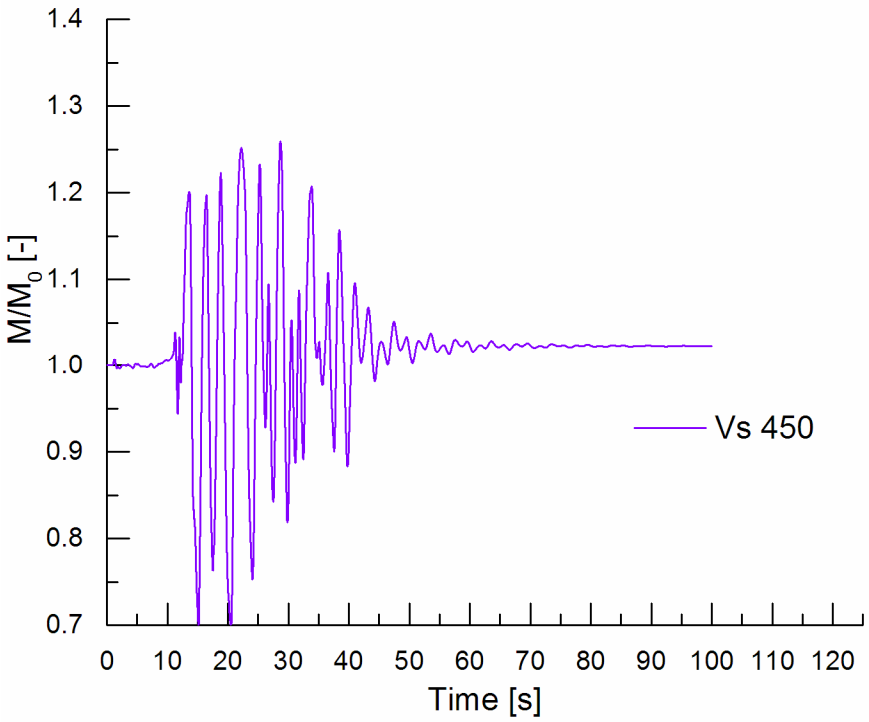

Figure 188: Coupled approach: ratio between the value of the initial bending moment and the value of the bending moment during the Greece seismic event acting on the section in correspondence to the central slab in the left retaining wall

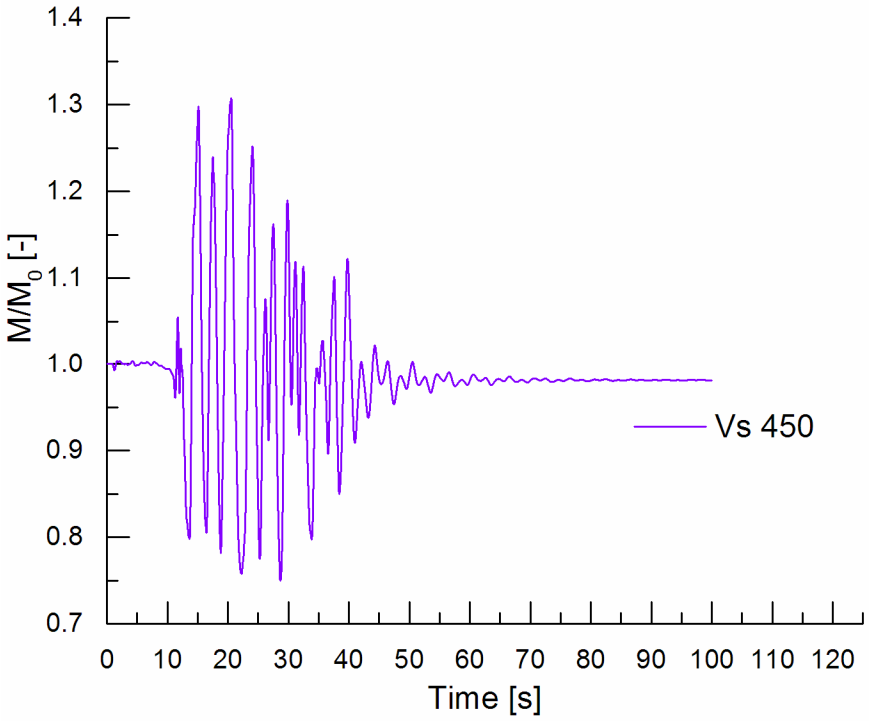

Figure 189: Coupled approach: ratio between the value of the initial bending moment and the value of the bending moment during the Greece seismic event acting on the section in correspondence to the central slab in the right retaining wall

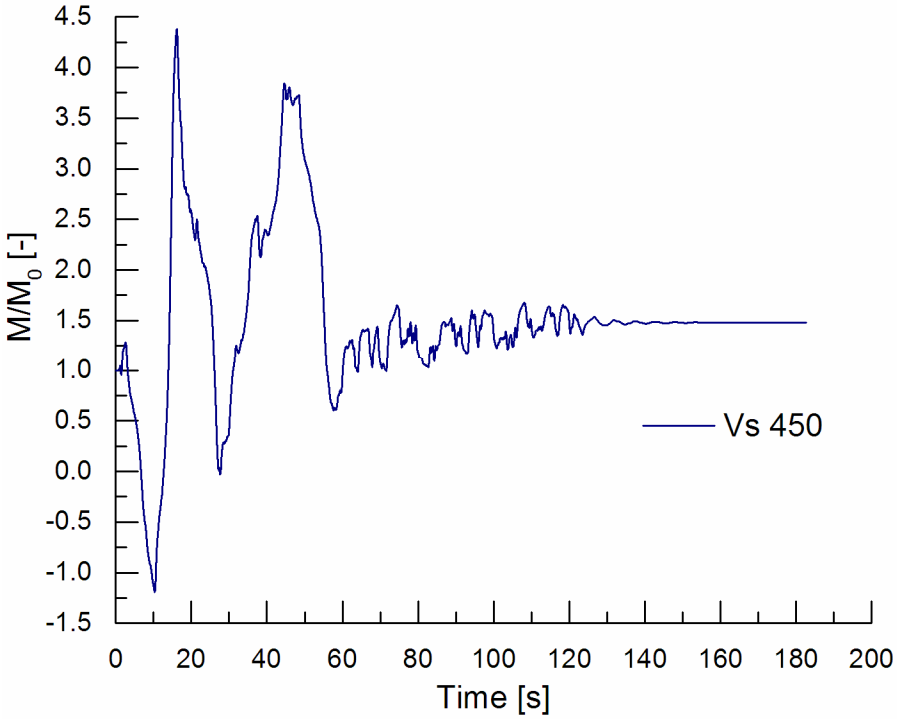

Figure 190: Coupled approach: ratio between the value of the initial bending moment and the value of the bending moment during the Lima seismic event acting on the section in correspondence to the central slab in the left retaining wall

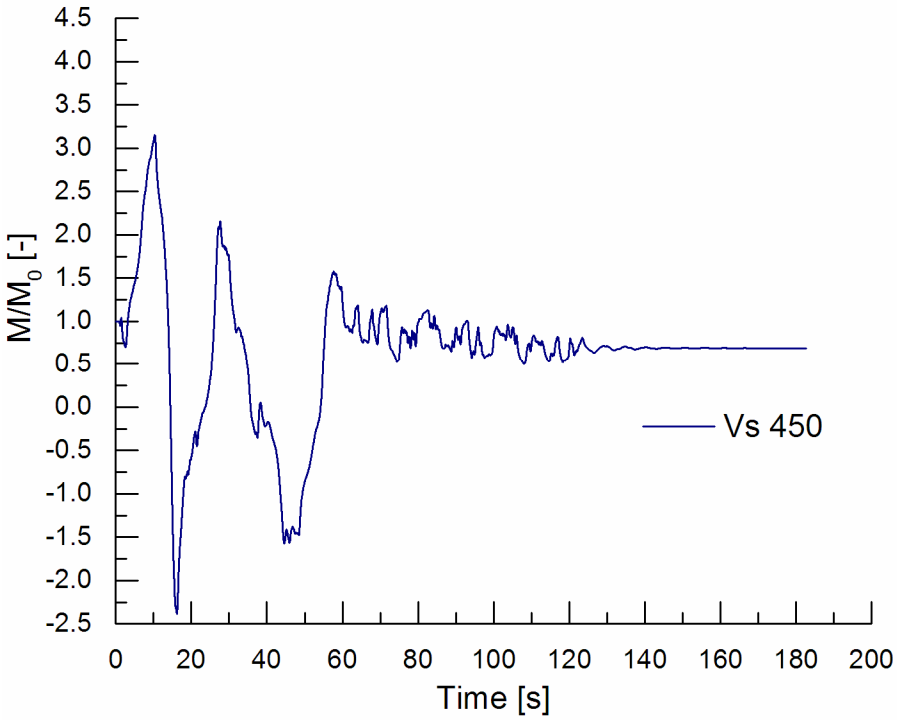

Figure 191: Coupled approach: ratio between the value of the initial bending moment and the value of the bending moment during the Lima seismic event acting on the section in correspondence to the central slab in the right retaining wall

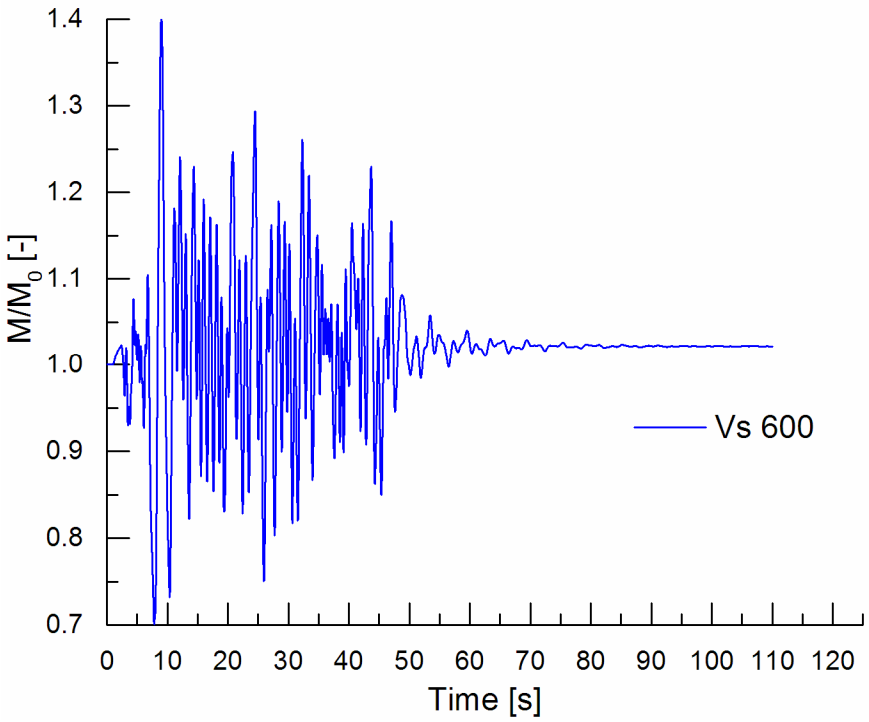

Figure 192: Coupled approach: ratio between the value of the initial bending moment and the value of the bending moment during the Montenegro seismic event acting on the section in correspondence to the central slab in the left retaining wall

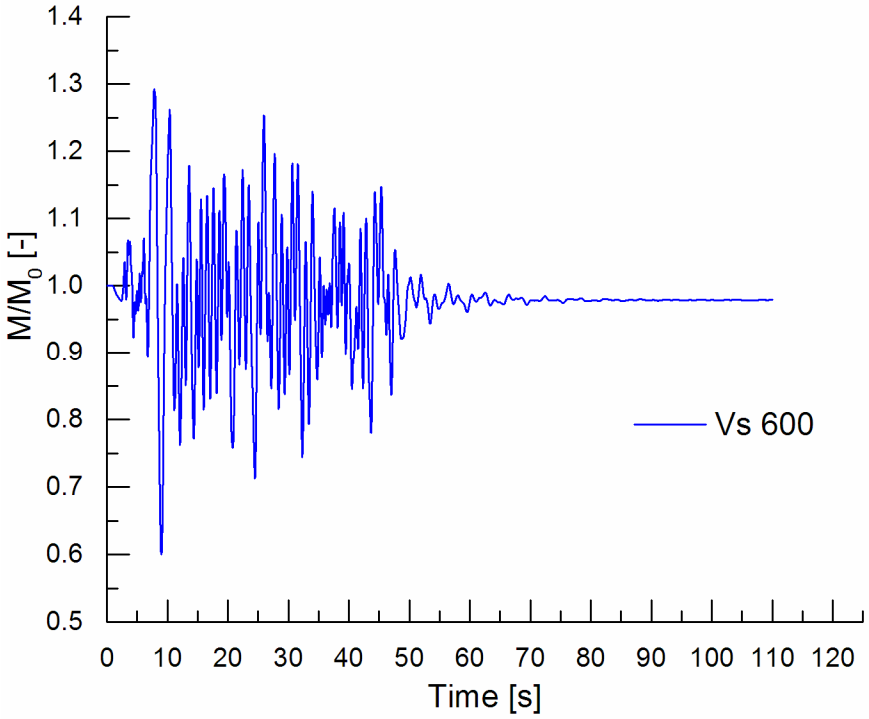

Figure 193: Coupled approach: ratio between the value of the initial bending moment and the value of the bending moment during the Montenegro seismic event acting on the section in correspondence to the central slab in the right retaining wall

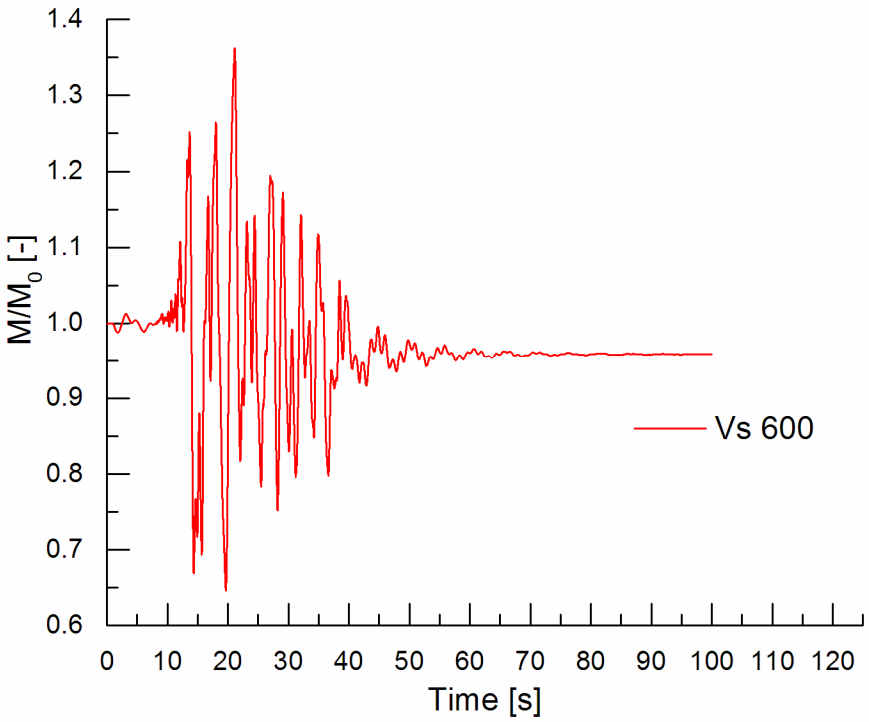

Figure 194: Coupled approach: ratio between the value of the initial bending moment and the value of the bending moment during the Amatrice seismic event acting on the section in correspondence to the central slab in the left retaining wall

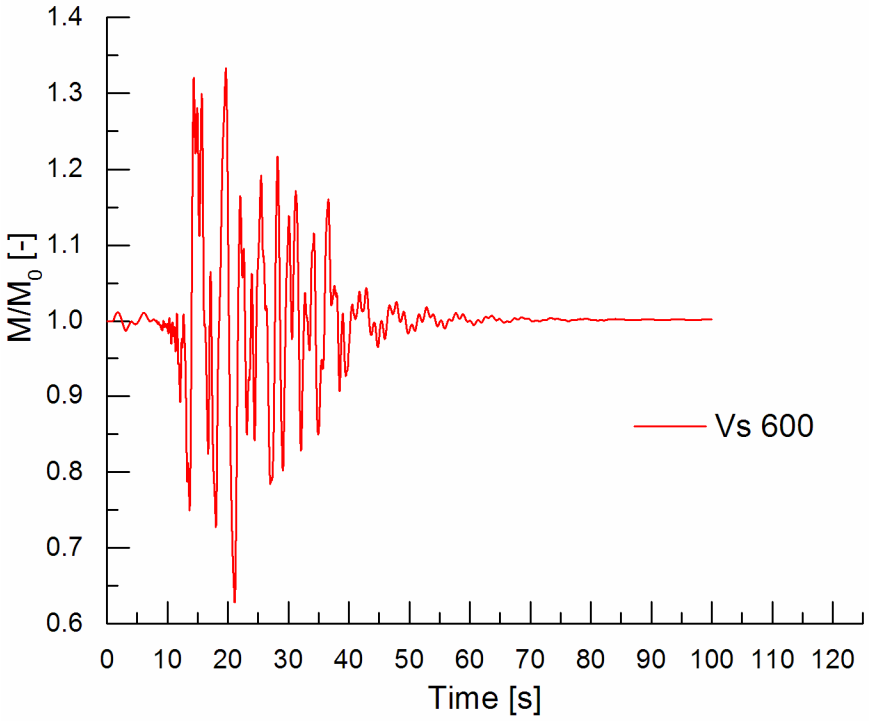

Figure 195: Coupled approach: ratio between the value of the initial bending moment and the value of the bending moment during the Amatrice seismic event acting on the section in correspondence to the central slab in the right retaining wall

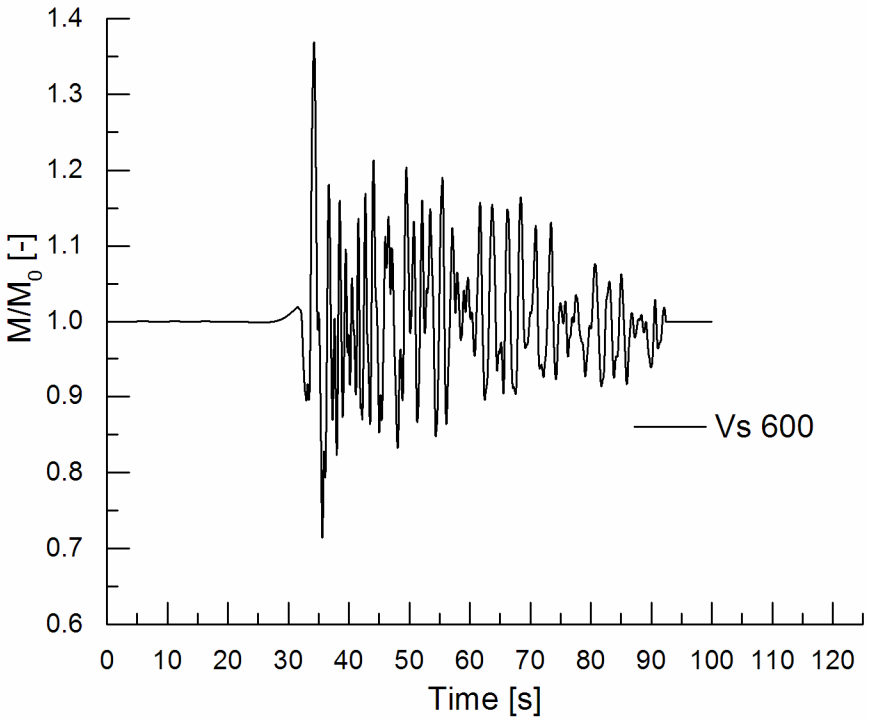

Figure 196: Coupled approach: ratio between the value of the initial bending moment and the value of the bending moment during the L'Aquila seismic event acting on the section in correspondence to the central slab in the left retaining wall

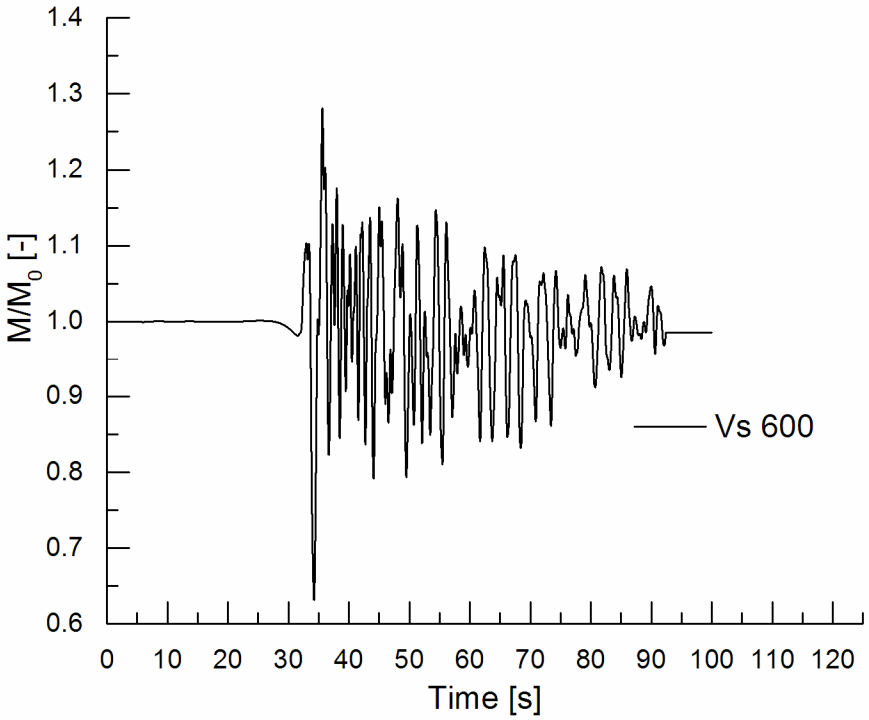

Figure 197: Coupled approach: ratio between the value of the initial bending moment and the value of the bending moment during the L'Aquila seismic event acting on the section in correspondence to the central slab in the right retaining wall

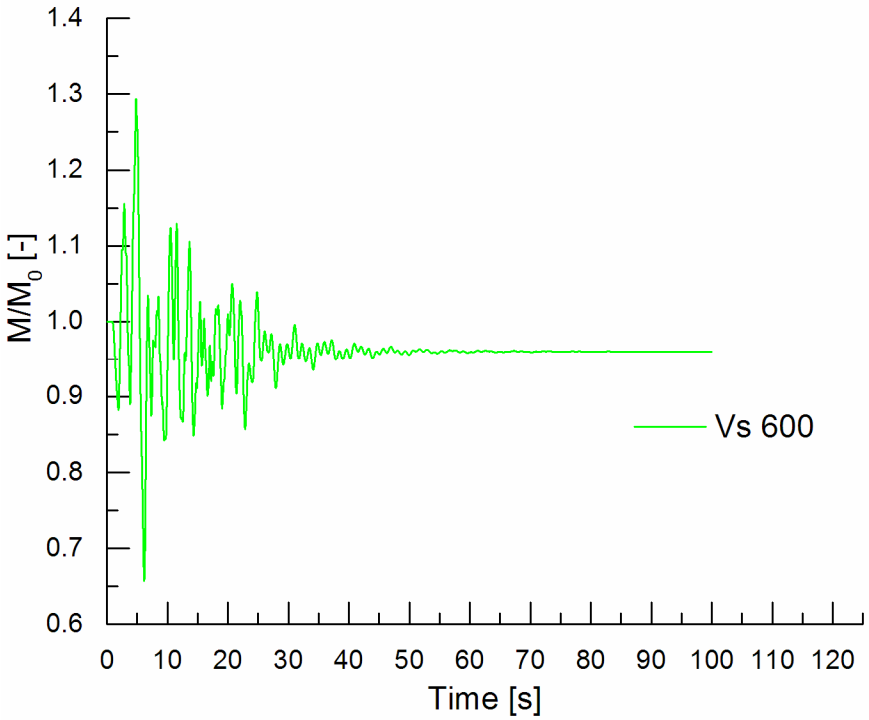

Figure 198: Coupled approach: ratio between the value of the initial bending moment and the value of the bending moment during the Firuli seismic event acting on the section in correspondence to the central slab in the left retaining wall

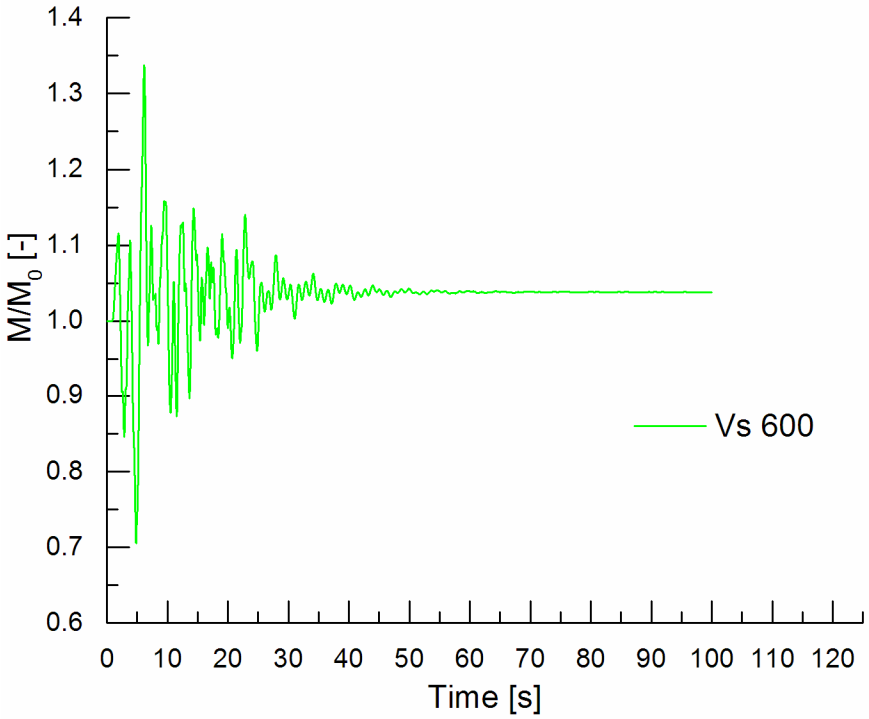

Figure 199: Coupled approach: ratio between the value of the initial bending moment and the value of the bending moment during the Firuli seismic event acting on the section in correspondence to the central slab in the right retaining wall

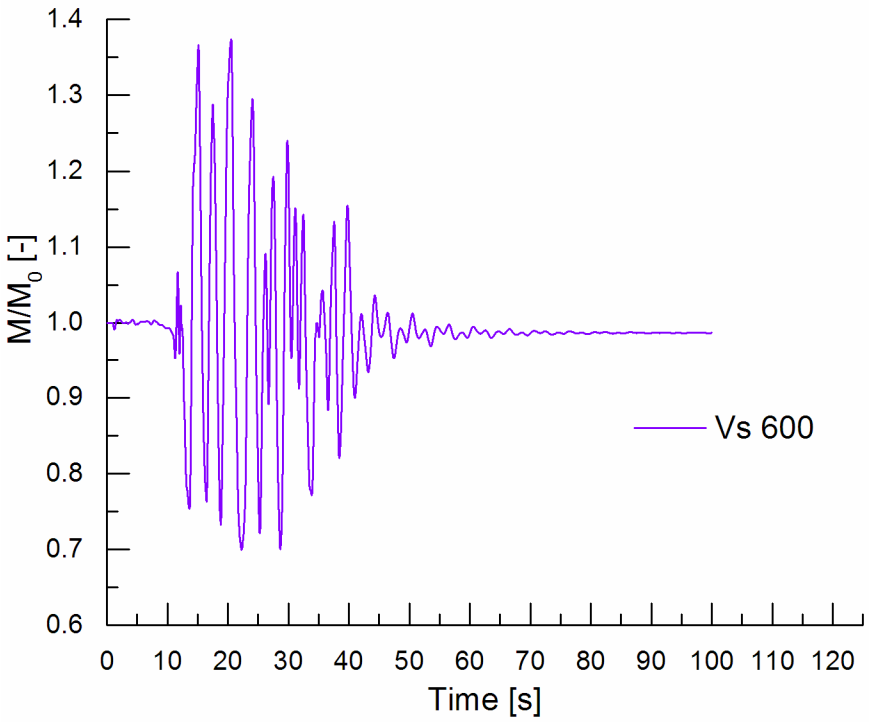

Figure 200: Coupled approach: ratio between the value of the initial bending moment and the value of the bending moment during the Greece seismic event acting on the section in correspondence to the central slab in the left retaining wall

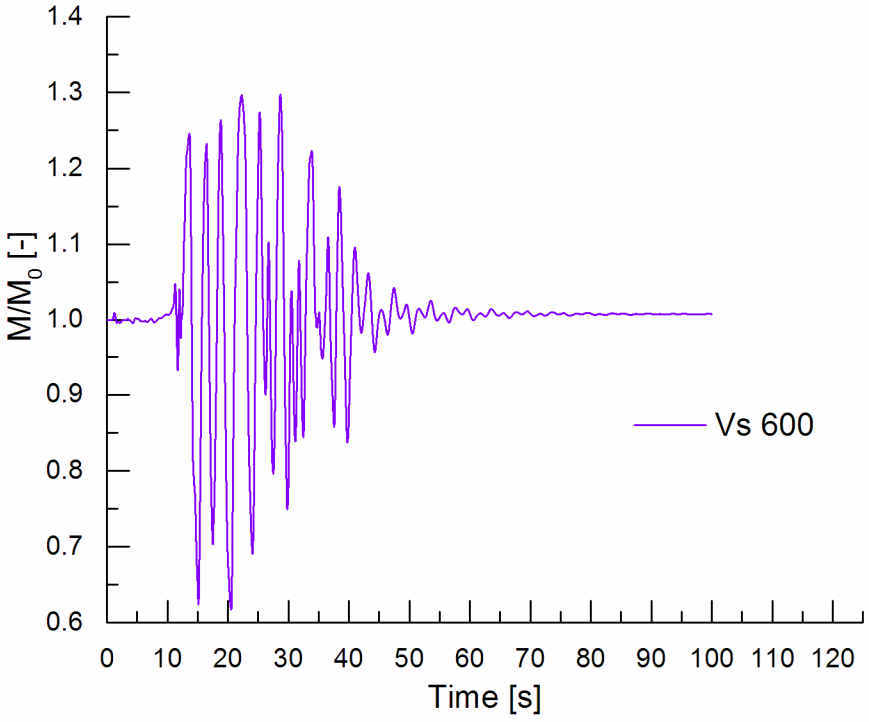

Figure 201: Coupled approach: ratio between the value of the initial bending moment and the value of the bending moment during the Greece seismic event acting on the section in correspondence to the central slab in the right retaining wall

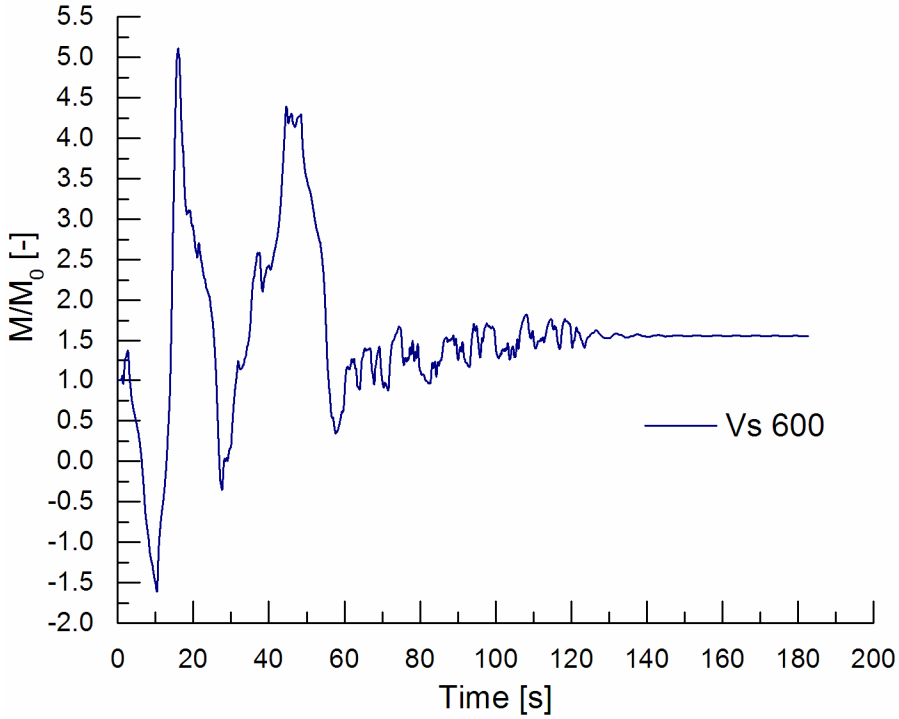

Figure 202: Coupled approach: ratio between the value of the initial bending moment and the value of the bending moment during the Lima seismic event acting on the section in correspondence to the central slab in the left retaining wall

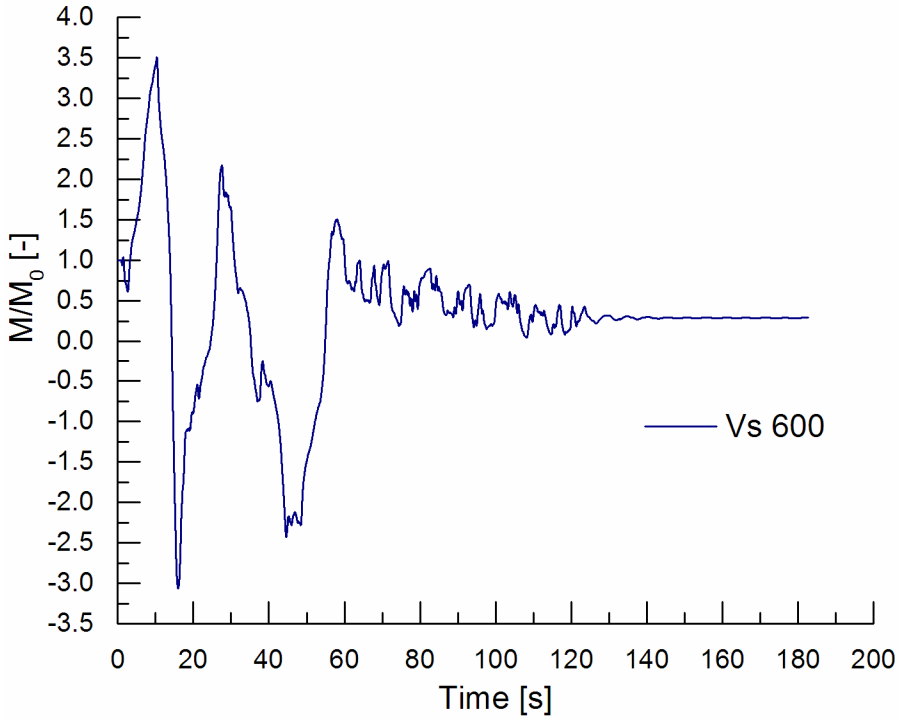

Figure 203: Coupled approach: ratio between the value of the initial bending moment and the value of the bending moment during the Lima seismic event acting on the section in correspondence to the central slab in the right retaining wall

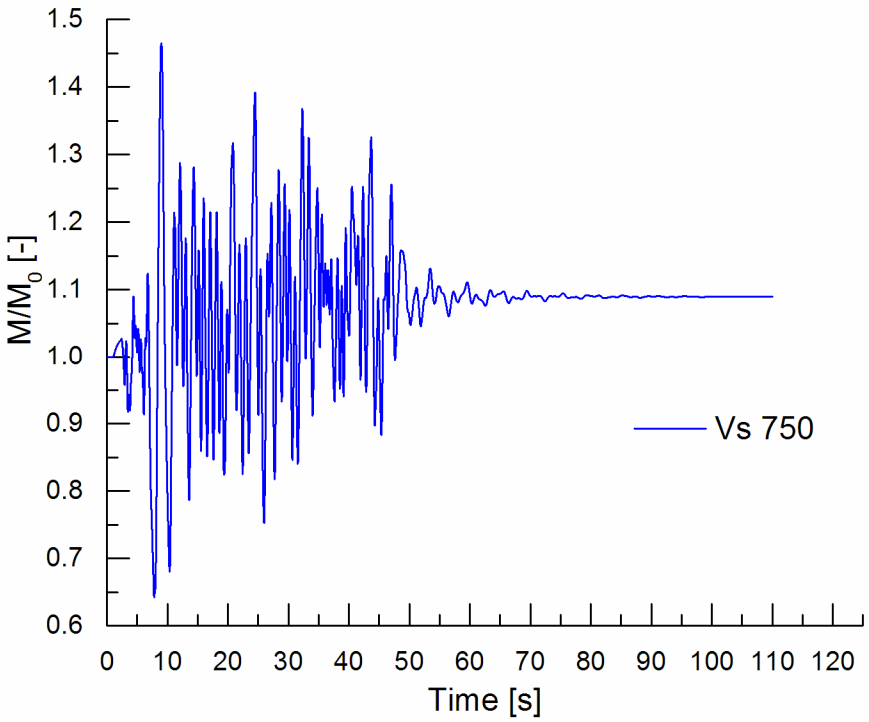

Figure 204: Coupled approach: ratio between the value of the initial bending moment and the value of the bending moment during the Montenegro seismic event acting on the section in correspondence to the central slab in the left retaining wall

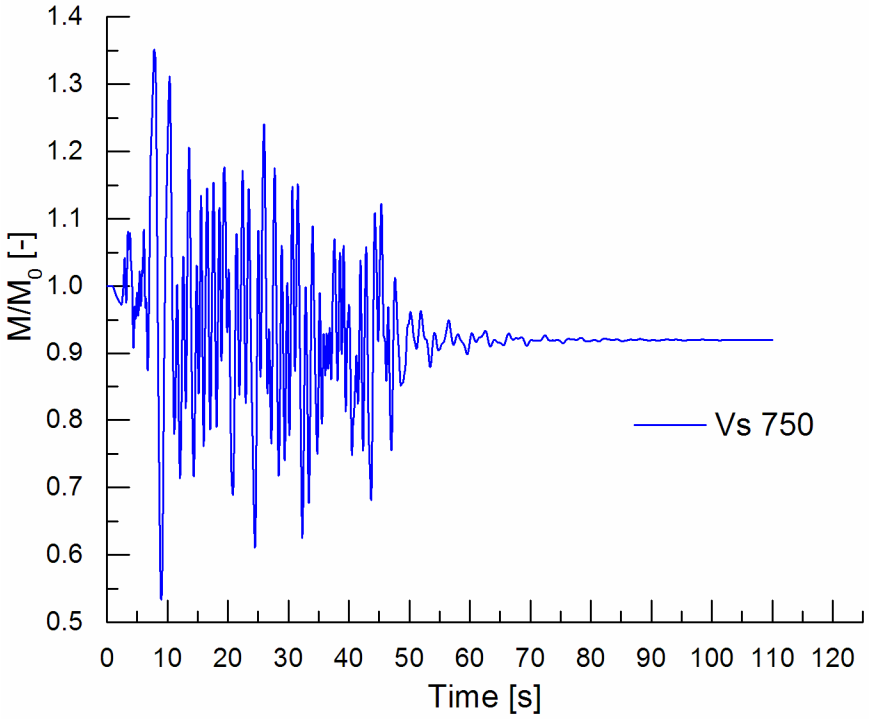

Figure 205: Coupled approach: ratio between the value of the initial bending moment and the value of the bending moment during the Montenegro seismic event acting on the section in correspondence to the central slab in the right retaining wall

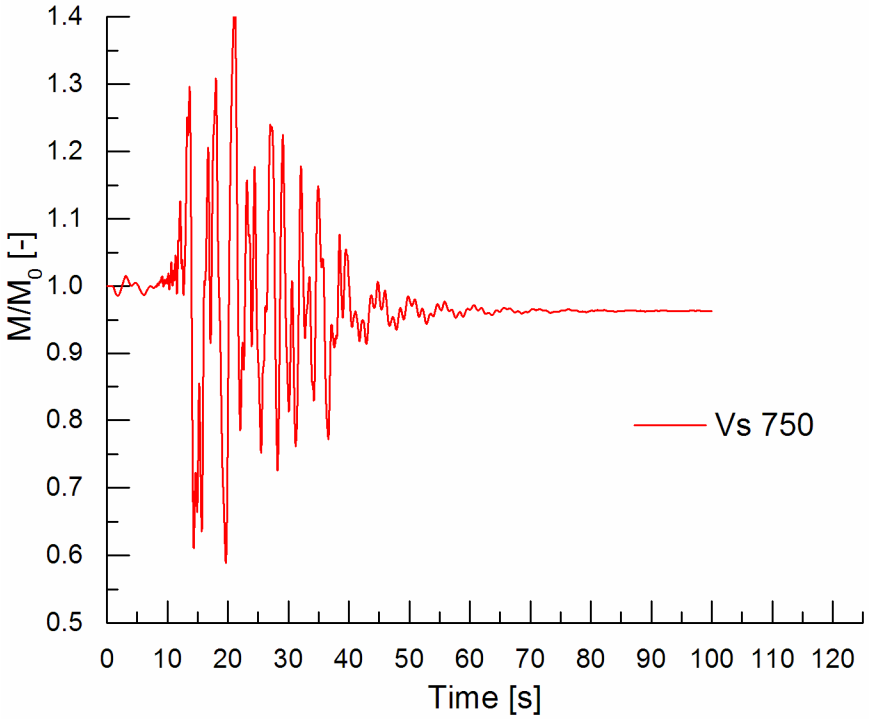

Figure 206: Coupled approach: ratio between the value of the initial bending moment and the value of the bending moment during the Amatrice seismic event acting on the section in correspondence to the central slab in the left retaining wall

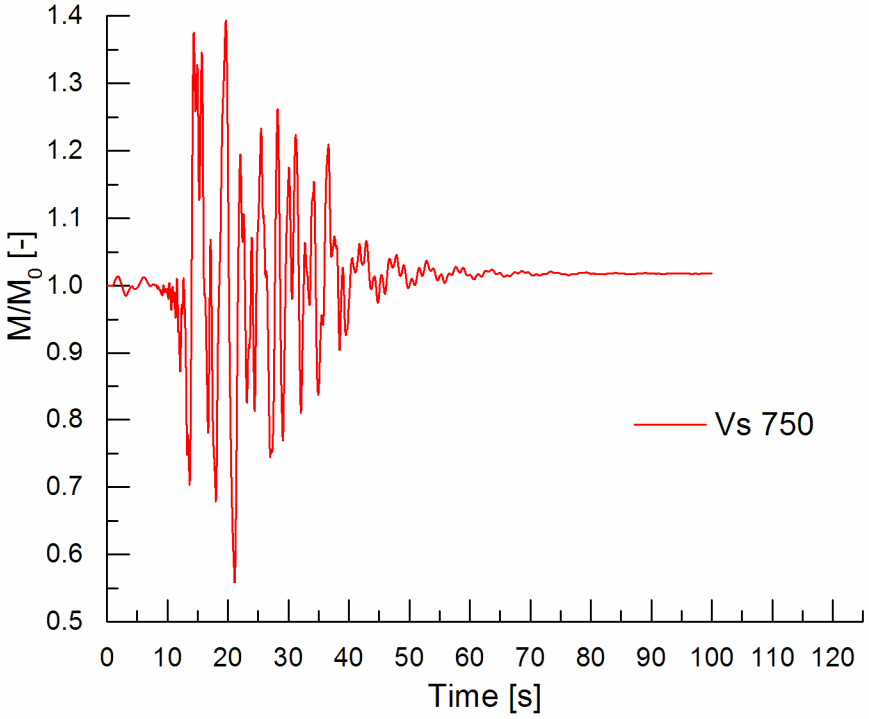

Figure 207: Coupled approach: ratio between the value of the initial bending moment and the value of the bending moment during the Amatrice seismic event acting on the section in correspondence to the central slab in the right retaining wall

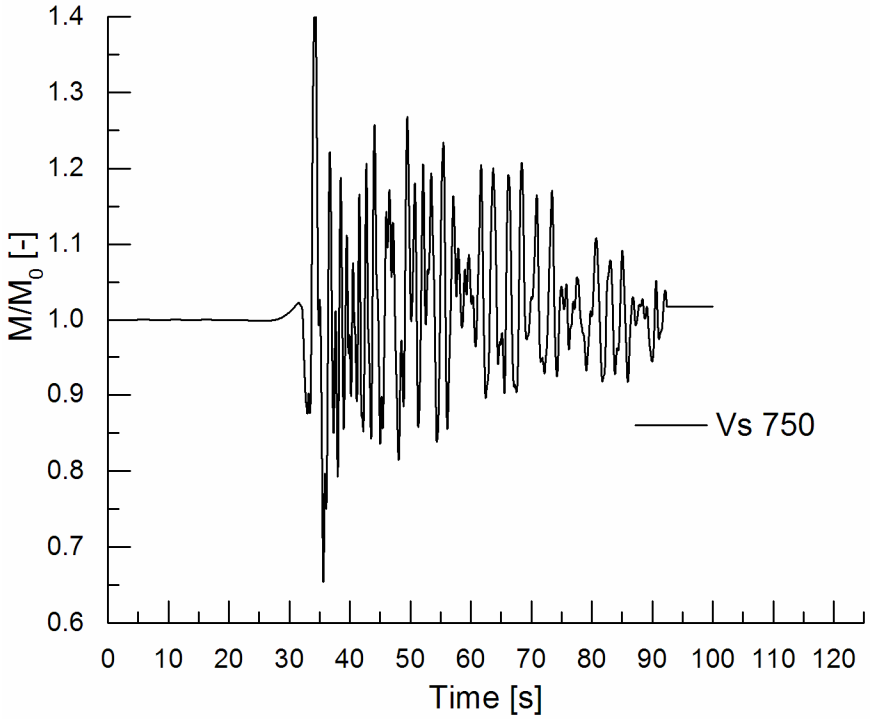

Figure 208: Coupled approach: ratio between the value of the initial bending moment and the value of the bending moment during the L'Aquila seismic event acting on the section in correspondence to the central slab in the left retaining wall

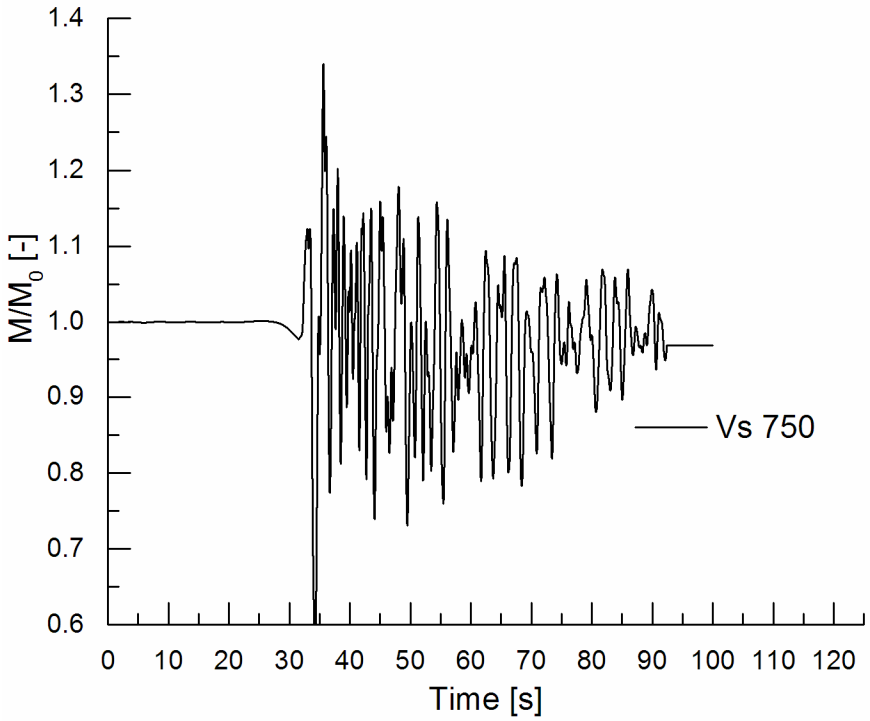

Figure 209: Coupled approach: ratio between the value of the initial bending moment and the value of the bending moment during the L'Aquila seismic event acting on the section in correspondence to the central slab in the right retaining wall

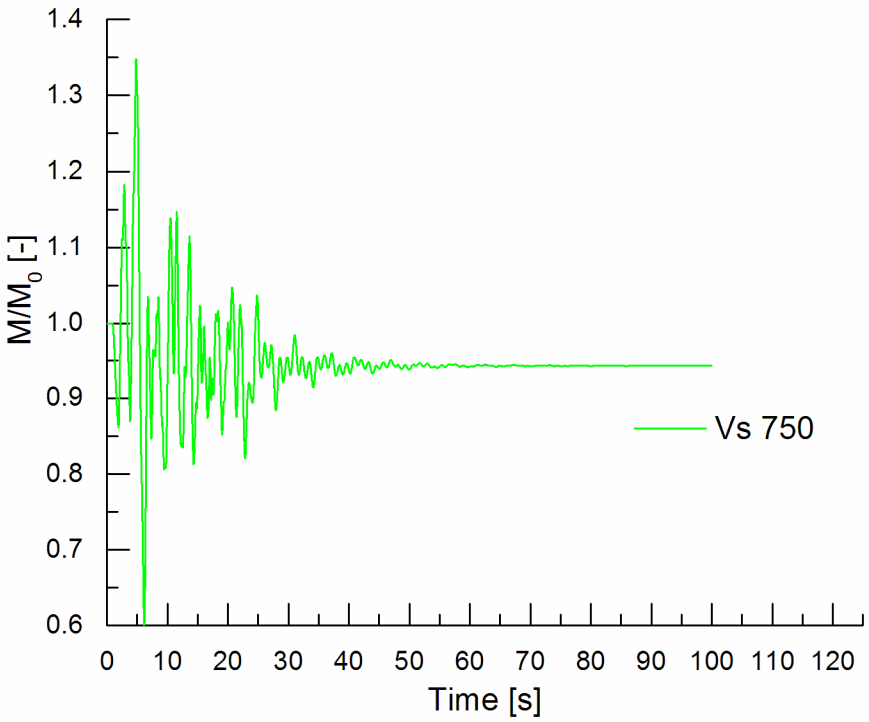

Figure 210: Coupled approach: ratio between the value of the initial bending moment and the value of the bending moment during the Friuli seismic event acting on the section in correspondence to the central slab in the left retaining wall

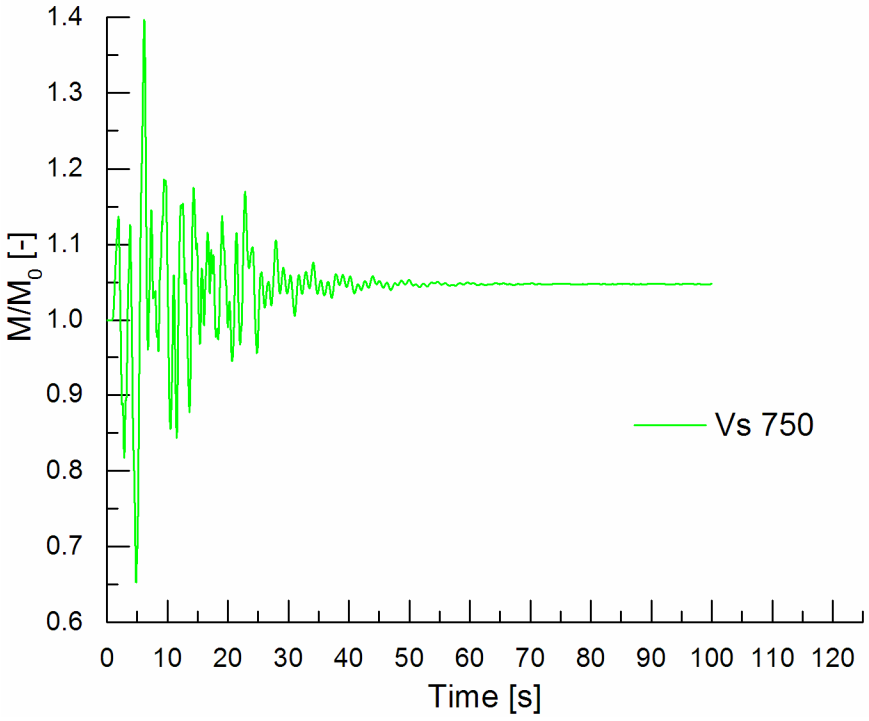

Figure 211: Coupled approach: ratio between the value of the initial bending moment and the value of the bending moment during the Friuli seismic event acting on the section in correspondence to the central slab in the right retaining wall

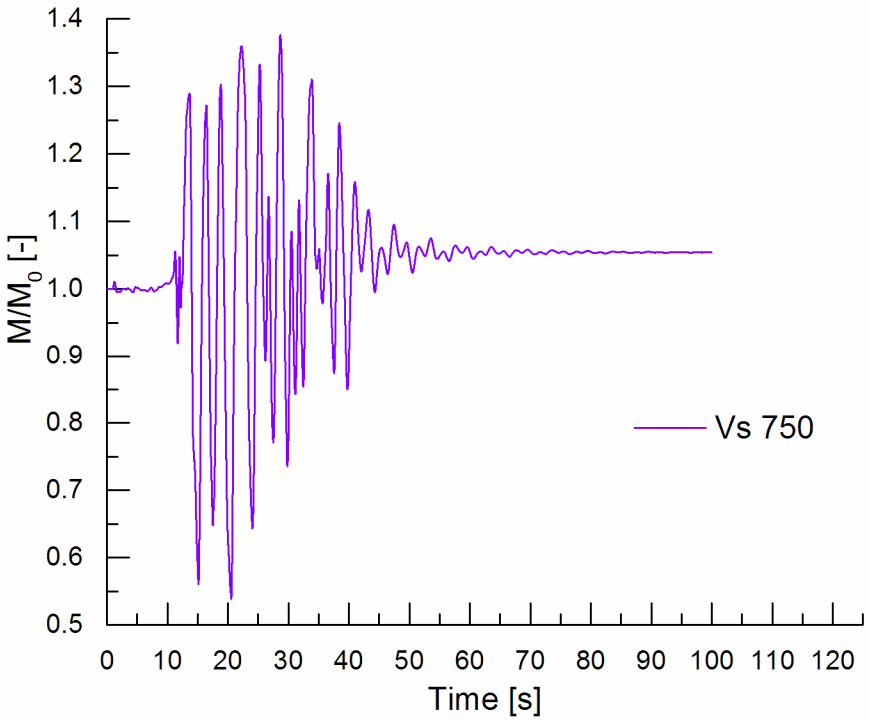

Figure 212: Coupled approach: ratio between the value of the initial bending moment and the value of the bending moment during the Greece seismic event acting on the section in correspondence to the central slab in the left retaining wall

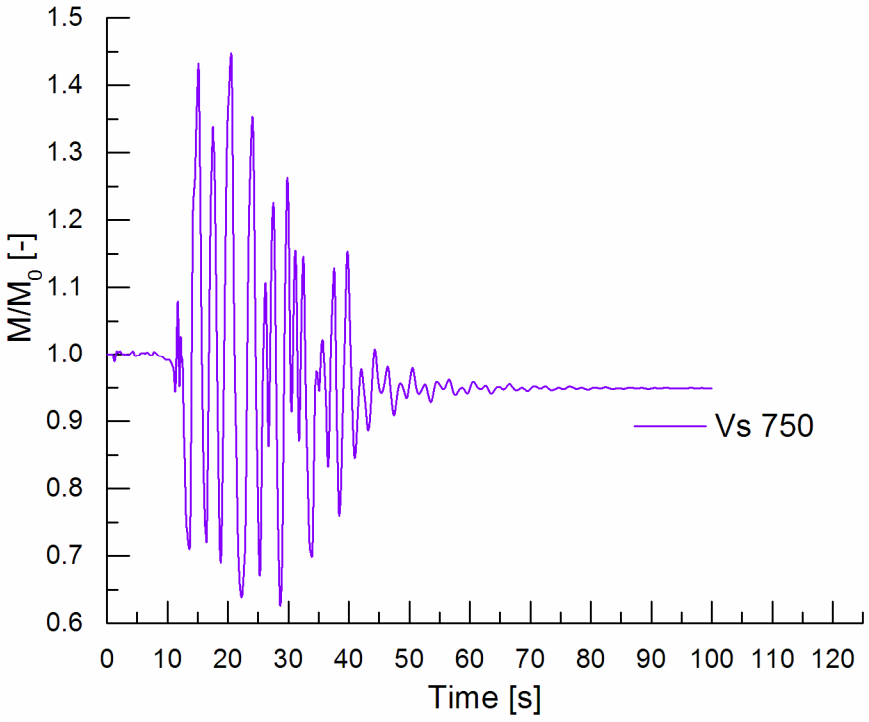

Figure 213: Coupled approach: ratio between the value of the initial bending moment and the value of the bending moment during the Greece seismic event acting on the section in correspondence to the central slab in the right retaining wall

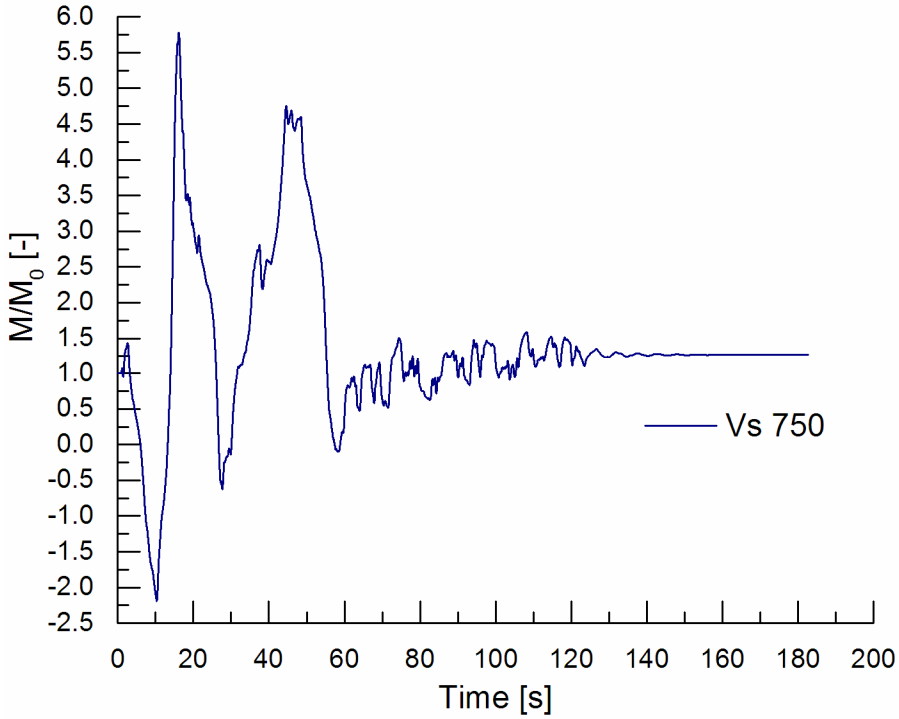

Figure 214: Coupled approach: ratio between the value of the initial bending moment and the value of the bending moment during the Lima seismic event acting on the section in correspondence to the central slab in the left retaining wall

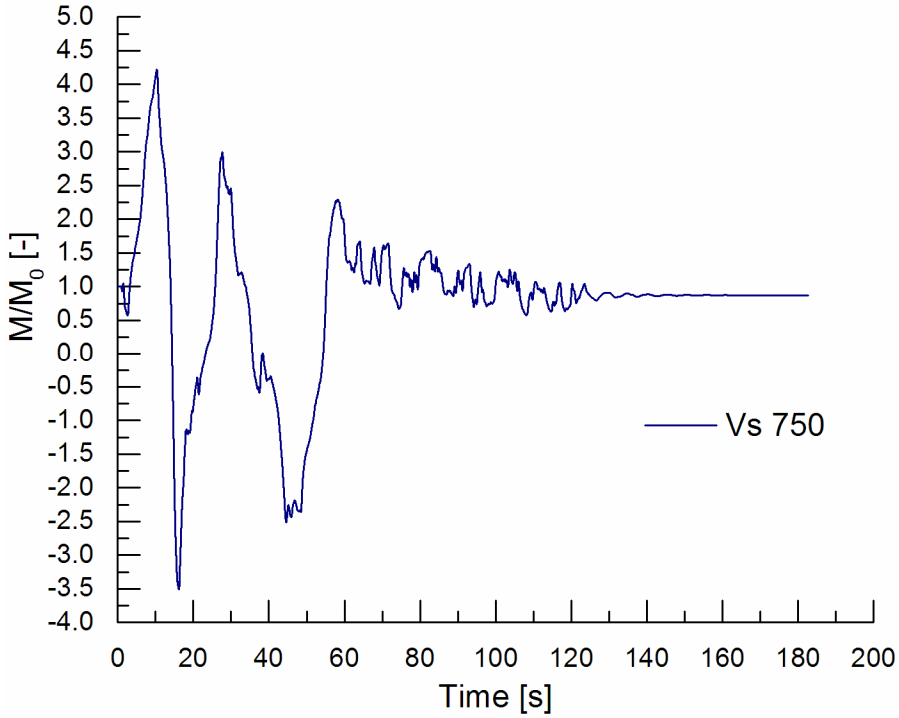

Figure 215: Coupled approach: ratio between the value of the initial bending moment and the value of the bending moment during the Lima seismic event acting on the section in correspondence to the central slab in the right retaining wall

Table 17: Comparison between the initial and the residual moment acting on the section in correspondence of the central slab

MONTENEGRO				
Profile		**Moment**		
Vs		**Initial**	**Residual**	Δ
[m/s]		[kNm]	[kNm]	[%]
360	**L**	518	540	**4**
	R	518	493	**-5**
450	**L**	451	457	**1**
	R	451	444	**-2**
600	**L**	370	378	**2**
	R	370	366	**-1**
750	**L**	312	340	**9**
	R	312	289	**-7**

GREECE				
Profile		**Moment**		
Vs		**Initial**	**Residual**	Δ
[m/s]		[kNm]	[kNm]	[%]
360	**L**	518	529	**2**
	R	518	503	**-3**
450	**L**	451	462	**3**
	R	451	445	**-1**
600	**L**	370	373	**1**
	R	370	367	**-1**
750	**L**	312	330	**6**
	R	312	298	**-4**

AMATRICE				
Profile		**Moment**		
Vs		**Initial**	**Residual**	Δ
[m/s]		[kNm]	[kNm]	[%]
360	**L**	518	503	**-3**
	R	518	521	**1**
450	**L**	451	441	**-2**
	R	451	461	**2**
600	**L**	370	355	**-4**
	R	370	375	**1**
750	**L**	312	301	**4**
	R	312	320	**3**

L'AQUILA				
Profile		**Moment**		
Vs		**Initial**	**Residual**	Δ
[m/s]		[kNm]	[kNm]	[%]
360	**L**	518	530	**2**
	R	518	510	**-2**
450	**L**	451	453	**1**
	R	451	448	**-1**
600	**L**	370	370	**0**
	R	370	368	**-1**
750	**L**	312	318	**2**
	R	312	305	**-2**

FRIULI				
Profile		**Moment**		
Vs		**Initial**	**Residual**	Δ
[m/s]		[kNm]	[kNm]	[%]
360	L	518	500	**-4**
	R	518	529	**2**
450	L	451	435	**-4**
	R	451	467	**4**
600	L	370	355	**-4**
	R	370	388	**5**
750	L	312	295	**-6**
	R	312	329	**5**

LIMA				
Profile		**Moment**		
Vs		**Initial**	**Residual**	Δ
[m/s]		[kNm]	[kNm]	[%]
360	**L**	518	710	**37**
	R	518	316	**-39**
450	**L**	451	668	**48**
	R	451	313	**-31**
600	**L**	370	577	**56**
	R	370	109	**-71**
750	**L**	312	397	**27**
	R	312	274	**-12**

4. CASE STUDY: LIMA METRO LINE 2

4.1. Project description

The new Lima Metro line 2 is the first underground structure project in Perù. The area where the Lima Metro line 2 is located extends from Puerto del Callao (near the harbor) to Municipalidad de Ate. The total length of the line is about 26.87 km and the tunnel length is about 21 km, where 13.60 km are excavated with tunnel boring machine (TBM) and the remaining with the new Austrian tunneling method (NATM). The project includes 27 stations realized by Cut and Cover method (Table 18).
The project involves the realization of the first part of the Lima Metro line 4 (Figure 216), totally excavated with TBM and the stations are realized by Cut and Cover method.
The characteristics of the tunnel supports and the construction types of the stations depend on geological and geotechnical conditions and on the possible presence of water.

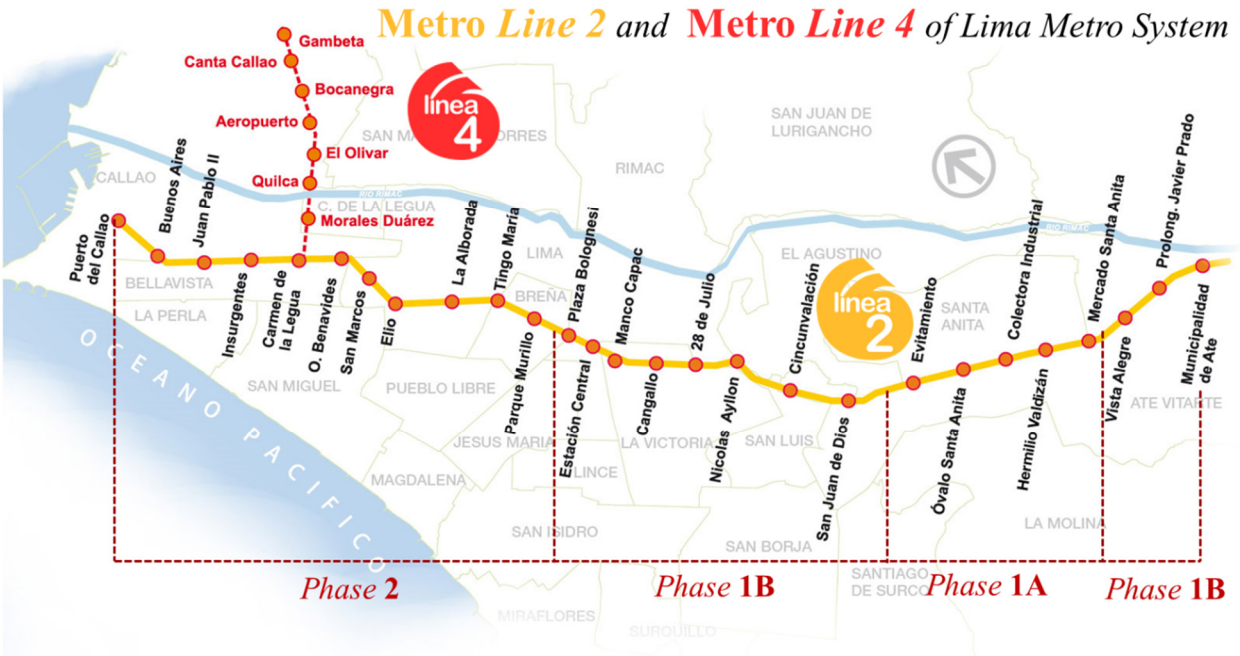

Figure 216: Lima Metro Line 2

Table 18: Numbers of the project

	METRO *Line 2*	METRO *Line 4*
Number of Stations	27	8
Number of Shafts	26 + 2	7 + 2
Line Total Length	26.87 km	7.65 km
Tunnel Excavated with TBM	13.60 km	5.10 km
Tunnel Excavated with N.A.T.M.	7.40 km	-
Stations Erected with C & C	27	8

The construction phase will be developed in two distinct phases:
- Phase 1: expected to be completed within 4 years after the start of construction (year 2018 in the estimated schedule):
  - phase 1A is expected to be operational in February 2017 as it requires 3 years of construction;
  - phase 1B is expected to be completed within 4/5 years after the start of construction (year 2018 in the estimated schedule).
- Phase 2: is expected to be completed in about 6 years after the start of construction (year 2020 in the estimated schedule).

4.2. Hydrogeological, geological and geotechnical framing

The soils in the project area were interested by different surveys, in particular in the part of the line involved in the phase 1A: 16 drilling, 7 test pits (5 to 10 meters deep) in order to determinate the soil stratigraphy and 16 seismic tomographies that include seismic refraction lines (70 to 140 m length) and MASW in order to evaluate the seismic waves velocity and for the acquisition of seismic profile, were performed.
The investigations have shown the sequence of these following lithological units (Table 19) having different mechanical proprierties:

- a backfill consisting of silty sands with gravels and anthropically reworked materials;
- inorganic clay of low to medium plasticity and inorganic silt of low plasticity;
- silty sand;
- poorly graded gravel with sand, clay and silt;
- diorite, tonalite and philonian rocks.

Table 19: Mechanical proprierties of lithological units

Soil type	**γ**	**W**	**% passant # 0.08 mm**	**LL**	**IP**	**c'**	**φ'**	**V_s**	**E_{max}**	**E_{static}**	**ν**
	[kN/m^3]	[%]	[%]	[%]	[%]	[kPa]	[°]	[m/s^2]	[MPa]	[MPa]	[-]
Backfill	16.7	10.7	25	0	0	0	28	200	174	17	0.3
clays and silts	17.38	23.7	80	35.5	12.6	8	26	260	181	23	0.25
sands	16.95	9.1	34	0	0	5	30	200	176	35	0.3
gravel	20	3.8	0	0	0	15	34	400	208	42	0.3
gravel	22	3.3	0	0	0	32	39	750	915	183	0.3

From the hydrogeological point of view, the Gran Lima aquifer consists of Quaternary alluvial deposits of Rimac and Chillon valleys. These deposits are characterized by the presence of boulders, gravel, sand and clay interspersed in layers and/or mixed. Another aspect is the presence of groundwater level that changes during the project area. In particular, the groundwater is located near the harbor zone in correspondence to the first part of line 2 and to the total of line 4.

4.3. Tectonics and seismicity

Perù is located on the east coast of the Pacific in so-called "Cinturon de Fuego del Pacifico" area that due to the interaction between the South America plate and Nazca plate, which generates a subduction zone near the Perù coast, represents one of the most active earthquake zones in the world. For this reason, a study of seismic risk of the project area was carried out to evaluate the correct seismic parameters. This study is based on seismic hazard determination which is defined as the exceedance probability of a determinate ground motion intensity value due to an earthquake in a given location and during a defined time interval. According to this study (with deterministic and probabilistic methods) and accounting to the spatial variability of the seismic action, the maximum value of the peak ground acceleration equal to 0.40 g has been obtained. For the evaluation of seismic design parameters five representative zones, each having different geophysical and geological characteristics, were considered (Table 20).

Table 20: Peak ground acceleration values

Location		**type of soil (ASTM)**	**PGA [g]**			
			200 [y]	**475 [y]**	**1000 [y]**	**2500 [y]**
Pto 1 Inicio L2	P. K. 1+800 L2	B	0.330	0.430	0.526	0.659
Pto 2 Inicio L4	P. K. 1+150 L4	B	0.326	0.423	0.517	0.655
Pto 3 Centro Historico	P.K. 11+700 L2	B	0.321	0.417	0.509	0.643
Pto 4 Etapa 1A	P.K. 19+500 L2	B	0.314	0.409	0.499	0.634
Pto 5 Final L2	P.K. 25+500 L2	B	0.309	0.402	0.489	0.619

4.4. Mercato Santa Anita Metro Station

The first step of the evaluation of the seismic vulnerability of the new Lime Metro line 2 is the study of the seismic behavior of the metro stations included in the Phase 1A, in particular of the Mercato Santa Anita Metro Station. In this area, as mentioned before, the groundwater is present but at great depth and does not interested the structures. The investigations around this area have shown the sequence of four lithological units having different geomechanical characteristics (Table 21).

Table 21: Lithological units (Etapa 1A)

Stratigraphic Column Etapa 1A										
Soil type		***h*** **(m)**	***γ*** **(kN/m^3)**	***c'*** **(kPa)**	***φ'*** **(°)**	***ν***	***E'*** **(MPa)**	***G*** **(MPa)**	***V_P*** **(m/s)**	***V_S*** **(m/s)**
backfill	R	1.7	16.7	0	28	0.3	17	7	300	200
gravel	GP-Ss	0.9	20	15	34	0.3	42	16	750	400
gravel	GP-Sm	6.1	21	27.5	36.5	0.3	82.5	31		460
gravel	GP-Sf	51.3	22	40	39	0.3	183	70	1500	750

In the Figure 217 the seismic signal frequency domain in comparison with the first three natural frequencies of the soil profile (Table 22) is reported. In this case, the fundamental frequencies are evaluated according to Maugeri et al. (1988) and it is possible to notice that the main peaks of the Fourier Transform are near the first mode bandwidths.

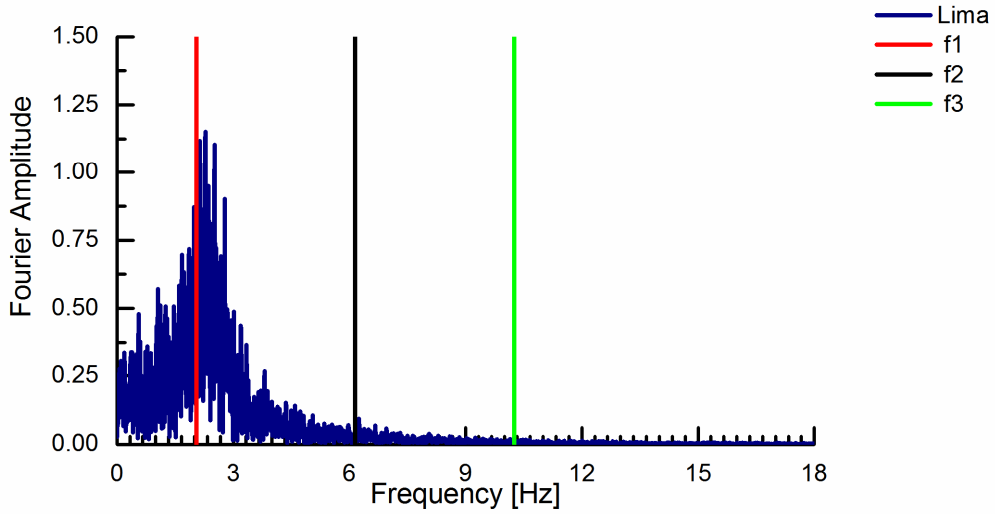

Figure 217: Seismic signal frequency domain and the main natural frequency of the soil profile evaluated according to Maugeri et al. (1988)

Table 22: First three natural frequencies of the Etapa 1A soil profile

f1	f2	f3
[Hz]	[Hz]	[Hz]
2.05	6.15	10.25

The station, as mentioned in the previous paragraph 3.2, is characterized by a rectangular plan (132.16 × 29.00 m) and it is subdivided into 3 different zones (Figure 218). Each zone is, further, subdivided into 3 different levels.

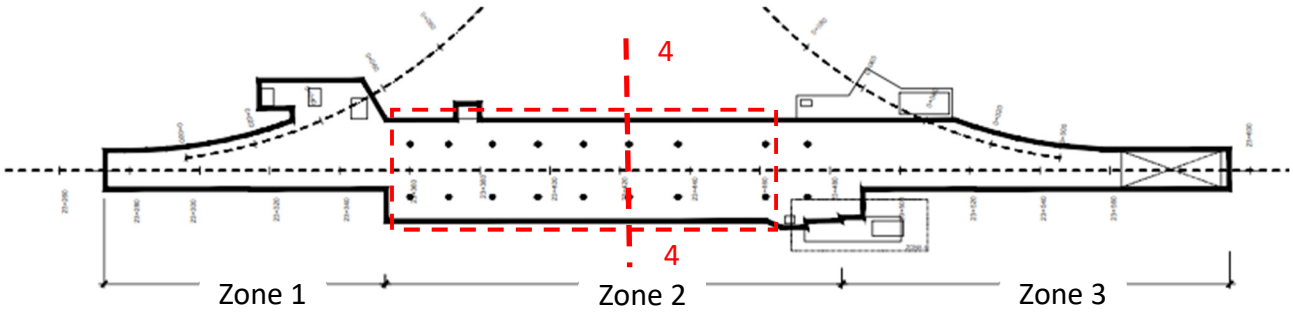

Figure 218: Mercato Santa Anita Metro Station

The principal structural elements that characterized the metro station are described in the previous Chapter 3.

The seismic input used in the evaluation of the seismic vulnerability of Mercato Santa Anita Metro station is the Lima seismic signal (already described in the previous sensitivity analysis) which it has been obtained according to the study of seismic risk of the project area described in paragraph 4.3. The principal characteristcs of the synthetic seismic signal are summarized in Table 23. The recording has been corrected with a low-pass filter at the cut-off frequency of 18 Hz.

Table 23: Characteristics of the seismic design action

Return period = 1000 y			
Moment Magnitude M_w	Fault distance	Fault type	V_s
8.7	45 km	subduction	1050 m/s

4.5. Numerical modelling

In the case of Mercato Santa Anita metro station, one 2D finite element model representing both structure and soil is implemented.
The FEM of section 4-4 is characterized by plane strain elements, and the geometry and the computation grid are shown in Figure 219. The dimensions of the model have been fixed in order to avoid the boundary effects and in this case have been taken equal to three times the size of the structure (in horizontal and vertical direction). The maximum size of computation mesh elements has been fixed in order to allow the correct propagation of harmonic with 18 Hz maximum frequency, which is the maximum frequency of the seismic signals adopted in this study, according to Kuhlemeyer and Lysmer (1973). The formulation used to optimize the size of the mesh is the following:

$$h \leq \left(\frac{1}{8} \div \frac{1}{5}\right) \frac{V_s}{f_{max}}$$

To minimize reflection effects on vertical lateral boundaries of the grid, free field boundary conditions available in MIDAS GTS library have been used. The structure is represented by linear elastic beams while for the soil an elastic perfectly plastic model with Mohr-Coulomb strength rule, characterized by the mechanical properties shown in Table 21, was adopted. The soil hysteretic behavior was modeled using the already described shear modulus decay curves given by Seed and Idriss (1970) and Stokoe et al. (2013). The hysteretic damping is, however, computed by applying the generalized Masing criteria implemented in the computer code mentioned before. The contact between soil and walls was modeled by using elastic-perfectly plastic interface elements, with a friction angle equal to 20°. The values of the stiffness of the interface elements are evaluated according to MIDAS GTS NX Manual (2017):

$$K_n = \frac{E_{0ed,i}}{t_v}$$

$$K_t \frac{G_i}{t_v}$$

where:

$$G_i = R \cdot G_{soil}$$

$$E_{oed,i} = 2\,G_i\,\frac{(1-\nu_i)}{(1-2\,\nu_i)}$$

and

- t_v = the virtual thickness which depends on the difference in stiffness between soil and structure and the value varies from 0.01 to 0.1. In this study the value considered is equal to 0.05 for each model;
- R = strength reduction factor taken as 1.

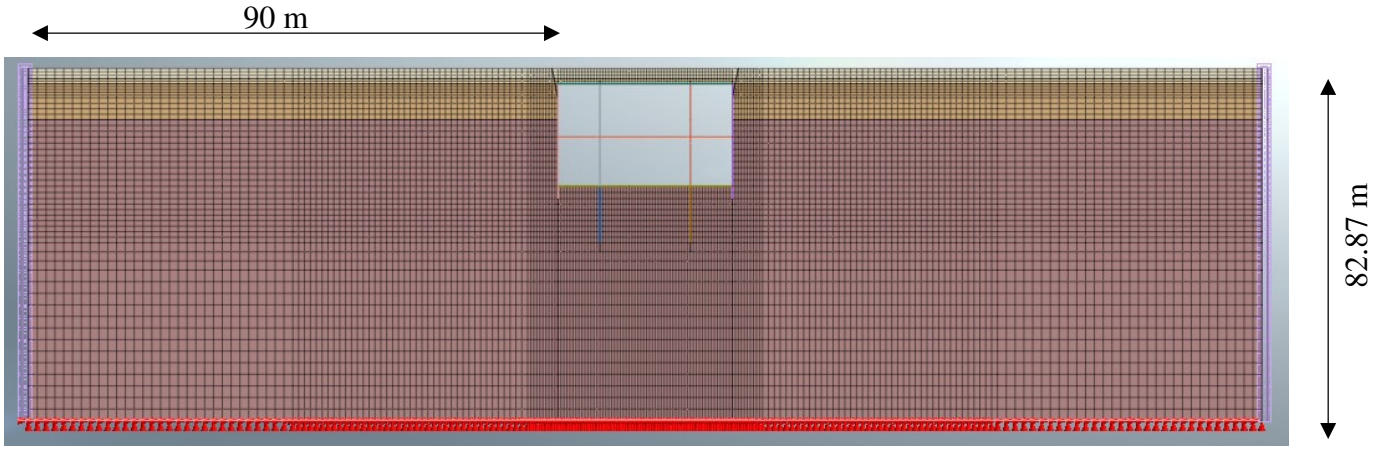

Figure 219: Section 4-4 FEM

4.6. Decoupled Approach

The concept of the decoupled approach used for the evaluation of the seismic behavior of the Mercato Santa Anita metro station is the same adopted in the previous sensitivity analysis, described in the Chapter 3. In this case, two different approaches are considered for the evaluation of the soil column displacements without taking into account the presence of the underground structure: the first is based on the equivalent linear method, always schematizing the soil profile through DEEPSOIL (Hashash et al., 2016) and the results are shown in Figure 220. The displacement at the ground level obtained by the equivalent linear method is equal to 11 cm and the trend of the displacements is according to the first vibration mode shape of the soil profile, as already highlighted by the previous Figure 217 where it is clear which the seismic signal mainly excites the first fundamental frequency of the soil profile.
The relative displacement applied at the roof of the structure is equal to (Figure 220):

$$\delta_A - \delta_B = 3\ [mm]$$

This contained value is due to the high value of the soil profile initial stiffness which strongly depends on the shear wave velocity that characterizes the lithological units. In fact, the initial shear modulus is obtained by the following relation:

$$G_0 = \rho \cdot V_S^2$$

The results, in terms of bending moment acting on the retaining walls, are showed, starting from the static values, in Figure 221. The increment of the value of the bending moment acting on the section in corresponce to the central slab, that represents the section characterized by the maximum value of the bending moment acting on the retaining walls, due to the seismic action is equal to the 3% of the initial value obtained by the static condition.

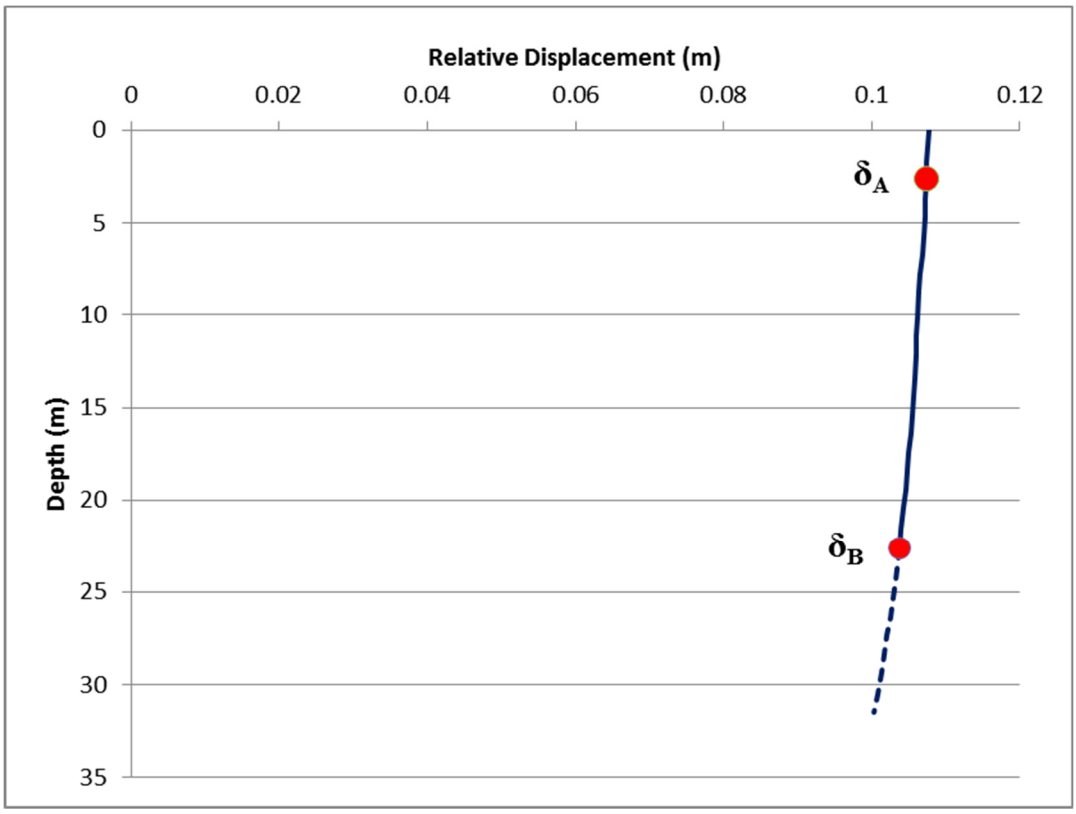

Figure 220: Trend of the displacements obtained by the equivalent liner method

The second approach, according to the analysis described in the previous Chapter 3, is to obtain the displacements at the depth of the roof and the base of the underground structure through the fully non-linear dynamic analysis.
In this case, the relative displacement obtained by the non linear analysis is greater than the relative displacement previously evaluated by the equivalent linear approach and it is equal to 7.5 mm but the increment of the bending moment (always evaluated in the section in correspondence to the central slab) is, however, low in comparison to the value of the initial moment due to static condition, that is about 8% (Figure 222).
The difference of the values of the relative displacement obtained by the two approaches, used in this study, is due to the non-linear beavior of the soil profile and how this has been taken into account during the analysis.

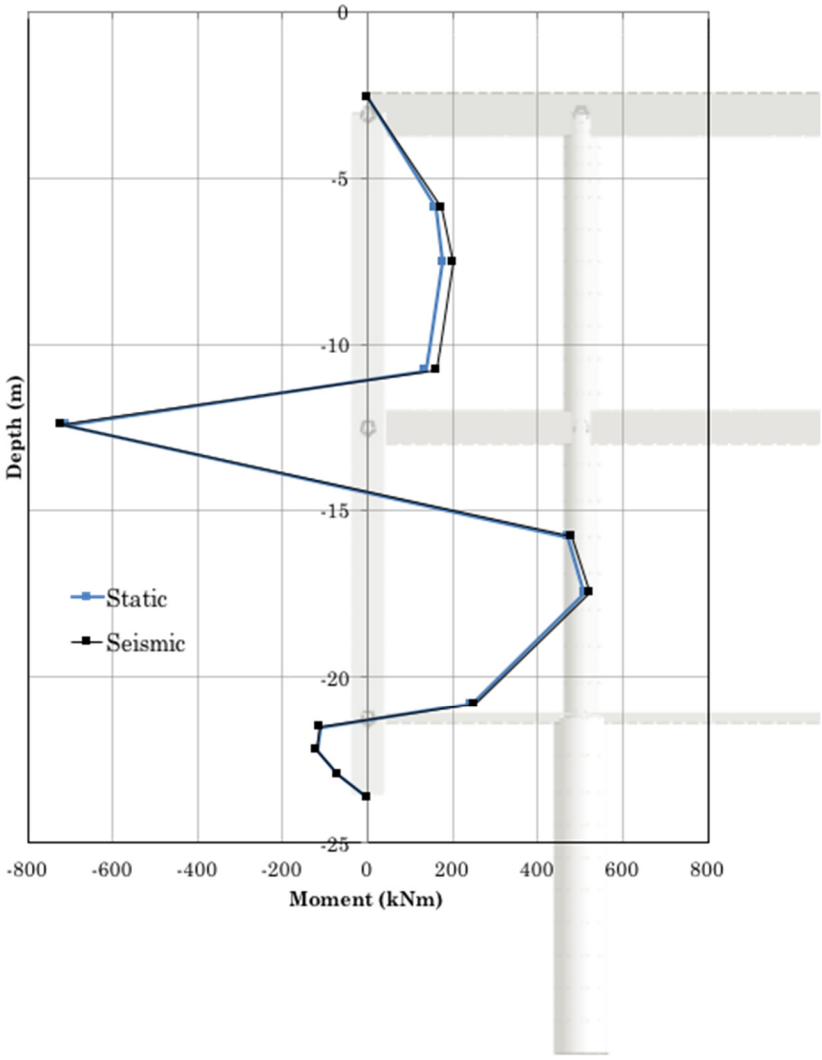

Figure 221: Equivalent linear analysis: reults in terms of bending moment acting on the concrete retaining walls

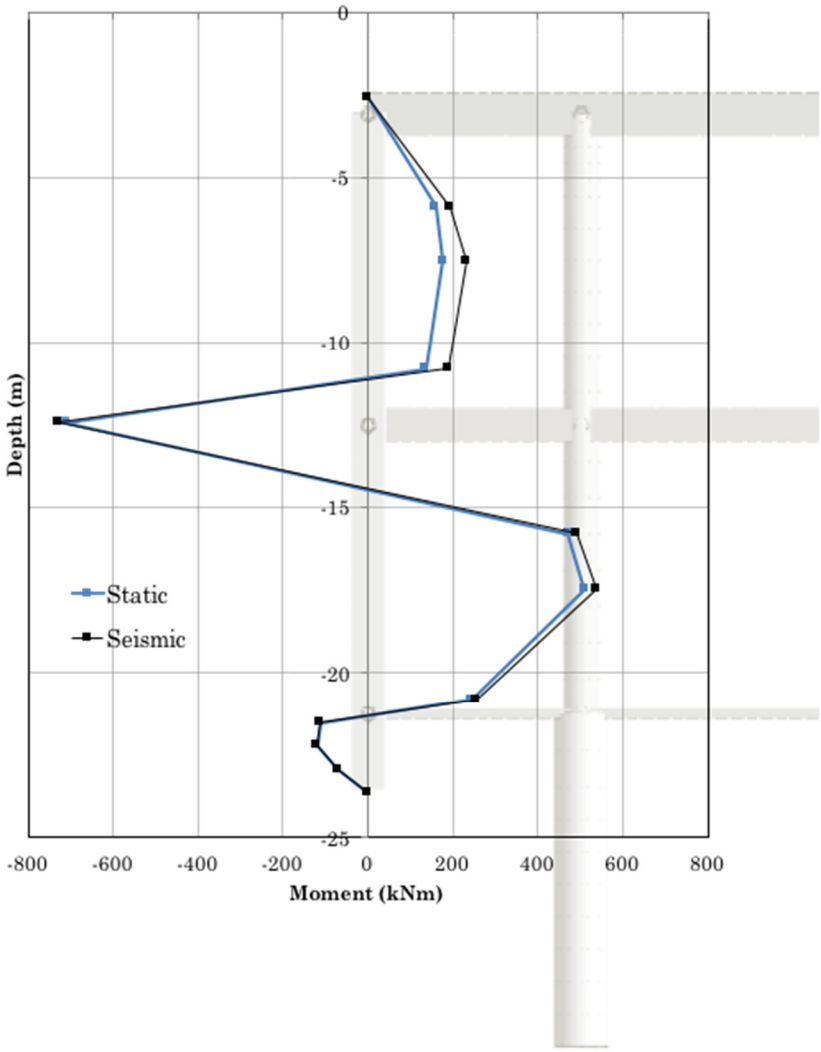

Figure 222: Non-linear analysis: reults in terms of bending moment acting on the concrete retaining walls

4.7. Coupled Approach

The evaluation of the seismic behavior of the Mercato Santa Anita metro station through the use of the coupled approaches was carried out by a fully non-linear dynamic analysis in time domain, considering the Finite Element Model described in the previous paragraph 4.5.
The structural condition of the metro station under the considered static loads are determined by performing a construction stage analysis, accounting to all the main phases involved in the construction of the station and in order to reproduce the excavation and the realization of the structure with cut and cover method (Figure 223), before the dynamic stage of the analysis (Figure 224). These construction phases and the loads considered in the static analysis are the same described in the previous paragraph 3.6.
The static analysis has pointed out the characteristic behavior of the retaining walls of the metro station's structure: it appears similar to a double multi-span (simply supported) beams. The presence of the central slab influences the behavior of the retaining walls under static and seismic loading.

In Figure 225 the value of the bending moment acting on the retaining walls obtained by the static loads (blue line), the value of the envelope of the bending moment due to the seismic action (black line) and the value of the residual bending moment acting on the retaining walls at the end of the seismic event (red line) are reported.
As seen above for the sensitivity analysis, the loads distribution on the retaining walls appears slightly asymmetric, while at the end to the seismic event (residual moment) it tends to balance.
The maximum increment of the bending moment due to the seismic action, always evaluated in the section in correspondence of the central slab, obtained by the coupled approach is near to 1100 kNm, while the residual moment acting in correspondence to the same section is equal to 110 kNm.
The high values of the increment obtained by the non-linear analyses are in according to the resonance effects induced by the seismic signal on the Etapa 1A soil profile. In fact, as mentioned before, the Lima seismic signal mainly excites the first vibration mode of the soil column.
The following Table 24 summarized the results obtained by the different approaches always in terms of bending moment acting on the section in correspondence to the central slab.

Table 24: Results of the different approaches in terms of bending moment acting on the section in correspondence to the central slab (DA = Decoupled Approach - EL = Equivalent Linear Analysis - NL = Non Linear Analysis - CA = Coupled Approach)

Approach	**Moment [kNm]**
DA - EL	**719**
DA - NL	**730**
CA - NL	**1701**

This significant difference in terms of value of bending moment acting on the retaining walls is due to the characteristics of the seismic signal, the non-linear behavior of the soil column and how this is defined, the interaction between the seismic signal and the soil column (resonance effects) and the type of analysis used (contemporaneity of the action, dynamic effects, etc).
In Table 24, it is possible to observe which, for the decoupled approach, the final value of the bending moment obtained at the end of the seismic event is significantly conditioned by the initial value due to the static loads because the seismic condition shows low values of increment both in the case of Equivalent Linear Analysis (3% of the initial value) and in the case of Non Linear Analysis (8% of the initial value) while it is not that for the coupled approach where the increment is significant (near 2 times the value obtained by the static analysis).

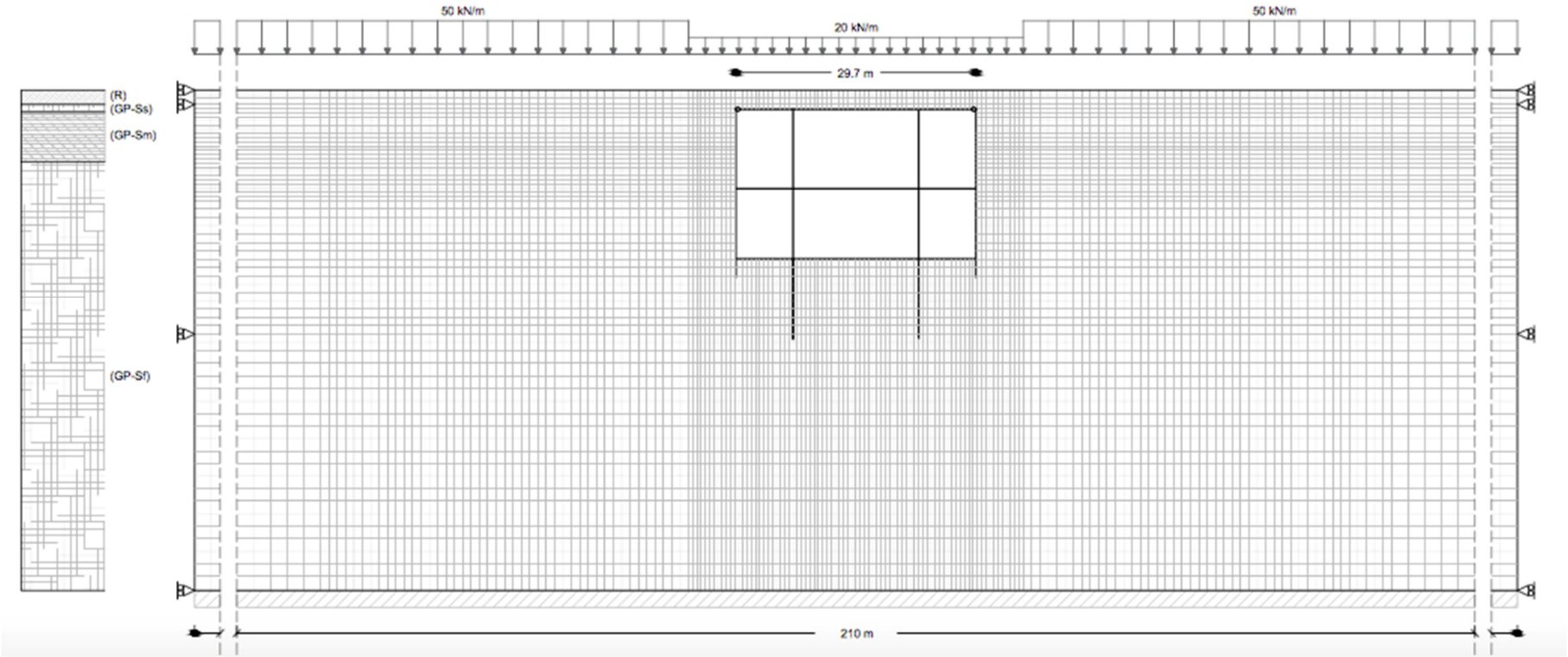

Figure 223: FEM static condition

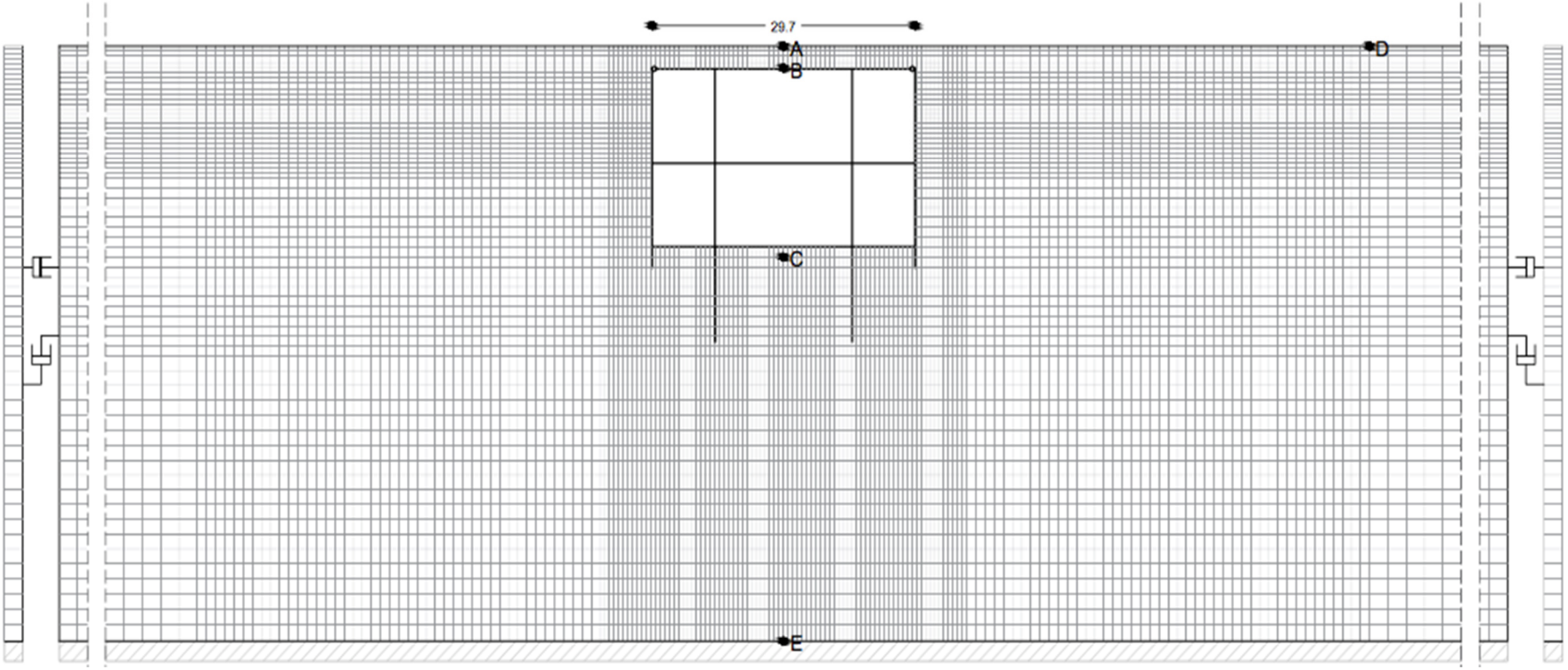

Figure 224: FEM dynamic condition

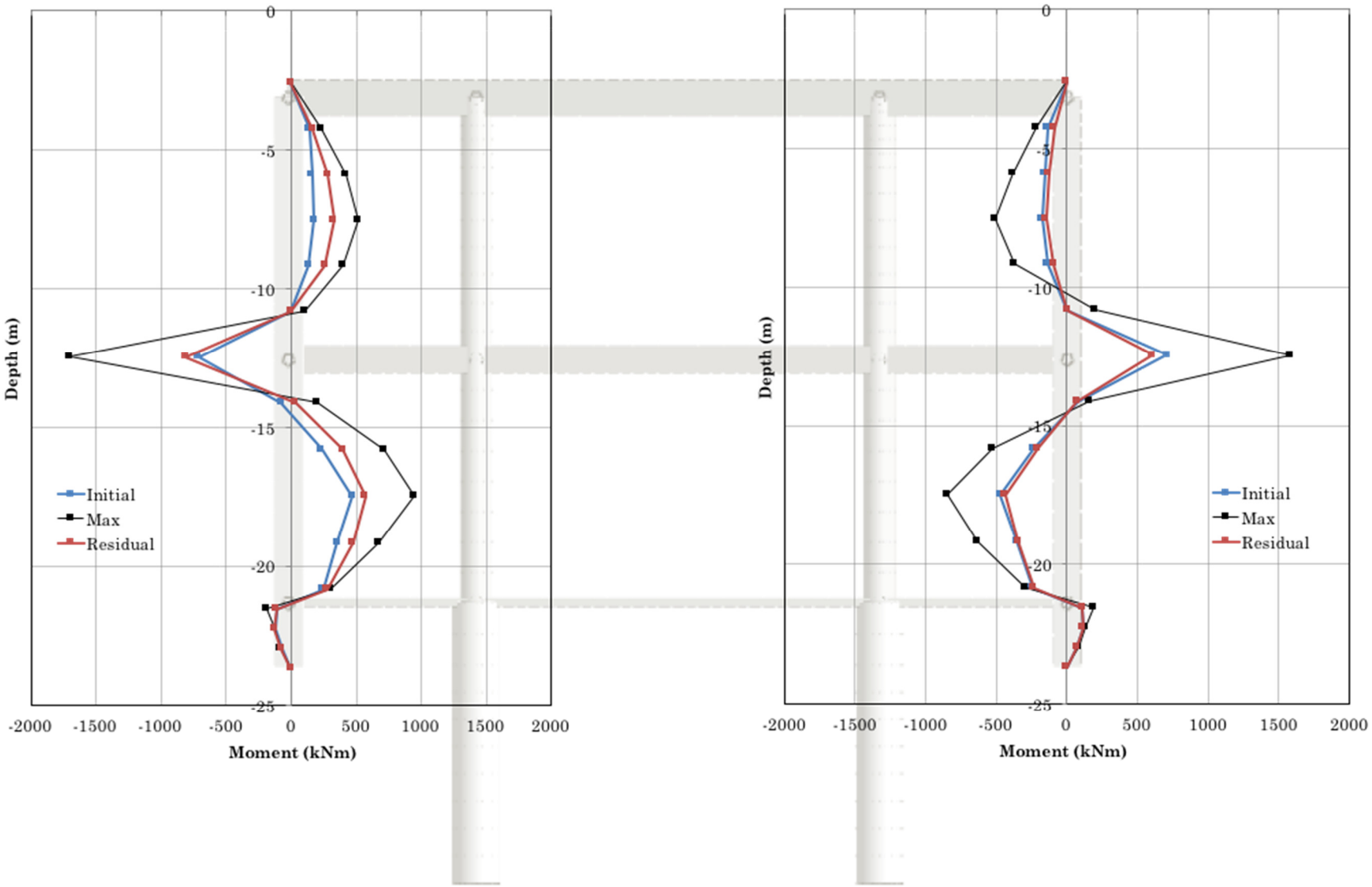

Figure 225: Coupled approach: bending moment acting on the retaining walls

5. CONCLUSIONS

The seismic behavior of a shallow underground structure has been analysed considering the Perfomance-Based Design approach. Four different types of soil profiles characterized by value of shear waves velocity between 360 m/s and 750 m/s subjected to six different seismic inputs (five natural acceleration time histories taken from the European Strong-Motion Database (Amatrice, Montenegro, L'Aquila, Friuli and Greece) and one synthetic accelerogram (Lima) have been analysed. The seismic signals have been selected between that of events with Magnitude between 6 and 7 and the peak ground acceleration value between 0.4 g and 0.6 g but characterized by different Arias intensity values. Only the synthetic accelerogram is characterized by a value of magnitude greater than 7, namely equal to 8.7.

All the seismic inputs, adopted in this study, showed resonance effects with the first vibration mode of the different soil profiles, leading to an increase of the shear strain in the deeper soil layers and, consequently, additional damping. The geometry of the system and the presence of the structure generate an amplification of the seismic motion behind the walls and at the center of the excavaton due to focusing phenomena of the waves and seismic motion attenuation in front of the retaining walls and to the diffraction phenomena of the waves. Only for the Lima seismc input was possibile to observe a seismic motion attenuation in the center of the excavation but a greater amplification of the seismic action behind the walls compared to the other seismic inputs. This phenomenon is due to the system damping of some frequencies that characterized the seismic input. The presence of the structure, furthermore, due to the its high stiffness, has produced additional reflections for the soil-structure interaction effects.

For the evaluation of the structural response, decoupled approach, considering the soil deformations induced by the seismic action without accounting the stiffness of the structure, and coupled approach, through the implementation of numerical models, have been performed. The results are discussed in terms of bending moment acting on the concrete retaining walls, considering the most loaded section that is the section in correspondence to the central slab (Figure 16). For the application of the decoupled approach, the displacements were evauated with two different methods: the first has involved the schematization of the soil profiles with DEEPSOIL (Hashash et al, 2016) and the execution of the Equivalent Linear analysis and the second method the displacements are obtained by a fully non-linear dynamic analysis.

The dispacements obtained by the equivalent linear analysis showed a trend resulting from the first vibration mode shape of the soil column. According to the previous considerations, in fact, the seismic signals mainly excite the first fundamental frequency of the soil profiles. Moreover, the displacement, evaluated at the ground level, decreases, significantly, when the stiffness of the soil column increases, in fact the maximum displacement, equal to 12 cm, was obtained for the soil profile characterized by V_S = 360 m/s under Lima seismic signal.

The results of the equivalent linear analysis indicated that the maximum increase of bending moment is equal to 110 kNm, using Montenegro seismic input while it was possible to see as the increase of bending moment due to the seismic load is almost negligible in cases where the soil profile is characterized by shear waves velocity equal to V_S = 600 m/s and V_S = 750 m/s.

Considering the fully non-linear 1D dynamic analyses results, the maximum increment of bending moment occurred in the profile characterized by V_S = 360 m/s for Montenegro earthquake and it is equal to 125 kNm.

The difference of the results, in terms of bending moment acting on the section in correspondence to the central slab, obtained by the equivalent linear analysis and that resulted from non-linear

analysis were between 2% and 4% for all the natural accelerograms. This limited value is due to the incidence of the value of the moment obtained under static conditions on the value of the final moment compared to the increment due to the seismic action.
The same situation has not been obtained for Lima seismic input where the difference between the results obtained by the equivalent analysis and the results obtained by the non linear analysis was significant (greater than 40% for the soil profiles characterized by V_S = 360 m/s and 450 m/s and almost 20% for the soil profiles characterized by V_S = 600 m/s and 750 m/s).
The results of the coupled approach showed that for all the accelerograms the increment due to the seismic action was higher for the soil profiles characterized by V_s = 600 m/s and 750 m/s in contrast to the decoupled approach results. The maximum increment, also in this case, occurred under Lima seismic signal and was equal to 1493 kNm for the soil profile characterized by V_S = 750 m/s. For the natural accelerograms, instead, the maximum increment obtained was about 150 kNm always under Montenegro seismic input. The trend of the maximum value of the bending moment, obtained during the seismic event, acting on the section in correspondence to the central slab, showed a decrease of the maximum value when the soil column stiffness increases. Only for the Lima seismic input the maximum value of the bending moment was obtained for the soil profile characterized by V_S = 450 m/s according to the resonance effects highlighted by the Figure 28.
Figures 226, 227, 228, 229, 230 and 231 show the summary of the results obtained by the different approaches for all the seismic inputs.

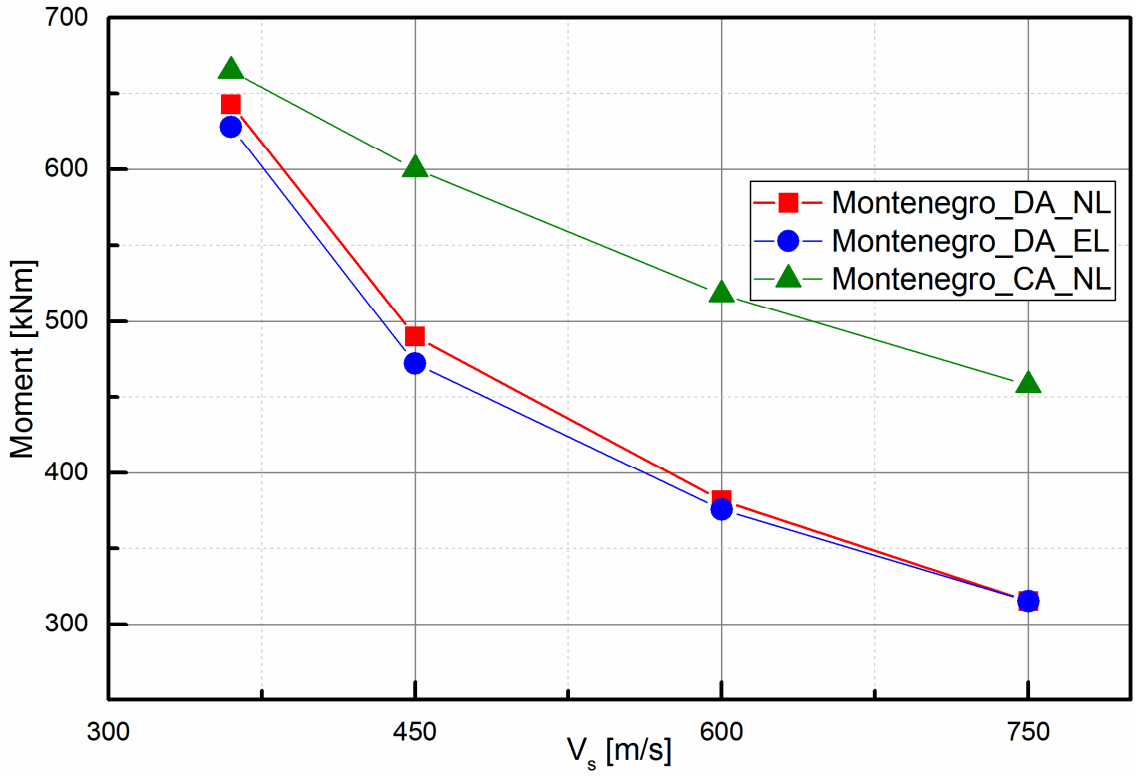

Figure 226: Comparison of the results for Montenegro seismic input

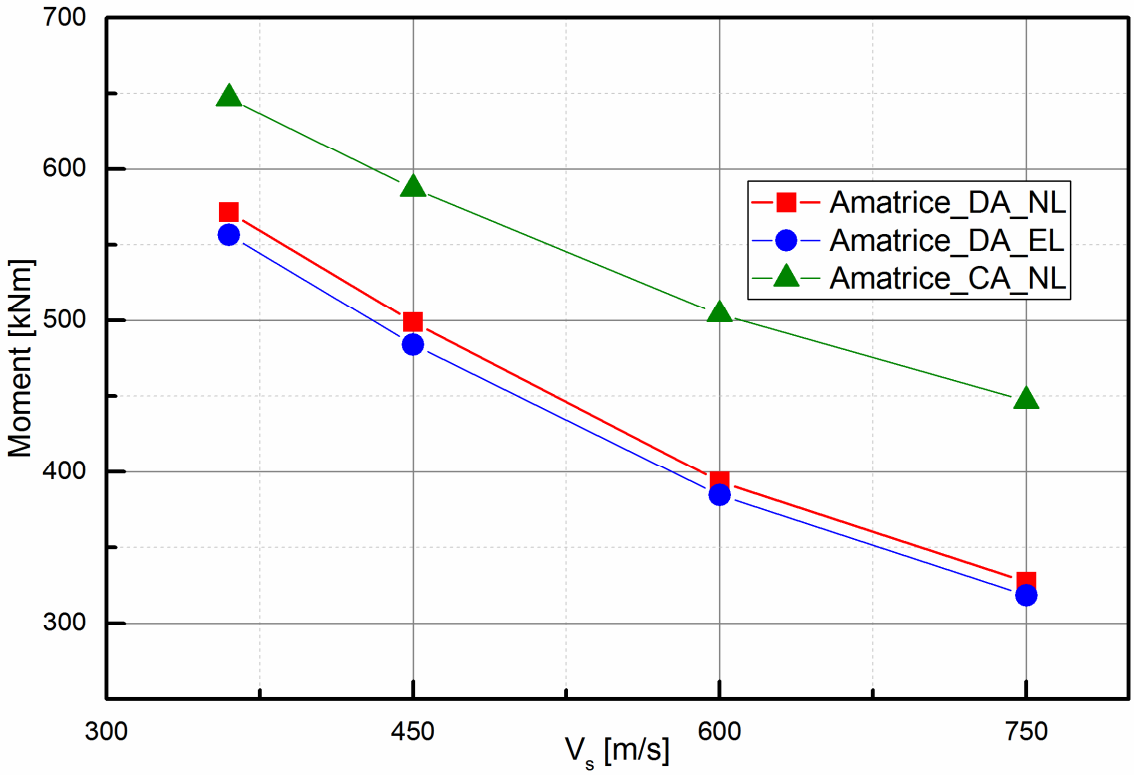

Figure 227: Comparison of the results for Amatrice seismic input

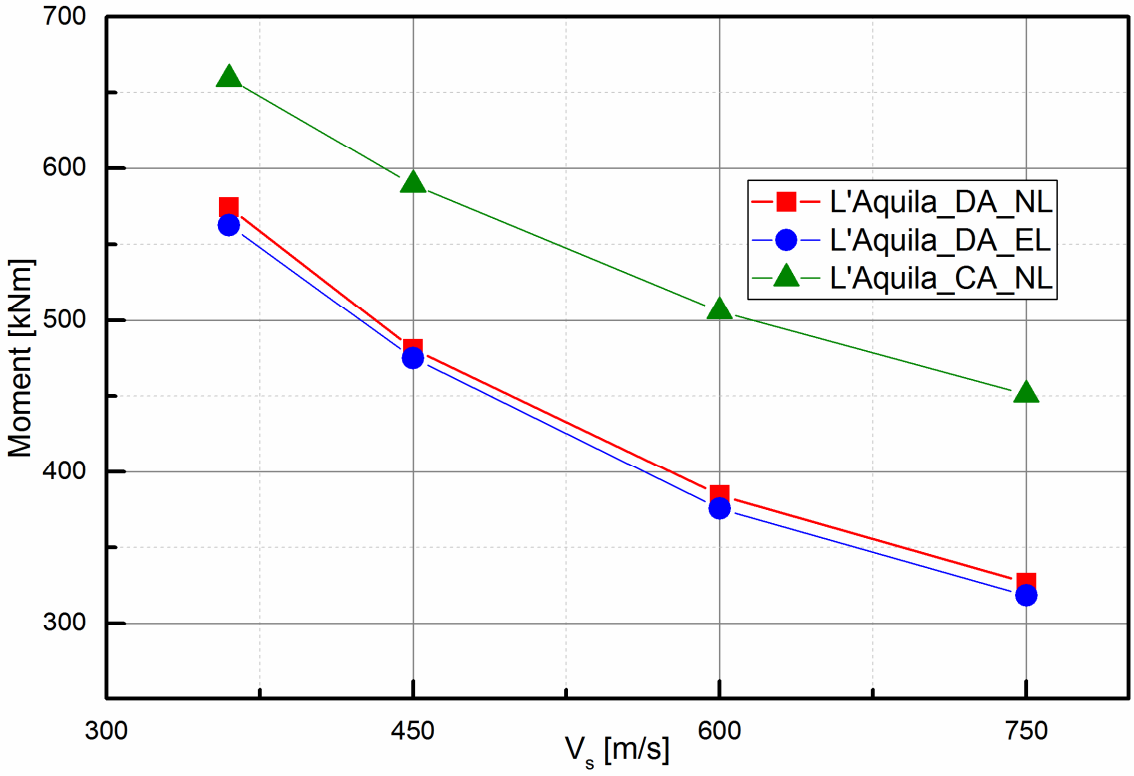

Figure 228: Comparison of the results for L'Aquila seismic input

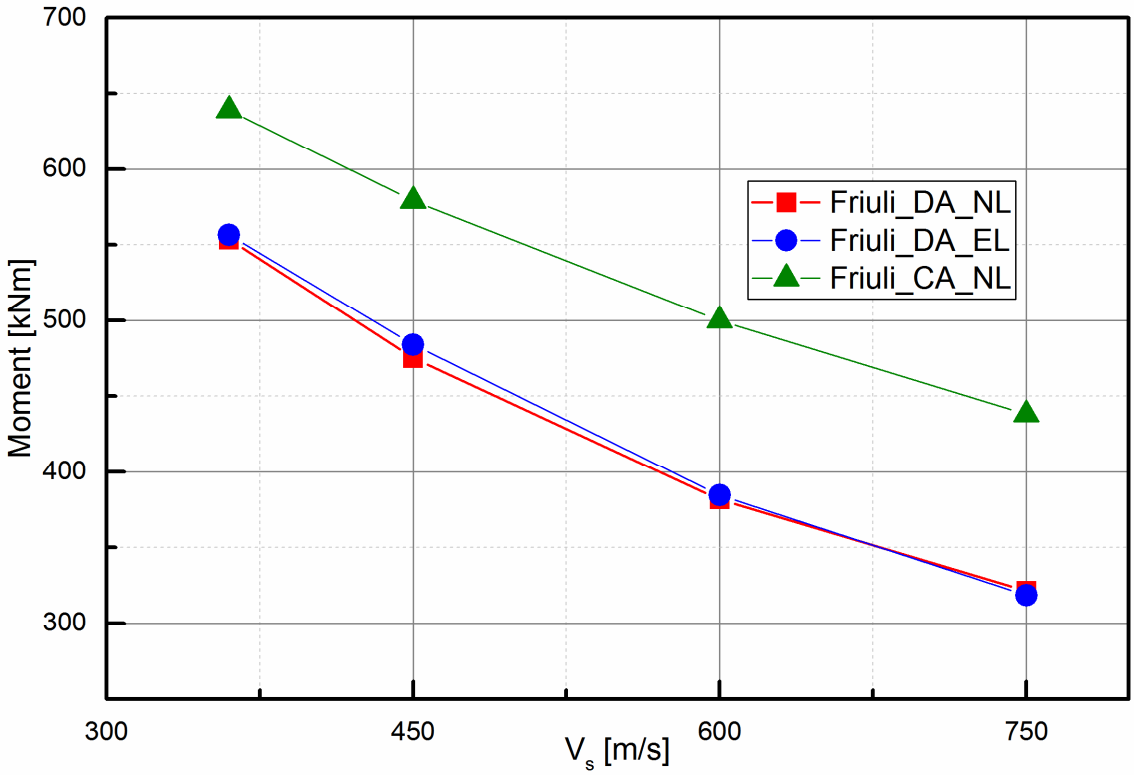

Figure 229: Comparison of the results for Friuli seismic input

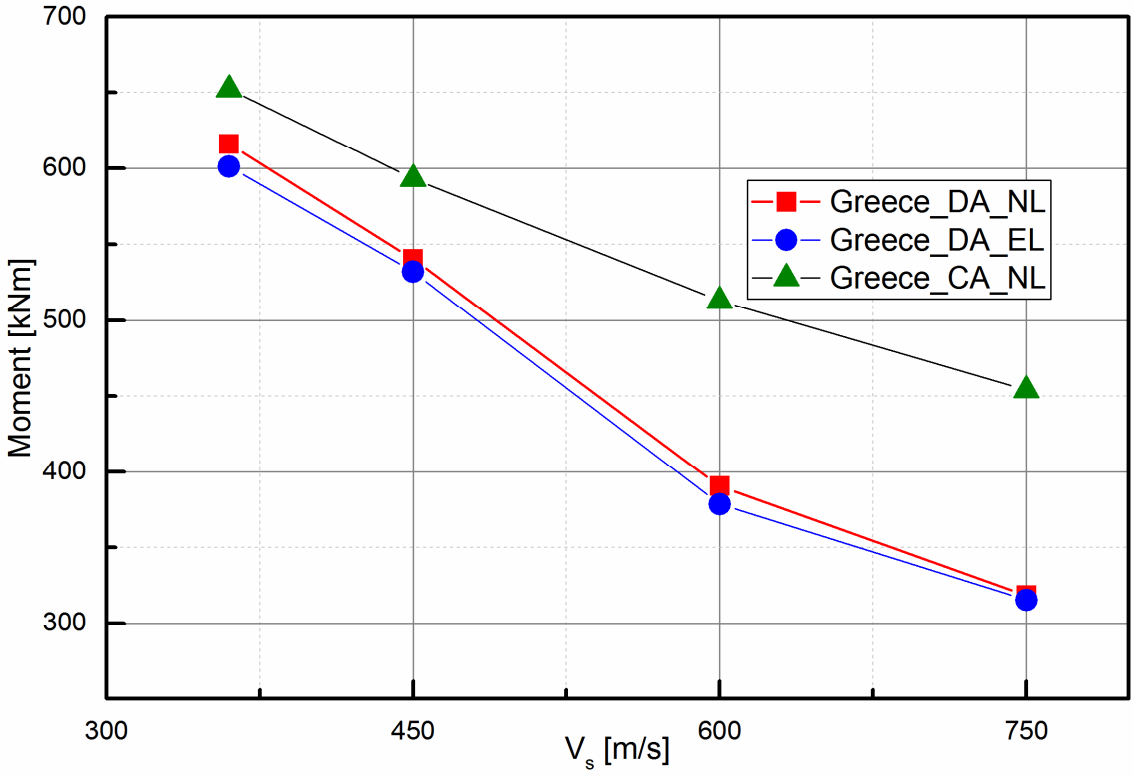

Figure 230: Comparison of the results for Greece seismic input

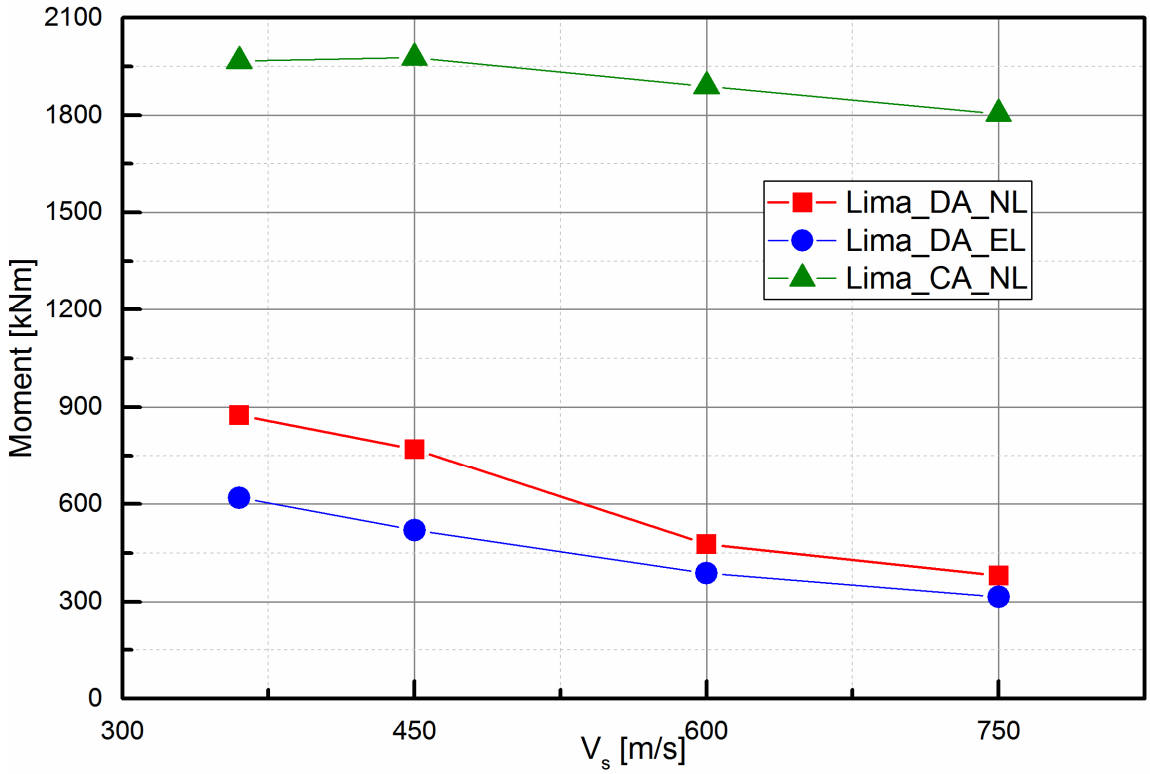

Figure 231: Comparison of the results for Lima seismic input

The values, in terms of maximum bending moment acting on the section in correspondence to the central slab during the seismic event, obtained by the coupled approach are always greater than the values obtained by the decoupled approach. These differences are most significant for the synthetic accelerogram (Lima) where the decoupled approach appears underestimate the internal actions on the structural elements while for the natural accelerograms (Montenegro, Amatrice, L'Aquila, Friuli and Greece) are moderate for the soil profiles characterized by a low stiffness, confirming their validity, but tending to increase for the soil profiles characterized by $V_S = 600$ m/s and 750 m/s. This difference in behavior between the synthetic signal and the natural accelerograms is due to the particular characteristics of the Lima seismic input (symmetry of the signal, frequency content, high value of Arias Intensity, duration, etc). Furthermore, the results obtained are affected by the different assumptions which characterize the methods. In particular, the decoupled approach tends to lose the criterion of the contemporaneity of the actions because they are considered only the maximum displacement that occurs during a seismic event. Another important aspect is due to the non-linear behavior of the soil and how it is taken into consideration during the analysis because in Lanzo & Silvestri (1999) is indicated as the equivalent linear analysis is not suitable for the event characterized by high value of the seismic motion parameters like Lima signal.
Taking as a reference the case study, described in the Chapter 4, the results obtained by the different approaches are in according to the considerations abovementioned. In fact, the decoupled approach understimates the values of the bending moment acting on the concrete retaining walls.

REFERENCES

Anastasopoulos I, Gazetas G. (2010). Analysis of cut-and-cover tunnels against large tectonic deformation. *Bulletin of Earthquake Engineering 8(2)*: pp. 283-307.

Anderson D.G., Martin G.R., Lam I. and Wang J.N. (2008) NCHPR611: *Seismic analysis oand design of retaing walls, buried structures, slopes and embankments*. Wahington, DC: National Cooperative Highway Research Program, Transportation Researck Board.

Baker J.W., Cornell A. (2005) A vector-valued ground motion intensity measure consisting of spectral acceleration and epsilon. *Earthquake Engineering and Structural Dynamics 34*: pp. 1193-1217.

Bickel J.O. (1996) Tunnel engineering handbook; Chapman and Hall, New York.

Bobet A. (2003) Effect of pore water pressure on tunnel support during static and seismic loading. *Tunneling and Underground Space Technology, 18(4)*: pp. 377-393.

Bobet A. (2010) Drained and undrained response of deep tnnels subjected to far-field shear loading. *Tunneling and Underground Space Technology 25(1)*: pp. 21-31.

Dowding C.H., Rozen A. (1978) Damage to rock tunnels from earthquake shaking. *Journal of Geotechnical Engineering Division*, ASCE 104: pp. 175-191.

FHWA (Federal Highway Adminidtration) (2009) *Techincal manula for design and construction of road tunnesls - Civil elements. Publication No. FHWA-NHI-10-034*. Washington DC: Department of transportation, Federal Highway Administrator.

Gazetas G. (1991a) Formulas and charts for impedances of surface and embedded foundations. *Journal of Geotechnical Engineering, ASCE 117(9)*: pp. 1363-1381.

Gazetas G. (1991b) Foundation vibrations. In H.-Y Fang (ed.), *Foundation engineering handbook*: pp. 553-593. USA: Springer.

Gazetas G., Gerolymos N., Anastasopoulos I. (2005) Response of three Athens metro underground structure in the 1999 Parintha earthquake. *Soil Dynamics and Earthquake Engineering 25*: pp. 617-633.

Gerolymos N., Gazetas G. (2006) Winkler model for lateralresponse of rigid caisson foundations in linear soil. *Soil Dynamics and Earthquake Engineering 26(5)*: pp. 347-361.

Hashash Y.M.A., Hook J., Schmidt B., Yao J. (2001) Seismic design and analysis of underground structures. *Tunnelling and Underground Space Technology 16*, pp. 247 – 293.

Hashash Y.M.A., Karina K., Koutsoftas D., O'Riordan N. (2010) Seismic design considerations for underground box structures. In Proc. of earth retention conference 3, Bellevue: ASCE.

Hashash Y.M.A., Musgrove M.I., Harmon J.A., Groholski D.R., Phillips C.A., Park D. (2016) DEEPSOIL 6.1, User Manual. Urbana, IL, Board of Trustees of University of Illinois at Urbana-Champaign.

Hoeg K. (1968) Stresses against underground structural cylinders. *Journal of Soil Mechanics and Foundations Division, ASCE 94*: pp. 833-858.

Hosseini M.M., Pajouh M.A., Hosseini F.M. (2010) The limitations of equivalent linear site response analysis considering soil nonlinearity properties. 5th International Conference on Recent Advances in Geotechincal Earthquake Engineering and Soil Dynamics, 24-29 May, Missouri University of Science and Technology.

Huo H., Bobet A., Fernandez G., Ramirez J. (2006) Analytical solution for deep rectangular structures subjected to far-field shear stresses. *Tunneling and Undergorund Space Technology 21(6)*: pp. 613-625.

Idriss I.M., Sun J.J. (1992) Shake91: A computer program for conducting equivalent linear seismic response analysis of horizontally layered soil deposits. User's Guide, Center for Geotechincal Modeling, Civil Engineering Department, UC Davis.

Iida H., Hiroto T., Yoshida N., Iwafuji M. (1996) Damage to Daikai subway station. In *special issue on geotechnical aspects of January 17 1995 Hyogoken-Nanbu earthquake*. Japan: Soil and Foundatons.

ISO (International Organization for Standardization) (2005) ISO 23469: *Bases for design of structures - Seismic actions for designing geotechnical works. Internation Standard ISO TC98/SC3/WG10*. Geneva: International Organization for Standardization.

Itasca Consulting Group Inc., 2007 FLAC ^{2D}: Fast Legrangian Analysis of Continua.

JRA (Japan Road Association) (1992) Guide specifications of design and construction of underground parking lots. Tokyo: Ministry of Transportation.

Kanai K. (1995) Engineering Seismology, University of Tokyo Press.

Kawashima K. (2000) Seismic design of underground structures in soft ground: A review. In Kusakabe, Fujita & Miyazaki (eds.). *Geotechnical aspects of undergournd construction in soft ground*. Rotterdam: Balkema.

Kawashima K. (2006) Seismic analysis of undrgorund structures. *Journal of Disaster Research 1(3)*: pp. 378-389.

Kiyomiya O. (1995) Earthquake-resistant design features of immersed tunnels in Japan. *Tunneling and Undergorund Space Technology 10(4)*: 463-475.

Kolsky H. (1963) Stress waves in anelastic solids. *Journal of Geophysical Research Vol. 68 - Issue 4*: pp. 1193-1194.

Kontoe S., Zdravkovic L., Potts D., Mentiki C. (2008) Case study on seismic tunnels response. *Canadian Geotechnical Journal 45*: pp. 1743-2764.

Kouretzis G.P., Andrianopoulos K.I., Sloan S.W., Carter J.P. (2014) Analysis of cirucla tunnels due to seismic P-wave propagation, with emphasis on unreinforced concrete liners. *Computers and Geotechnics 55*: pp. 187-194.

Kramer S.L. (1996) Geotechnical Earthquake Engineering; Prentice-Hall, New Jersey.

Kuasel E., Christian J.T., Roesset J.M. (1976) Nonlinear behaviour in soil-structure interaction. *Journal of Geotechnical Engineering Division, ASCE 102(11)*: pp- 1159-1170.

Kuhlemeyer R. L., Lysmer J. (1973) Finite element method accuracy for wave propagation problems. *Journal of Soil Mechanics & Foundations Division*. ASCE, 99(SM5): pp. 421-427.

Lanzo G., Silvestri F. (1999) Risposta sismica locale. Teoria ed esprienze. Hevelius, Italy.

Luco N., Cornell A. (2007) Structure-specific scalar intensity measures for near-source and ordinary earthquake ground motions. *Earthquake Spectra Vol. 23*: pp. 357-392.

Maugeri M., Carrubba P., Frenna S.M. (1988) Frequenze e modi di vibrazione di terreni eterogenei. Associazione Geotecnica Italiana.

MIDAS GTS NX (2017), Analysis Reference.

Mononobe N., Matsuo H. (1929) On the determination of earth pressures during earthquakes. In Proc. of the second world conference on earthquake engineering. Tokyo.

Newmark N.M. (1968) Problems in wave propagation in soil and rock. In Proc. of international symposium on wave propagation and dynamic properties of earth materials. New Mexico: University of New Mexico Press.

Okabe S. (1926) General theory of earth pressure and laboratory testing on seismic stability of retaing walls. *Journal od the Japanese Society of Civil Engineering 12(1)*: pp. 123-134.

Owen G.N., Scholl R.E. (1981) Earthquake engineering of large underground structures. Report No. FHWA/RD-80/195. Federal Highway Administration and National Science Foundation.

Pagliaroli A., Lanzo G., Sanò T. (2007) Confronto fra tre codici di calcolo 2D della risposta sismica locale. XII Congresso Nazionale "l'Ingegneria sismica in Italia", ANIDIS.

Park K.H., Tantayopin K., Tontavanich B., Owatsiriwong A. (2009) Analitycal solution for seismic-induces ovaling of circular tunnel lining under no-slip interface conditions: A revisit. *Tunneling and Undergoround Space Technology 24(2)*: pp. 231-235.

Pavlovic N. (2004) Ground response analysis as an essential part of earthquake-resistant structures design; Asia 2004, Conference on Earthquake Engineering, ASEP, Manila 2004.

Penzien J, Wu C. (1998) Stresses in linings of bored tunnels. *Earthquake Engineering and Structural Dynamics 27*: pp. 283-300.

Penzien J. (2000) Seismically induced racking of tunnels lining. *Earthquake Engineering and Structural Dynamics 27*: pp. 683-691.

Pitilakis K., Tsinidis G. (2014) Performance and seismic design of underground structures. In M. Maugeri & Soccodato C. (eds.). *Earthquake geotechnical engineering design, Geotechincal Geological and Earthquake Engineering, 28*: pp. 279-340. Switzerland: Springer international publishing.

Pitilakis K., Tsinidis G. (2016) Recent advances on the seismic behaviour and design of tunnesl. AGI 2016.

Power M., Rosidi D., Keneshiro J., Gilstrap S., Chiou S.J. (1998) Summary and evaluation procedures for the seismic design of tunnels. Final report task 112-d-5.3(c). Buffalo: National center for earthquake engineering research.

Roesset J.M., Whitman R.V. (1969) Theroretical background for amplification studies - Research Report R69-15, M.I.T. Department of Civil Engineering.

Schnabel P.B., Lysmer J., Seed H.B. (1972) SHAKE, a computer program for earthquake response analysis of horizontal layered sites. Report No. EERC72-12, December.

Seed H., Whitman R.V. (1970) Design of earth retaingn structure of dynamic loads. In Proc. of ASCE speciality conference on lateral stresses in the ground and design of earth retaining structures. Ithaca.

Seed H.B., Idriss I.M. (1970) Soil moduli and damping factors for dynamic analysis. Report No. EERC 70-10, University of California, Berkeley.

Sharma S., Judd W.R. (1991) Undergorund opening damage from earthquakes. *Engineering Geology 30*: pp. 262-279.

Shome N., Cornell A., Bazzurro P., Carballo J.E. (1998) Earthquakes, Records and Nonlinear Response. *Earthquake Spectra Vol. 14*: pp. 469-500.

Soccodato F.M., Tropeano G. (2015) The role of ground motion characters on the dynamic performance of propped retaining structures; 6ICEGE, 6th International Conference on Earthquake Geotechnical Engineering, 1 – 4 November 2015, Christchurch, New Zealand.

St. John C.M., Zahrah T.F. (1987) Aseismic design of underground structures. *Tunneling and Undergorund Space Technology 2(2)*: pp. 165-197.

Stokoe K.H., Jung M.J., Menq F.-Y., Liao T., Massoudi N., McHood M. (2013) Normalized shear modulus of compacted gravel. 18th International Conference on Soil Mechanics and Geotechnical Engineering, Paris, France.

Tothong P., Luco N. (2007) Probabilistic seismic demand analysis using advanced ground motion intensity measures. *Earthquake Engineering and Structural Dynamics 36*: pp. 1837-1860.

Tsai N.C., Housner G.W. (1970) Calculation of surface motions of a layered half-space. *Bulletin of the Seismological Society of America 60(5)*.

Vamvatsikos D., Cornell A. (2005) Direct estimation of seismic demand and capacity of multidegree-of-freedom systems through incremental dynamic analysis of single degree of freedom approximation. *Journal of Structural Engineering 134 - Issue 4*.

Vazauros P., Karamanos S.A., Dakoulas P. (2010) Finite element analysis of buried steel pipelines under strike-slip fault displacements. *Soil Dynamics and Earthquake Engineering 30(11)*: pp. 1361-1376.

Vazauros P., Karamanos S.A., Dakoulas P. (2012). Mechanical behaviour of buried steel pipes crossing active strike-slip faults. *Soil Dynamics and Earthquake Engineering 41*: pp. 164-180.

Vrettos C. (2005) Design issues for immersed tunnel foundations in seismic areas. In Proc. of the first Greece-Japan worshop on seismic design, observation, and retrofit of foundations. Athens.

Wang J.N. (1993) Seismic Design of Tunnels; Parson Brinckerhoff Inc., New York.

Wang W.L., Wang T.T., Su J.J., Lin C.H., Seng C.R., Huang T.H. (2001) Assessment of damage in mountain tunnels due to the Taiwan Chi-Chi earthquake. *Tunneling and Underground Space Technology 16*: pp. 133-150.

Wang Z.Z., Gao B., Jiang Y.J., Yuan S. (2009) Investigation and assessiment on mountain tunnels and geotechnical damage after the Wenchuan earthquake. *Science in China, Series E-Technological Scinces 52(2)*: pp. 546-558.

Wells D.L., Coppersmith K.J. (1994) New empirical relationships among magnitude, rupture length, rupture width, rupture area, and surface displacement. Seismological Society of America.

Yoshiwa K., Fikuchi G. (1984) Earthquake damage to railway tunnels in Japan. *Advances in Tunneling Technology and Subsurface Use 4(3)*: pp. 75-83.

Zucca M., Crespi P., Longarini N. (2017) Seismic vulnerability assessment of an Italian historical masonry dry dock. *Case Studies in Structural Engineering (7)*: pp. 1-23.